

UCLA

UCLA Electronic Theses and Dissertations

Title

Terahertz imaging and sensing for ophthalmic evaluation of corneal diseases

Permalink

<https://escholarship.org/uc/item/2q22f82v>

Author

Sung, Shijun

Publication Date

2017

Peer reviewed|Thesis/dissertation

UNIVERSITY OF CALIFORNIA

Los Angeles

Terahertz Imaging and Sensing for Ophthalmic Evaluation of Corneal Diseases

A dissertation submitted in partial satisfaction of the
requirements for the degree Doctor of Philosophy
in Electrical Engineering

by

Shijun Sung

2017

© Copyright by

Shijun Sung

2017

ABSTRACT OF THE DISSERTATION

Terahertz Imaging and Sensing for Ophthalmic Evaluation of Corneal Diseases

by

Shijun Sung

Doctor of Philosophy in Electrical Engineering

University of California, Los Angeles, 2017

Professor Warren Grundfest, Chair

In the span of electromagnetic wave band from microwave to X-rays, Interactions of biological tissue and light at the terahertz (THz) wavelength band ($\lambda \sim 30\mu\text{m} - 3\text{mm}$) are particularly unique for two reasons. First, the THz band retains a large dielectric constant for water from the microwave region while its shorter wavelength enables imaging applications with $< 1\text{mm}$ resolution. Second, the effect of scattering from typical soft tissue structures (i.e. cells, collagen matrix, etc.) is less in the THz band compared to that in higher-frequency bands (IR band and up). Using this balance of properties, our study applies non-invasive THz sensing to study diseases and conditions that compromise our body's ability to balance water in tissues.

This study focuses on developing a novel medical imaging technology using THz frequency waves to accurately assess and image the tissue water content of the cornea, which is a critical refractive and protective component of the eye. In ophthalmology, most corneal disorders such as Fuchs endothelial dystrophy (failure of stromal hydration regulation), Keratoconus (corneal ectasia), pseudophakic bullous keratopathy (unintentionally damaged endothelial layer), and

corneal graft rejection result in corneal edema. Corneal edema is a contributing factor leading to corneal opacity, and if left untreated, can lead to chronic vision impairment. Accurate corneal tissue water content (CTWC) measurement, therefore can help with early diagnosis and intervention for corneal diseases and further our understanding of the formation and progression of corneal disorders.

This work details the development of a THz remote-sensing technique based on rigorous electromagnetic model of cornea-THz interaction, and an imaging system that can be practically implemented in the clinical setting. A novel ophthalmic THz imaging system is designed and implemented to perform completely non-contact, all normal-incidence imaging of the corneal surface. The imaging system uses a wavelength independent quasioptical design that achieves a <1.4 mm spatial resolution at 650 GHz. The corneal hydration sensing capability of this imager is demonstrated in *in vivo* corneas. For the first time, THz images of a living cornea showed the onset of acute corneal edema from endothelial damage. The THz imaging system is currently being used in the first phase of the clinical study to evaluate healthy and diseased corneas of patients with corneal graft and corneal dystrophies.

The thesis of Shijun Sung is approved.

Benjamin S. Williams

Daniel B. Ennis

Oscar M. Stafsudd

Sophie X. Deng

Zachary Deis Taylor

Warren Grundfest, Committee Chair

University of California, Los Angeles

2017

Table of Contents

Chapter 1 : Introduction	1
1.1. Statement of the problem and the study objective	1
1.2. Limitations of clinically available measurement techniques	6
1.3. THz frequency devices, technology, and system integration.....	9
1.3.1. THz source and detector devices	11
1.4. THz Imaging: Theory and Implementation.....	14
1.4.1. THz-tissue interaction.....	14
1.5. THz imaging of tissue hydration – A survey of metrics	20
1.5.1. Image formation	24
Chapter 2 THz Imaging System Design	27
2.1. Quasioptical Approximation and Beam transformation.....	27
2.2. Quasioptical imaging components.	30
2.2.1. 90° Off-axis parabolic mirror: geometry	31
2.3. Transformation of Gaussian beam by 90° OAP reflectors.....	34
2.4. OAP mirror Systems	37
2.4.1. Imaging System Implementation.....	40
2.4.2. Confocality of the imaging system.....	48
2.5. Distortion of beam shape and polarization profile	53
2.5.1. Field distortion and Polarization Aberration	53
2.5.2. Design Rule 1: Matched (symmetric) orientation	56
2.5.3. Design rule 2: Magnify the detector	59
2.6. THz imaging system design: Conclusion.....	64
Chapter 3 : THz-Corneal Tissue Interaction: Electromagnetic Modeling and First <i>in vivo</i> Experiment.....	66
3.1. Revisiting the anatomy of cornea.....	66
3.2. Stratified media model analysis	68
3.2.1. Problem set-up and assignment of tissue properties.....	68
3.2.2. CTWC gradient models	72
3.2.3. First-pass observations	75
3.2.4. Cornea EM models: The scope of Analysis	77

3.3. THz reflectivity of corneal tissue at 100GHz and 525GHz	79
3.3.1. Theoretical test systems	79
3.3.2. 100 GHz reflectivity	80
3.3.3. 525GHz reflectivity	83
3.3.4. Cornea EM Modeling: Conclusion.....	86
3.4. In vivo corneal imaging study	87
3.4.1. THz sensing systems	87
3.4.2. In vivo study design.....	93
3.4.3. CCT measurements.....	95
3.4.4. THz reflectivity vs CCT at 100GHz and 525GHz	97
3.4.5. Analysis	101
3.4.6. Discussion: experimental and imaging method shortfalls.....	105
3.5. First in vivo Experiment - Conclusions	106
Chapter 4 Non-contact, All-normal Incidence corneal Imaging System.....	107
4.1. Introduction	107
4.2. Anatomy (geometry) of cornea for THz imaging	109
4.3. Spherical surface imaging	115
4.3.1. Spherical surface scanning principle	115
4.3.2. Effective imaging optic f/# and offset	117
4.4. Quasioptical imaging system design	119
4.4.1. Single imaging mirror design	119
4.4.2. Verifying quasioptical analysis: Physical Optics Analysis	133
4.4.3. Imaging system design analysis: Discussion.....	136
4.4.4. Angular scanning system design	137
4.4.5. Double mirror (angular) scanning: Physical optics analysis	146
4.4.6. Alignment sensitivity - Optical system POV analysis.....	149
4.4.7. Angular-Scanning System: Discussions	152
4.5. THz Corneal Imaging System: System engineering, implementation, and image reconstruction	153
4.5.1. Coordinate transformations, Mapping, and Sampling Schemes.....	153
4.5.2. System implementation	158

4.6. Imaging Results	161
4.6.1. Imaging of characterization targets	161
4.6.2. Imaging data fits to quasioptical and physical optics analysis	164
4.6.3. Characterization target limitations.....	172
4.6.4. Corneal phantom.....	173
4.7. Conclusion: Non-contact THz Ophthalmic imaging system development.....	174
Chapter 5 : In vivo Imaging of Corneal Tissue in Human.....	177
5.1. Non-contact in vivo imaging study	178
5.1.1. Descemet's Membrane Stripping (DMS) Experiment Protocol	179
5.1.2. Modifications to experiment protocol	182
5.1.3. Imaging results and discussion of the experimental outcome	183
5.1.4. Discussion: Experimental Challenges and Pitfalls	185
5.2. Safety of THz imaging	187
5.2.1. Mechanisms of Possible Tissue Damage.....	187
5.2.2. Animal radiation safety study.....	190
5.2.3. Safety of the Exposure Level.....	194
5.3. Human imaging system engineering.....	196
5.3.1. Human interfacing	199
5.3.2. Multiple frequency (spectrally resolved) measurements.....	202
Chapter 6 Conclusion.....	207
6.1. Final Words	212
References	213

List of Figures and Tables

Figures

Figure 1-1. Anatomy of Cornea.	3
Figure 1-2. Healthy cornea vs diseased cornea with cornea edema that compromised visual acuity.	3
Figure 1-3: Plot of equation (1) with physiologic relevant thickness range (shaded region).	7
Figure 1-4. Complex dielectric constant of liquid water at room temperature, at 0.1-1THz, computed by Double-Debye relaxation model.	16
Figure 2-1. 90° Off axis parabolic mirror geometry for a 25.4 mm EFL mirror.	31
Figure 2-2. Half angle and numerical aperture of a circular-cut parabolic mirrors with A = 25.4mm.	33
Figure 2-3. Distortions of a Gaussian beam input by a single 90° off-axis parabolic (OAP) mirror.	35
Figure 2-4. Transformation of Gaussian beam by general quasi-optical Gaussian beam system and the sizes/locations of input and output beam waists. Image adapted from [59].	36
Figure 2-5: A pair of identical off axis parabolic mirrors. One mirror provides illumination, and the other one collects the reflected signal at a specular direction.	38
Figure 2-6: A single-pixel THz imager, with four off-axis parabolic (OAP) mirrors labeled OAP 1-4.	39
Figure 2-7: A direct-detection, focused beam THz imaging system	40
Figure 2-8: Beam overlap in axial extent.	43
Figure 2-9: Frequency dependent resolution parameters.	43
Figure 2-10: Measurement of the transverse spot size (Top) and Depth of Focus (DOF) (Bottom).	47
Figure 2-11: Beam path displacement for off-focal plane reflections.	48
Figure 2-12: Beam walk-off and smearing at the detector plane.	50
Figure 2-13: Beam centroid (energy center) walk-off resulting from axial displacement of the imaging plane.	51

Figure 2-14 THz beam profile and polarization state while propagating through a series of OAP mirrors, from a y-polarized Gaussian TEM ₀₀ source.....	55
Figure 2-15. Image formations in the antisymmetric and symmetric optics orientations.	57
Fig 2-16: Re-design of the THz imaging system with optics orientation matching to cancel off-axis aberrations.	57
Fig 2-17: Field and polarization distortion correction by matched (compensated) optics orientation.	58
Figure 2-18. Displaced beam reaching the final mirror (OAP4)	59
Figure 2-19. Focused beam displacement in 25.4mm EFL OAP4.	62
Figure 2-20. Focused beam displacement 50.8mm EFL OAP4.	63
Figure 3-1: Corneal structure.	66
Figure 3-2: Typical axial profile of the corneal tissue water content (CTWC) measured by [25]	67
Figure 3-3: Stratified media model for cornea.....	70
Figure 3-4: Candidate CTWC gradients for CTWC sensitivity simulations. (left) pinned front, (middle) pinned back, and (right) global.	73
Figure 3-5. E-field penetration into the corneal tissue at 100GHz and 650GHz.....	75
Figure 3-6. THz reflectivity of corneal tissue from the anterior side as a function of CTWC, for the fixed CCT = 550um	76
Figure 3-7. THz reflectivity of corneal tissue from the anterior side as a function of CCT, for the fixed CTWC = 79%.	76
Fig 3-8: System center frequencies and quality factors with Q = 5, 50 at 100GHz and 525GHz.	79
Figure 3-9: Dependence of corneal reflectivity on CTWC and thickness computed at 100 GHz.	82
Figure 3-10: Dependence of 525 corneal reflectivity on CTWC and thickness computed at center frequency of 525GHz.....	84
Figure 3-11: 100GHz sensing system. (a) System block diagram. (b) Illumination geometry (c) Biasing scheme demonstrating low frequency chopping combined with high frequency FMCW.	88
Figure 3-12: 525GHz imaging system. (a) System block diagram. (b) Illumination geometry. (c) Photoconductive switch power spectral density and detector spectral responsivity.....	89

Figure 3-13: Sensitivity analysis of the 100GHz system (left) and 525GHz system (right). Experimental details in [88],[40].	91
Fig 3-14: Rabbit cornea imaging. (top) Rabbit model placed below the THz and millimeter wave imaging systems. (bottom) Close up of rabbit cornea and mylar window	93
Fig 3-15: CCT measurements for all rabbits in the trial and their associated CTWC levels computed with equation (18). Rabbit 5 has a large outlier at time 50 mins which was not included in the linear fits.	96
Figure 3-16: 100 GHz point measurements plotted against the CCT measurements reflected in the lower x-axis.	98
Fig 3-17: 525GHz reflectivity maps of CTWC for all five rabbits, showing noticeable shifts of reflectivity contrast over the course of imaging experiment.	99
Figure 3-18: Computed reflectivity at 100GHz and 525GHz on CTWC and corneal thickness.	102
Figure 3-19: ‘Cross-section’ 2D reflectivity functions of Figure 3-18.	103
Figure 4-1: (a) Decentration and (b) “regular” astigmatism in corneal anatomy.	110
Figure 4-2: Average radius of curvature (RoC) variations (Δr from equation (44)) in cornea from Fourier decomposition analysis applied to healthy cornea, Keratoconus, and grafted cornea.	112
Figure 4-3. Displacement of Radius of Curvature (RoC) and Center of Curvature CoC	113
Figure 4-4: Scanning principle to raster-scan over spherical surface in a transformed rectilinear coordinate.	116
Figure 4-5: Half angles of 90° OAP mirrors.	117
Figure 4-6: Single mirror, rectilinear scanning imaging system design comprised of three distinct subsystems; Three scan locations are plotted.	119
Figure 4-7. Raypath diagram of the beam scanning showing (a) respective parabolic mirror segmentation location, (b) definition of spot size on the surface of the cornea, and (c) thin lens equivalent of the overall beam path.	121
Figure 4-8. (a) Spot size and beam coupling efficiency of the imaging system	127
Figure 4-9: Physical optics analysis of the imaging system.	133
Figure 4-10. Double mirror, angular scanning imaging system design.	138
Figure 4-11. Raypath diagram of the double mirror, angular scanning system. (a) Parabolic mirror segmentation and (b) thin lens equivalent of the overall beam path.	140
Figure 4-12. Spot size and beam coupling efficiency of the angular scanning system.	142

Figure 4-13. Field distribution computed with Physical Optics method for 2-mirror imaging system.	146
Figure 4-14. Target alignment tolerance gauged by observing signal distribution at the detector.	151
Figure 4-15. Sampling scheme mappings between a 90°, 76.2mm CA, 25.4 PFL OAP imaging mirror and an 8 mm RoC sphere (cornea).	157
Figure 4-16. Non-contact THz imaging system implementation.....	159
Figure 4-17. Corneal coverage by 76.2 mm CA, 25.4 PFL OAP.....	160
Figure 4-18. 650GHz of the characterization targets.....	162
Figure 4-19. Imaging field analysis with uniform brass ball calibration target.....	165
Figure 4-20. Imaging performance analysis with Al strip resolution target.	167
Figure 4-21. Imaging performance analysis with “checkerboard” target.	170
Figure 4-22. Time lapse Images of drying contact lens (Left to right).....	173
Figure 4-23. System Development timeline.	175
Figure 5-1. In vivo imaging study with non-contact THz imaging system.	180
Figure 5-2. Time series 650GHz image of the left eye immediately after the Descemet’s membrane stripping.	184
Figure 5-3. Histological analysis of corneas from control and experimental group.....	192
Figure 5-4. Maximum Exposure Level limit listed by ANSI standard (Blue) for 10 seconds CW exposure, and extrapolated MPE level into the lower THz region (Shaded red).	195
Figure 5-5. Non-contact THz imaging system equipped with human subject interfaces	197
Figure 5-6. Eye positioner apparatus.	199
Figure 5-7. Eye camera and machine-vision assisted alignment process.	200
Figure 5-8. Two-frequency transceiver subsystem.....	203
Figure 5-9. Preliminary analysis of field distribution of truncated collimated 100GHz beam...	205
Figure 5-10. 650GHz images of healthy human cornea	206

Tables

Table 1. A survey of prevalence of corneal diseases involving corneal edema in U.S.	2
Table 2. Geometric properties of 90° off-axis parabolic mirrors.....	33
Table 3. Resolution computations.....	42
Table 4. Properties of the focused beam by a pairs of OAP mirrors	45
Table 5. Comparison of predicted transverse and axial imaging performance.....	46
Table 6. Measured sensitivities.....	100
Table 7.: Spherical coverage angle by imaging reflector f/#	118
Table 8. Partial CCT data.....	186
.....	

Acknowledgement and Dedication

I am indebted to Profs. Warren Grundfest and Zachary Taylor for the many years of their support for my passion and endeavors, and giving me the environment in which I could “stretch my wings”. I have grown, both professionally and personally, in their thoughtful guidance and powerful mentorship. I am privileged to have learned from their vision and expertise, which I hope to carry on to my scientific career.

I deeply thank the mentors and who have guided me through this project. Prof. Deng has given critical feedbacks and discussion from a medical scientist’s and clinician’s point of view for this project, and her inputs helped to shape the work to its final form. Profs. Ennis, Stafsudd, and Williams provided numerous inputs to the THz project since my Master’s study. In the final stages of this project, Professor Llobart at TU Delft helped to expand the system design approach with a powerful physical optics method.

I gratefully acknowledge former members of the terahertz team. I inherited the groundwork performed by Drs. David Bennett and Priyamvada Tewari, who were my first graduate mentors and kind teachers. James (Jim) Garritano’s work was the foundation for cornea EM analysis in Chapter 3, and I continued from his remarkably thorough modeling of the cornea. Dr. Bryan Nowroozi guided the team through animal study designs and protocols. Without his help, we couldn’t have succeeded in any of our animal studies. Skyler Selvin did an amazing job on imaging system hardware programming and 100GHz FM modulator circuit, which were the most crucial addition to the system.

I worked with phenomenal researchers and students at UCLA throughout this project. Division of Laboratory Animal Medicine staffs (Sonia, Guillermo, Ataki) were most accommodating and

crucially helpful in our animal studies. Students and staffs of the Grundfest lab and Center for Advanced Surgical and Interventional Tech. shared their knowledge, patience (with our overnight experiment frenzies), and companionship throughout this project. For Meghedi, Will, Nathan, Shyam, Alan, George, Ahmad, Rory, David, Jason, and others, I am thankful.

I am most fortunate for the companionship and countless help of Ashkan Maccabi and Neha Bajwa, who started journey with me from the start. They were the co-pilots of this project. Ashkan was the spirit of the lab and my second brother. He was always the first to roll up his sleeves and help with any problems in the lab. His kind gestures and genuine friendship were the greatest gift to our team. Neha Bajwa was ever so kind to both me and Ashkan despite our constant mischiefs. She was my role model, always humble, an amazing researcher, and the backbone of this project.

All these years, there have been unwavering support of my friends: Hyemin, Xuan, Connie, Gabe, Pil, and many more.

I dedicate this work to my mother, father, and brother, who have endured an arduous life of immigrants together in the unfamiliar land, and opened this path of life for me. It wasn't easy and it left us many scars, but I am most grateful that we are all here.

In memory of Hyunjung Oh and her dreams,

Shijun Sung

March 22, 2017, Los Angeles.

Curriculum Vitae

Shijun Sung

EDUCATION

Electrical Engineering, Ph.D., (Expected March 2017)
Thesis: Terahertz Imaging and Sensing for Ophthalmic Evaluation of Corneal Diseases
Advisor: Prof. Warren Grundfest M.D., FACS, Physical and Wave Electronics
University of California Los Angeles

Electrical Engineering, M.S., 2013
Thesis: Terahertz Imaging and Remote Sensing Design for Applications in Medical Imaging
University of California Los Angeles

Electrical Engineering, B.S., 2011
University of California Los Angeles

RESEARCH

Center for Advanced Surgical and Interventional Technology (March 2010 – Present)
UCLA Department of Electrical Engineering / Bioengineering

Doctoral research in the field of Terahertz (THz) science and technology for medical imaging applications

- Clinical applications:
 1. Ophthalmology: Developed a non-contact, direct measurement technique and instrument for measurement of corneal tissue hydration, targeting early detection of corneal edema in corneal dystrophies and transplanted graft, in the 5-year NEI funded study.
 2. Surgery and Wound Treatment: Performed imaging study of tissue hydration and perfusion in damaged/inflamed tissue in three NIH-funded studies. Investigated imaging-based methodologies for early detection of failing wounds in burn, ulcer, and traumatic wounds by studying tissue hydration dynamics.
- THz imaging science:
 1. Designed and performed studies investigating random rough surface scattering at THz frequencies
 2. Designed and fabricated instruments for quasi-optical THz systems for remote-sensing, imaging and spectroscopy

Undergraduate Research

Harran Group, UCLA Department of Chemistry and Biochemistry (Sep 2009 –Jan 2010)
- Research Title: Synthesis of inhibitor of an exogenic enzyme Ghrelin-O-acyl transferase

Liao Group, UCLA Department of Chemical Engineering (Jun 2008-July 2009)
- Research Title: Phenotyping of Keio Knockout Strains (Escherichia Coli) response to Nitric Oxide

Plasma Physics Laboratory, UCLA Department of Physics and Astronomy (Mar 2008 –July 2008)
- Research Title: High-magnetic field plasma deposition experiment electronics

TEACHING/MENTORING

UCLA Center for Excellence in Engineering Diversity (2011 – 2015)
- Led yearly internships for underrepresented Los Angeles area high school students in STEM field. (8+ students)

UCLA Department of Bioengineering (2011 – Present)
- Mentored and trained 10+ undergraduate students in biomedical imaging/ device development research projects

UCLA Engineering Science Corps Outreach Program (2011 – Present)
- Led summer-long extensive research mentorships for 5+ high school students

Student tutor, Physics - *UCLA Academic Advancement Program AAP* (2010-2011)
Reader - *UCLA Electrical Engineering, EE103 (Numerical Computing)* (2010-2011)

SELECT PUBLICATIONS/ PRESENTATIONS

Journal Publications

Non-contact, normal incidence THz imaging system for Human Cornea (Part A,B)

Shijun Sung, Skyler Selvin, Neha Bajwa, Somporn Chantra, Bryan Nowroozi, James Garritano, Jacob Goell, Alex Li, Sophie X. Deng, Nuria Llobart, Elliott Brown, Warren S. Grundfest, and Zachary D. Taylor

Assessment of Corneal Hydration Sensing In the Terahertz band: In-vivo Results at 100 GHz. J. Biomed. Opt. 17 (9), 2012

David Bennett, Zachary Taylor, Priyamvada Tewari, **Shijun Sung**, Ashkan Maccabi, Rahul Singh, Martin Culjat, Warren Grundfest, Jean-Pierre Hubschman, Elliott Brown.

THz sensing of corneal tissue water content: in vivo imaging results, IEEE Trans. THz Sci. & Tech. 2015

Zachary Taylor, James Garritano, **Shijun Sung**, Neha Bajwa David Bennett, Bryan Nowroozi, Priyamvada Tewari, James Sayre, Jean-Pierre Hubschman, Sophie Deng, Warren Grundfest.

THz sensing of corneal tissue water content: modeling and analysis of electromagnetic properties, IEEE Trans. THz Sci. & Tech. 2015.

Zachary Taylor, James Garritano, **Shijun Sung**, Neha Bajwa David Bennett, Bryan Nowroozi, Priyamvada Tewari, James Sayre, Jean-Pierre Hubschman, Sophie Deng, Warren Grundfest.

10th European Conference on Antenna and Propagation

S. Sung, et al. *Engineering Consideration for Clinical Translation of THz Imaging Technology*

Association for Research in Vision and Ophthalmology, Annual Meeting 2015

S. Sung, et al. *Direct measurement of corneal tissue water content by reflection imaging at Terahertz Frequency*

The 7th National Center for Image Guided Therapy/ NIH Image Guided Therapy Workshop (2014)

S. Sung, et al. *Assessment of In-vivo Corneal Hydration using Terahertz Imaging.*

N. Bajwa, et al. *In vivo Confirmation of THz Wound Edema Imaging for Burn Surgery Using MR*

Infrared-millimeter wave-THz (IRMMW-THz) 2014

S. Sung et al., *Analysis and Optimization of TH imaging Optics with Off-Axis Parabolic Mirrors*

National Radio Science Meeting (URSI) 2014

S. Sung, et al. *Fixed Back-Focal-Distance THz Objective Design for Medical Imaging Application*

International Society for Optics and Photonics (SPIE)

Invited Paper: **Sung, S.**, et al. *Preliminary results of non-contact THz imaging of cornea,* SPIE BiOS 2015.

Invited Paper: **Sung, S.**, et al. *Optical design for translation of THz medical imaging technology.* SPIE OPTO. 2014.

Sung, S., et al. *Fast-scanning THz medical imaging system for clinical application.* SPIE OPTOs. 2012.

Sung, S., et al. *Reflective measurement of water concentration using millimeter wave illumination.* SPIE NDE. 2011.

TECHNICAL/ ACADEMIC TRAININGS

- *Optical system design simulation /analysis* - Advanced Systems Analysis Program (ASAP: Breault Research, Tuscon, AZ)

- *UCLA Advanced Neuroimaging Training Program* (July 2011)

Trained in functional neuroimaging methods and MRI-based neuroimaging data acquisition, signal processing, experimental design, and data analysis

ORGANIZATIONAL/ VOLUNTEER SERVICES

Volunteer (197+ hours): Ronald Reagan Medical Center/ Santa Monica UCLA Hospital (2009-2010)

Volunteer translator (English-Korean), Los Angeles Food Policy Council (2013)

Core staff in Sunday School program, St. Agnes Korean Catholic Church (2007- 2011)

AWARDS & PATENTS

2011 Neuroscience Training Program Grant Recipient/ Participant – Summer 2011

HSSEAS Dean's Non-Resident Tuition Fellowship, Winter 2012 /Spring 2012

Best Paper Award: 2016 THz Science and Tech., by the IEEE Microwave Theory and Techniques Society (MTT-S)

“Novel THz imaging instrument and scanning mechanism for non-contact, orthogonal imaging of spherical surface”

(Provisional U.S. Patent. No 62116.327)

Chapter 1 : Introduction

1.1. Statement of the problem and the study objective

This work aims to develop a new diagnostic medical imaging technology using terahertz (THz) frequency; specifically, this technology is applied to imaging of tissue water content of cornea and investigation of the development of corneal disease and dystrophy in terms of its most critical characteristic: its ability to regulate hydration of tissue.

The cornea is a refractive and protective component of the eye and critical for vision. It is the toughest soft tissue in the body and directly protects the rest of the visual anatomy from the outer environment. The cornea provides the majority of the focusing power (46 of the average 59 total diopters) of refractive power in the eye [1]. In order to maintain its optical clarity and shape, it is carefully regulated to have a narrow range of hydration content and maintenance of its matrix. The average hydration level of the tissue typically measures ~ 78% water by volume [2]. This regulation is mostly performed by a layer of specialized cells of the endothelium.

In ophthalmology, many corneal disorders such as Fuchs' endothelial dystrophy, keratoconus (corneal ectasia), pseudophakic bullous keratopathy (unintentionally damaged endothelial layer), and corneal graft rejection result in corneal edema from dysfunctions of endothelial cells. Corneal edema is a contributing factor in development of the corneal opacity, in which the optically

transparent tissue to become opaque, as can be seen in Figure 1-2. Corneal opacification results from the presence of additional materials such as fluid, scar tissue, inflammatory debris, or metabolic byproducts within corneal tissue. Such outcomes could be caused by congenial conditions, degenerations, endothelial or other types of dystrophies, inflammatory and immunologic, metabolic process, depositional, neoplastic, and other conditions [3].

If left untreated, corneal edema leads to chronic vision impairment. Abnormal corneal tissue water content (CTWC) can be an indication of endothelial cell function decline, or in the case of cornea transplant, the grafted cells are not successfully accepted by the host. Hence, abnormal corneal water content is a key indicator of endothelial malfunctions and corneal dystrophies and a target for ophthalmic evaluation of cornea.

Table 1. A survey of prevalence of corneal diseases involving corneal edema in U.S.

Disease/Condition	Prevalence in U.S.	Remarks
Corneal dystrophy	278,000 nationwide [4]	Analyzed by claim data
- Fuchs Dystrophy	4% of people over the age of 40 [5, 6]	
Corneal Transplant	+40,000 cases/year performed nationwide [7]	
Keratoconus	167,400 nationwide (0.054%) [8]	Varies widely according to geographic location

Many of such diseases measurably perturb corneal water content and are defined by the deterioration of the cornea’s water-regulating process [9-11]. Other conditions, such as keratoconus, have poorly understood mechanics, yet have been observed to exhibit non-uniform changes in water concentration of the cornea [12]. The water content of the cornea can also be chronically affected by medical procedures such as including Laser-Assisted in situ Keratomileusis (LASIK), Laser-Assisted Sub-Epithelial Keratectomy (LASEK) [13]. In corneal graft surgeries, immune rejection is preceded by the formation of edema and the reversibility of rejection events

tends to diminish with abnormal increases in CTWC [13]. The survival rate of rejected grafts can be generally improved by optimizing the intervention strategy, and the early detection of the formation of edema is critical to this process [14].

The capabilities to measure corneal tissue water content (CTWC) can provide a better understanding of the formation, development, and progression of corneal disorders. If the onset of the clinical manifestation of the edema can be screened early, CTWC sensing and imaging can be a directly relevant clinical method for early diagnosis and intervention.

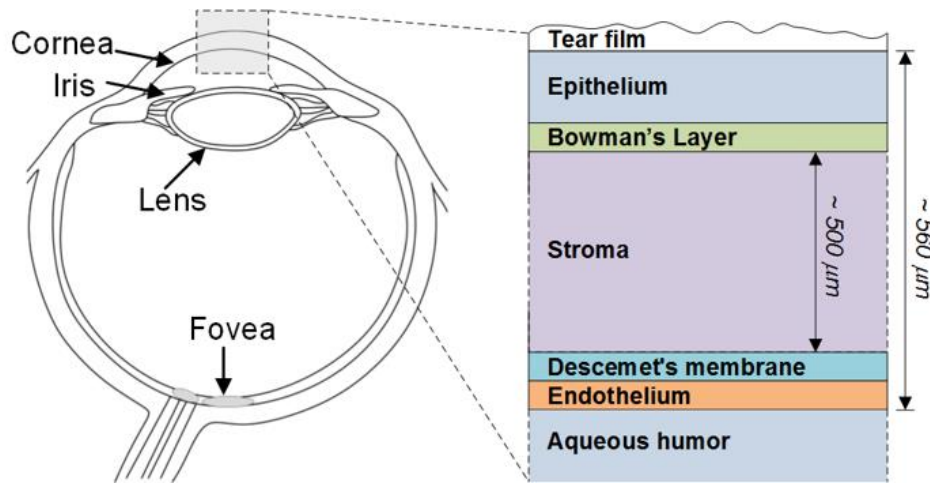


Figure 1-1. Anatomy of Cornea.

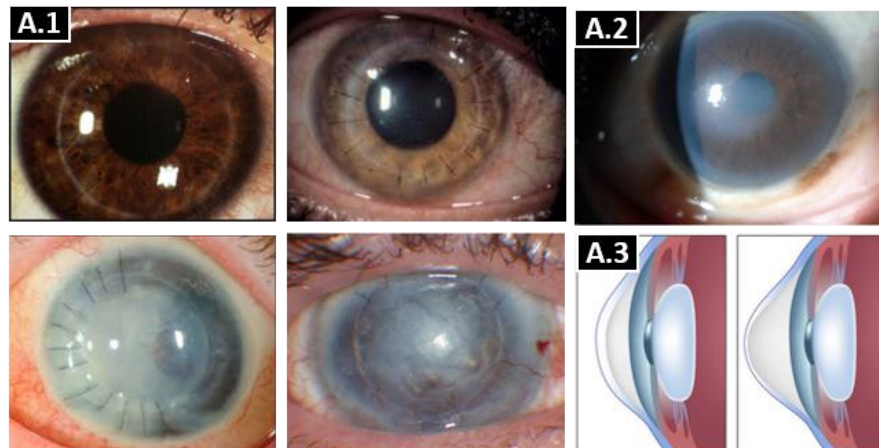


Figure 1-2. Healthy cornea vs diseased cornea with cornea edema that compromised visual acuity.

A.1. Top: Clear, deep cornea with functioning endothelial layer after successful corneal transplant. [15] Bottom: Corneal graft failure. [16] A.2. Fuchs Dystrophy [17]; A.3. Keratoconus [18]

However, accurate and non-invasive *in vivo* measurement of human CTWC remains yet elusive and there is no standard technique. Although there are powerful new techniques such as optical coherence tomography that can provide depth resolved, μm resolution of ocular anatomy and pathology, interaction of the corneal tissue at optical wavelengths are almost entirely scatter dominated, and small but critical changes in CTWC are not detected with optical techniques.

THz wavelength addresses many of the critical difficulties in measuring CTWC. First, among many interesting interaction with biological tissues, THz frequency band ($f = 100\text{GHz} - 10\text{THz}$) closely interacts water in tissue with non-ionizing photon energy (4.1 meV at 1 THz). Second, THz wavelength (3mm - 30 μm) is the only wavelength band that will penetrate deep enough to cornea, but not significantly bypass it, and sense the dielectric properties of cornea. Imaging capability can visualize possibly localized hydration abnormality.

In order to harness above two critical advantages, this study investigated terahertz (THz) remote-sensing technique for precise CTWC measurement, and developed a novel imaging technique and instrument that can be practically implemented in the clinical setting. Using the developed imaging system, a clinical study section is designed to test if THz CTWC measurement can provide medically relevant information about the progress of corneal tissue failure. The main objectives of this work are organized in four aspects.

1. Establish electromagnetic modeling of THz–cornea tissue interactions according to the anatomy of the cornea and its dielectric properties in the frequency band of interest (from 0.1THz to 1THz); Explore frequency dependent tissue hydration sensing sensitivity, changes in THz response to variations in corneal anatomy and disease pathology, and possibility of using spectral features.

2. Test the validity of the modeling experimentally *in vivo*.
3. Develop an ophthalmic THz imaging system suitable for practical use in clinics. THz sensing scheme must be able to detect minimal sign of the onset of corneal edema, while such device should be compact, non-contact, and perform rapid imaging of corneal surface with ease.
4. Perform imaging studies in the preliminary clinical trial for healthy cornea (control group) and diseased cornea of various stages (Exploration group). The exploration group consists of patients with corneal graft and corneal dystrophies.

1.2. Limitations of clinically available measurement techniques

The current standard method to measure CTWC is by the extrapolation using the central corneal thickness (CCT) measurements, which is usually measured with ultrasound or optical coherence tomography (OCT) based pachymetry. CTWC is inferred from the assumption of a nearly linear relationship between CCT and the average water content of the cornea [19]:

$$H = \frac{m_{H2O}}{m_{H2O} + m_{dry}} = \frac{CCT - 0.091}{CCT + 0.051} \quad (1)$$

This method was established in 1965 from the empirical fit of 11 healthy *ex vivo* human corneas from a cornea bank. [20]. The model does not account for physiologic corneal thickness variation and deviations are 20% or greater [2]. For example, a healthy person with corneas too thin to be considered candidates for photorefractive surgery ($< 450 \mu\text{m}$), would have predicted water content values of $\sim 70\%$, a clearly faulty prediction of tissue water content, and the physicians I interacted with understand the shortfall of this relationship.

A generalized linear fit approach also suffers from repeatability of calibrating standard. One such example is a ‘base’ cornea thickness of a dehydrated cornea. The linear fit of the hydration model predicts that a dehydrated corneal would have a thickness of 90 micrometers; however the measured value reported in the literature is ~ 200 micrometers [20]; the original equation uses thickness of $\sim 127 \mu\text{m}$ [19]. A plot of equation (1) is displayed in Figure 1-3 where the shaded area spans the physiologic range of thicknesses observed in healthy cornea and the dotted line is a linear fit to equation (1) within the physiologically relevant range (shaded region) with an approximate slope of 40%/mm.

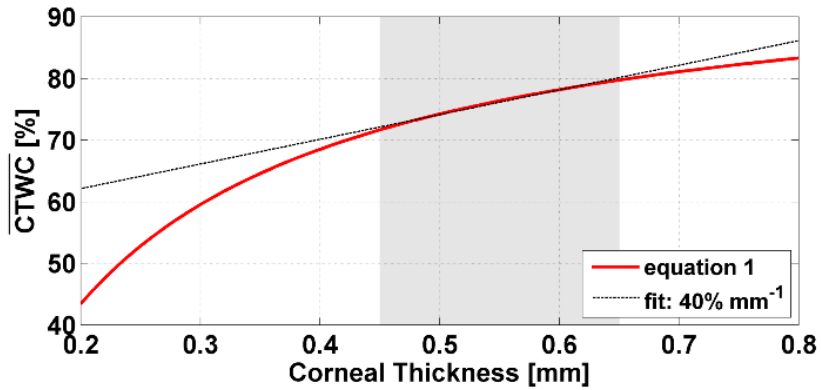


Figure 1-3: Plot of equation (1) with physiologic relevant thickness range (shaded region). A linear fit to equation (1) within the shaded region is represented by the dotted line.

While ultrasound or optical based pachymeters provide very accurate distance measurements, the mapping from thickness to water content is extremely inaccurate and severely limits the utility of the technique. There are many stark disagreement and inconsistency between published CCT values and estimated CTWC in conditions such as graft rejection, Fuchs Dystrophies, and Keratoconus [21]. Corneal thickness also changes throughout the day, and the guideline for clinical practice recommend making measurements in the morning [3]. These observations further demonstrate the poor understanding between the coupling of thickness and CTWC and indicate that CTWC measurement is both a clinical and a basic research problem.

There are several studies that used optical techniques to characterize CTWC. The investigated methods include optical coherence tomography (OCT) [22], near infrared reflectometry (laser Doppler) [23], and confocal Raman spectroscopy [24]. Of those listed above, only confocal Raman has provided an absolute measurement of corneal water content [25]. However, the scattering cross section of water is very small and the measurements must use unacceptable integration times or unsafe fluence levels [25-27].

The significant role that CTWC plays in visual acuity and limitations of clinically available techniques present an opportunity for THz sensing and imaging techniques. Given the tissue

constituents, geometry, and location, imaging and sensing CTWC deals with less confounders than that of any other *in vivo* application studied in THz medical imaging. Furthermore, the required field of view (FOV) is small (~ 1 cm diameter) and does not change based on the pathology/disease/injury of interest. These conditions call for highly specialized and efficient system design optimized for ophthalmologic application.

1.3. THz frequency devices, technology, and system integration

Terahertz (THz) frequency band spans into the far-infrared and sub-millimeter (3mm – 0.1 mm) region of the electromagnetic spectrum with frequencies loosely designated from 100 GHz to 10 THz [28]. In the vapor phase polar compounds, THz frequency energy corresponds to the several rotational and vibrational modes between C-O, C=O, and H-O. Atmospheric water has a distinct spectral feature in the THz band, notably at 0.558THz, 0.753THz, 0.989THz, 1.099THz and at other frequencies. THz frequency is particularly sensitive to vapor phase water. In atmosphere, sharp water line at ~550GHz compels many experiments to be performed in dry chamber. THz radiation's sensitivity to water has long been sought after in space exploration, astronomy, and atmospheric studies. Promising applications of THz technologies includes (and are not limited to) radioastronomy, atmospheric science, security applications in screening and illicit material detection, non-destructive evaluation (NDE), communications technology, biological and medical sciences, and spectroscopy.

Yet, the THz region has been the least studied frequency band because of the challenges in generation and detection in this frequency band with conventional metallic or semiconductor materials. Development of THz detectors, especially for room-temperature operation, is difficult in both photonics and electronics fronts. The photon energy ($h\nu$) in the THz region is much less than $k_B T$ of room temperature (0.0256 eV), hence atomic and molecular transitions cannot be used at room temperature since quantized states separated by $h\nu$ at THz frequency tend to have the same populations [29].

On the other hand, significant attenuation hinders electronic transmission and guiding of THz frequencies (too fast for free carriers to respond) in semiconductor devices. typical semiconductors at room temperature (i.e. GaAs) have $\omega\tau > 1$ near 1THz [29]. Considering a simple Drude AC

conductivity model [30], it can be understood that THz energies are not efficiently coupled into free carriers. Transmission of THz wave through traditional microstrips or metallic waveguides is also very lossy because of high skin-depth losses of conductors. For example, a single-mode rectangular metal waveguide at THz frequencies display nearly 80dB/m attenuation at 1THz, which increases at a rate proportional to approximately $f^{3/2}$ [31].

Past and recent advancements and innovations in THz source and detector technology have helped applying THz science and technology in many areas of research and industry in more practical way, opening doors to applications that were once thought not feasible. THz technologies used throughout this study is such an example. Not only they provided the prospect of developing practical clinical device, but with near-future evolution of technology in sight, one can envision dramatically more practical and sophisticated implementation of THz science. There are several well-organized reviews on THz technology and devices [28]. In this section, several candidate technologies for THz emission and detection are discussed for their potential for incorporation into THz imaging systems.

1.3.1. THz source and detector devices

1.3.1A Active THz illumination

Generation of ultrafast THz pulse using Photoconductive switch (PCS) is a powerful technique to provide broadband THz radiation up to 10 THz [28]. Motivated by its usefulness in the THz time-domain spectroscopy technique, PCS (as well as photomixers made from similar material) based techniques continued to improve in output power, reliability, and packaging. Notably, THz sources with PCS antenna can incorporate smaller, cheaper, and more efficient telecom lasers at 1550nm. Current PCS technology research have made possible dramatically improved THz conversion efficiency [32] and scaling of output power by large-area PCS devices and arrays.

Metamaterial structures and quantum cascade laser closed the THz gap from the photonics side, opening doors to new sources of illumination for THz imaging and holography. A dramatic improvement in powerful heterodyning spectroscopic techniques is also a major milestone of these devices. QCLs, with higher operating temperature [33], and improved beam shapes [34], are strong candidate for miniature integration of the THz source in many applications.

Generation of THz frequency from solid state devices are similarly useful as the QCLs at much lower frequency, and can generally provide milliwatts of power. Gunn diodes are relatively cheap and robust oscillator to generate frequencies upto 130GHz. A Schottky diode multipliers can provide milliwatts of power in the lower frequency band, but the output power falls dramatically beyond 1 THz. These devices are typically mounted on the rectangular waveguides to define the operation frequency region, which can attached to antenna structures that couple THz radiation in and out of the waveguide.

1.3.1B THz detection

Detection of the THz radiation deals with similar challenges as generation of THz detection. Silicon based diodes and transistors do not efficiently respond to THz frequency changes, while there are no natural materials with bandgap close to THz photon energy range. There are three key methods that makes THz detection possible with practical devices at room temperature.

Room-temperature calorimetric terahertz detectors, such as pyroelectric detectors, microbolometers or Golay cell detectors, measure the heating of a substance that changes properties as a function of temperature change. Some of these uncooled thermal sensors can be fabricated in arrays to realize a focal plane staring array [35]. However, the response time of the thermal detectors are close to DC (on the order of hertz) and the measured signals are subjected to a large $1/f$ noise.

On the other hand, solid state detectors are fast detectors utilizing fast charge transport between the metal-semiconductor junctions. Schottky diodes have lowered effective work function and barrier height by Schottky effect, resulting in low forward voltage drop and turn-on voltage. SDs are also majority carrier device (from the semiconductor to metal) with no minority carrier injection, producing very little reverse current overshoot when switching from a forward conducting mode to a reverse blocking state. The lack of associated capacitive delay gives SD fast switching speed, ($\sim > \times 10$ than p-n junction device) and gives higher cut-off frequency near 1 THz.

Zero-bias operation is possible in SD by optimizing Schottky contacts with a very low barrier. Especially for low-signal detection, zero-bias operation gives the best SNR because it significantly reduces the sources of flicker noise ($1/f$) and gives sensitivities close to the thermal noise floor. For stronger signals flicker noise will become dominant again.

Lastly, the photoconductive switch can be used as a detector to sample the broadband THz pulses in THz time-domain spectroscopy set up. THz pulse sampling with a photoconductive

switch detector is simpler than electro-optic sampling of the pulse and the detector can be fabricated into a singular module which utilizes the same ultrafast laser source. Innovations in delay line scanning method have dramatically enhanced the usefulness of the PCS detector. A long signal acquisition time from delay line scanning were often quoted as a significant shortfall of the time-domain spectroscopy. The electronic delay line scanning uses beat frequency mode sweeping [36] to bring the acquisition time closer to the limit by the inherent detector sensitivity. Although the PCS detector sensitivity is lower compared to solid state detectors, it is a powerful tool for rapid THz time domain spectroscopy [37, 38].

1.4. THz Imaging: Theory and Implementation

1.4.1. THz-tissue interaction

The theoretical framework to understand interaction between THz radiation and biological tissue can be first considered with parameters of classical electromagnetic wave interaction in terms of permittivity (polarizing effect by the material) and conductivity (movement of ions within the material). In the molecular level, the range of photon energy (2.0×10^{-22} to 1.3×10^{-20} J) corresponds to consecutive rotational states of diatomic polar molecules ($E \sim 1.602 \times 10^{-22}$ J). In liquid phase, molecular interaction is overdamped by hydrogen bonding and proximity of adjacent molecules. At frequencies below 6THz, molecular interactions give rise to corresponding relaxation time τ at particular resonant frequencies. This dielectric relaxation model has been shown to predict permittivity and conductivity of various polar materials that agrees with experimentally determined complex dielectric constant [39]. A good topical review on this subject are provided by Smye et al [40].

A simplest THz-tissue interaction model can be considered by looking at key tissue constituents and their contribution in interacting with THz radiation. However, a tissue cannot be simply called a mixture of various substances. A living tissue is a complex organization of water, protein, fat, and bodily fluids of various state, whose standard “healthiness” is determined by homeostatic balance of many parameters. The electromagnetic properties (scattering, macroscopic dipole interaction) and/or optical properties (scattering, molecular level transition) of tissue are not only determined by its constituents but also by its particular states (oxygenation, hydration, etc), molecular organization (i.e. nature and density of extracellular network), and anatomical features (presence/density of blood vessels, exocrine glands, etc). Hence, understanding THz-tissue interaction must be accommodated with investigation and exploration with measurements.

1.4.1A: Water

Because the water is a particularly fundamental and abundant constituent in nature and biological tissue, there have been numerous studies of water ([39, 41]) that are matched with experimental measurement of complex dielectric constant $\varepsilon^*(\omega)$. Debye relaxation model is a widely validated method to predict $\varepsilon^*(\omega)$, computed as a sum of relaxation function. Equation (2) can be often truncated to give equation (3) using the first two terms which represent two adjacent relaxation poles nearest to the THz band. Comparison of measured values of resonant frequencies f_1 and f_2 may be found in [42].

$$\varepsilon_w(f) = \varepsilon_\infty + \sum_{k=1}^N \frac{\varepsilon_{k-1} - \varepsilon_k}{1 - j2\pi f/f_k} \quad (2)$$

$$\varepsilon_w(f) = \varepsilon_\infty + \frac{\varepsilon_0 - \varepsilon_1}{1 - j(2\pi)f/f_1} + \frac{\varepsilon_1 - \varepsilon_\infty}{1 - j(2\pi)f/f_2} \quad (3)$$

Figure 1-4 plots the $\varepsilon^*(\omega)$ over 0.1THz – 1THz range using the Double Debye relaxation model [43] at room temperature. which fits well with experimental data measured by Ronne et al [44]. Both the real and imaginary component of $\varepsilon_{\text{water,liquid}}$ are a monotonically decreasing magnitude in this region. [42, 43].

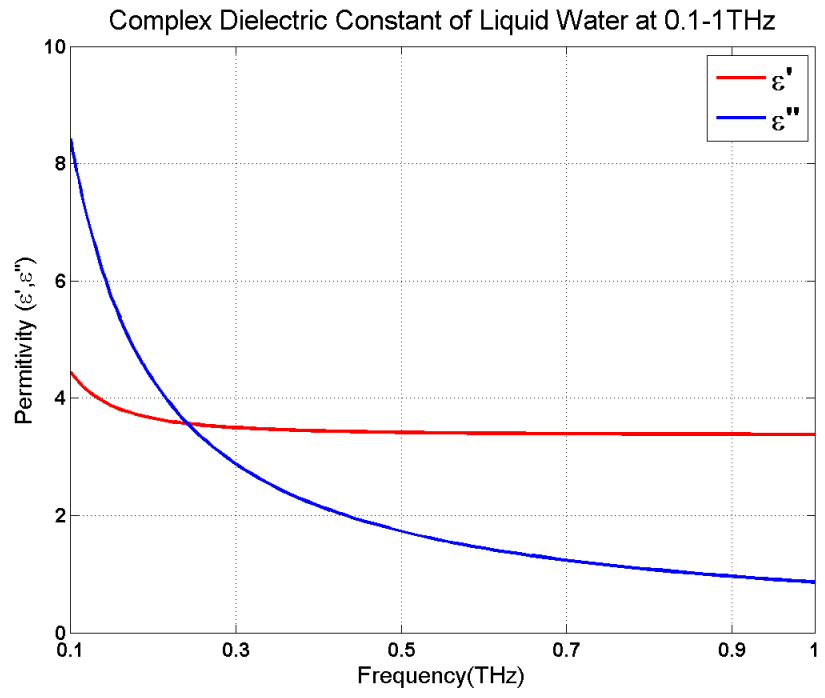


Figure 1-4. Complex dielectric constant of liquid water at room temperature, at 0.1-1THz, computed by Double-Debye relaxation model.

1.4.1B Biological tissue and mixed media model

Compared to $\epsilon^*_{\text{water}}(\omega)$'s large, monotonic dielectric function, the rest of the tissue constituents – fat, protein, nucleic acid, extracellular matrix containing mono/polysaccharide, minor amount of inorganic material, etc. – have weaker dielectric interactions and varies in their magnitude and features. Only some of the major tissue components could be fully characterized in the THz band. Because soft tissues are typically more than 65% water and $\epsilon^*_{\text{water}}(\omega)$ has the largest in magnitude among all tissue constituents, it can be hypothesized that the macroscopic THz property of the tissue is dominated by $\epsilon^*_{\text{water}}(\omega)$ over any possibly distinct spectral features of other constituents [42].

Several experimental observation support this expectation. Point-measurement or imaging systems based on THz time-domain technique measured spectra of in-vivo human tissues by different tissue types. Looking at the magnitude alone, the spectral features of in-vivo human skin by [45] lacks any distinct features and are similar to that of liquid water.

However, it is incorrect to say presence of water is the only observable feature in the THz-tissue interaction. Some studies show that there are clear spectral difference between normal and abnormal (i.e. cancerous) tissue. In particular, [46, 47] discusses difference in THz reflectivity between normal and cancerous breast tissue in $\epsilon^*_{\text{water}}(\omega)$, either or both in real/imaginary part at certain frequencies. Another study reports a statistically significant difference in the absorption coefficient and refractive index spectra in fibrous and cancer tissue [48].

Yet the presence of water is the most readily observed property of the tissue with the THz band. The dielectric property of the tissue are most largely determined by its water content, therefore the tissue water content difference can be a powerful contrast mechanism in THz imaging. A motivation for developing THz imaging and sensing techniques is in the ability to observe and

study the formation of disease and monitor bodily process in which our body's ability to regulate water balance is affected. For an example, a THz reflection image can show hydration profile of the tissue inferred by the THz reflectivity.

Given the small size of capillaries, cells, and other structures in tissue with respect to THz wavelengths, the electromagnetic properties of many tissues are assessed on a macroscopic scale as opposed to a microscopic scale. Biological tissue may be considered as a locally homogenous mixture, in which the water is a principal component. This approach suggests the use of effective media theory to model and predict the aggregate dielectric properties of the tissue in terms of its material composition. Given the exclusively large dielectric constant of water, we may further approximate tissue dielectric components into water (tissue hydration) and non-water components (collagens, elastins, and other proteins.)

$$\hat{\epsilon} \text{ s. t. } \sum_{k=1}^N \left(\frac{\hat{\epsilon} - \epsilon_w}{\epsilon_k + 2\hat{\epsilon}} \right) p_k \quad (4)$$

$$\hat{\epsilon} \text{ s. t. } p_w \left(\frac{\hat{\epsilon} - \epsilon_w}{\epsilon_w + 2\hat{\epsilon}} \right) + (1 - p_w) \left(\frac{\hat{\epsilon} - \epsilon_c}{\epsilon_c + 2\hat{\epsilon}} \right) = 0 \quad (5)$$

The Bruggeman model is one of the commonly used effective media theories, (also known as dielectric mixing theory [49-51] that shows a stable range of numerical solution over the large range of ratios of binary mixtures. The Bruggeman model is written in its general form in (4) for N number of constituents, where ϵ_k the complex dielectric constant and p_k is the volume fraction of the component k . The sum of all fractions ($p_1 + p_2 + \dots$) should be unity. The effective dielectric constant of the mixture ($\hat{\epsilon}$) is the value that satisfies the equation (4). It is noted that there are N solutions to equation (4), but only one of the solution is sensible, meaning that the value of $\hat{\epsilon}$ has

positive real part. The dielectric constant for non-water components are difficult to be measured in a standardized method (there are none). Structural and biomechanical properties changes from different preparation method contributes to different spectral responses [42]. However, the real part of refractive index for most abundant non-water components (elastin, collagen, etc) ranges from 1.5 to 2.5 and nearly consistent over the 0.1-1THz frequency range. On the other hand, the imaginary component is significantly less (very small loss-tangent) compared to that of water. Therefore, the equation (4) can be simplified to a binary form in equation (5), in which $k=1$ fraction is water and its frequency-dependent properties found by equation (3), and $k=2$ fraction is simply considered to have ϵ_2 ranging from $1.5 + i0$ to $2.5 + i0$. The Bruggeman model shows good agreements with many different mixture systems [52, 53], and in our own experiment as well [54].

1.5. THz imaging of tissue hydration – A survey of metrics

A THz sensing/imaging system should be able to discern physiologically relevant water content changes. In other water-sensing applications in space or atmospheric studies, THz detection need to be sensitive to the presence of the water and for the large part, need to differentiate the cases between “no water” to “some water” in the image or spectroscopic contrast. In the case of hydration content quantification, THz sensing systems need to differentiate a minute difference in tissue water content. In our problem – detecting corneal hydration content – the target conditions are clinically defined by as little as 1% hydration change from the 79% average tissue water content. As it will be discussed in Chapter 3, such difference corresponds to roughly 0.2 in the magnitude of dielectric constant at 500GHz-700GHz band. Then, a THz sensing system need to differentiate between ~0.3% reflectivity changes. Sensing problem is further complicated from the inhomogeneous nature of the tissue. Typically, tissues that are directly exposed to the outer environment are composed of dead cells and are dry (i.e. the stratum corneum layer of the skin). Meaningful tissue hydration regulation (our focus of interest) happens at deeper part of the tissue.

The minimum differentiable water concentration difference is limited by the signal to noise ratio. The effect of the noise in the reflectivity measurement is described by equation (6), where R denotes the reflectivity of the measured sample. $\frac{\partial R_{Sample}}{\partial C_{water}}$ is the responsivity of the sensing system, or the reflectivity change per unit change in the water concentration of the target. When $\Delta R = \Delta R_{noise}$, where ΔR_{noise} represents the noise in the reflectivity data, ΔC_{water} gives the water concentration change that is equivalent to the noise level (NE Δ WC).

$$\Delta C_{water}(C_{water}) = \frac{\Delta R_{noise}(C_{water})}{\frac{\partial R_{Sample}(C_{water})}{\partial C_{water}}} \frac{\partial R_{THz}}{\partial C_{water}} \Delta C_{water} \geq \delta_{error} \quad (6)$$

The noise level R is a function of the detector's Noise Equivalent Power (NEP) and pre-detection bandwidth, while the detector responsivity $\frac{\partial R_{Sample}}{\partial C_{water}}$ is determined by the inherent responsivity of the detector types and the post-detection bandwidth. Typical benchtop THz detectors have NEPs ranges from $[10^{-13} - 10^{-16} \text{ W}/\sqrt{\text{Hz}}]$ for cryogenic bolometers that operates at $< 4 \text{ K}$ operating temperatures to $[10^{-12} - 10^{-10} \text{ W}/\sqrt{\text{Hz}}]$ for room-temperature devices. For practical application end, cryogenic devices present many restrictions. Aside requiring cryogenic support for the system, these detectors have highly limited sensing power range and typically demands recurring, labor-costly device calibration process.

The detector's response time also puts limitations on certain device choices. Thermal detectors such as pyroelectric detectors have response time on the order of 10^{-1} to 10^{-2} seconds and requires seconds of integration time for a sufficient signal to noise ratio. However, in-vivo targets are typically not stationary – not necessarily in the sense that the target is actively moving, but rather there are constant natural involuntary processes such as breathing, blood flow (diastolic and systolic cycles) and in case of eye, saccades (random eye movements) and blinking. Aside from the difficulty in realizing sufficient integration time, overall imaging time required for slow detectors will be proportional to the number of pixels. If we are to acquire an image pixel-by-pixel, slow detectors are not feasible at all. Hence, it is only feasible to consider fast room temperature devices for *in vivo* imaging applications.

There are several detector device types that operates at room temperature that are viable options for in vivo imaging applications. Schottky diode (SD) [1] detectors have response time on the

order of 10^{-9} sec and less and superior NEP ($10^{-12} \text{ W}/\sqrt{\text{Hz}}$) compared to most room-temperature thermal detectors. SD is still subject to RC time constant (series resistance and junction capacitance) and have less responsivity at higher frequencies, however its sensitivity below 1 THz are superior to that of any other detector types. SD detectors are mounted in metallic waveguides to define its pre-detection bandwidth. Detection is sensitive to frequencies that can be supported by the chosen waveguide [3]. For example, WR 1.5 structure supports approximately 500 – 700 GHz. Feed elements such as horn antennas typically accompany the detector to provide directional gain and aperture size.

However, SD detector devices also present limitations rising from its waveguide-mounted design. Because of the small aperture size of the waveguide, these devices are sensitive to the beam shape and coupling. Dispersing the directivity of the antenna only partially helps with this issue, and the alignment of the beam position to the detector aperture is most critical requirement in using SD detector. This aspect is further discussed in Chapter 2.

Optoelectronic detectors, such as PCS based detectors used for time domain techniques are also a viable candidate. Most time-domain techniques no longer use mechanical delay lines, replaced by the electronic sampling technique using the tunable differential frequencies created by a tunable-frequency laser and a fixed frequency laser [36]. Leveraging the high repetition rate of the pulsed lasers, PCS detectors can now achieve milliseconds of acquisition per pixel, at the expense of SNR and frequency resolution. While the time domain technique is a powerful technique that achieves spectral broadband spectral measurement, optoelectronic detectors have inherently less responsivities than SD detectors. The limitations of detector directivity and alignment requirement are also similar to those for the SD detector devices.

Lastly, there is the issue of available active THz power. Typically the output power of bench-top THz sources fall in the range from microwatts to milliwatts (limited to frequencies $>0.8\text{THz}$). Currently available THz power is not sufficient to be used for flood illumination or array-based image acquisition. Therefore, in many of the pioneering experiments that explored biomedical THz imaging application, the imaging set up used focused beam illumination and detection. Almost all THz imaging systems used in research and industrial applications are single-beam optimized system in order to provide sufficient SNR. Optical designs of the THz imaging system also partially reflect this requirement and are typically single-beam optimized.

1.5.1. Image formation

1.5.1A Pixel-by-Pixel Imaging

The simplest method to construct a THz image is to stitch together pixels containing localized THz measurement. The resolution of the image can be defined by how small of an area can be measured at a time. Consider an imaging system with illumination by a single point source and single-pixel measurement at a time. The best lateral imaging resolution is determined by the combined effect of the size of the focused illumination on target and the equivalent “focus” of the detector. This is an equivalent idea for single-beam microscopy. In fact, many of the concepts from optical imaging can be used for THz imaging. Within the limits of quasioptical approximation, we can apply concepts such as diffraction limit and image transfer functions to THz imaging. In general, microscopy techniques can be also applied for THz imaging system. For example, a confocal microscopy set up have been demonstrated by [55].

Since all of the THz illumination energy is focused into a pixel, the pixel-by-pixel imaging scheme is the best method for SNR. Scarcity of the illumination power and the effectiveness of the single-element detectors further compel use of this method. Many of the pioneering THz imaging experiments were performed by raster scanning the target in transverse plane at the focal plane of the THz imaging optics (i.e. [56]). This method is a good starting point to explore THz imaging of small targets. In this set up, imaging geometries are well defined and near diffraction limit resolution images can be produced with an appropriate choice of optics.

However, this THz imaging set up only sees the rigid imaging plane defined by the raster-scanning plane and the focus of the imaging optics. For surface imaging, this method necessitates the use of a flat dielectric window to push down target surface. When carefully applied, dielectric flattening windows remove a significant amount of image clutter and enables well-calibrated

measurement. In some applications, however, use of dielectric windows that make contact with the target perturbs the measurement and the state of the imaging target. An example of such implication in this study is discussed in in conclusion of Chapter 3.

Moving the target by a scanning stage is also often not feasible or desirable in practical medical imaging applications. While it is also possible to move the THz device assembly over the target, this method is also limited in its rigid imaging plane. Therefore, the advantages of raster-scanning set up in simplicity and good resolution are largely countered by its limited use for more general application and imaging speed. Beam scanning methods can improve imaging speed and system miniaturization. In flood illumination or passive imaging set up, there are also several novel quasioptical imaging system design that utilizes efficient beam scanning mechanism with a single detector [57].

1.5.1B Additional Discussions

Active vs Passive? In passive imaging, the source of the signal is the blackbody radiation of the target as a function of temperature subject to the microscopic and macroscopic environment between the source and the observer. Considering the blackbody radiation power over the 0.1-1 THz band, passive THz imaging to gain any information about characteristics/state of biological tissue would be looking for fractional difference in femtowatts of power, over the natural temperature fluctuation and absorbers along the probing beam pathway; signal difference is not expected from even drastically abnormal state of bodily tissue. Thus, passive imaging technique is not feasible in THz band for medical imaging, while it is a strong alternative for security imaging applications.

Reflective vs Transmission? Transmission mode imaging, in which input THz probing beam passes through the target and detected on the other side, is a simpler and more robust method of characterizing the material of interest because the transmitter and the detector can be placed on-axis. Moreover, the transmission beam path tends not to be modified significantly by the target geometry. As long as enough signal passes through the sample, the probing beam actually “probes” all of the material it passed. Although it is not an imaging technique, pulse oximetry is an excellent example of transmission mode acquisition of a tissue characteristic (blood oxygenation).

The main advantage for transmission geometry is the more controlled set up for material characterization. The calculation of tissue properties in transmission mode are less perturbed by factors such tissue adhesion, contour, and random rough surface scattering that can cause variation in phase [58]. Despite some advantages and of transmission imaging, reflection mode imaging is the only option for in vivo applications. There are no feasible tissue imaging cases where complete transmission of THz radiation is possible or appropriate.

Chapter 2 THz Imaging System Design

2.1. Quasioptical Approximation and Beam transformation

In THz imaging system design process, diffraction theory or computational approach are often too complex to include the effect of multiple reflections and repeated beam truncations. Instead, treatment of THz beam propagation with Quasioptical theory is a well-accepted approach for simple and in general, very accurate prediction of the beam propagation [59] using familiar parameters of Gaussian optics to characterize THz beam and imaging components.

Using the fundamental mode Gaussian beam distribution to describe a single THz beam, the field distribution of a propagating beam is written in the familiar complex Gaussian beam (equation (7)). The beam parameters w , R , and ϕ are determined as a function of propagation distance z from the beam waist and the waist radius w_0 (Equations (8)-(10)).

$$u = \left[\frac{2}{\pi w^2} \right]^{0.5} \exp(-r^2/w^2 - jkz - \frac{j\pi r^2}{\lambda R} + j\phi) \quad (7)$$

w = 1/e field radius at the beam waist

r = radial distance from the beam axis in the plane transverse to the direction of propagation

R = Radius of the curvature of the phase front

ϕ = Phase of the beam front

$$w = w_o \left[1 + \left(\frac{\lambda z}{\pi w_o^2} \right)^2 \right]^{0.5} \quad (8)$$

$$R = z + \frac{1}{z} \left(\frac{\pi w_o^2}{\lambda} \right)^2 \quad (9)$$

$$\phi = \arctan \left(\frac{\lambda z}{\pi w_o^2} \right) \quad (10)$$

This beam radius and the radius of curvatures can be conveniently expressed in the complex Gaussian beam parameter q (equation (11)). When taken reciprocal, it gives following relations in equations (12) and (13).

$$\mathbf{q} = z + jz_c \quad (11)$$

$$\frac{1}{q} = \frac{1}{R} - \frac{j\lambda}{\pi w^2} \quad (12)$$

$$w = \frac{\lambda}{\pi} \left[\Re \left\{ \frac{j}{q} \right\} \right]^{-1}, \quad R = \left[\Re \left(\frac{1}{q} \right) \right]^{-1} \quad (13)$$

The theory of complex paraxial wave optics allows to conveniently compute Gaussian beam (more generally termed: ‘Hermite-Gaussian beam’) transformation with ABCD ray matrices [60]. A Gaussian beam can be propagated through optical system that is composed of a series multiple paraxial elements using cascaded ABCD matrices of those elements. The output of such system is also a Gaussian beam. The complex beam parameter q of the output beam modified by a general ABCD matrix is given by equation (14). A list of ray matrices for free space propagation, thin/thick lenses, spherical mirrors, refractive interface, and other elements is provided in [59], which also provides discussions on the conditions in which paraxial approximations are valid.

$$q_{out} = \frac{A_k q_{in} + B_k}{C_k q_{in} + D_k} \quad (14)$$

2.1.1A Limitations of quasioptical approach

The quasioptical treatment of the THz beam is subject to the minimum value of w_0 , for which the Gaussian solution and the paraxial approximations are valid. A “reasonably conservative criterion” for the use of paraxial solution is $w_0 \geq 0.9\lambda$ [61]. Within this limitation, this method can be extended to handle propagation of more complex beams by decomposing it as the sum of Gaussian beams. A beam profile can be expanded as a sum of Gauss-Laguerre and Gauss-Hermite beam modes, and each higher-order mode beams can be propagated using equations (13) and (14). In a different approach, the Huygen’s Principle can be used to decompose the beam spatially in multiple fundamental mode Gaussian beams. The propagation of each “beamlets” can be computed, then added coherently to give the resulting beam profile. The latter method is a ground for the computational approach to analyze THz beam propagation in some software tools.

2.2. Quasioptical imaging components.

Low index lenses in the THz region can be manufactured from plastic compounds such as High-density polyethylene (HDPE), polyethylene thermoplastics, Polymethylpentene compound (i.e. PMP or TPXTM – Mitsui, Japan) that is transparent in visible region, and Teflon. These are relatively cheap materials with tolerable effects of aberration and scattering from machine tool-marks by light polishing. [29] On the other hand, refractive optics impose Fresnel reflection losses and material attenuation. The beam intensity profile after passing through the lens can be highly distorted from these two loss mechanism and the phase front shape may be different from that intended by the lens design. Therefore, refractive optics generally achieve less tight focusing.

Reflectors are generally more efficient in light collecting (low loss), can achieve higher numerical aperture, and do not introduce chromatic aberration. For this reason, focusing geometry reflectors are more frequently used in millimeter wave and THz regions. An example is an off-axis parabolic (OAP) mirror, which is a segment of a full paraboloid. Off-axis reflectors provide a focal point displaced from the mechanical axis of the parent reflector geometry, giving unobstructed access to the target. The parabolic shape of the reflector keeps the wave front at equal path lengths and does not cause spherical aberration. These properties are especially desirable when the THz source is pulsed, such as that produced by a photoconductive switch (PCS).

The main disadvantage of reflector optics, such as OAP mirrors, is in the lower tolerance for misalignment. In OAP reflectors, focused spot suffers a strong coma if the input beam is not aligned exactly along its optical axis. Asymmetries in the off-axis reflectors also gives rise to distortion of the beam shape and polarization profile. This is perhaps a unique problem of using the reflector geometry that is only moderately larger than the wavelength of the beam.

OAP reflectors (mirrors) perform the most basic level of beam transformation - collimation and focusing and they are extensively used for the THz imaging system design. Therefore, this section starts with the investigation of beam transformation by a single reflector. Then, the subsequent analysis shows how beam modification by each reflector components are compounded in multiple reflector systems.

2.2.1. 90° Off-axis parabolic mirror: geometry

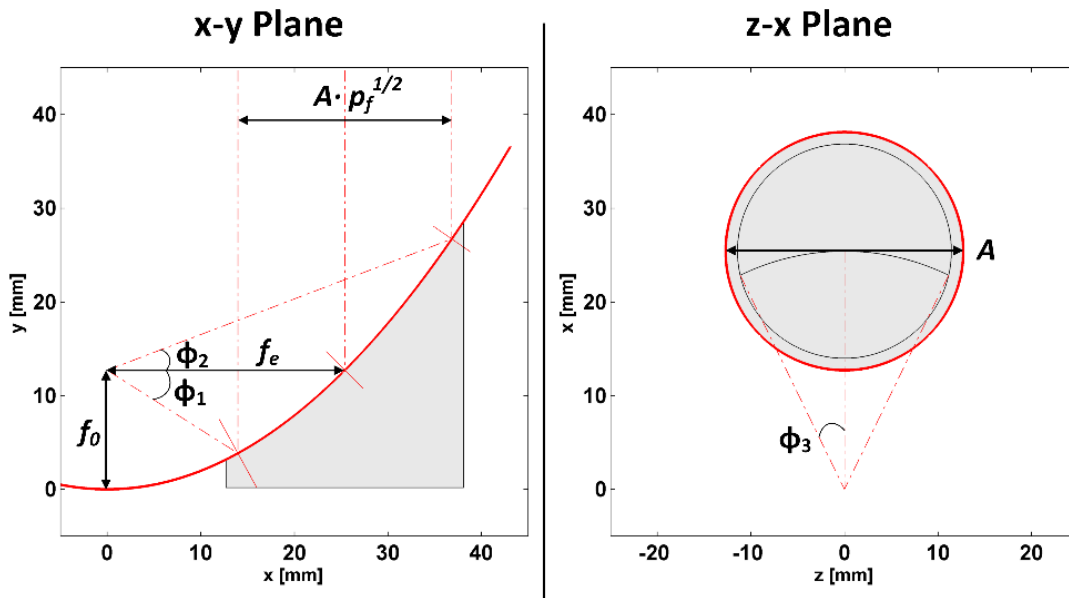


Figure 2-1. 90° Off axis parabolic mirror geometry for a 25.4 mm EFL mirror. (Left: Side view. Right: View looking into the clear aperture.)

Refer to the geometry labels in Figure 2-1 for a circular-cut OAP mirror, which is commonly available form by the optics manufacturer. For any rays that is parallel to the optical axis and incident on the mirror surface, the focal length is a distance between the local mirror surfaces to the focal point P. We can place the vertex of the parent parabola at the origin, and express the focal length as a function of beam location. f_0 denotes the parent focal length. For a 90° OAP mirror, f_e

(the effective focal length (EFL)) is defined as the focal length at the 90° reflection path at the center of the mirror. Additionally, the following parameters are designated:

A	Clear aperture diameter.
p_f	Percent fill defined as the transverse area of the beam divided by the clear aperture area assuming that the constant intensity contours of the beam are circular.
ϕ_1, ϕ_2	The half angles on the parabolic cut, formed between the raypaths of the central ray and the rays positioned at the edges of the mirror.
ϕ_3	The azimuthal half-angle bound by the central raypath and the ray that are tangent to the mirror edge
NA	Numerical Aperture: $NA_i = \phi_i/EFL$ (see Figure 2-1)

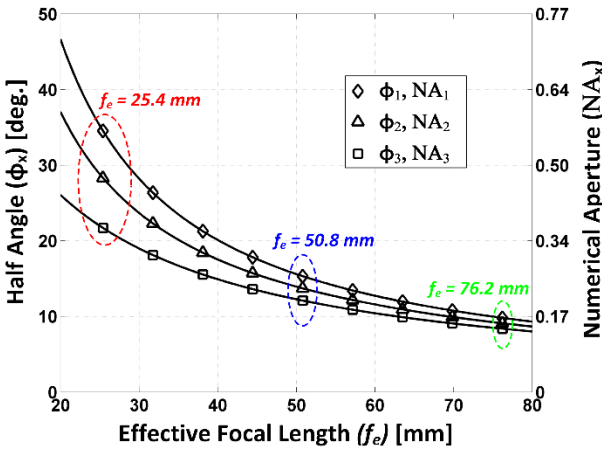
The following is observed about an OAP mirror, which is essentially a cut of a paraboloid: 1. the mirror's surface curvature is radially symmetric around the circular contour centered on the axis from which the parent paraboloid forms and the focal point coincides (z-x plane). 2. The curvature along the parabolic cut (x-y plane) is monotonically decreasing and it is asymmetric about the axis of any possible cuts.

Similarly to geometric optics definitions, the angular aperture (or the numerical aperture (NA)) specifies the “light-gathering power” and a measure of diffraction of the beam by the optic. The definition in Table 2 can be applied to any mirror cut shape. For circular-cut mirrors, the NA value representing the mirror can be loosely compared to the NA values of lenses. The half angles Φ_1 , Φ_2 , and Φ_3 are found by equations (15), (16), and (17) respectively. Note that at large f-numbers the paraxial approximation can be applied to equations (15) - (17) and the half angles fall proportional to f_e^{-1} . Figure 2-2 plots the half angle and the numerical aperture for the EFL = 25.4

mm, 50.8 mm, and 76.2 mm over an EFL range from 20 mm to 80 mm with A= 25.4 and a 90% fill factor.

Table 2. Geometric properties of 90° off-axis parabolic mirrors

EFL (mm)	Φ_1 (deg.)	Φ_2 (deg.)	Φ_3 (deg.)	NA ₁	NA ₂	NA ₃
25.4	21.70	34.54	28.32	0.37	0.57	0.47
50.8	12.10	15.33	13.72	0.21	0.26	0.24
76.2	8.38	9.81	9.10	0.15	0.17	0.16



$$\Phi_1 = \tan^{-1} \left(\frac{A\sqrt{p_f}}{4f_e} - \frac{f_e}{2f_e + A\sqrt{p_f}} + \frac{1}{2} \right) \quad (15)$$

$$\Phi_2 = \tan^{-1} \left(\frac{A\sqrt{p_f}}{4f_e} + \frac{f_e}{2f_e - A\sqrt{p_f}} - \frac{1}{2} \right) \quad (16)$$

$$\Phi_3 = \sin^{-1} \left(\frac{A\sqrt{p_f}}{2f_e} \right) \quad (17)$$

Figure 2-2. Half angle and numerical aperture of a circular-cut parabolic mirrors with A = 25.4mm.

2.3. Transformation of Gaussian beam by 90° OAP reflectors

Strictly speaking, the simplest form of quasioptical analysis with equations (13) and (14) cannot be applied to off-axis parabolic mirrors. The mirror surface does not perfectly match the Gaussian amplitude profile and the ‘thin lens approximation’ is not true for OAP mirrors. The collimation of a Gaussian beam by a 90° OAP mirror are shown in Figure 2-3 for the three mirrors of varying $f/\#$, whose diameter A is 25.4mm. In this set-up, a fundamental Gaussian beam with $w_0 = \lambda = 0.6\text{THz}$ and 10° divergence half angle is placed at the focus of the mirror. For s- and p-linearly polarized incidence, the field energy distribution and polarization profile of the collimated outputs of three mirrors are plotted. These outputs are computed with simulation tool (ASAP®, Breault Research), which utilizes the ‘beamlet’ approach discussed in section 2.1.

In all three mirrors, field distortion can be observed in the asymmetry of the beam. Polarization profile distortions are seen along the curvature contours of the mirror surface. For the mirror with highest focusing power (and thus most curvature), the distortion of amplitude and polarization profile is the largest. These outputs can be exactly predicted by the mathematical approach by [62], in which formulates the generation and propagation of a set of higher-order Hermite-Gaussian modes. However, mathematical complexity quickly takes over when this approach is applied to more than two mirrors in series.

Nevertheless, inspecting the overall field and polarization profile of the beam, the distortion by these fairly high NA optic can be considered ‘mild’ for certain use. In case of the reverse transformation, in which a collimated beam is focused into a spot, the effect of distortion essentially vanishes [62]. Therefore, if we just focus on the focusing operation of the mirror, we can still use the quasioptical method and treat the mirror surface as a thin lens to obtain output beam size and location.

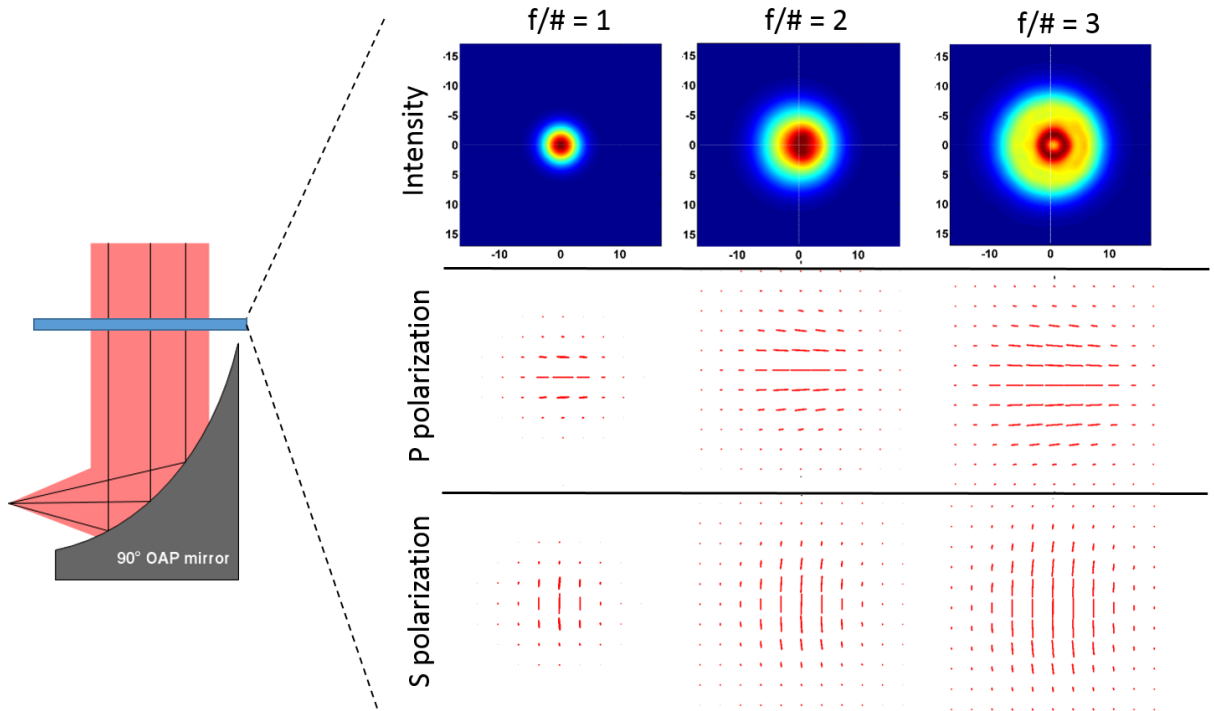


Figure 2-3. Distortions of a Gaussian beam input by a single 90° off-axis parabolic (OAP) mirror.

Consider a perfectly collimated THz beam input to the mirror shown in Figure 2-3. The quasioptical method discussed in section 2.1. will take the form of equations (20) - (22), with the following approximation for “ideal” focusing case:

1. The circular OAP mirror is treated as a thin lens whose focal length $f_m = \text{EFL}$
2. The system illumination beam is assumed perfect Gaussian ($M^2 = 1$)
3. The input beam is perfectly collimated and directly incident on the mirror aperture surface. In other words, the beam has $R = \infty$ and $d_{\text{in}} = 0$.
4. Effect of beam spill over is neglected by treating the $A \rightarrow \infty$

Equation (21) says that the location of the beam waste is always behind the geometric focal points of the lens. For large ratios of beam waist to wavelength (i.e. in systems operating in the UV to IR) $z_{R,1} \rightarrow \infty$, $d_0 \sim f_e$ and $\omega_{0,2} \sim (\lambda f_e) / (\pi \omega_{0,1})$. Surprisingly, the prediction of this radical

approximation matches very well to that of more sophisticated computation and the experimental characterization of the beam size. These comparisons are made in the following section.

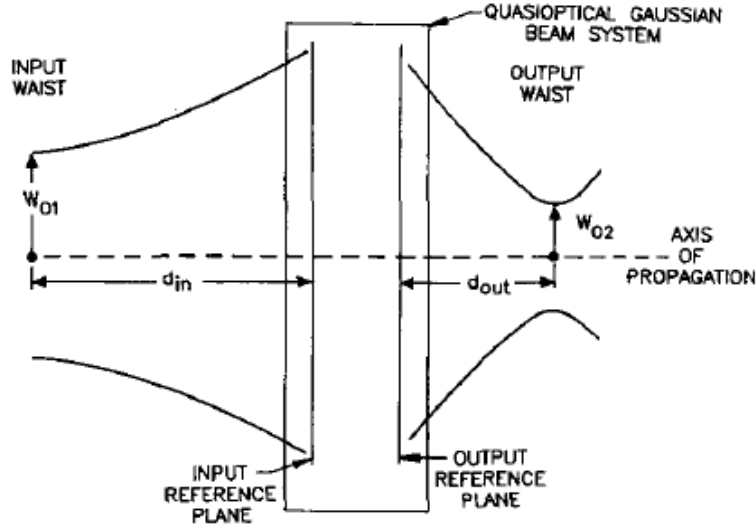


Figure 2-4. Transformation of Gaussian beam by general quasi-optical Gaussian beam system and the sizes/locations of input and output beam waists. Image adapted from [61].

$$w_{o\ out} = w_{o\ in} \left[\left(\left(\frac{d_{in}}{f_e} - 1 \right)^2 + \frac{z_c^2}{f_e^2} \right)^{0.5} \right]^{-1} \quad (18)$$

$$d_{out} = f_e \left[1 + \left(\frac{d_{in}}{f_e} - 1 \right) \left(\left(\frac{d_{in}}{f_e} - 1 \right)^2 + \frac{z_c^2}{f_e^2} \right)^{-1} \right]^{-1} \quad (19)$$

Under the assumptions 1-4,

$$z_{in} = \frac{\pi \omega_{in}^2}{\lambda} \quad (20)$$

$$d_{out}(f_m, z_{R,1}) = \left(\frac{1}{f_e} \right) \left[\left(\frac{1}{f_e} \right)^2 + \left(\frac{1}{z_{in}} \right)^2 \right]^{-1} = d_{out} \quad (21)$$

$$\omega_{out}^2(f_m) = \omega_{0,1}^2 \left[\left(1 - \frac{d_{out}}{f_e} \right)^2 + \left(\frac{d_{out}}{z_{in}} \right)^2 \right] \quad (22)$$

2.4. OAP mirror Systems

In the previous section, the beam distortion by an OAP mirror is visualized with a Gaussian beam. Wave optic simulation shows that the beam transformation by a single OAP mirror can be approximated with Gaussian beam theory, and that focused beam can be in fact considered an almost perfect Gaussian spot. However, it is not straightforward to determine if such approximation can be used in series when propagating Gaussian beams through a series of OAP mirrors. Because of the degree of freedoms in the orientation of each mirror and its asymmetric geometry, beam distortions are carried from mirror to mirror

A full-wave simulations or other adequate simulation tools, such as physical optics, should be used to fully understand the beam propagation through such system. However, such analysis mostly helps to verify the expected beam transformation and coupling, and not so much in the design process to achieve specific imaging performance.

Imaging performance through beam path analysis and Gaussian beam approximation, when used with proper design rules, can help with systematic design process for THz imaging system. In this light, it is instructive to look at some examples of OAP mirror systems that shows how beam transformations are carried through multiple quasioptical elements.

Consider a pair of OAP mirrors shown in Figure 2-5. Each mirrors are rotated about its optical axis such that their clear-aperture normal vectors are parallel and their focal spots overlap. The input collimated beam is focused by the first mirror (OAP2) on the focal plane. The reflected signal is collected by the symmetrically positioned receiving mirror (OAP3), which produces collimated output beam parallel to the input. This configuration functions similar to an objective lens in an optical microscope. By changing the focal length of the mirrors, the working distance, focusing power, and the angle of incidence can be changed.

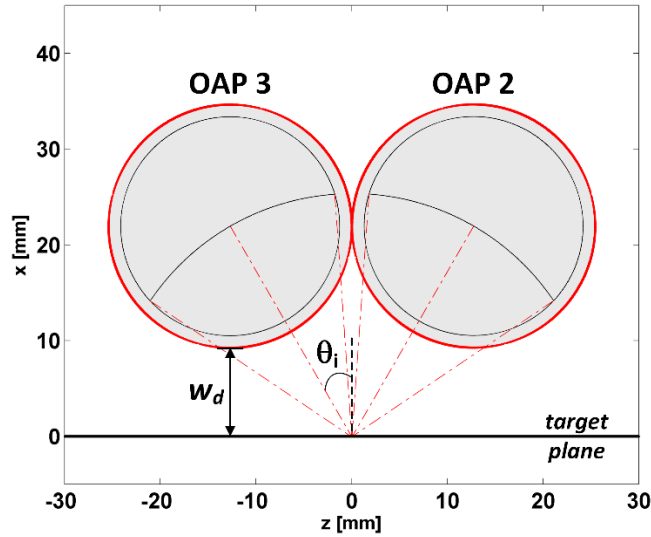


Figure 2-5: A pair of identical off axis parabolic mirrors. One mirror provides illumination, and the other one collects the reflected signal at a specular direction.

OAP mirror pairs are frequently used in THz experiment set up to provide active THz illumination and collect the returning signal. Since the input and output of the mirror pairs are collimated beams, a different mirror pair of various combinations may be used to select focusing power, incidence angle, and working distance. The exchangeable THz mirror pairs are used in the THz imaging system developed for in-vivo THz imaging studies of small animals [42] (Figure 2-6). In this system, the collimated input and output beams are relayed by two other OAP mirrors. The clear apertures of the OAP1/OAP2, and OAP3/OAP4 are concentric. Since both input and output are fixed, exchanging the “objective” mirror pair with a different numerical aperture (NA) and focal length. Meanwhile, the rest of the optics are not perturbed.

System design shown in Figure 2-6 facilitates exploring tradeoff relations between spot size, working distance, and incidence angle with different numerical apertures. Additionally, THz time of flight can be modulated by the THz objective rail carrier along the rail. Three different objective mirror pair sets are designed with 25.4mm, 50.8mm, and 76.2mm effective focal length (EFL) pairs of mirrors.

THz imaging modules constructed this way are very compact and have minimal power loss in the beam path. It is also very feasible to design and fabricate mechanical structures for these mirrors with standard machine shop techniques and tolerance. In this implementation, all components are mounted on a typical rail carriers attached to the same dovetail rail to keep the optical axes collinear.

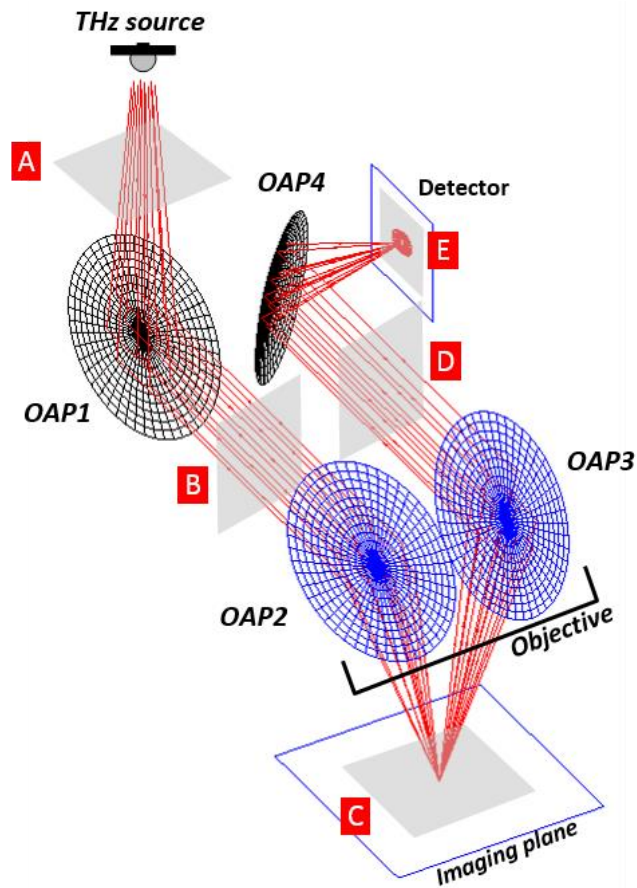


Figure 2-6: A single-pixel THz imager, with four off-axis parabolic (OAP) mirrors labeled OAP 1-4.

Fixed Parameters:

OAP1: $A = 25.4\text{mm}$; $EFL = 76.2\text{mm}$

OAP4: $A = 25.4\text{mm}$; $EFL = 25.4\text{mm}$

Variable optics (Objective mirror sets: OAP2,3)

Set 1: $A = 25.4\text{mm}$; $EFL = 25.4\text{mm}$

Set 2: $A = 25.4\text{mm}$; $EFL = 50.8\text{mm}$

Set 3: $A = 25.4\text{mm}$; $EFL = 76.2\text{mm}$

Distance between OAP1,4 and OAP2,3: 100mm

2.4.1. Imaging System Implementation

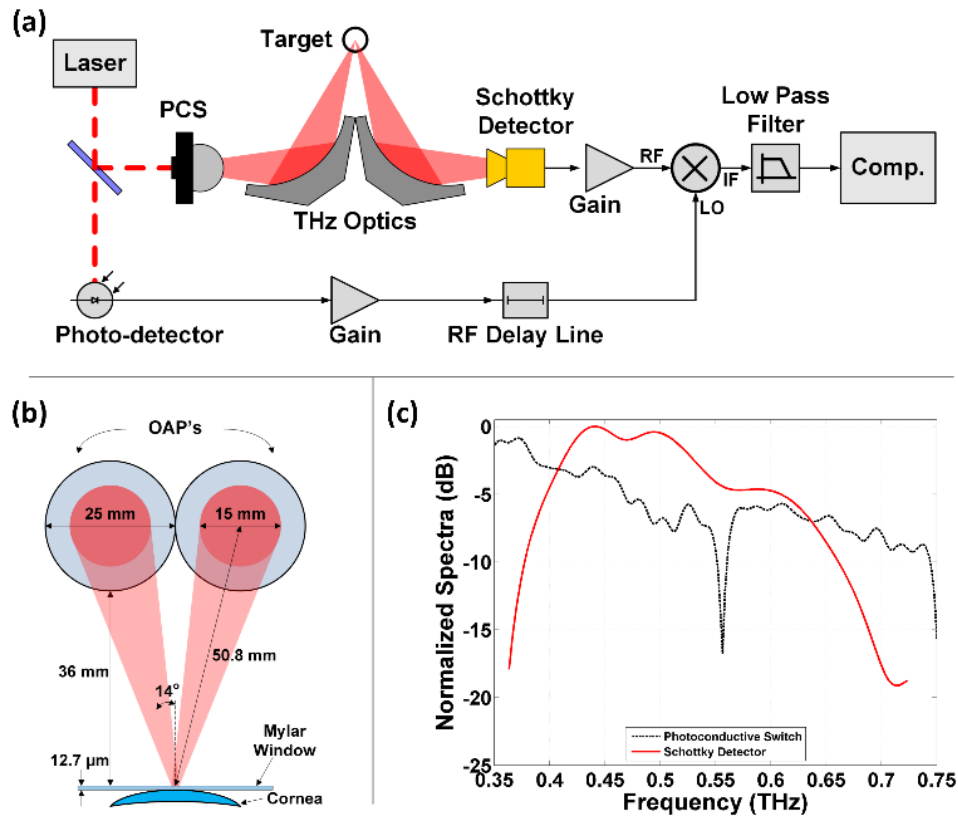


Figure 2-7: A direct-detection, focused beam THz imaging system

- (a): Block diagram of pulsed THz imaging system employing photoconductive source and zero-bias Schottky detector operating a center frequency of $\sim 525\text{GHz}$.
- (b): Illumination geometry with a dielectric flattening window
- (c): Photoconductive switch power spectral density and detector spectral responsivity.

The imaging system employs a photoconductive switch (PCS) as the THz source. The device is mounted on the backside of a silicon hyperhemispheric lens at the aplanar point for efficient free space radiation and to form more directed emission, resulting in $\sim 5^\circ$ half-angle. The PCS is pumped by a 780-nm mode-locked laser with a ~ 230 fs pulse width, 20 MHz repetition frequency, and ~ 8 mW of average power. The THz beam travels through the optics chain detailed in Figure 2-6.

A zero-bias Schottky diode detector (Virginia Diodes, Charlottesville, VA) is used for power detection. The signal focused by OAP4 is coupled to the feedhorn [63] of detector. The rectified THz pulses is amplified with 38 dB of gain and sent to a gated receiver driven with a reference RF pulse from the same laser. This system architecture gives an effective operational band proportional to the photoconductive switch power spectral density weighted by the Schottky diode spectral responsivity (Figure 2-7c [42]). Pixels are acquired with a 1ms integration time and imagery is generated by raster scanning the target beneath the fixed, focused THz beam using x and y axis stepper motors.

2.4.1A Quasioptical prediction of the imaging performance with Gaussian beam theory

Using the quasioptical approach discussed in this section, the transverse and axial imaging resolution of the system is modeled for three pairs of effective focal lengths (25.4mm, 50.8mm, 76.2mm). The transverse resolution is defined as the focused beam width produced by OAP2 at the focal plane. In x -axis, the beam is incident at an oblique angle determined by the focal length of the mirror pair, thus the effective beam width is calculated from the projection of the beam profile on to the focal plane.

The axial resolution of the system is a bit trickier to define. In the context of optical microscopy, the axial resolution may be defined by the axial dimension of the “Airy disk”, which roughly corresponds to the longitudinal point-spread function. In the single-beam THz imaging system, a similar way to characterize this concept is to find the active area of the illumination that is captured by the detector. The beam overlap is illustrated in Figure 2-8. Δd can be found from the Rayleigh length of the focused beam and the geometry of the objective mirror pairs. The length of 1/e beam overlap is computed with equation (18) for each of the mirror pairs.

$$\Delta d = 2\omega_{0,z} \left[\sin^2(\theta_i) - \left(\frac{\omega_{0,z}}{Z_{R,2}} \right)^2 \cos^2(\theta_i) \right]^{-1/2} \quad (23)$$

The frequency dependent transverse and axial resolution are plotted in Figure 2-9. The effective resolution of the imaging system shown in Figure 2-9 is calculated as the weighted average of spot size from the spectral responsivity of the system shown in Figure 2-8(c).

Table 3. Resolution computations

EFL (mm)	θ_i (deg.)	w_d (mm)	$w_{0,y}$ (mm)	$w_{0,z}$ (mm)	f_e-d_0 (mm)	Δd (mm)
25.4	30.00	9.30	0.52	0.45	0.05	1.81
50.8	14.48	36.49	0.93	0.90	0.42	7.21
76.2	9.59	62.43	1.36	1.34	1.41	16.13

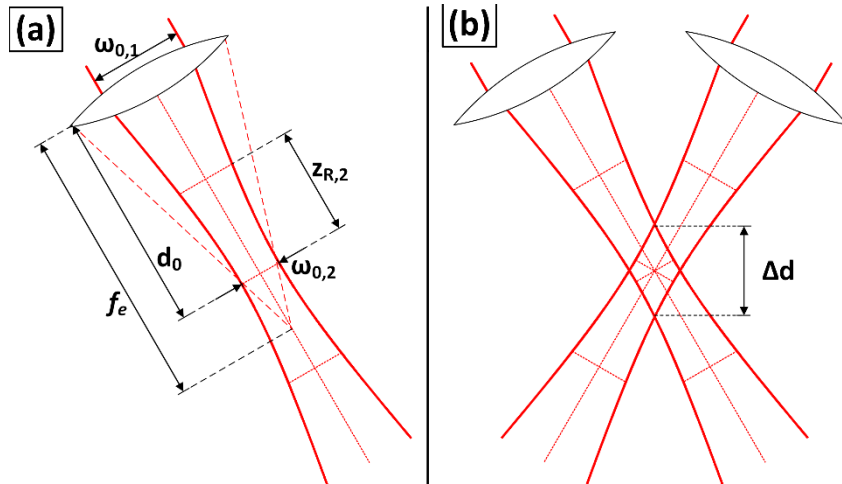


Figure 2-8: Beam overlap in axial extent.

- (a) Transverse axis parameters.
- (b) Depth resolution defined by the intersection of 1/e contours of two overlapping Gaussian beams.

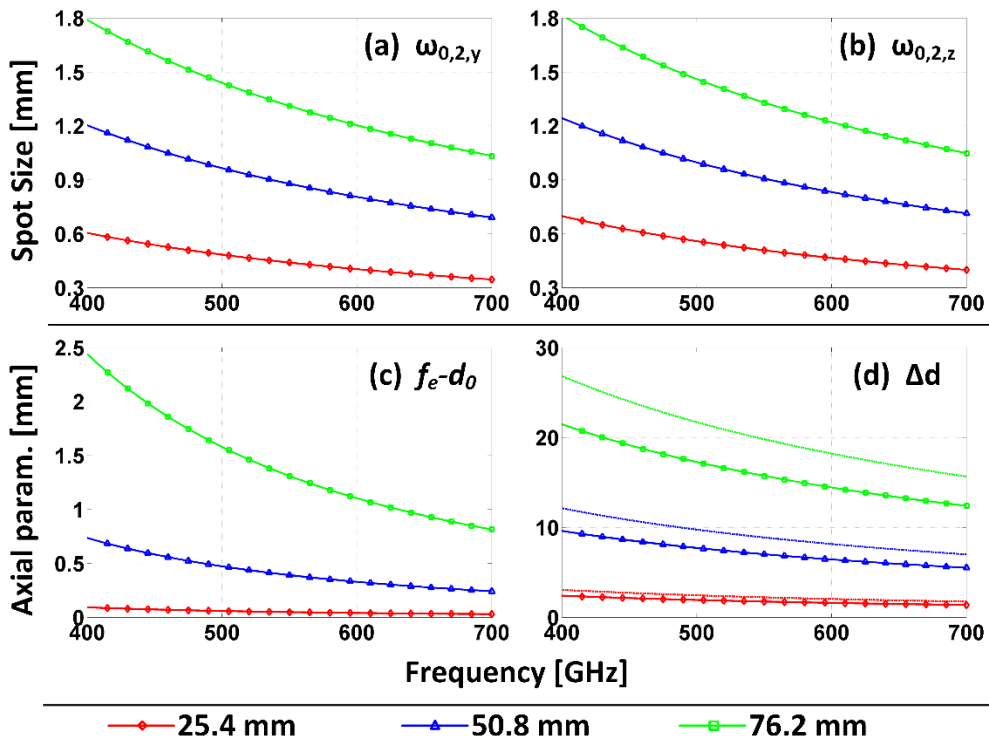


Figure 2-9: Frequency dependent resolution parameters.

- (a) Spot size along the y-axis
- (b) Spot-size along the z-axis
- (c) Axial offset of the beam waist location with respect to optic focal length.
- (d) Depth resolution defined by intersection of the 1/e contours of overlapping beams.

2.4.1B Comparison with measurement

The transverse resolution is measured by the knife-edge method [42]. Knife-edge method infers beam diameter of a known beam shape by sweeping a half-plane metal edge in the imaging plane and measuring the reflected power as a function of edge position. The resulting measurement is a good approximation of the spatial step response. The point spread function of the imaging system can also be estimated with measurements performed in two orthogonal directions.

The axial imaging performance of the system is measured in terms of Depth of Focus. The Depth of focus (DOF) is defined as the range of imaging plane location (in z) that the beam stays focused. The DOF is optimized for each application. If we are to use optical designs similar to that shown in Figure 2-6, a sufficiently large DOF is desired to tolerate minor curvatures and irregularities of tissue when measuring the tissue reflectivity, so that there is minimal change in signal strength from the probing geometry. On the other hand, more defined, narrower DOF is desired when the probing section depth need to be thin in certain applications. DOF is characterized by measuring return signal as a function of target displacement in $\pm z$ from the imaging plane.

In this imaging system, the DOF is measured as the range of imaging plane displacement ($\pm z$) from the exact focal plane until the collected signal drops to 50% of the peak power (occurring at the ideal alignment of target at the focal plane). The DOF measurement for each of the objective mirror pairs are shown in Table 4.

The result of the experimental result and the prediction of the quasioptical model are also compared to that computed with electromagnetic approach. A reflector antenna design tool (GRASP®, TICRA) simulated the knife-edge and DOF measurements. The total signal energy received at the detector is then calculated using the feedhorn antenna's beam pattern. The results of the measurement and EM simulation are plotted in Figure 2-10. The knife-edge measurement

matches very well with the prediction of the simulation, suggesting that the scope EM modeling is a good predictor of the imaging performance. For DOF, the measurement also matches very well with simulation for EFL = 25.4mm and 50.8mm pairs. However, the measurement for the 76.2mm EFL pair deviates from the prediction, collecting more signal for + displacement of the target.

The transverse spot size and Depth of Focus (DOF) for each pairs are tabulated in Table 4. The result of the Table 3 and Table 4 are combined in Table 5, by converting the transverse spot size metric to represent 1/e field energy, and comparing the beam overlap (Figure 2-8) to DOF measurement.

The transverse spot size measurement agrees very well between the quasioptical prediction, measurement, and EM simulation. In the scope of the measurement method (confined at the focal plane), this result suggests that treating the OAP mirrors with the quasioptical method is a good approximation of THz beam transformation by OAP mirrors and resulting imaging performance.

Other the other hand, the DOF measurement is consistently less than the dimension of the beam overlap. Inspecting discrepancies for each EFL pairs, it can be also observed that differences are not explained with a scale-factor either. Moreover, it is difficult to explain the asymmetric signal collection seen in Figure 2-10 with a simple “overlap” treatment. These observations suggests that the sensitivity of imaging system to axial position of the target depends not only the beam parameters, but the beam path geometries determined by the optical design.

Table 4. Properties of the focused beam by a pairs of OAP mirrors

EFL (mm)	w_d (mm)	q (deg)	10%-90% (mm)	DOF (mm)
25.4	9.3	30	0.61×0.69	0.8
50.8	36.5	14	1.2×1.3	4.0
76.2	62.4	9	2.1×2.6	11.7

Table 5. Comparison of predicted transverse and axial imaging performance

EFL (mm)	w_d (mm)	Spot size (mm)		DOF (mm)	
		Predicted	Measured	Beam overlap (Δd)	Measured
25.4	9.3	0.52×0.45	0.43×0.48	1.81	0.8
50.8	36.5	0.93×0.90	0.92×0.85	7.21	4.0
76.2	62.4	1.36×1.34	1.84×1.48	16.13	11.7

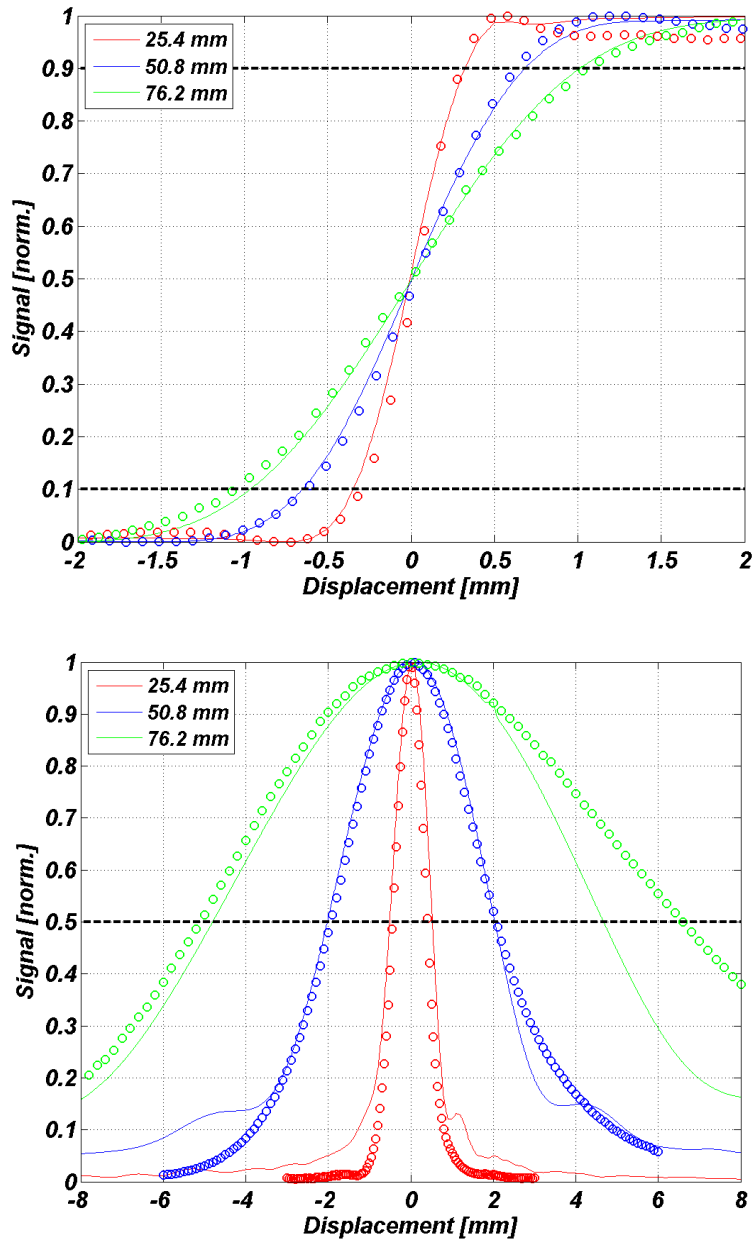


Figure 2-10: Measurement of the transverse spot size (Top) and Depth of Focus (DOF) (Bottom).

Top: Transverse spot size measurement at the target with Knife-edge technique. Half-plane metal target is swept across the spot location and received power at the detector is measured as a function of translation. Assuming the symmetry of the beam, the distance need to sweep across the relative signal strength at 10% and 90% is taken as spot size.

Bottom: Depth of Field (DOF) measurement (o) versus simulation (solid line) for each objective sets. Signal strength at the detector is measured as a metal target is displaced in $\pm z$. For 25.4mm, 50.8mm, and 76.2mm focal length objective pairs.

2.4.2. Confocality of the imaging system

Figure 2-11 illustrates the ray path of the beam when the imaging target is displaced from the focal plane. We can observe that not only the focus of reflected beam is displaced in z-axis, but the transverse location of the reflected beam also changes as a result of axial displacement of the target. This misalignment of the beam position seeds both positional and directional ray path displacement in the subsequent reflections by off-axis mirrors. For a single mirror or lens, this phenomenon is often described as a *coma*, when incident beam is no longer parallel to the optical axis of the mirror. When such beam is passed through multiple off-axis elements, the resulting beam shape and path are determined by the location and orientation of subsequent optical elements.

It is observed that in this objective mirror pair design, the position of the target plane at the overlapping focal point of the pair of mirrors is crucial to maintain correct beam path. Misprojection of focal point location results in angular displacement of the beam path upon reflection by OAP3, and subsequently the final focusing is not perfect by the last mirror (OAP4).

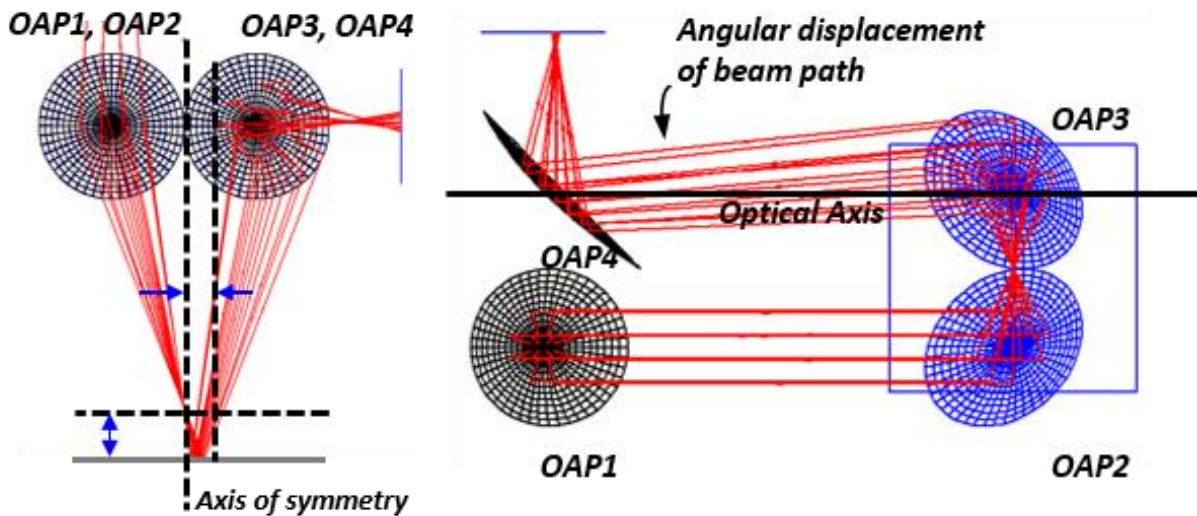


Figure 2-11: Beam path displacement for off-focal plane reflections.

In fact, this observation is similar to that of confocal imaging set-up, in which out-of-focus beam is obstructed by a pinhole aperture or diaphragm. At least two components in this system design are effectively behaving as pinholes: Overlapping focal point of the OAP2 and OAP3 requires both illuminating and reflected THz beams to coincide at the focal point, therefore acting as pinhole aperture the size of spot diameter. The size of the detector feedhorn aperture acts as the second pinhole. Together, ray paths must pass through both “pinhole” apertures, and the imaging plane is aligned to the last focusing mirror (OAP4).

Looking at the formation of the focused beam at the detector aperture helps to further understand the confocal operation of this system design. Figure 2-12A shows an overlay of five spots formed at the detector plane (FOV: 3mm x 4mm). The white diamond-shaped lines illustrates the aperture of the pyramidal feedhorn of the detector, measuring 3.8mm x 3.8mm on each diagonal axis. The numbered “spots” represent the focused beam profile resulting from five different positions of the target at $z = -10, -6, 0, 6, \text{ and } 10$ mm. At the correct target position (3), a properly focused beam forms at the center of the feedhorn cross section. The focused beam moves away from the center and disperses as the negative displacement increases ($3 \rightarrow 4 \rightarrow 5$). Positive target displacement ($+z$) results in beam walk-off in the other direction.

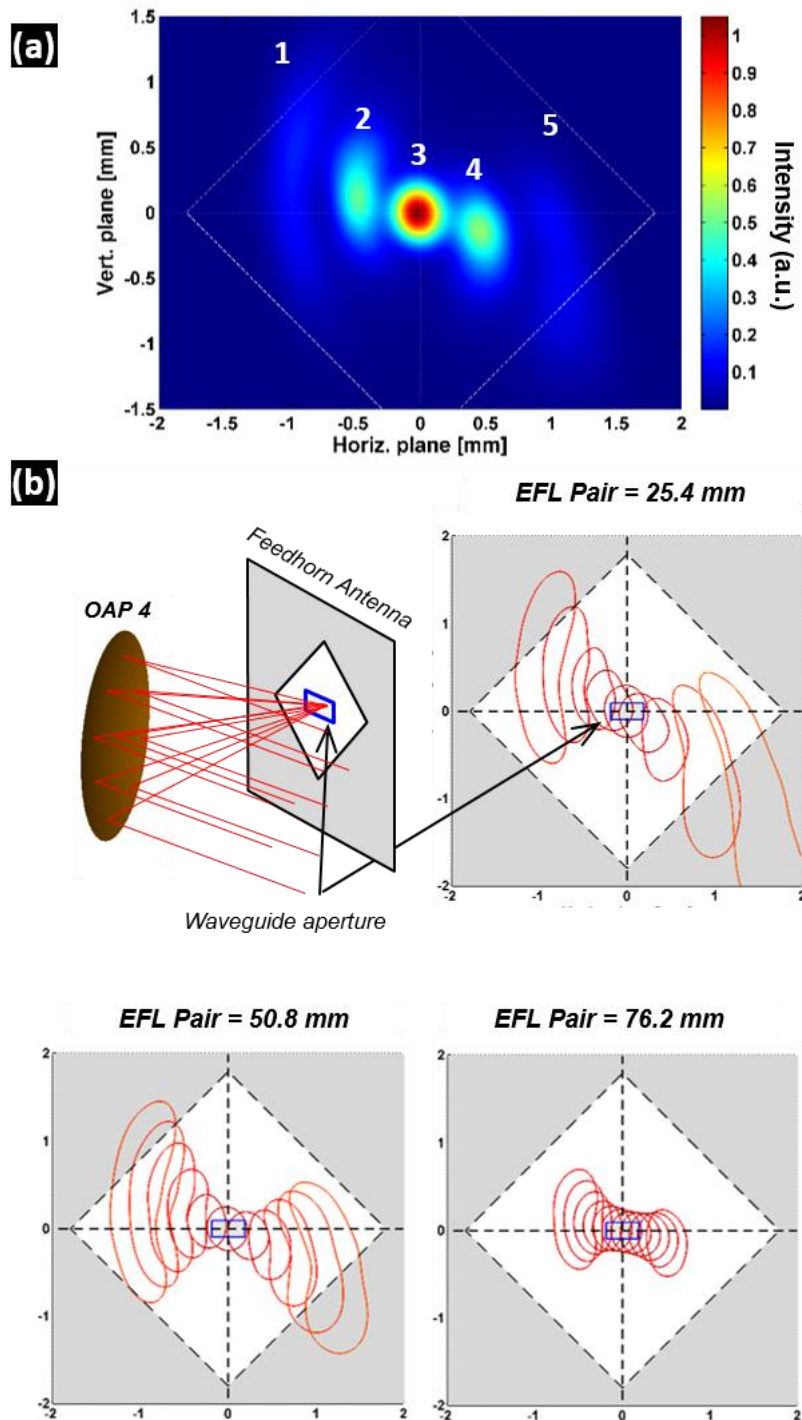


Figure 2-12: Beam walk-off and smearing at the detector plane.

(a): $z =$ (1) -10 mm, (2) -5 mm, (3) 0 mm, (4) +5 mm, (5) +10 mm.

(b): The beam walk-off effect is shown as the evolution of contour lines that moves away from the detector position and disperses as the target is displaced from the focal plane. For 25.4mm EFL pair, the displacement range is ± 3 mm. For 50.8mm and 76.2mm EFL pairs, the target displacement spans ± 10 mm. Blue rectangle denote the WR1.5 waveguide aperture.

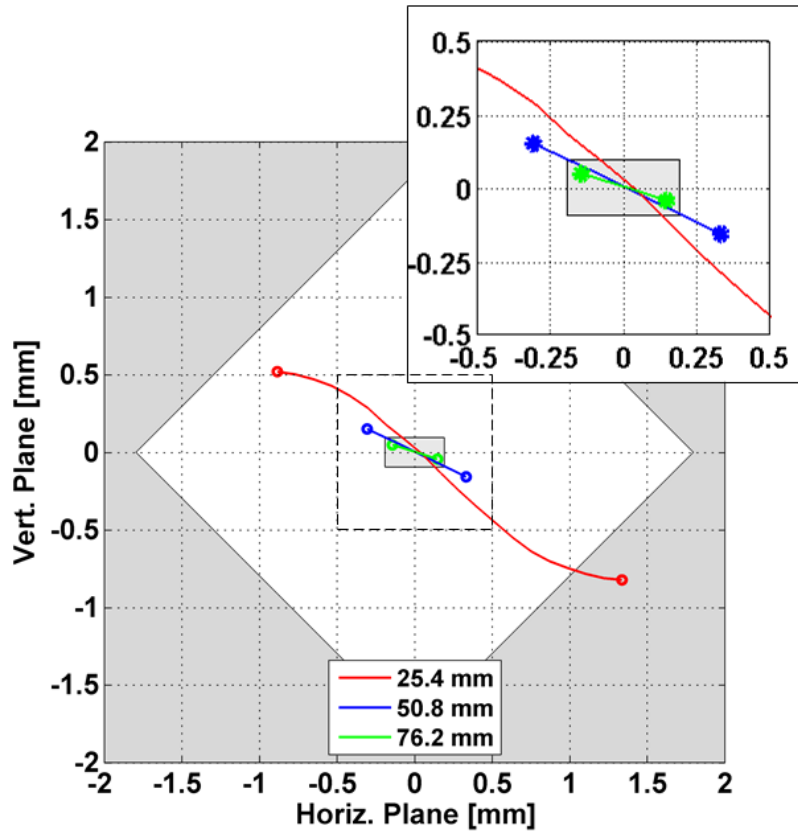


Figure 2-13: Beam centroid (energy center) walk-off resulting from axial displacement of the imaging plane.

Displacement ranges are ± 3 mm for 25.4mm objective pair (red), and ± 10 mm for 50.8mm (blue) and 76.2mm (blue) objective pairs. Gray brackets outline the 2.4mm x 2.4mm diamond-shaped feedhorn aperture and the WR 1.5 waveguide aperture.

The beam's displacements are re-plotted as a contour line (1/2 maximum power) for each mirror sets. For 25.4mm EFL set, target is displaced at 1mm increment, from -3mm to +3mm. For 50.8mm and 76.2mm pairs, the target is displaced at 2 mm increment from -10mm to +10mm. The 25.4mm pair demonstrate rapid walk-off of the THz beam from detector aperture. Beam walk-off distances for longer EFL pairs are not as dramatic.

As it is confirmed in the previous section (Figure 2-10), the signal collection at the detector is reliably predicted with electromagnetic treatment of beam-coupling using equation (24), where E_1 is the computed beam profile and E_2 is the detector feedhorn's beam pattern.

$$\bar{K}_3 = \frac{|\iint (\vec{E}_1 \cdot \vec{E}_2) dA|^2}{\iint |\vec{E}_1|^2 dA \iint |\vec{E}_2|^2 dA} \quad (24)$$

However, an optics-based explanation also seems to work very well in this case. We observe that the measured DOF correspond to the range in which the beam center location is falling within the WR1.5 waveguide aperture (gray rectangle). While the collected beam signal strength degradation is from both focused spot displacement and beam dispersion*, the beam walk-off is much faster. Therefore, it can be understood that the effect of beam walk-off is the dominating mechanism for signal coupling between the THz beam and the detector. The asymmetric displacement path also helps to explain the asymmetry of DOF seen in the measurement (Figure 2-10), without carrying out beam coupling calculations.

Confocal-like operation by the objective mirror pairs and the THz detector suggests that DOF can be manipulated by the optical system design and the detector's antenna performance. Depth of focus may be additionally altered as a function of the numerical aperture of the optics and illumination geometry (i.e. incidence angle). For example, DOF will be reduced as the distance between OAP1 and OAP4, as the collimated beam path is lengthened and diverging beam path strays away from OAP4.

2.5. Distortion of beam shape and polarization profile

2.5.1. Field distortion and Polarization Aberration

The quasioptical analysis proceeded under the assumption that the original Gaussian source beam would remain mostly Gaussian throughout the optical chain. However, it can be shown that a chain of mildly non-paraxial optics produce highly non-Gaussian beam when the distortion at each individual component is stacked and amplified by subsequent components.

To begin this investigation, a coherent, linear X-polarized THz source at $\lambda=0.5\text{mm}$ (0.6 THz) is propagated through the same optical system design. The field and polarization profiles are computed at each key point of beam propagation noted by A through E in Figure 2-6. The propagating beam is intercepted at each plane and the field energy distribution (beam pattern) and polarization profile of the beam are sampled.

Cross-polarization components are created from aberrations from OAP1 and OAP2, producing elliptically polarized states at the higher-order lobes due to path length difference. On the other hand, field distortion is not present at all in the focused spot. Even if there were any noticeable distortion up to this point, the THz field is well converged into a near-diffraction limited spot to produce nearly symmetric field profile.

The field distortion at C is not so apparent because the beam is focused very tightly. The effect of field distortion is most noticeable when the signal returning from the target is re-collimated (“D”). Yet, the centroid point of the beam is computed to be well over 2000mm away from the beam position, indicating that the beam is still well collimated and the beam path is unchanged.

It can be also observed that cross-polarization components are produced, indicated by circular polarization state observed in the side-lobes of the focused beam (in “C” and “E”). It is also noted that focused THz beams at the focal plane (‘C’) and the detector plane (‘E’) show rotated

polarization state. By inspecting the orientations of OAP 1-4, it can be understood that the rotation state at E is the sum of the angles of each mirror in respect to the original polarization angle of the source. A similar result can be obtained with a Y-polarized source [64].

We can expect that the degree of distortions observed in Figure **2-14** will increase with components that has more asymmetry in curvature about its central axis. Indeed, the objective pair with shorter focal length and larger NA result in larger degrees of distortion. The field energy distributions and the polarization profiles at D are shown for each of the objective pairs. The 25.4mm EFL pair produces the most severe distortion. By comparison, the field distortion from 76.2mm EFL pair shows arguably “better” beam profile than the shorter EFL pairs. Rotations of the transverse beam axis due to the rotations of the mirror pairs are also observed.

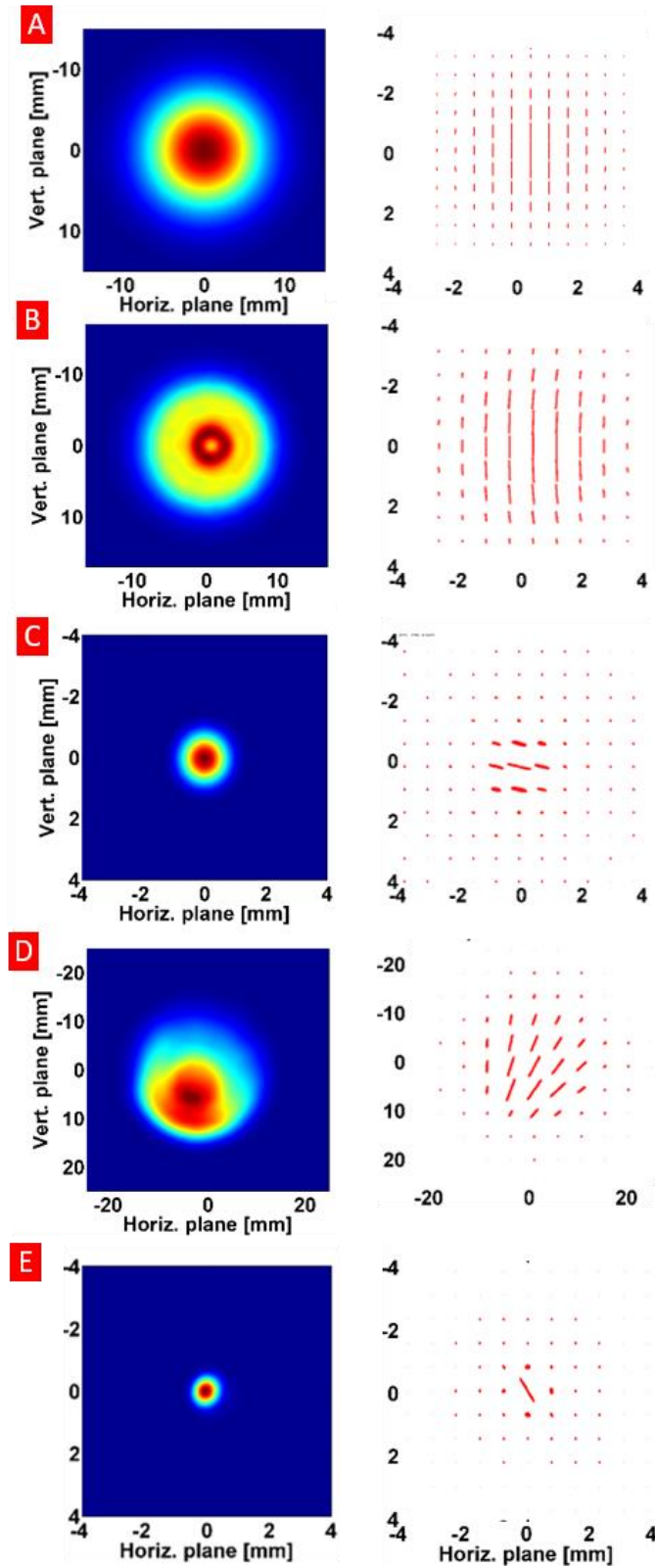


Figure 2-14 THz beam profile and polarization state while propagating through a series of OAP mirrors, from a y-polarized Gaussian TEM₀₀ source.

2.5.2. Design Rule 1: Matched (symmetric) orientation

From above analysis, it is clear that the mirror configurations in this system design are compounding distortions. However, when the asymmetric components are positioned in the symmetric orientation, the distortions by each component can in fact be cancelled by the symmetry. Within paraxial limit, the sum of curvatures that the beam ‘sees’ in the symmetric orientation is zero for the symmetric orientation of the optical components.

When a complete symmetry is not possible, the system design can still be optimized to avoid addition of symmetry and the component orientations are rather acting against each other. Figure 2-15 shows the image formation by OAP2 when the orientation of the OAP1 is flipped such that they are in the symmetric position. Although the EFL of OAP1 and OAP2 are different and the OAP is rotated 14° around the shared optical axis, the pair of mirrors perform almost like a pair of thin lens.

This design rule may be applied in the middle of the chain to minimize the source of most severe asymmetry. In the objective pair design, the second mirror (OAP3) can be turned around to realize zero distortion by the objective pair. Figure 2-17 shows dramatically improved beam profile at D compared to those seen in Figure 2-14, showing a restored beam profile and corrected polarization rotation as well.

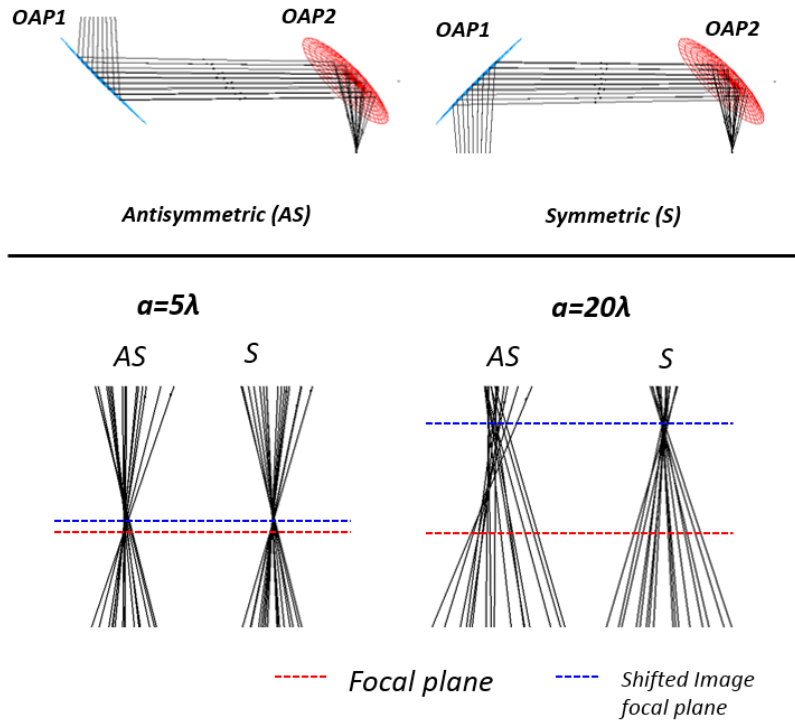


Figure 2-15. Image formations in the antisymmetric and symmetric optics orientations.

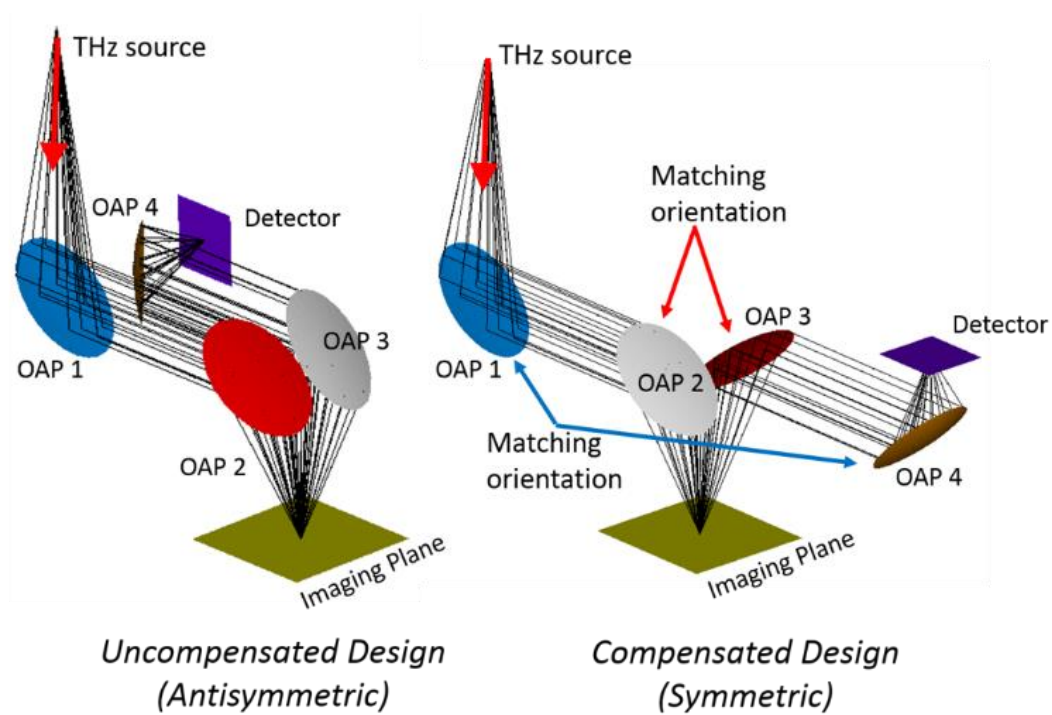
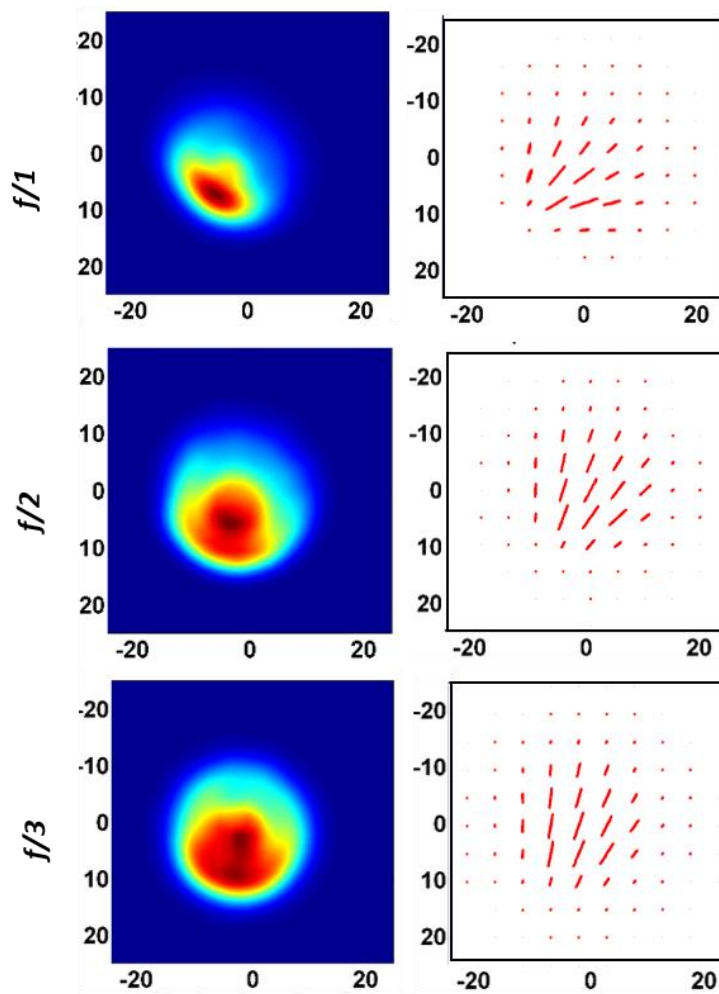


Figure 2-16: Re-design of the THz imaging system with optics orientation matching to cancel off-axis aberrations.

*Uncompensated orientation
(Antisymmetric)*



*Compensated orientation
(symmetric)*

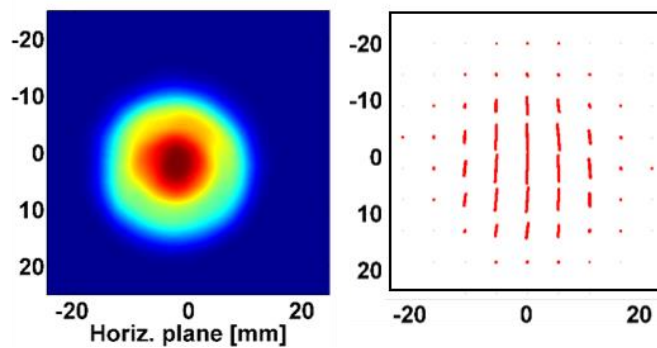


Figure 2-17: Field and polarization distortion correction by matched (compensated) optics orientation.

2.5.3. Design rule 2: Magnify the detector

As shown in the section 2.3, beam path displacement of the returning signal causes the focused signal to form outside of the detector aperture, thus it is the major mechanism of signal loss. The analysis in section 2.3.2 investigated the effect of using different focus powers of the objective mirror pair in generation of beam path displacement. On the other hand, properties of the fixed parameter mirrors – OAP1 and OAP4 –determines the efficiency of collecting signals. The $f/\#$ of the OAP4 can be considered as a measure of effective magnification of the detector aperture. By providing the largest effective magnification of the detector aperture, the walk-off distance can be minimized such that the returning signal is more likely to fall within the narrow detector aperture.

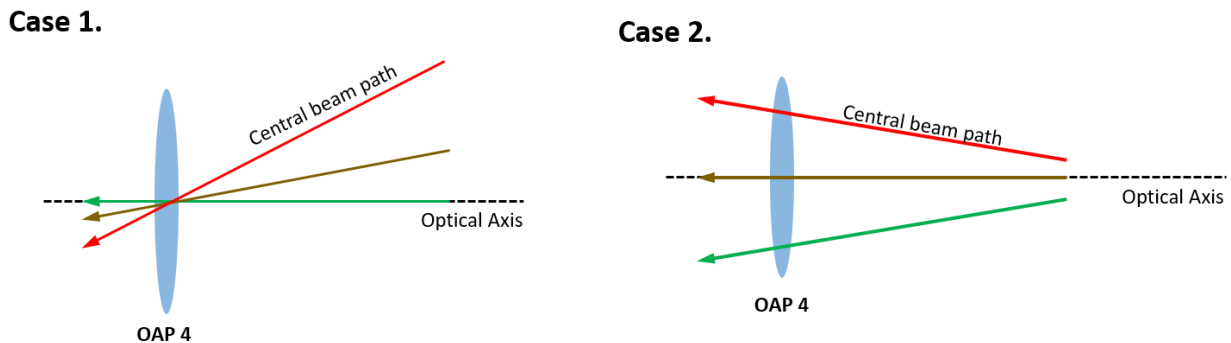


Figure 2-18. Displaced beam reaching the final mirror (OAP4)

Figure 2-18 illustrates the two cases of displaced beam reaching the last OAP mirror that focuses the received beam to the detector (OAP4). A collimated beam is incident to OAP4, whose central beam path is angularly displaced. In case 1, the beam is incident at an angle but the central beam path still passes through the center of the mirror. In case 2, the beam is angularly displaced at some distance away from the mirror, and the central beam path is displaced from the optical axis of the OAP4. Upon inspection of Figure 2-11, it is noted that case 2 better represents the

displaced beam path in the system discussed in previous sections. The beam pattern formed at the detector aperture plane (“E” in Figure 2-6) is computed for the input beam that is not parallel to the optical axis of OAP4.

In Figure 2-19, a collimated beam source with $w_0 = 10\text{mm}$ are placed $d = 100\text{mm}$ away from OAP4 (EFL = 25.4mm), similar to the original beam path geometry shown in Figure 2-6. This beam is given $\pm 5^\circ$ angular displacement in its path, resulting in $\sim 8\text{ mm}$ displacement of the beam position from the axis by the time it hits OAP4. This input beam profile is intercepted at $d = 50\text{mm}$, (“Collimated beam Input cross-section”) and plotted in Figure 2-19. The field energy and polarization profile of the resulting focused spot are also plotted for each \pm displacements in either transverse axis. The center of the detector plane, where the detector aperture is placed, is denoted by white axis lines.

It can be observed that \pm displacements of the input beam in z-axis result in different spot sizes at the detector plane because the input beam is incident on different surfaces. Displacement in Y axis result in symmetric spot walk-off, as expected from the y-axis symmetry of the OAP4. However, the walk-off distance in each of the cases are comparable. The same analysis is performed for a longer focal length (EFL = 50.8mm) OAP4, and the result is plotted in Figure 2-20. The displacement behavior is similar to that seen in shorter EFL mirror. However, it can be confirmed that the displacement distance is proportionally for longer EFL mirrors. Therefore, for the same input beam, a shorter focal length mirror result in lesser beam walk-off on the focal plane and makes a better case for coupling the return signal to the detector.

The opposite applies to the source-collimating mirror. In this case, we are interested in minimizing the beam path displacement of the collimated beam (OAP1 \rightarrow OAP2) caused by the misalignment of the source to OAP1’s focus. For the same degree of misalignment of the source

position, a longer focal length mirror will result in less angular displacement of the output collimated beam.

Fortunately, this design rule was correctly applied in the system design shown in Figure 2-6. A 76.2mm EFL mirror serves the source (OAP1) while a 25.4mm EFL (OAP4) provides gain to the detector. The effective magnification of the detector aperture to the source, therefore, is 3:1.

OAP 4
 A = 25.4mm
 EFL = 25.4mm

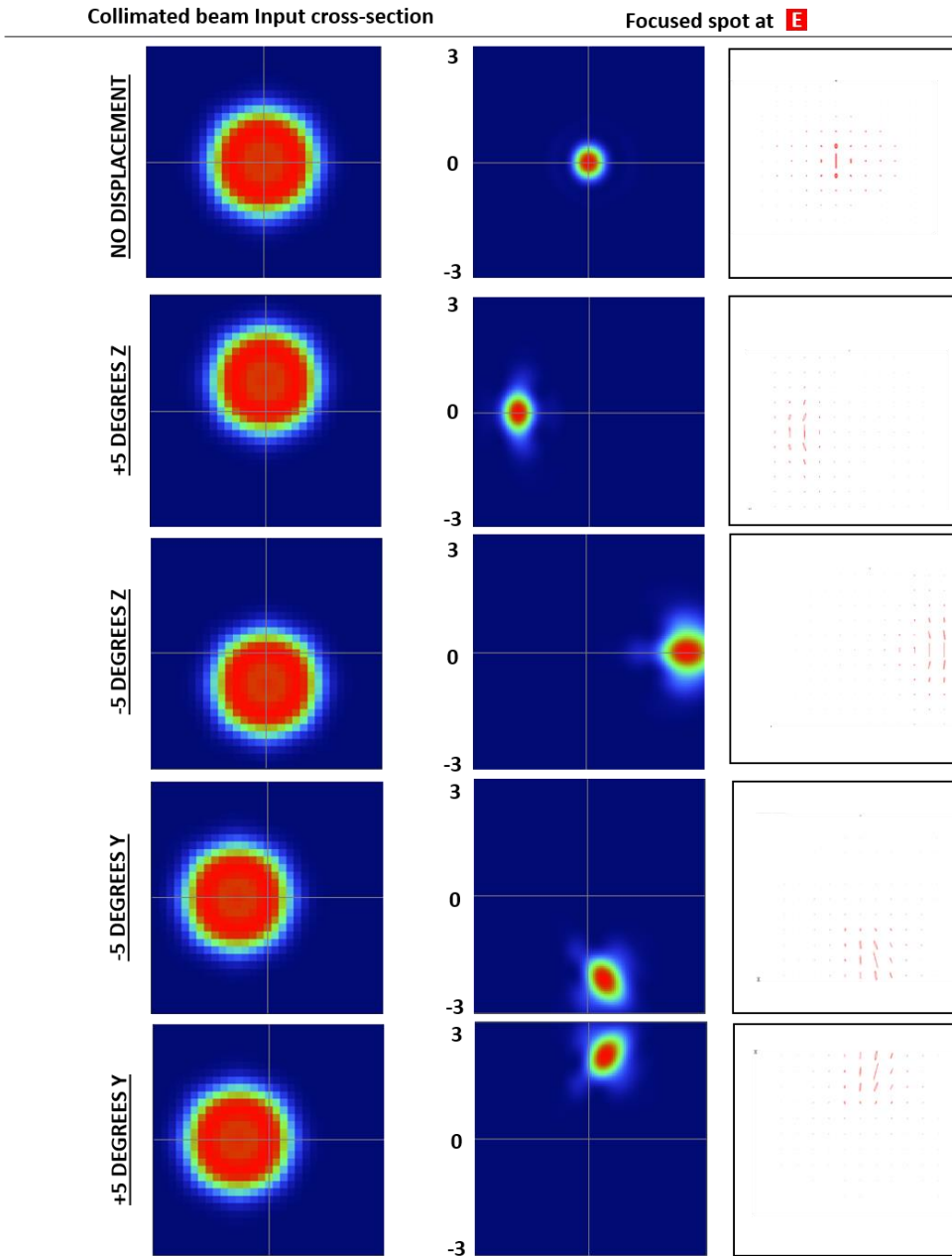
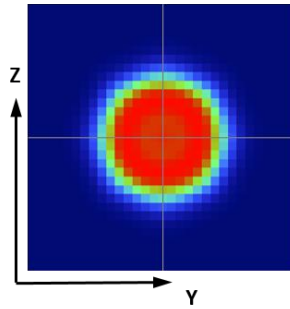
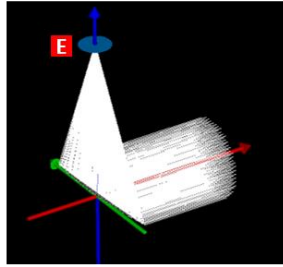
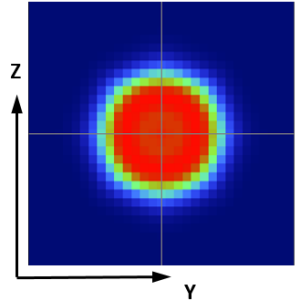
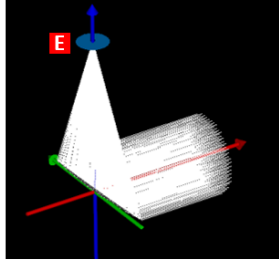


Figure 2-19. Focused beam displacement in 25.4mm EFL OAP4.

OAP 4
 A = 25.4mm
 EFL = 50.8mm



Collimated beam Input cross-section

Focused spot at **E**

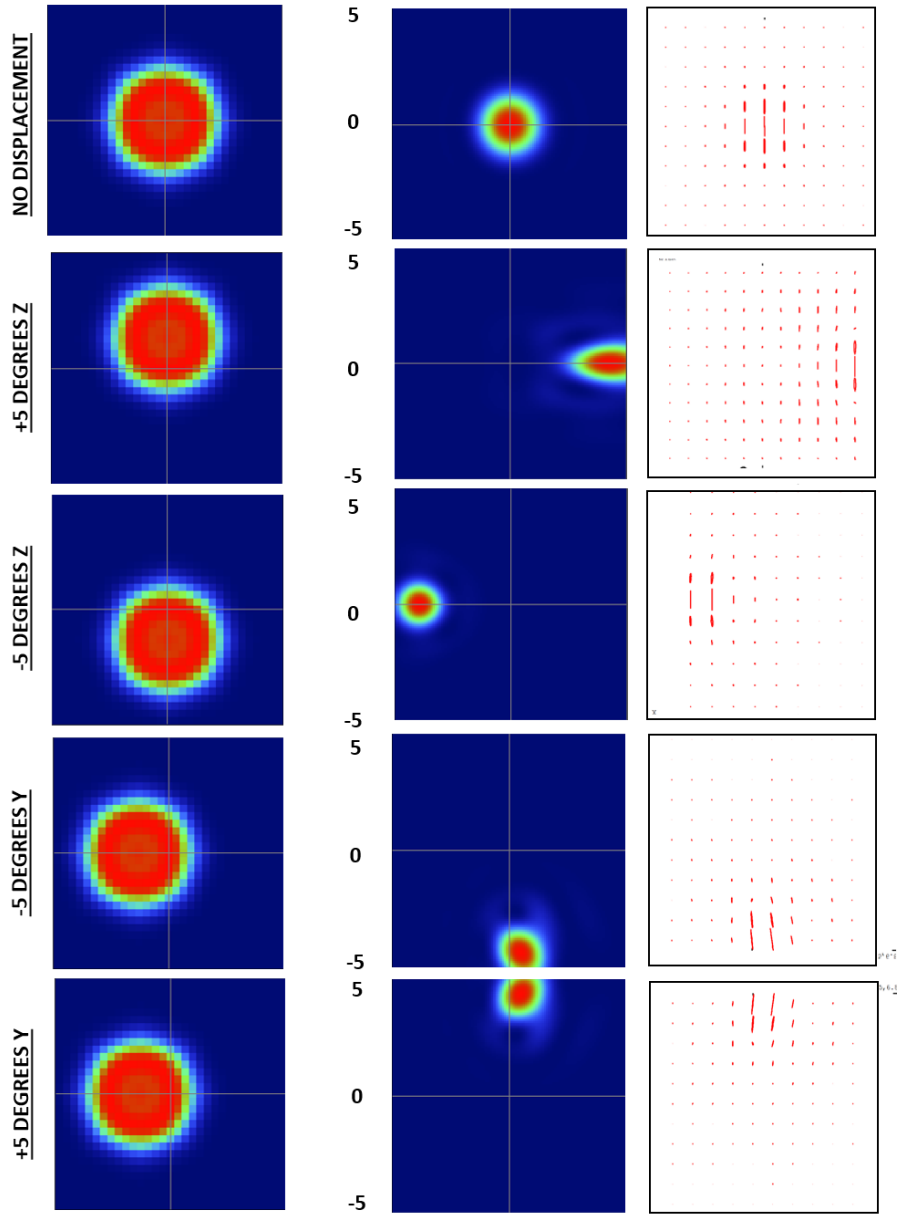


Figure 2-20. Focused beam displacement 50.8mm EFL OAP4.

2.6. THz imaging system design: Conclusion

The Gaussian beam theory and quasioptical formulation of THz beam propagation are highly useful methods to model, approximate, and analyze THz beam propagation through optical components whose dimensions are comparable to the wavelength. Because of the quasioptical nature of THz imaging, most THz imager designs are single-beam optimized systems that performs focused illumination and focused detection. This type of imaging system design can produce good signal-to-noise ratios but limits the imaging operation to a narrow imaging plane. In a geometric ray-tracing analysis, it is observed that when multiple OAP mirrors in series are relaying THz beam, the signal reaching the detector is screened by a narrow tolerance of beam path alignment with each OAP mirrors. Effectively, this behavior results in narrow depth of focus, resembling a confocal imaging scheme.

Two design rules are discussed in sections 2.5.2. and 2.5.3. , which further helps the case of using quasioptical modeling of THz beam transformation in the optical system design process. The first design rule provides a method to cancel off-axis distortions by matching asymmetric optical elements in symmetric orientations. The second rule helps to reduce the effect of the beam displacement rising from the off-axis reflector geometry.

However, this confocal behavior is not always desired in THz biological tissue imaging in reflection mode because THz waves are rapidly attenuated in water-rich soft tissue. The electrical skin depths (δ) in human skin range from tens of micrometers upto a millimeter in the THz band [42], while the typically achievable axial resolution are on the order of millimeters, as shown in this chapter. Imaging plane underneath the surface of the tissue cannot be accessed easily in biological targets, especially given the available THz illumination power and detector sensitivity. THz beams are mostly reflected on surface, therefore when using this kind of system, the imaging

FOV must be a flat surface. Strongly for this reason, many of the pioneering experiments in THz biological imaging used thin dielectric window to gently push down the tissue. Without it, the reflected signal is displaced as seen DOF characterization (Figure 2-10) upon encountering a curved surface or a sufficiently rough surface. The novel beam scanning system design presented in Chapter 4 removes this critical requirement for the THz corneal imaging.

Chapter 3 : THz-Corneal tissue Interaction: Electromagnetic Modeling and First *in vivo* Experiment

3.1. Revisiting the anatomy of cornea

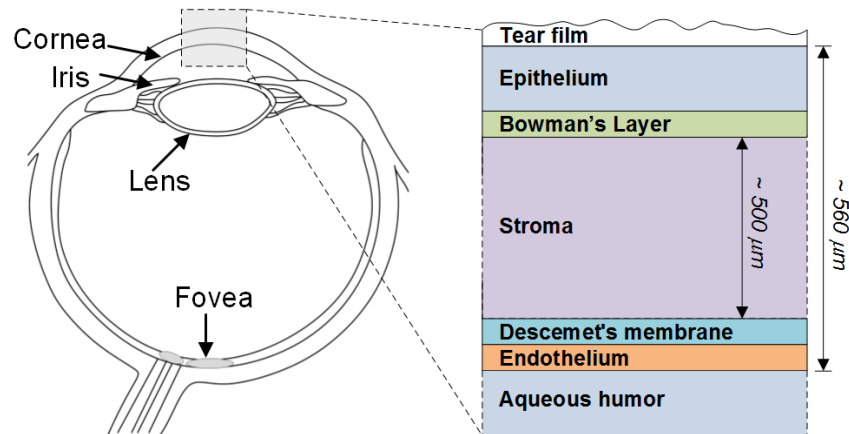


Figure 3-1: Corneal structure.

The bulk of the cornea is composed of the Stroma. All other layers are between $5\ \mu\text{m} - 15\ \mu\text{m}$ (approximately optically thin at THz wavelengths). The cornea sits atop a body of water called the Aqueous humor.

The surface layer of the cornea (epithelium) is covered by a thin layer of fluid called the tear film, which is replenished by blinking, reflex tearing, and a number of other mechanisms [65-68]. The bottom layer of the cornea (endothelium) lies adjacent to the aqueous humor, a fluid that is almost entirely water and is kept at higher than the atmospheric pressure. Bordering the aqueous humor, the endothelium is a layer of specialized cells whose function is to regulate the water content of the stroma using the aqueous humor as the reservoir. A single layer of squamous

epithelial cells produce and maintain a thin layer of collagenous substance, called the Descemet's membrane.

All of the structures are optically thin ($< 15 \mu\text{m}$) with respect to THz wavelengths except the stroma, which typically makes up $\sim 90\%$ of the total thickness ($\sim 522 \mu\text{m}$). The stroma is believed to have axial water content distribution similar to that plotted in Figure 3-2. This profile was measured by confocal Raman spectrometry technique by [25], obtained from rabbit eyes ($N = 10$). The water content changes almost linearly, starting from $\sim 83\%$ at the endothelium boundary and dropping to $\sim 77\%$ at the epithelium. Such distribution seem to match the steady-state solution of the diffusion equation, with the boundary conditions of water source (aqueous humor) at the epithelium and evaporation at the epithelium. The fluence level used in this measurements, however, exceeded $1600\text{W}/\text{cm}^2$. At such energy density, it is likely that the corneal tissue properties have been affected and the overall accuracy of the measurement was not reliable. However, this is the most complete *in vivo* dataset of CTWC that we could find.

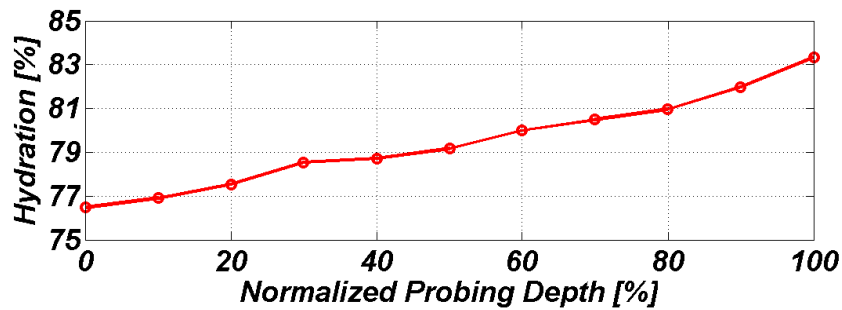


Figure 3-2: Typical axial profile of the corneal tissue water content (CTWC) measured by [25]

3.2. Stratified media model analysis

3.2.1. Problem set-up and assignment of tissue properties

In the ordered, layered tissue structure of the cornea, the dimensions of the most structures such as macroscopic collagen fiber structures, scars, and vesicles found in the cornea are on the order of $\sim 50 \mu\text{m}$. On the other hand, the surface roughness of the cornea is optically smooth with a root mean square (RMS) surface height standard deviation of $\sim 0.129 \mu\text{m}$ [68]. Therefore, we can hypothesize that the effect of scattering at the THz band are significantly reduced compared to other types of tissues. These considerations suggest that the corneal tissue structure can be treated as a stratified layers, in which tissue properties are uniform in the transverse extent but varying in depth. It is not known how the CTWC varies in the transverse extent. Only the assumptions of axial water content distribution is partially supported by the measurement.

Therefore, we set up the cornea as a smooth stratified medium whose dielectric constant is defined by axially varying tissue water content distribution. The responses of the corneal tissue to THz radiation can be computed using classical electromagnetic problem with multi-layer dielectric slabs. This approach helps to preclude the effect pertinent to anatomical features (curvature), and allows to focus on how the tissue's depth-varying tissue water content affect THz sensing. There are few expectation for this modeling:

1. The stroma is composed almost entirely of collagen and water, thus the stromal tissue can be treated as a binary mixture of water and collagen. Then, the Bruggeman model (Equation (5) discussed in Chapter 1 can be used to predict the effective dielectric constant of stromal tissue ($\hat{\epsilon}$) with the following known parameters:
 - ϵ_c : Dielectric constant of collagen
 - ϵ_w : Dielectric constant of liquid water computed with the Debye model (Equation (2)). The

frequency dependent dielectric properties of water are captured by the double Debye model [69] (equation (2)), using the parameters and corner frequencies ($\epsilon_0, \epsilon_1, \epsilon_\infty, f_1, f_2$) discussed in Chapter 1.

- p_w : Water volume fraction

$$\epsilon_w(f) = \epsilon_\infty + \frac{\epsilon_0 - \epsilon_1}{1 - j2\pi f/f_1} + \frac{\epsilon_1 - \epsilon_\infty}{1 - j2\pi f/f_2} \quad (25)$$

$$\hat{\epsilon} \text{ s. t. } p_w \left(\frac{\hat{\epsilon} - \epsilon_w}{\epsilon_w + 2\hat{\epsilon}} \right) + (1 - p_w) \left(\frac{\hat{\epsilon} - \epsilon_c}{\epsilon_c + 2\hat{\epsilon}} \right) = 0 \quad (26)$$

2. Because of large absorption of water in the tissue, the majority of the back-reflected signals are from the epithelium and the stroma. At longer wavelengths, the wave penetrates deeper into the stroma and will be affected by the presence of the aqueous humor, which acts like a lossy electrical back short. In such case, the spectral response of the tissue will depend on the thickness of the stromal layer.

The problem set-up is illustrated in Figure 3-3. The axial water content distribution of the cornea is discretized into thin layers whose dielectric function is homogenous and water content dependent. The complex electric permittivity ϵ of each slab is then calculated using the Bruggeman effective media theory. The stromal layer is discretized to layers 1 through N-1 and each layer is assigned axially dependent dielectric property as a function of CTWC.

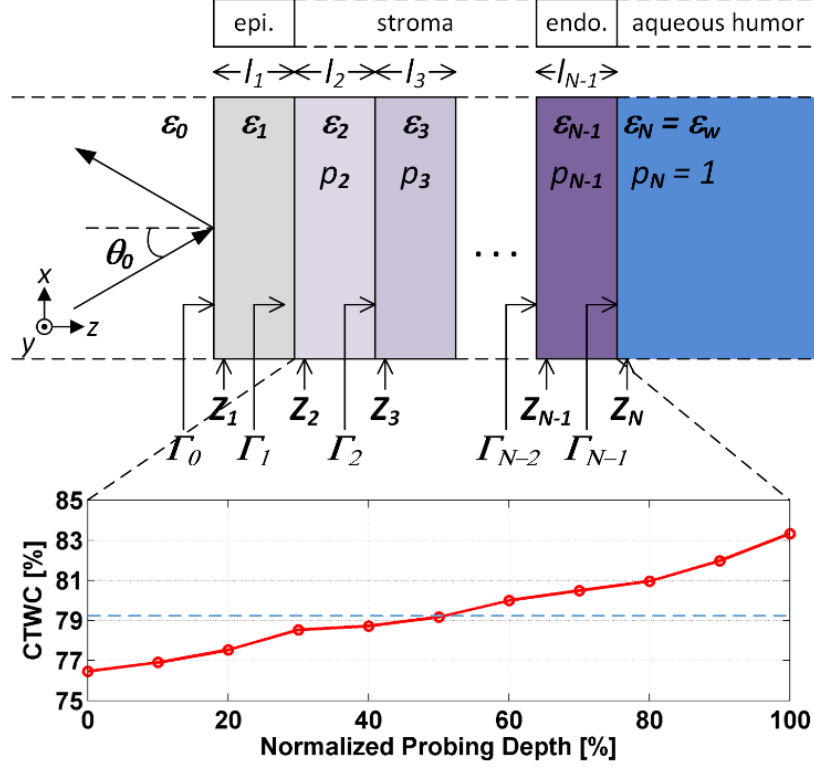


Figure 3-3: Stratified media model for cornea.

3.2.1A Computing the anterior reflectivity

For the i th layer of the model, the effective electrical length (equation (27)), the Fresnel reflection coefficient ρ (equation (28)), and the field reflection coefficient (equation (29)) are the following.

$$\delta_i = \frac{2\pi}{\lambda} l_i \sqrt{\hat{\epsilon}_i} \cos(\theta_i) \quad (27)$$

$$\rho_i = \frac{\sqrt{\hat{\epsilon}_{i-1}} \cos(\theta_{i-1}) - \sqrt{\hat{\epsilon}_i} \cos(\theta_i)}{\sqrt{\hat{\epsilon}_{i-1}} \cos(\theta_{i-1}) + \sqrt{\hat{\epsilon}_i} \cos(\theta_i)} \quad (28)$$

$$\Gamma_i = \frac{\rho_i + \Gamma_{i+1} e^{-j2\delta_i}}{1 + \rho_i \Gamma_{i+1} e^{-j2\delta_i}}, \quad \Gamma_N = \rho_N \quad (29)$$

Each discretized layer's thickness is set at 10 μm , such that the computed anterior reflectivities converge to a differential less than 10^{-6} for thinner layer assignment. The Fresnel reflection coefficient from layer $i-1$ to layer i is written as a function of the complex effective dielectric

constants and the complex permittivities and electrical lengths. In equation (28), the Fresnel coefficient here has been written for TE polarization, and it can be re-written for TM polarization as well. The field reflection coefficient Γ from layer $i+1$ to N is given in equation (29), where Γ_N is defined as the Fresnel coefficient between the final layer of the cornea and the aqueous humor and Γ_0 is the total reflection coefficient of the cornea. With a plane wave incidence on the anterior surface, the THz reflectivity is computed via the familiar transfer-matrix method [70].

3.2.1B Assignment of THz source and detector characteristics

The reflectivity of the cornea tissue can now be computed with a specific measurement method.

Equation (30) describes the computed reflectivity of the cornea with the following parameters:

- $S_s(f)$: Source power spectral density
- $S_D(f)$: Detector spectral responsivity
- p_w : Tissue water fraction
- d : Corneal thickness (CCT)
- f, Ω_f : Illumination center frequency (f), and the bandwidth (Ω_f) of the system of interest.

Equation (30) can be interpreted as the weighted average of the corneal THz reflectivity where the weights are determined by the spectral response of the measuring system [42]. The sensitivity of the derivative of (30) with respect to parameters of interest. Note that (30) models a broadband measurement as an incoherent sum.

$$\mathcal{R}(p, d) = \frac{\int_{\Omega_f} S_s(f) S_D(f) |\Gamma_0(p_w, d, f)|^2 df}{\int_{\Omega_f} S_s(f) S_D(f) df} \quad (30)$$

3.2.2. CTWC gradient models

The sensitivity modeling system should also consider key anatomical/pathological features that are directly relevant to the sensing result. One such case is the different ways that the axial CTWC gradients can vary. The dynamics of CTWC gradients in *in vivo* corneal pathology is not well known. Therefore, we must consider possible ways CTWC can vary from the understanding of disease models, and investigate THz-tissue interaction for all of these cases.

Water in the corneal tissue is lost to the environment from epithelium through evaporation. Water diffuses through endothelium from the aqueous humor (Figure 3-1), while the endocelial cells actively regulate the influx. Corneal diseases that perturb CTWC can have the dysfunction locally in either the epithelium or endothelium. It is plausible to hypothesize that tissue water content change is more prominent in either anterior or posterior of the tissue because of the origin of dysfunction.

Therefore, we can consider the two cases: 1. CTWC is varying from posterior side from the endothelium and CTWC is relatively undisturbed near the epithelium 2. The opposite occurs, where CTWC is primarily changing at the anterior layers and is not changing at the posterior boundary. From here on these cases will be referred to as “Pinned Front” and “Pinned Back,” respectively. Lastly, the “global” hydration change model is also very possible, in which CTWC content changes are uniform across the epithelial, endothelial adjacent stromal areas as well as the interior of the stroma. These models are visualized in Figure 3-4.

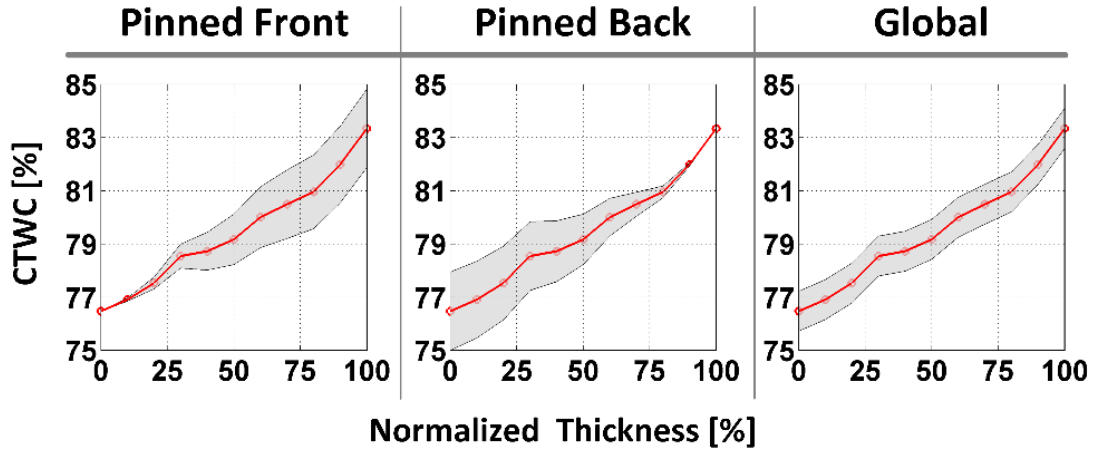


Figure 3-4: Candidate CTWC gradients for CTWC sensitivity simulations. (left) pinned front, (middle) pinned back, and (right) global.

CTWC change model according to each case are normalized in the following formulation so that the water content profile changes represent the same amount of extra (or less) water in the entire tissue. Diffusion, which is thought to contribute to the overall distribution of TWC in the cornea [71], suggests that in gradient types 1 and 2 the deviation of CTWC from normal may be exponentially distributed. This behavior, as well as the global shifts, were modeled with the following equations:

$$g(x, \alpha) = \alpha(e^{x/\sigma} - 1), \sigma = \frac{100}{\ln(2)} \quad (31)$$

$$H_{front}(x, \alpha) = p_w(x) + g(x, \alpha) = H_1(x, \alpha) \quad (32)$$

$$H_{back}(x, \alpha) = p_w(x) + g(100 - x, \alpha) = H_2(x, \alpha) \quad (33)$$

$$H_{global}(x, \alpha) = p_w(x) + \alpha \left[\frac{1}{\ln(2)} - 1 \right] = H_3(x, \alpha) \quad (34)$$

- x : the normalized depth [0%, 100%] in to the cornea, from the anterior boundary (0%) to the posterior boundary (100%).
- $p_w(x)$: Axial TWC profile shown in Figure 3-3
- $g(x)$: Deviation from normal $p_w(x)$; σ is defined such that the range of $g(x)$ is bounded by

$[0, \alpha]$ and α is the variable that modulates the CTWC and is defined such that the average CTWC, computed by taking the mean value of equations (32) - (34) are equal and satisfy the following equivalence relations:

$$\overline{H}_N(\alpha) = \frac{1}{100} \int_0^{100} H_N(x, \alpha) dx, \quad (35)$$

$\forall N = 1, 2, 3$ (for pinned back, pinned front, and global cases)

$$\overline{H}_1(\alpha) = \overline{H}_2(\alpha) = \overline{H}_3(\alpha), \forall \alpha \in (-\infty, +\infty) \quad (36)$$

Gradients 1, 2, and 3 are displayed in the left, middle, and right panels respectively in Figure 3-4 where the red line denotes axially varying CTWC (same as the curve in Figure 3-3) and the shaded neighborhoods indicate the ranges explored in this simulation by varying the parameter α .

Equations (31) - (36) enable a direct comparison for the expected THz properties of different pathologies through a shared, common, average CTWC which we denote here as \overline{CTWC} . Currently, corneal pachymetry does not discriminate between distributions but gives a corneal tissue water content that is assumed to be an average of the entire depth. \overline{CTWC} is used in throughout the discussion as a basis of comparison of signals from different pathologies. For the remainder of discussion, the following labeling is used.

$$CTWC = H_N(x, \alpha), N = 1, 2, 3 \quad (37)$$

$$\overline{CTWC} = \overline{H}_N(\alpha) \forall \alpha, \forall N = 1, 2, 3 \quad (38)$$

3.2.3. First-pass observations

A first-pass look at frequency-dependent THz reflectivities of corneal tissue are shown in Figure 3-6. Corneal reflectivities for a given CCT = 550 μ m are computed as a function of tissue hydration ([75%-81%]) for monochromatic illumination at six frequencies from 100GHz through 600GHz. For a given CCT, the reflectivity increase is almost linear for frequencies within this range. For lower frequencies, the magnitude of reflectivity change per tissue hydration change is larger; at 200GHz (0.2THz), reflectivity changes are about 0.32%//% Δ CTWC, while at 600GHz, this slope drops to 0.1%//% Δ CTWC. These observations are indeed expected from the frequency-dependent dielectric constant of water, which is the source of signal contrast.

Moderately changing the value of the CCT and performing the same calculation mostly shifts the reflectivity curves up and down for certain frequencies. The CCT-dependent reflectivity dependence is plotted in Figure 3-7. It is observed that the THz reflectivity is much less sensitive to change in thickness. Frequencies above 300 GHz seem to be not sensitive at all to the thickness of the tissue in the given range. If we look at the electric field magnitude penetrating into the cornea (Figure 3-5), the higher frequencies attenuate appreciably before the radiation reaches the back of the cornea. Frequencies below 300 GHz still effectively “sees” the aqueous humor, and the measurement becomes sensitive to the thickness changes of the corneal tissue.

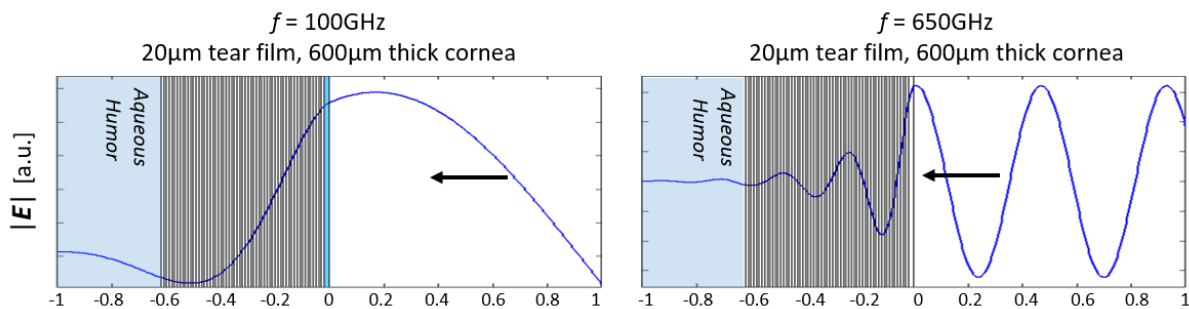


Figure 3-5. E-field penetration into the corneal tissue at 100GHz and 650GHz

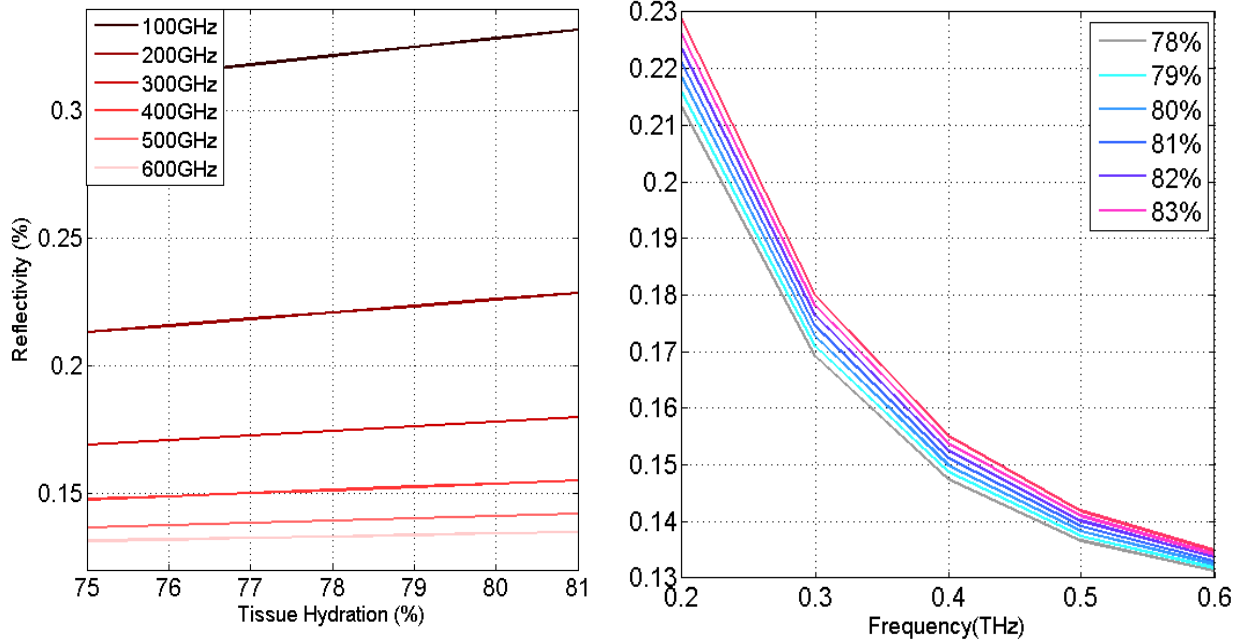


Figure 3-6. THz reflectivity of corneal tissue from the anterior side as a function of CTWC, for the fixed CCT = 550um

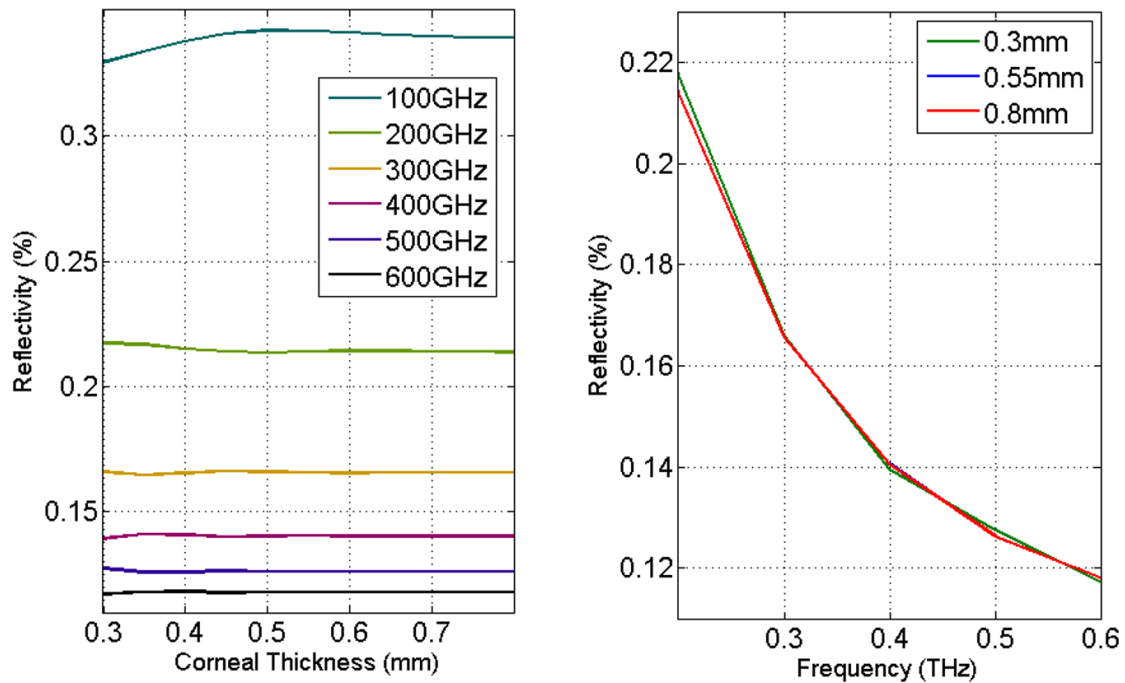


Figure 3-7. THz reflectivity of corneal tissue from the anterior side as a function of CCT, for the fixed CTWC = 79%.

It is observed that the THz reflectivity is much less sensitive to change in thickness

3.2.4. Cornea EM models: The scope of Analysis

The analysis proposed in this section is a 1D plane wave model that is effectively restricted to the measurement at the apex of the cornea with a plane wave illumination. This EM problem set up requires the surface to be sufficiently flat and large in respect to the wavelength and the dimension of the measurement beam. The beam must have a flat beam front, which is a case at the beam waist of a Gaussian beam or in a perfectly collimated beam. The effect of scattering from the geometry of the corneal surface are neglected.

As discussed in Chapter 2, most of the THz imaging systems illuminate with a beam focused by a broadband reflective or refractive optic and are restricted to this measurement set-ups only. However, the advantage stops short here. If we are to obtain an image of cornea, the curvature of the cornea must be conformed to a flat field or the problem beam must orbit around the center of the curvature of the cornea in order to maintain the uniform illumination geometry.

This model is also capable of including the tear film. The tear film cannot be replicated *ex vivo* [72, 73] and its thickness measurements *in vivo* ranges over few micrometers to tens of micrometers [65-68]. If we are to use a dielectric window to flatten the cornea, tear film will be pushed out of the surface and prevented from re-forming between the window and cornea. Because the first *in vivo* experiment had to be performed with a flat-field imaging system, the presence of tear film is precluded in the following analysis for now. Lastly, there are currently no means of independently verifying the accuracy of the three gradient cases considered because there is no way to axially resolve CTWC distributions *in vivo* without harming the eye.

The analysis is centered at the hypothesized characteristics of a healthy human corneal tissue, setting the CCT value at 0.625 mm and the $\overline{\text{CTWC}}$ value of 79.4% using the data from [25]. The model simulates all combinations of CCT and $\overline{\text{CTWC}}$ value in the [0.200mm 0.800mm] CCT range

and [75% 83%] \overline{CTWC} range. These ranges represent physiologically relevant possible CCT values and CTWC disturbance range for most known cases. In summary, the analysis space explores possible combinations of the following parameters:

1. Varying corneal thickness – 200um to 800um
2. Varying CTWC – 75% to 83%
3. Pinned front, pinned back, and global CTWC change cases

Within this data set, the sensitivity of the measurement according to thickness change or hydration change can be easily extracted by the following relations:

3.3. THz reflectivity of corneal tissue at 100GHz and 525GHz

3.3.1. Theoretical test systems

The full spectral (center frequency and bandwidth) dependence of equations (2) - (8) with two additional degrees of freedoms (CTWC and CCT) is difficult to be visualized. Therefore, the following analysis focused on the investigation of a fully define CTWC/CCT dependence of THz reflectivity of using theoretical test systems that models the systems introduced in Chapter 2. The analysis is performed with a pre-defined center frequency and bandwidths to investigate the performance of two different quality factor values ($Q = 5, 50$) centered at 100 GHz and 525 GHz. These values model the two systems [42, 74-79] that are used in *in vivo* rabbit imaging study discussed in the following section, and the result of this simulation is used to interpret the result of the *in vivo* imaging trial. The reflectivity of the whole space is calculated with a modified version of equation (30), where the source and detector spectra have been combined into a single power spectral density $S_n(f)$ [80]. A plot of the four spectral densities is displayed in Figure 3-8. A Gaussian distributed spectrum models power spectral densities [81].

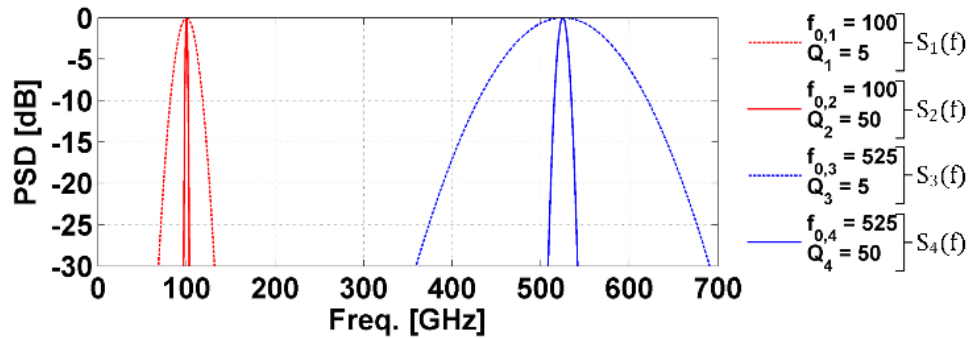


Figure 3-8: System center frequencies and quality factors with $Q = 5, 50$ at 100GHz and 525GHz.

3.3.2. 100 GHz reflectivity

The corneal reflectivity as a 2-D function of CTWC and CCT is plotted in Figure 3-9 for the three candidate CTWC gradient distributions, and for the two different Q factors, resulting in total of 6 plots. The x-axis spans central corneal thickness (d in equations (30) - (8)) values from 0.2 mm to 0.8 mm and the y-axis spans average CTWC volume fractions (\overline{CTWC}) values (axial average of p in equations (30) - (8)) from 75% to 85%. The pixel values are plotted in units of % reflectivity and all six figures are mapped using a shared color scale.

Black contour lines traces CTWC/thickness pairs which yield the same reflectivity for visual help. Three white lines are drawn for each plot that allows us to look at the “cross section” of the 2-D space. The vertical line is drawn for average human CCT at 0.650mm and represents reflectivity change as a function of hydration change, similar to those plotted in Figure 3-6. The horizontal line represents reflectivity change resulting from CCT change for the fixed CTWC at 79%, similar to those plotted in Figure 3-7. The curvilinear line represents simultaneous CTWC and CCT changes modeled by equation 1, which is currently understood to be the typical relation in corneal edema formation.

As indicated by the color bar in Figure 3-9, the reflectivity changes spans from 31.7% to 38.5%. This entire reflectivity range is spanned by the pinned back case, while the global case spans ~ 90% of this reflectivity range. Pinned Front case presents the most challenging environment to perform CTWC sensing at 100GHz. Reflectivity changes along the hydration changes are minimal compared to other cases (Pinned back, Global). This result makes sense, as the high absorptivity of water confines the majority of the millimeter wave-tissue interaction to the cornea’s top surface. In other words, these plots indicate that the change of THz reflectivity due to changes in top layers of the cornea is masking the contributions from the underlying layers. Consequently, the presence

of the aqueous humor is somewhat screened by the loss incurred from transmission through the upper layers. In the pinned back and global cases, corneal hydration changes result in $\sim 1.2\%/ \%CTWC$ or higher gradient.

The reflectivity change as a function of CCT changes are non-monotonic in all three cases. However, the magnitude of its gradient is much less than that due to the hydration change. Nevertheless, if the thickness of the cornea is changing along with CTWC, the thickness information is combined in the reflectivity reading. Measurement of the corneal thickness can deconvolve this information.

It is observed that 2-D corneal reflectivity function seem to not vary appreciably to the system bandwidth. The thickness- \overline{CTWC} maps for the $Q = 5$ and $Q = 50$ systems are nearly identical. This is due to the extremely thin geometry of the cornea with respect to the wavelength within the cornea: $n_{\text{cornea}} \sim 2.91 - j1.45$, $\lambda_{\text{cornea}}(f = 100\text{GHz}) = \lambda_{c,100} \sim 1.03 \text{ mm} > t_{\text{cornea}}$. At these frequencies $m \cdot \lambda_{\text{cornea}}/2 > t_{\text{cornea}}$ for all integers $m > 1$, thus only one longitudinal mode is supported by the lossy cavity, and the difference between integrating over a larger bandwidth ($Q = 5$) and smaller bandwidth ($Q = 50$) does not change the number of accessed longitudinal modes.

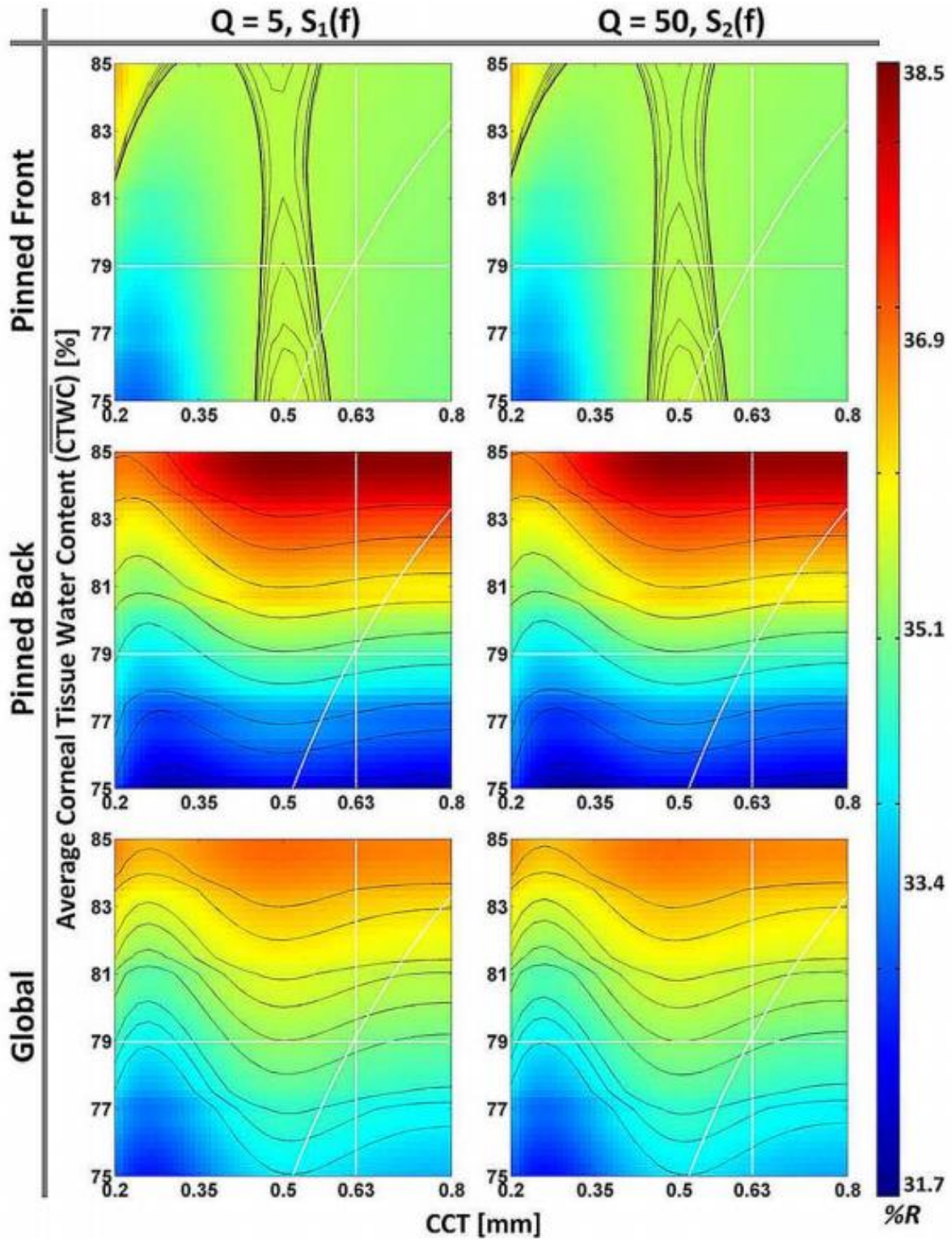


Figure 3-9: Dependence of corneal reflectivity on CTWC and thickness computed at 100 GHz.

3.3.3. 525GHz reflectivity

The 2-D THz reflectivity functions for the band covered by the 525 GHz system are plotted in Figure 3-10 for the three candidate TWC distributions and two Q-factors. These plots use the same CCT range (0.2 mm to 0.8 mm) and CTWC range (75% to 85% hydration) as Figure 3-9 and the white cross-section line for reflectivity change paths exploring thickness variation, \overline{CTWC} variation, and simultaneous \overline{CTWC} and thickness variation.

The six plots in Figure 3-10 are displayed with a shared color map and the reflectivity ranges from 16.4% to 17.6%. The reflectivities at 525GHz display overall lower reflectivity and a smaller reflectivity range than that displayed in Figure 3-9 due to the significant decrease in water's permittivity and thus the intrinsic sensitivity (dR/dp) compared to 100 GHz. Similar to the reflectivity function for 100GHz, the pinned back case represents most favorable environment to sense the change in CTWC because the water content change is concentrated in the anterior layer of the cornea. Pinned front case shows similarly challenging outcome, showing very little reflectivity gradient for CTWC change.

Contrary to 100GHz functions, there is a noticeable difference in the reflectivity maps between the $Q = 5$ and $Q = 50$ systems. At 525 GHz, the approximate refractive index of the cornea is $n_{\text{cornea}} \sim 2.1 - j0.45$ resulting in a central illumination wavelength in the cornea of $\lambda_{\text{cornea}}(f = 525 \text{ GHz}) = \lambda_{c,525} \sim 0.272 \text{ mm}$ in numerous integer multiples of $\sim \lambda_{c,525}/2$. This effect can be seen by comparing the spaces for the two quality factors at each CTWC gradient case where each $Q = 50$ space displays a larger range than its $Q = 5$ counterpart. The broadband illumination reduces the etalon-like interference effect, because the relative contribution of each frequency's etalons decreases as the operating bandwidth grows.

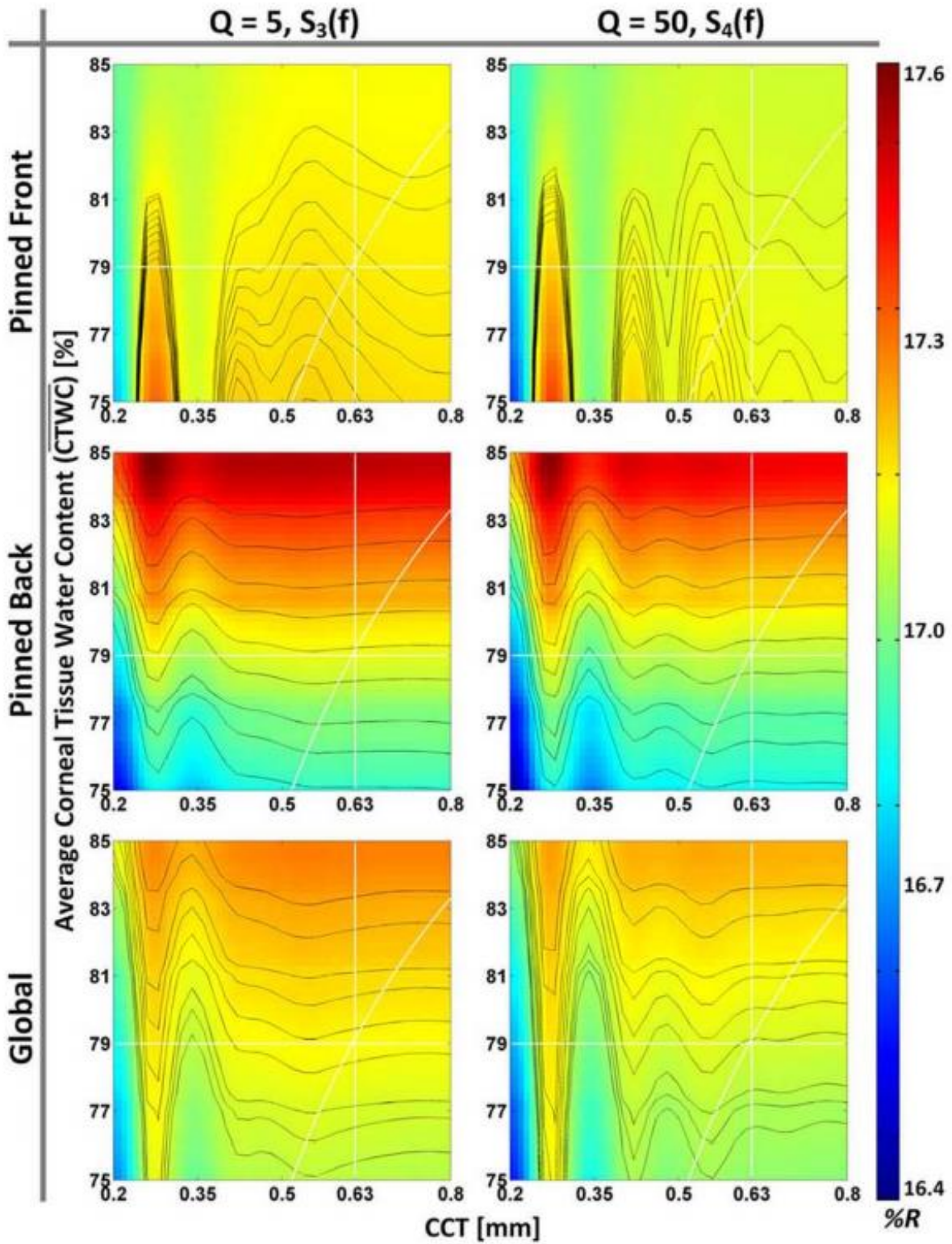


Figure 3-10: Dependence of corneal reflectivity on CTWC and thickness computed at center frequency of 525GHz.

In contrast to the 100 GHz measurement, in the global shift case, the change in reflectivity from thickness change is much less in the 525 GHz measurement especially over the thickness ranges beyond 0.400 mm. For a given reflectivity measurement and no information about the CCT, the possible of CTWC range is the vertical range covered by black contour line. For measurement with sufficient bandwidth ($Q=5$ or less), this range is less than 0.2% in change in CTWC for thicknesses larger than 0.400mm. On the other hand, this range is upto 1% in the 100GHz case. Therefore, 525GHz system can perform CTWC sensing in the Global Shift and Pinned Back cases without an accompanying thickness measurement.

One last interesting point that arises from this analysis is the differences between the predicted CTWC sensitivities calculated with each gradient type. Because there is no known relation between axial CTWC distributions and pachymetry measurements, a spectral measurement of THz reflectivity measurements may allow to ascertain this information.

3.3.4. Cornea EM Modeling: Conclusion

Because of the cornea's layered structure and its thickness comparable to THz band wavelength, the THz-cornea interaction is similar to a lossy etalon formed by a thin film. The THz reflectivity of cornea is a frequency-dependent 2D function of CTWC and CCT. The THz reflectivity map shows the transition from thickness-sensitive CTWC reflectivity near 100GHz to thickness-invariant reflectivity near 525GHz that is mostly sensitive to anterior layer of the cornea. Investigating the trend of responses in the three candidate CTWC gradient types, it is further understood that the majority of THz sensing occurs at the anterior layer of the cornea, and the choice of frequency determines effective sensing depth of the measurement. Taking advantage of the little physiologic variation of corneal structure, a strong set of *a priori* knowledge on corneal geometry precludes the need for phase sensitive measurements and may even allow for depth resolved measurements of the axial CTWC distribution. The result recapitulates this study's original motivation in using the THz band for this sensing application. THz band is the able to sufficiently penetrate into the cornea and sense its dielectric property, and not significantly by pass it (in microwave frequency) or reflect off the tear film (in infrared frequency). The next phase of this study investigates whether the reflectivity changes predicted by this model can be observed in the living cornea, and follows the prediction of the model.

3.4. In vivo corneal imaging study

Unfortunately, there is no alternative imaging target that reflects physiological process of an in vivo cornea. Ex-vivo corneas, no matter how carefully prepared, had already gone through days in the deceased state and are highly hyper-hydrated from the posterior side and highly dried from the exposed anterior side. Corneal tissue may be excised and its hydration reconstituted, however all of the relevant tissue hydration characteristics would be modified. Furthermore, there is no physiological processes that maintains the relevant tissue characteristics of the corneal tissue. The THz sensing system must be eventually demonstrated on an in vivo model, in which sensing data is obtained from intact corneal tissues maintained by physiological processes. However, before considering the use of live animals in the imaging study, there must be a sufficient exploration with ex-vivo and phantom substitute to test the feasibility of the measurement set-up and characterize the system's performance.

3.4.1. THz sensing systems

Two CTWC sensing systems were used in this study. The first system operates at 100 GHz using a Gunn diode source and a pyroelectric detector. This system was used to explore the validity of effective media theory [82] and the utility of 100 GHz CTWC sensing *in vivo* [74]. The size of the focused spot is ~4.5mm and obtaining imaging data was not meaningful, thus in this study, the measurement was confined to a point measurement at the corneal center. The second system, introduced in Chapter 2, operates at a center frequency of ~ 525 GHz using a broadband illumination from a photoconductive switch source. This system was used in a number of *in vivo* imaging study that succeeded in generating TWC based contrast in rat skin models [77, 83-87].

A block diagram of the millimeter wave reflectometer is shown in Figure 3-11(a). A WR 10 waveguide-mounted Gunn diode (Spacek labs, CA) [88] produces a linearly polarized radiation

with a FWHM emission angle of $\sim 10^\circ$ and an average power of 10 mW. The 100 GHz radiation is focused onto the target at a 20° incidence using a pair of 50 mm diameter, 100 mm focal length plano-convex teflon (PTFE) lenses. Reflected illumination was collected by a symmetric placement of a second pair of plano-convex PTFE lenses and focused onto a pyroelectric detector with an NEP of ~ 1 nW [89] (Figure 3-11(b)) .

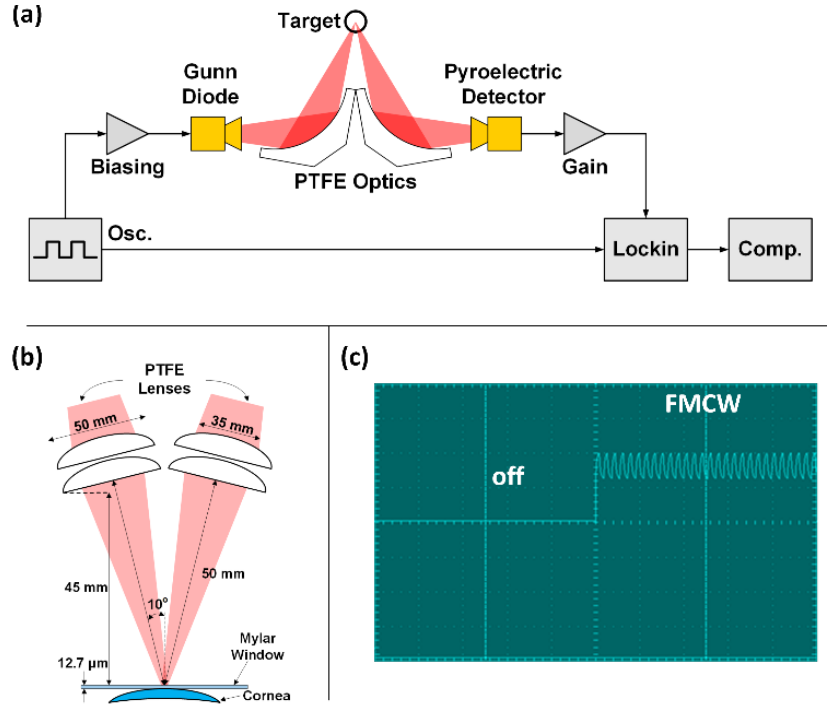


Figure 3-11: 100GHz sensing system. (a) System block diagram. (b) Illumination geometry (c) Biasing scheme demonstrating low frequency chopping combined with high frequency FMCW.

The Gunn diode was frequency modulated over the ~ 3 GHz range centered at 99GHz (Figure 3-11(c)) at the sweeping frequency of ~ 1 KHz. The pyroelectric detector displayed significant $1/f$ noise up to ~ 25 Hz, therefore the sensing signal is amplitude modulated (AM) at 30 Hz. Given the very low response speed of the pyroelectric detectors (~ 10 Hz), 30 Hz AM was found to be the optimal trade-off point between the signal strength and noise that will give the best SNR. The output of the pyroelectric detector was fed into a lock-in amplifier with a 1 ms time constant resulting in an effective data acquisition rate of ~ 10 Hz. This arrangement produced ~ 66 sweeps through the RF spectrum in one on-cycle of the amplitude modulation, effectively providing a time

averaged broadband signal to the detector and mitigating coherence effects that arise from the narrow instantaneous source line width and the non-zero Q of the optics train. The post detection signal to noise ratio (SNR) was ~ 30 dB. Knife edge measurements confirmed a 10% - 90% spot size of ~ 4.5 mm, a diameter slightly smaller than the 5 mm diameter of the ultrasound pachymetry probe. For the comparison, a block diagram for the 525GHz imaging system and its corresponding illumination geometry is displayed Figure 3-12(a) and (b). The THz source, receiver electronics, and system design is also elaborated in [42].

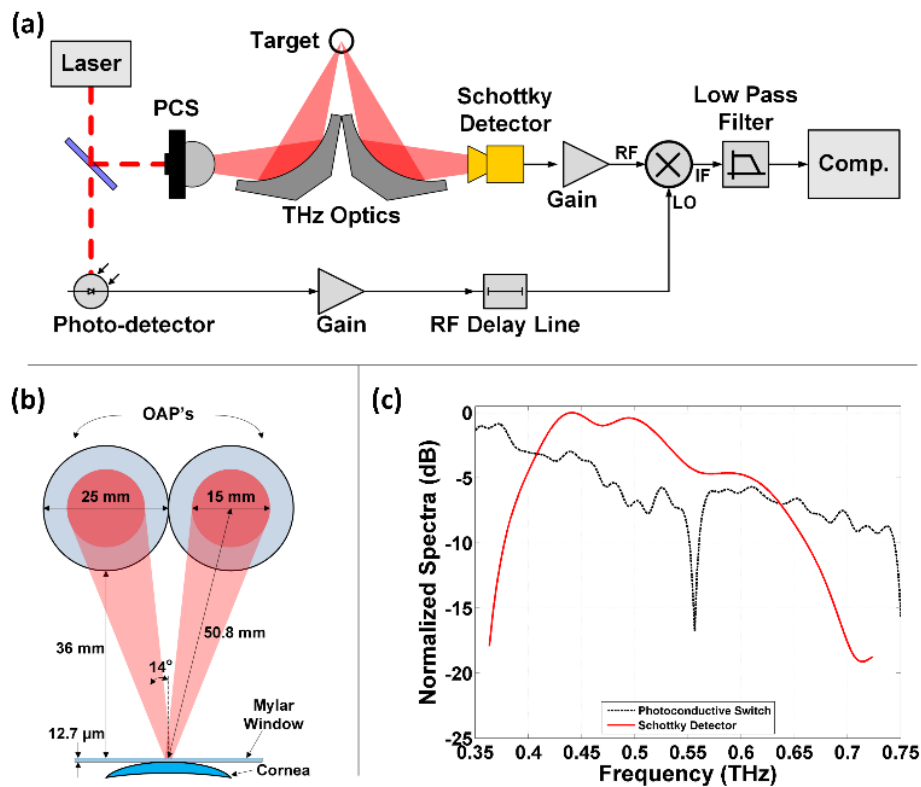


Figure 3-12: 525GHz imaging system. (a) System block diagram. (b) Illumination geometry. (c) Photoconductive switch power spectral density and detector spectral responsivity.

Hydration sensitivity

The hydration sensitivity of the system is defined by the minimal amount (%) of hydration change in the target observable by the reflectivity change in the presence of noise. A most straightforward method to measure the hydration sensitivity of a system is to perform drying-towel

experiments, in which a thin, wet towel is left to dry while its THz reflectivity and the weights are measured over the course of drying. The precise water fraction of the target can be calculated from the weight data.

In these experiments a 0.15 mm thick polypropylene towel was wetted with a volume of water and the reflectivity and weight of the target were probed until the target weight had dropped to its dry value. The polypropylene (PP) towel was chosen because of the tiny fibers and frequency independent index [90] provide a low loss, nearly dispersion free target constituent across the frequency bands of interest. While uniform, wetted cellulose or polymer cloths can be a good representation of thick, heterogeneous tissue such as skin, muscle, fat, etc. they are not optimal for cornea since it is difficult to create tissue water gradients and striated structures that accurately mimic *in vivo* cornea. However, drying targets provide most precise measurement of the reflectivity vs precise water fraction, because this method can measure changes in reflectivity by producing very small drops in the reflectivity. It is noted that in using the 100GHz system for reflectivity measurement, the larger wavelength and longer-focal length optics provide much larger DOF than the 525GHz system. At 100GHz, the radiation also probes deeper into the wet tissue, therefore the set-up lends increased sensitivity to the presence of a backing. Thus a suspended target mounting is recommended.

The hydration sensitivity and the experiment details are elaborated in [91] for the 100GHz system and [42] for the 525GHz systems, using a number of different calibration targets [92]. Aforementioned experiments characterized Noise Equivalent Delta Water Content (NE Δ WC) under the hypothesis that the tissue of interest mimics a half space (no index discontinuities in the thickness dimension) and that changes in tissue water content are distributed somewhat evenly throughout the probing depth of the imaging system. In this section, we also report the

characterization of Noise Equivalent Reflectance Difference (NERD), which imposes a systematic limit on how small of a change in reflectance can be resolved. The results of the drying experiments over water content fractions relevant to the cornea are displayed in Figure 3-13 for each system.

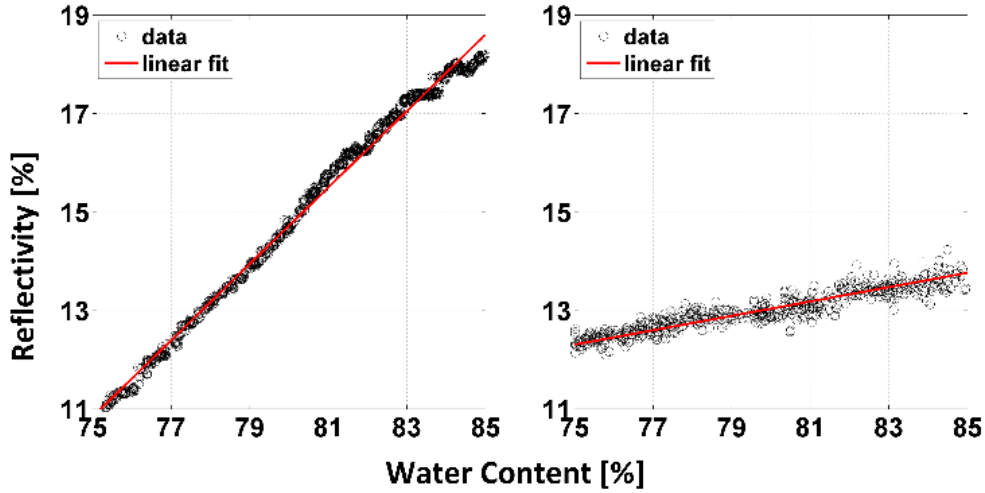


Figure 3-13: Sensitivity analysis of the 100GHz system (left) and 525GHz system (right). Experimental details in [91],[42].

It is noted that the slopes of the 100GHz system is much higher (0.78 %/%) than the 525GHz system (0.15 %/%) due to the difference in water dielectric coefficient. The measurement noise of the 525GHz system is also ~ 2.5X larger than the 100GHz system. While receiver architectures and the noise characteristics of the detector used in the 100GHz system is much cruder than the 525GHz system, the superior performance of the former is attributed to differences in post detection bandwidth which is orders of magnitude lower (30 Hz vs ~ 10 GHz).

$$NERD = \sqrt{\frac{SSE}{N}} = \sqrt{\frac{1}{N} \sum_{i=1}^N [y_i - f_i]^2} \quad (39)$$

$$NE\Delta WC = NERD \left(\frac{dR_s}{dp_w} \right)^{-1} \quad (40)$$

The NERD characterization is performed with regression analysis as described in equation (39) where y_i are the reflectivity measurements at a particular water content percentage, f_i is the least squares fitted line evaluated at the same water content percentage that yielded measurement y_i , SSE is the sum of square errors between the measurement and fit, and N is the total number of points used to compute the fit [91].

Then the NE Δ WC can be found Equation (40), for a particular NERD and the system's responsivity where R_s is the measured sample reflectivity, p_w is the water volume fraction [91]. While the NE Δ WC derived from the NERD from the PP towel target is not directly applicable to the cornea, it is instructive to demonstrate inherent differences associated with the choice of the center frequency. The sensitivity characterization is compiled in Table I. The 100GHz system achieved a NERD of 0.0587% and the 525GHz system achieved a NERD of 0.1204%.

Table I: Noise equivalent metrics

System center freq.	Slope $\left(\frac{dR_s}{dp_w}\right)$ [%/-%]	NERD [%]	NEΔWC [%]
100GHz	0.7765	0.0587	0.0763
525GHz	0.1459	0.1204	2.3761

3.4.2. In vivo study design

The study was approved by the University of California's Institutional Animal Care and Use Committee (IACUC) that reviewed the study design, humane treatment of animals, and the presence of sufficient merit of using animal models. The study used White New Zealand male rabbits, which are a common model for the human cornea [93-95] because of the similarities in size, shape, and CTWC.

Rabbits were handled by UCLA's Department of Laboratory Animal (DLAM) veterinarian staffs. Five rabbits were anesthetized using 30 mg/kg and 5 mg/kg of Ketamine and Xylazine, respectively, followed by intubation with a 1.5 mg/ml flow of Isoflurane to maintain the anesthesia. Each rabbit is secured in the lateral position on a custom designed mount with head support panel. The position and angle of the rabbit's head was adjusted to accommodate the rabbit's neck and head while it was intubated (Figure 3-14).

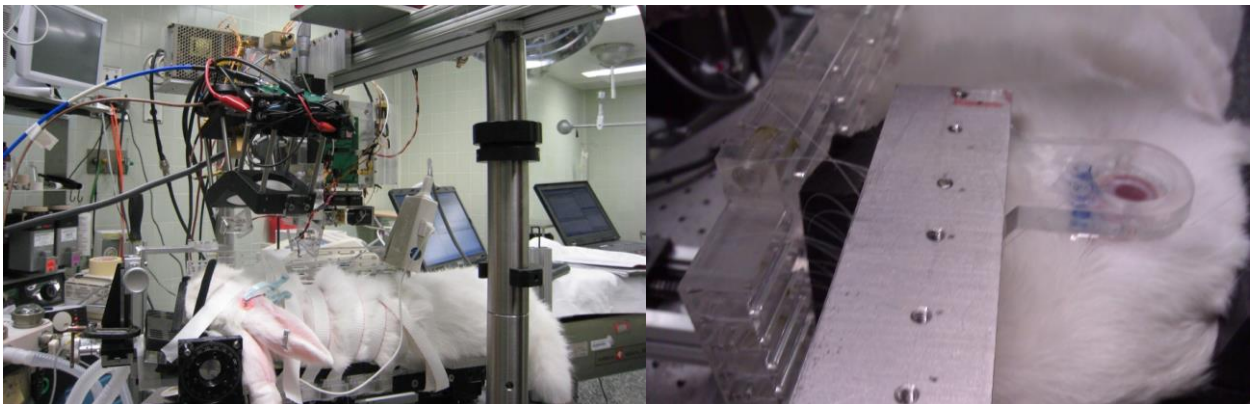


Figure 3-14: Rabbit cornea imaging. (top) Rabbit model placed below the THz and millimeter wave imaging systems. (bottom) Close up of rabbit cornea and mylar window

Next, the right eye was gently held open and dry heat by an air blower was applied for 15 min. A 12.7 μm Mylar window was lowered onto the cornea's surface to secure it in place and constrain

it to a horizontal planar geometry. The following measurements were then obtained in the listed order every 10 to 20 minutes for the subsequent imaging period.

1. Thickness measurement: 5 individual readings were taken using the ultrasound pachymeter and their average was recorded. These measurements were through the Mylar window by placing the probe tip directly on the top of the window. The substrate thickness was subtracted out.
2. 100GHz reflectivity: 100 GHz reflectivity was obtained with the system described in Figure 3-11. The reflectivity signal is averaged with the lock-in amplifier with an integration time of 1 second. A class I, 650 nm targeting laser was employed to ensure the correct position of the focused 100 GHz beam.
3. 525GHz reflectivity and imaging: An image of a 20 mm x 20 mm FOV was obtained with 0.5 mm pixel width (40x40 pixels) with the imaging system described in Chapter 2.

The thickness and 100 GHz point measurements each required ~ 1 minute acquisition time while the THz imaging required ~ 5 minutes. With the Mylar window separating the epithelium from the outside environment, the dehydrated cornea was expected to increase in TWC to a slightly hyper-hydrated state over the course of one to two hours.

3.4.3. CCT measurements

While rabbit corneas are a very good physiologic model of human cornea for their healthy CTWC (~79%) and the radius of curvature (~8mm), they are, on average, thinner than healthy human cornea, ranging from ~ 0.3 mm to ~ 0.5 mm as compared to the ~ 0.45 mm to ~ 0.7 mm spanned by human cornea. Therefore, the human CCT to CTWC relation in the equation (1) was modified in the same functional form for rabbits in equation (18) [96]. Equation (18) is only used to give an idea of expected CTWC changes, and the exact measurement – CCT – will be consistently used for subsequent analysis.

$$H_{human} = \frac{CCT - 0.091}{CCT + 0.051}, \quad CCT \sim \epsilon [0.45, 0.7] \quad (41)$$

$$H_{rabbit} = \frac{CCT - 0.075}{CCT + 0.062}, \quad CCT \sim \epsilon [0.3, 0.5] \quad (42)$$

The CCT measurements for all five rabbits are displayed in Figure 3-15 throughout the entire course of the CTWC monitoring experiments. The data points represent averages of 5 measurements taken for each time point. Linear fits are superimposed on the data points. Each rabbit displayed an increase in CCT as a function of time with an average rate of ~25.6±4 microns per hour. The estimated mean CTWC is indicated by the y-axis on the right side of the figure and was computed with the modified relation.

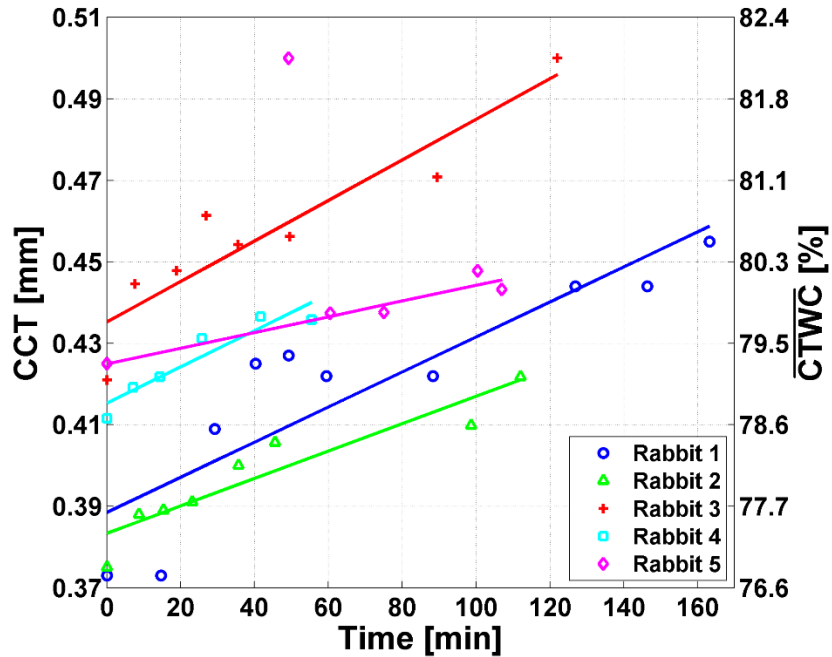


Figure 3-15: CCT measurements for all rabbits in the trial and their associated CTWC levels computed with equation (18). Rabbit 5 has a large outlier at time 50 mins which was not included in the linear fits.

The different starting value of the CCT for each rabbit cornea at the start of the experiment reflects the intrinsic, large physiologic variation of *in vivo* corneas. While the CCT values are different from 0.373 mm to 0.425 mm range and indicates a range of CTWCs from 76.8% to 79.4% according to the CCT \rightarrow CTWC relation, all animals were determined by the attending veterinarian to have healthy corneas just prior to anesthesia and the commencement of experiments. A $\overline{\text{CTWC}}$ value of 76.8% suggests compromised corneal health whose deteriorated state would be detected upon visual inspection. Once again, this is a further illustration of the limitation of using CCT measurement to infer CTWC.

3.4.4. THz reflectivity vs CCT at 100GHz and 525GHz

The 100GHz and 525GHz reflectivities are plotted against the corresponding CCT measurement in Figure 3-16(a). The estimated \overline{CTWC} found by equation (1) is labeled as the second x-axis on the top margin. The 100GHz system set up was a point-measurement thus the direct plot of the data is represented in Figure 3-16(A), which shows a clear positive correlation between the increasing reflectivity and the increasing CCT value. For the 525GHz reflectivity, a region of interest (ROI) is defined, indicated by a dotted circle on the first image of each image series. The diameter matches that of the ultrasound probe employed in the pachymetry measurements, and the location indicates the same area where the 100GHz beam was positioned. In addition to laser targeting, small fiducial markers (transparent to THz illumination) on the Mylar window helped ensure repeatable probing location. The FOV was intentionally larger than the rabbits' corneas, guaranteeing the absence of cornea in the periphery of the images and allowing for accurate monitoring of system drift and noise.

The corresponding CTWC increases predicted by CCT theory are displayed on the top x-axis. THz reflectivities are computed with the indicated region of interest as a function of acquired CCT measurements reflected in the lower x-axis. The corresponding CTWC increases predicted by CCT theory are displayed on the top x-axis. A zoom-in of the first point in the rabbit 4 series is displayed in the inset demonstrating the difference in variation between estimated system noise and contrast observed in the 5 mm diameter FOV

Six time-course THz images for each of the five rabbit are shown in Figure 3-17 with a standard 'jet' false color map, where red areas correspond to increased reflectivity and blue less. Each set has been normalized to its' individual maximum pixel value. The images are arranged from left to right. The first image is taken at the beginning of the monitoring and the last image at the end time

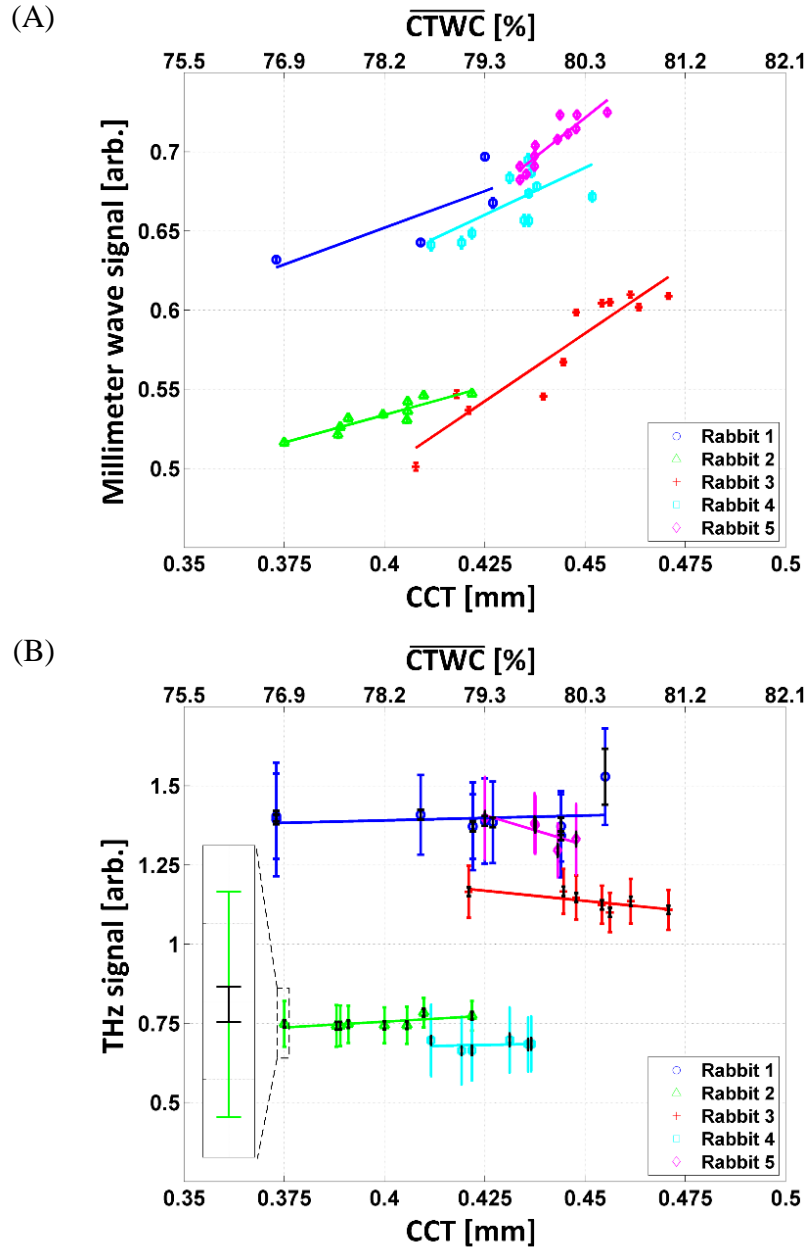


Figure 3-16: 100 GHz point measurements plotted against the CCT measurements reflected in the lower x-axis.

point as plotted in Figure 3-15. The images reveal noticeable shifts in contrast throughout the cornea for the duration of the experiment. The perimeter of the cornea is also changes with time suggesting that the corneal thickness is sufficiently perturbed to increase the total surface area of cornea touching the window as the cornea swells.

The average reflectivities of the regions of interest are plotted against corresponding CCT value in Figure 3-16(b). The larger error bars correspond to the variation within the ROI and the smaller error bars indicate system noise characterized in [97]. A zoom-in of one of the data points on the right side of Figure 3-16(b) demonstrates the standard deviation of the pixel value within the ROI and the system noise. The 525GHz measurement shows nearly no correlation between the THz reflectivity and CCT measurements. Rabbits 1 and 2 display slight increases in reflectivity while rabbits 3, 4, and 5 display slight decreases. In both cases the total change is, at maximum, nearly an order of magnitude less than the variance.

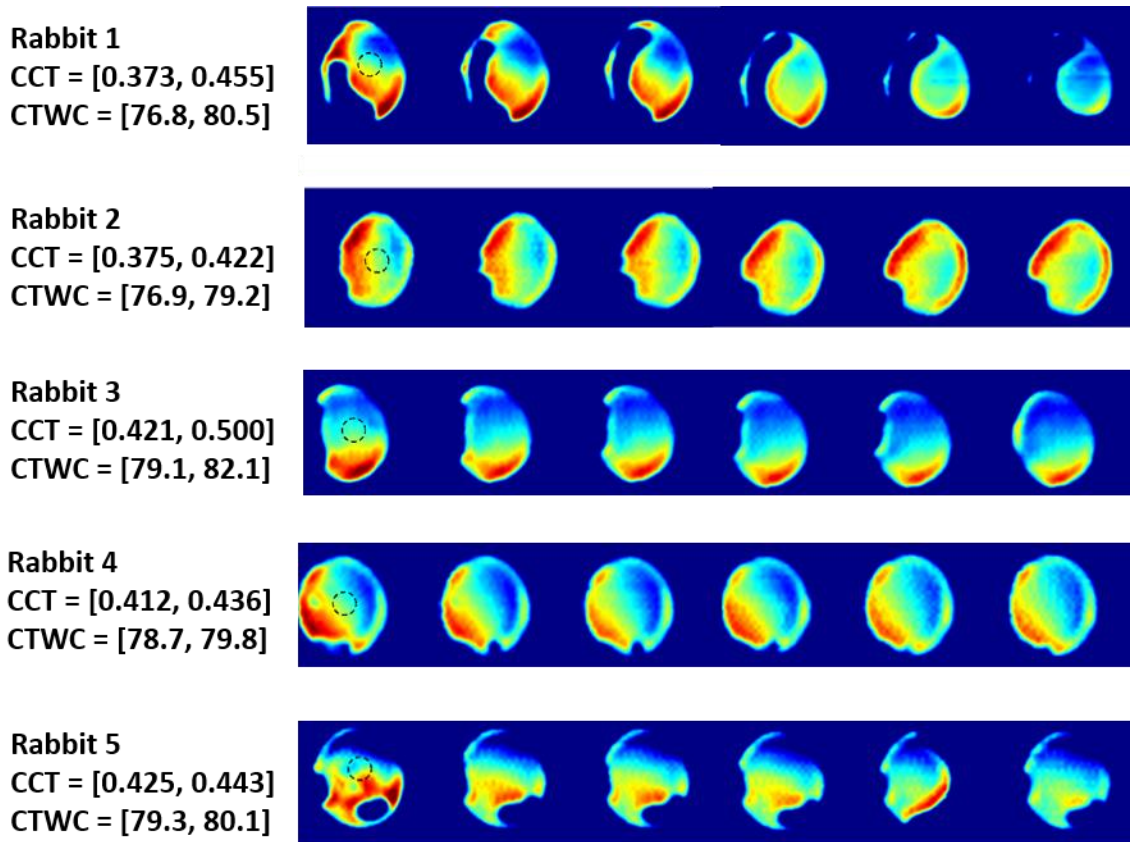


Figure 3-17: 525GHz reflectivity maps of CTWC for all five rabbits, showing noticeable shifts of reflectivity contrast over the course of imaging experiment.

Reiterating the precaution that the CCT/\overline{CTWC} relationship described in equations (18) and (1) is approximate, the sensitivity of each system is analyzed in terms of CCT directly. Thickness sensitivity was computed using equation (43), where $\max(\sigma_n)$ is the maximum standard deviation of the reflectivity signal observed in rabbit n and df_n/dC is the slope of the regression line for rabbit n . The resulting ratio H_{sens} describes the minimum thickness change that the system can differentiate. The results are tabulated in Table 6, which shows that the 100GHz measurements are sensitive to few micrometers of CCT changes, while the 525GHz measurements are confirmed to have essentially no relation to the CCT change.

$$H_{sens} = \frac{\max(\sigma_n)}{df_n/dC} \quad (43)$$

Table 6. Measured sensitivities

Rabbit (n)	Measured CCT slope $\mu\text{m/hr}$	Measured 100 GHz CCT sensitivity (μm)	Measured 525 GHz CCT sensitivity (μm)
1	25.8	3.27	582.6
2	20.2	3.14	98.2
3	29.9	1.4	-64.2
4	26.7	3.11	476.0
5	11.6	1.29	-34.2

3.4.5. Analysis

In order to interpret this outcome, we come back to the 2D reflectivity function models delineated in Figure 3-9 and Figure 3-10. The 2D reflectivity space as a function of CTWC and CCT is recomputed for the operating spectra of both systems with the 12.7 μm thick Mylar window included in the stratified media model. The three white lines, similar to those used Figure 3-9 and Figure 3-10, are plotted corresponding to the constant thickness, constant $\overline{\text{CTWC}}$, and simultaneous $\overline{\text{CTWC}}/\text{CCT}$ paths plotted using equation (18). The resulting 2D functions are mostly similar to those shown in Figure 3-9 and Figure 3-10. The 525GHz reflectivity functions are similar to that of $Q = 5$ system in Figure 3-10, albeit with slightly larger maximum reflectivities and reflectivity ranges. This difference arises from the photoconductive switch PSD and Schottky diode spectral responsivity which are skewed towards the lower frequencies.

The ultrasound pachymeter used in these experiments relies on a pulse echo methodology with range gating [98] to ascertain the axial location of the acoustic impedance discontinuity at the endothelium/aqueous humor interface. None of the steps in the protocol were thought to have compromised this discontinuity, so thickness values extracted by our ultrasound measurements were assumed to be accurate. Since our empirical observation confirms the increasing thickness of cornea, only the constant CCT, varying CTWC cases can be excluded.

The “cross section” along the two white line path (for constant CTWC, varying CCT case (horizontal line) and simultaneous CCT/CTWC case (curvilinear line) are plotted in Figure 3-19. The constant CTWC, varying CCT lines were drawn at the volumetric average CTWC of 79.4%. While a comprehensive analysis would plot a family of curves at varying constant CTWC percentages (i.e. at 77%, 78%, 79%, 80%, 81%, etc.), it is instructive to instead look at the trends of changes in relative CTWC. In this case, constant $\overline{\text{CTWC}}$ profiles produce nearly identical

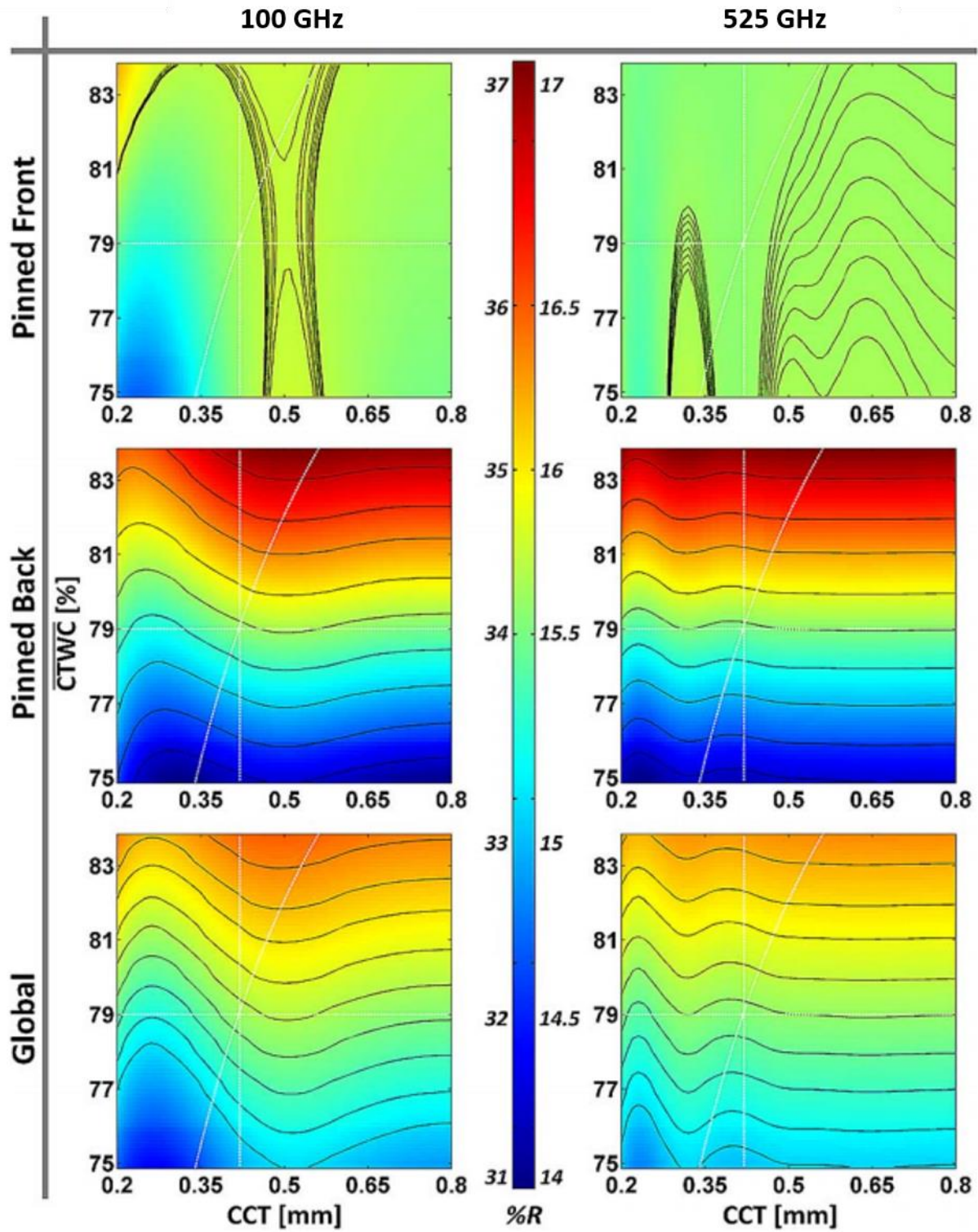
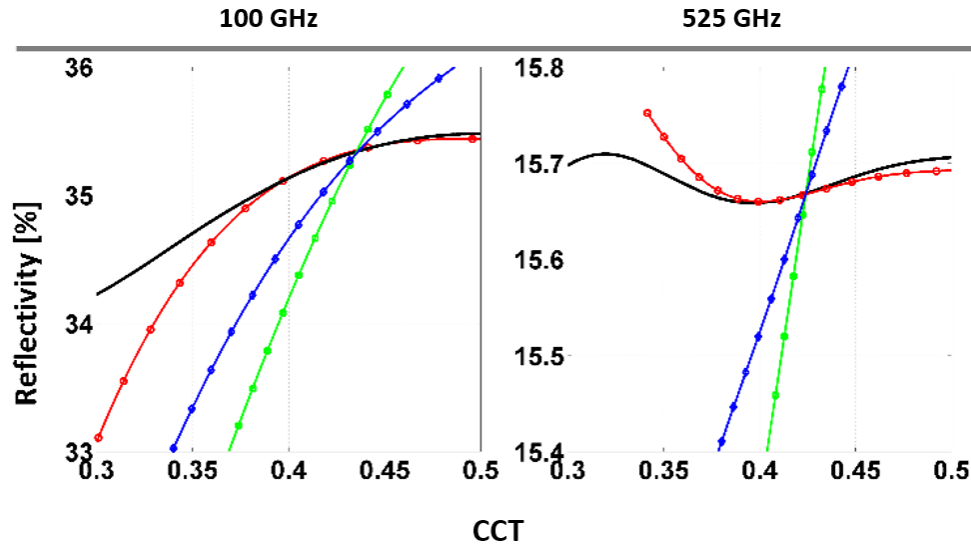


Figure 3-18: Computed reflectivity at 100GHz and 525GHz on CTWC and corneal thickness.



Legends

Constant CTWC (79%):	— Pinned Front	— Pinned Back	— Global
CCT/CTWC varying together:	—○— CCT projection	—□— CCT projection	—◇— CCT projection

Figure 3-19: ‘Cross-section’ 2D reflectivity functions of Figure 3-18.

variation trends within given CTWC value range (77%-81%), thus fixing the analysis to 79.4% is sufficient.

The positive slope of the 100GHz data alone suggests that any of the hypothesis – constant CTWC/changing CCT or simultaneous CCT/CTWC change for any of the possible CTWC distributions – are viable case. On the other hand, the NERD measurement of the 525GHz system indicates that the reflectivity changes less than 0.1% could not be detected. Given the CCT change range observed during the experiment, we can preclude the simultaneous CTWC/CCT changing case for pinned back and global distribution of CTWC. In other word, in order to observe our experimental outcome with observed CCT change range, either the CTWC gradient is a pinned front case (red contour in Figure 3-19: ‘Cross-section’ 2D reflectivity functions of Figure 3-18) or we have a constant CTWC/changing CCT case for any of the possible CTWC distributions.

Lastly, we considered the expectation of the applied protocol in animal. The methods used to perturb CTWC in this experiment protocol - applying dry air and then a dielectric window contact – only confidently made direct perturbation to the anterior portion of the cornea. On the other hand, histologic analysis of the tissue confirmed that there were no permanent damages in the deeper layers of the cornea. Therefore, we may hypothesize that the outer layer of the cornea were most affected and that the pinned front cases is rather unlikely. This consideration lowers the likelihood of pinned front cases.

From these considerations, we conclude that the only explanation that fits the experimental outcome is that the cornea was undergoing a thickness change while the CTWC stayed relatively constant. While the difficulties associated with perturbing healthy CTWC without injuring corneal tissue are known [99], it is surprising that the CCT changed so significantly for an apparent lack in CTWC change. This experiment provides evidence for potentially poor correlation between corneal thickness and CTWC *in vivo*. The lack of a one-to-one mapping between corneal thickness and CTWC and the inability of pachymetry to correct for physiologic variation is well known, yet this represents the first *in vivo* study with quantitative observations of the inaccuracies.

3.4.6. Discussion: experimental and imaging method shortfalls

The foremost challenge in interpreting the experimental data was in the difficulties in assigning correct y-axis absolute scale (THz reflectivity). The narrow focal imaging plane alignment restriction discussed in Chapter 2 required alignment set up and time that could not be afforded with anesthetized living animal in the operating room. Once the imaging trial started, each animal was not disturbed for the duration of the experiment so we could use the reflectivity measurement set. With an ensemble of data, we could analyze the trend with confidence.

However, this requirement also added significant confounder to our experimental outcome. It is likely that part of the perturbation observed in corneal thickness was caused by the use of the Mylar window which applies pressure to the corneal tissue and underlying structures. Although care was taken to ensure that the window is applied with as little static force as possible, it took certain amount of coercion to conform the corneal tissue flat within the field of view. Moreover, this process is definitely not reproducible for each animal.

The application of the window also prevented the formation of the tear film and therefore, altered a natural physiological state. At this point, there is no way to gauge what effect the window had on the animal's response. Even if all of these confounders may be understood, THz corneal imaging and sensing cannot proceed to human imaging with window application requirement.

Therefore, a clear conclusion is that CTWC studies requires non-contact, windowless imaging method. This requirement presents a significant engineering design challenge to systems/optical engineers given the poor performance of traditional THz medical imaging system design when interrogating curved surfaces.

3.5. First in vivo Experiment - Conclusions

Our first in vivo experiments empirically demonstrated the sensitivities of the 100GHz and 525GHz sensing systems to physiologic changes in live rabbit corneas. 100GHz reflectivity increases with CCT value with good correlation, while the combined analysis with 525GHz reflectivity measurement allowed to deduce how the corneal tissue is perturbed and what kind of reflectivity changes can be observed for each hypothesized case of corneal CTWC change mechanics. The 525GHz $\overline{\text{CTWC}}$ maps, however, displayed marked reflectivity increases in some areas, decreases in others, and relative lack of CTWC change in the region probed with the pachymeter.

The aqueous humor immediately below the cornea can be sensed as a half space depending on operational parameters such as frequency, angle of incidence, CTWC, etc., which can markedly change measured CTWC value. For this reason, we believe that multi-frequency measurements are needed to realize more accurate CTWC sensing systems. Reflectivity maps at multiple frequencies and modeling-based predictions can produce both CTWC and thickness maps simultaneously. A single frequency or single band integrated measurement is not sufficient to decouple the contribution of CTWC and CCT to THz reflectivity. Furthermore, a single frequency measurement is very difficult to be calibrated to give precise reflectivity axes.

Lastly, the contact between the imaging/sensing system and cornea confounds both the measurement and the state of the cornea. Non-contact, spectrally resolved measurements are imperative for resolving contributions from different mechanisms.

Chapter 4 Non-contact, All-normal Incidence Corneal Imaging System

4.1. Introduction

Our first in vivo cornea imaging experiment and the model based analysis of the measurements suggests that the non-surgical protocols intended to alter the hydration content of the in vivo cornea actually modified only the thickness of the cornea while leaving the CTWC relatively unperturbed. It is likely that the contact pressure of the window altered natural and intended response of the cornea, severely limiting the further applicability of such protocol.

The experiment demonstrated key weaknesses in the exploration of THz imaging for CWTC diagnostics with current techniques. Not only active imaging of the corneal surface is difficult with simple x-y scanning techniques, such method cannot be practically implemented in the clinical setting. Nearly all THz imaging modalities currently being applied to medical diagnostic research require contact through the application of a dielectric field flattening window. It is clear from these limitations that THz imaging of corneal water content requires a new THz imaging system architectures that can acquire reflectivity maps of the cornea in vivo without contact.

Therefore, the next phase of THz-CTWC sensing and imaging study must develop a beam scanning imaging system that can create reflectivity maps of the cornea without contact. This section describes the design, development, and successful implementation of the non-contact, uniform imaging field beam scanning system that keeps the imaging target and the THz devices stationary.

The system architecture relies on the observation that cornea is nearly a perfect hypohemishpere with respect to a THz wavelength. Additionally, the expected person to person (intra patient/intra subject) variability of the morphological/geometric variation from an ideal sphere are also limited as a function of THz wavelength. Finally, the hypohemispherical diameter of the cornea (corneal extent) displays a quite limited variation when normalized by THz wavelengths. These three elements enable one to assume a curvature and field of view a priori with a high degree of confidence. Thus, corneal imaging is unique amongst all THz medical imaging applications and allows the system design to accommodate only a very limited set of use cases.

4.2. Anatomy (geometry) of cornea for THz imaging

Before we move forward, we must consider the question: How spherical is the cornea?

In general, both the anterior and posterior corneal surface are aspherical. Comparing to the average radius of curvature of the surface, the deviation from the average “ideal” sphere increases toward the periphery. For example, human cornea can be astigmatic, having different curvature (and hence optical power) as a function of cross-sectional meridian angles. Characterization of corneal topology is a critical information for visual acuity correction procedures such as Laser-Assisted in situ Keratomileusis (LASIK) and Photorefractive Keratectomy (PRK) where photonic base ablation of the corneal stroma is performed to modulate the measured, non-ideal corneal topology to one that minimizes refractive wave front aberrations. Luckily for us, corneal topology mapping is a mature field and corneal surface profiles can be obtained with the Videokeratography [100] or Scheimpflug photography [101] techniques which interpret the surface height measurements in refractive power at each local surface.

In particular, Videokeratography [102] can be used to construct dioptric power maps from corneal surface height data, which can be further fitted to a parametric surface to analyze higher-order surface features from disease or refractive surgery [103]. However, despite the maturity of topology mapping technology, there is no standardized method for analyzing topographic information [104].

The Fourier decomposition analysis of the corneal surface by Hjortdal et al [104, 105] allows to explore the deviations between average human cornea topology and an ideal sphere in terms of focal power and hence the radius of curvature (RoC) of the analyzed surface. This spectral decomposition method characterizes the corneal surface’s deviation from ideal spherical surface

by Fourier components for healthy and diseased cornea eyes [104]. The fundamental mode (first term in the Fourier series expansion) can be attributed to de-centration (pictorial representation in

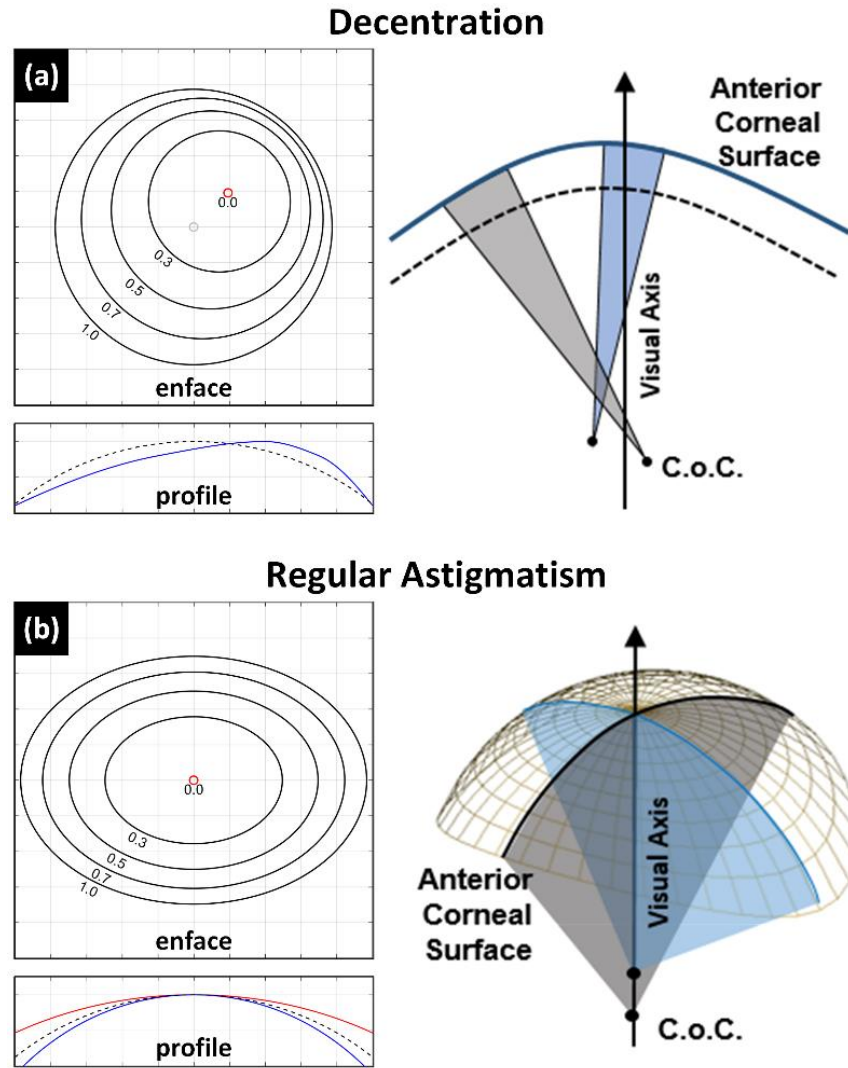


Figure 4-1: (a) Decentration and (b) “regular” astigmatism in corneal anatomy.

Decentration: Local surfaces may be shaped such that their centers of curvature (CoC) are not coincident with CoCs from adjacent surface and may not lie on the expected optical axis.

Astigmatism: The cornea is not radially symmetric and contours from different axes may lie at different locations along the optical axis

Figure 4-1(a)), and the second term is attributed to “regular” astigmatism (pictorial representation in Figure 4-1(b)). Higher order Fourier terms are grouped together as “higher order surface irregularities” and contribute less to the overall corneal shape than either decentration or

astigmatism. In general, all of these parameters increase for equal height contour lines further from the corneal apex.

To compute the standard deviation in radius of curvature (RoC) expected in a sample of patients the Fourier components available in [104] were utilized. These values were reported as diopters across the meridian cross-section as a function of radial distance from the center of cornea and the meridian angle. The diopters were averaged and converted to an expected RoC deviation using equation (1) where P_i is optical power in diopter, n is the refractive index of the cornea (taken to be $P_{\text{typical}} = 44$, $n = 1.376$), and Δr is the resulting standard deviation in the RoC.

$$\Delta r = (n - 1) \left(\frac{1}{P_2} - \frac{1}{P_1} \right) \quad (44)$$

The average RoC deviation from the first term in the series (decentration), the second term in the series (astigmatism) and the higher order terms are displayed in Figure 4-2 for healthy eyes (N=25), Keratoconic eyes (N=13), and grafted cornea (N=20) [104]. Data for endothelial dystrophies such as Fuchs was not available during the preparation of this manuscript. However, while the planned initial target diseases of this technology are endothelial dystrophies, the expected deviation of corneal shape from ideal is anticipated to be the greatest in Keratoconus and corneal graft rejection thus these pathologies serve as sufficient upper bounds on the spherical properties of endothelial diseased cornea.

For normal healthy eyes, decentration produces a mean RoC displacement deviation of ~0.05 mm, regular astigmatism is slightly higher at ~0.08 mm, and the sum total of higher modes contributes a negligible ~ 0.015 mm. Keratoconus is a condition where the cornea thickens and the CCT increases at a rate faster than the periphery. The mean RoC displacement deviation arising for decentration, astigmatism, and higher order irregularities, are ~0.4 mm, ~0.35 mm, and ~0.08 mm respectively. Finally, for a grafted cornea, where a patient's diseased cornea has been removed

and transplanted with a donor cornea the mean RoC displacement deviation arising from decentration, astigmatism, and higher order irregularities, are ~0.3 mm, ~0.35 mm, and ~0.08 mm respectively.

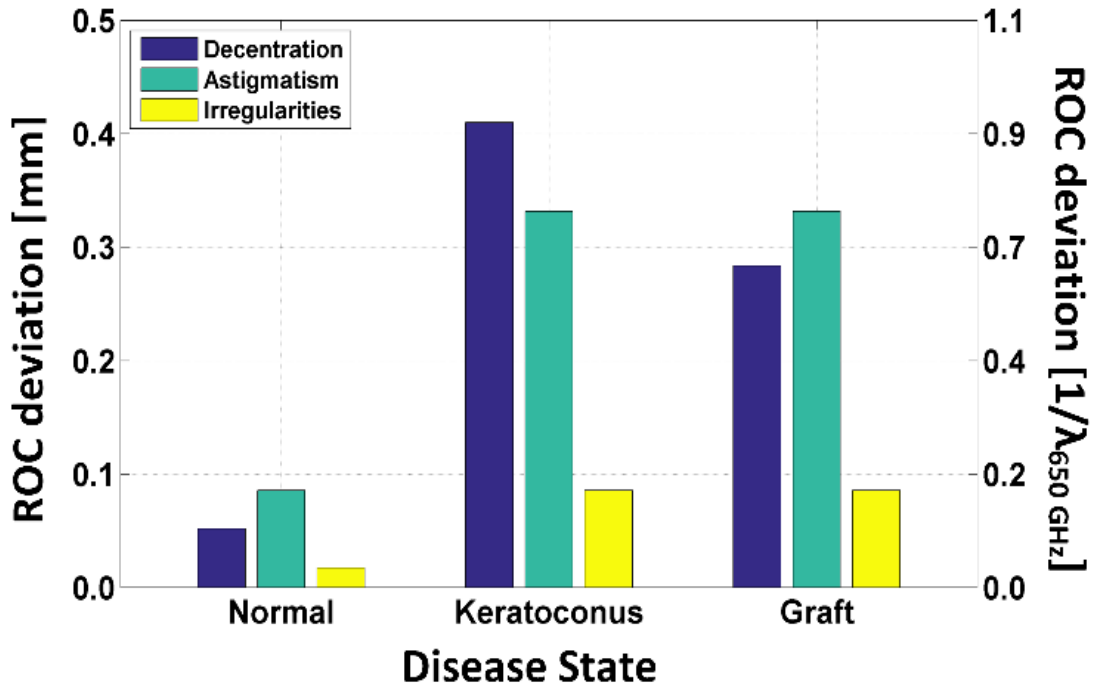


Figure 4-2: Average radius of curvature (RoC) variations (Δr from equation (44)) in cornea from Fourier decomposition analysis applied to healthy cornea, Keratoconus, and grafted cornea.

The RoC variation is delineated into decentration, regular Astigmatism, and higher order irregularities [104]. The maximum RoC variation is less than λ (@650 GHz).

The RoC deviation data in Figure 4-2 represents the expected geometric variation from an ideal sphere. It is also instructive to view this variation in geometry with respect to the wavelength of the THz frequency illumination. Consider the imaging systems presented in the following sections of this manuscript and Part B operating at 650 GHz corresponding to a free space wavelength of 0.462 mm. When normalized to wavelength, the corneal radius of curvature is $\sim 8 \text{ mm}/0.462 \text{ mm} = 17.32\lambda$. To add bounds on the deviation we assume that the variations described by the decentration, astigmatism, and higher order irregularities are uncorrelated and that total standard

deviation can be computed as the square root of the sum of squares of each individual standard deviation. This results in the following normalized geometry: Normal, healthy cornea = $17.32\lambda \pm 0.21\lambda$, Keratoconus = $17.32\lambda \pm 1.16\lambda$, and grafted cornea = $17.32\lambda \pm 1.01\lambda$ corresponding to coefficients of variance ($100 \cdot \sigma / \mu$) of 1.21%, 6.69% and 5.83%. Hence, with respect to the illumination wavelength, the corneal surface can be considered, to first order, an ideal sphere with maximum expected deviations approximately one free space wavelength.

For the reasons that will shortly become clear in the next section, we are actually interested in the locations of the center of curvature (CoC) for each local anterior corneal surface, or pertinent to the conclusions from Figure 4-2, what is the distribution of CoC locations. Therefore, we should re-write the expression for RoC deviation to CoC deviation, or show that they can be approximated to be similar. Figure 4-3 illustrates the relationship between RoC vector and CoC vector. Videokeratoscopy captures surface height data and compares it to an ideal sphere (we know this because the concentric ring image projection is a physical ideal sphere), then computes the power from it. Hence, the normal vector at each local surface (red line, Figure 4-3) always originate from the original ideal spherical surface. Its magnitude is the RoC at the surface. When the vectors pointing to the center of curvature (CoC vector) is in the same direction as the normal vector (RoC vector), CoC deviation is equivalent to RoC deviation.

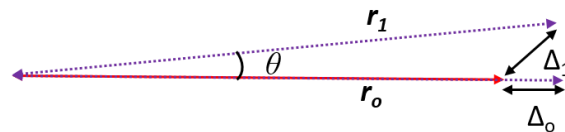


Figure 4-3. Displacement of Radius of Curvature (RoC) and Center of Curvature CoC

Next, consider the CoC vector's direction is not necessarily toward the true center of curvature (Purple vector, Figure 4-3). The end of the red arrow (r_o) depicts the true CoC center, while the

purple vector points to possible center of the curvature vectors with the same magnitude (r_1) but pointing to a different direction. Then the magnitude of the CoC deviation (Δ_1) compared to the RoC deviation (Δ_o) can be expressed as following.

$$\mathbf{r}_o = \mathbf{x}(r_o)$$

$$\mathbf{r}_1 = \mathbf{x}(r_1 \cos\theta) + \mathbf{y}(r_1 \sin\theta)$$

$$\Delta_o^2 = (r_o - r_1)^2$$

$$\Delta_1^2 = (r_o - r_1 \cos\theta)^2 + (r_1 \sin\theta)^2$$

Then, the CoC deviation (Δ_1) and RoC deviation (Δ_o) are different by the equation (45).

$$\Delta_o^2 - \Delta_1^2 = 2 r_o r_1 (1 - \cos^2\theta) \tag{45}$$

For reasonably small angle θ , $1 - \cos^2\theta$ is a very small term and the CoC deviation will be almost equal to the RoC deviation. While there is no direct measurement of θ , it can be at least concluded that CoC deviation is a reasonably small fraction of the dimension of the radius of curvature.

4.3. Spherical surface imaging

4.3.1. Spherical surface scanning principle

Active imaging of a spherical surface can be performed by positioning the CoC of the target coincident with the focal point of an OAP mirror and then transmitting a collimated illumination beam into the clear aperture of the mirror, parallel to the CA normal (Figure 3-1). The focused radiation is normal to the spherical surface and, in the limit of geometric optics, has a phase front curvature equal to the spherical surface RoC. The reflected, diverging beam is re-collimated by the OAP mirror and arrives coincident with the transmitted beam path. Moving the transverse location of the collimated beam while maintaining a path parallel to the mirror's clear normal sweeps the location of the illumination spot on the spherical surface, and an image can be constructed. The retro-directive nature of this arrangement is compatible with any transceiver design that can multiplex/demultiplex the input and output beams through the use of, e.g., a wire grid, thin film, or polarizing beam splitter.

This imaging technique accomplishes spherical surface (θ, ϕ) imaging by the geometrical projection of the target's spherical surface into a planer coordinate system (x, y) . This is a restatement of the Fourier-Transform property of an optical focusing element as demonstrated with a 90° off-axis parabolic mirror (OAP) in Figure 3-1. Unlike the Mercator projection which transforms the surface from spherical coordinates via a cylindrical projection to rectilinear coordinates, this method performs mapping from spherical coordinates via projection by a paraboloid surface into a rectilinear coordinate system and represents a conformal mapping of a spherical surface to an orthogonal, rectilinear projection. Although this exact mapping operation is uncommon, it shares resemblance to the more familiar conic orthographic mapping projections in cartography such as the Lambert Conformal Conic Projection [106].

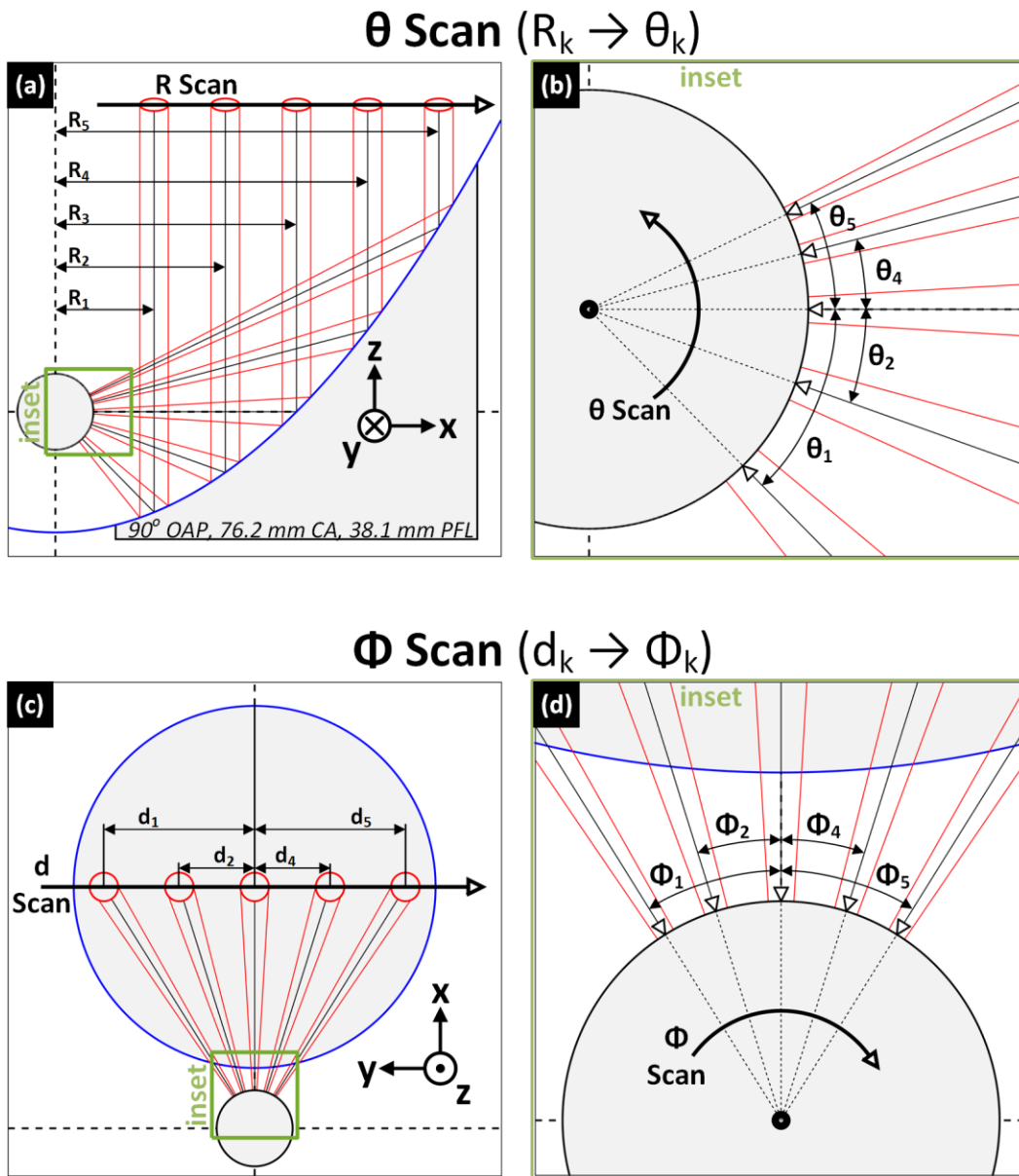


Figure 4-4: Scanning principle to raster-scan over spherical surface in a transformed rectilinear coordinate.

OAP mirror is used to project each ray path originating from the center of the curvature of the spherical target to rectilinear coordinates parallel to the optical axis. Beam scanning over the spherical surface is performed by X-Y- translation of the beam location.

4.3.2. Effective imaging optic $f/\#$ and offset

The maximum extent of target surface coverage is determined by the $f/\# = f_e/A = 2f_0/A$ of the mirror where f_e is the effective focal length (EFL), f_0 is the parent focal length (PFL) and A is the clear aperture diameter (Figure 4-5(a)). A human cornea spans $\sim 60^\circ$ ($\pm 30^\circ$) about its apex, thus an imaging optic should approach $f_e/A = 2 \cdot \tan(30^\circ) \sim 1.15$ to span $\pm 30^\circ$ in both azimuthal and elevation from the corneal apex.

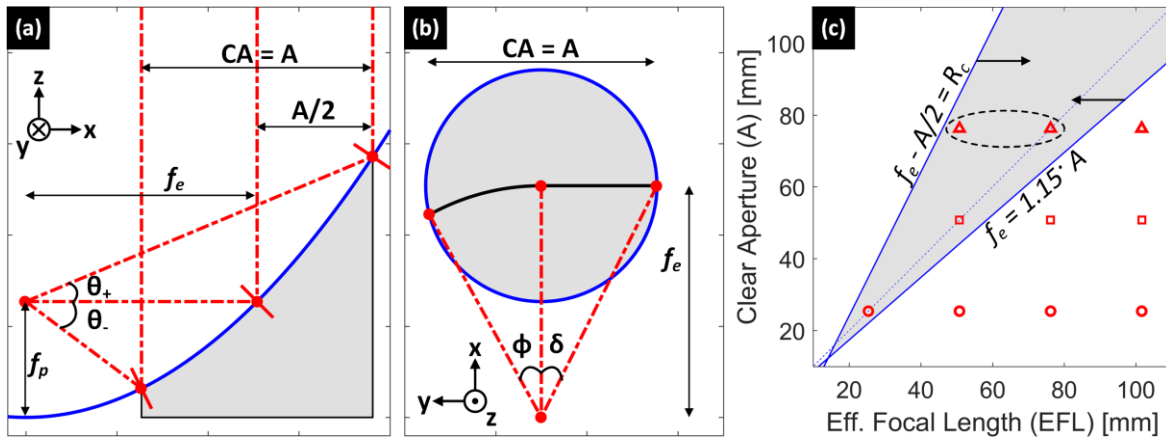


Figure 4-5: Half angles of 90° OAP mirrors.

(a): Side view.

(b): Clear aperture view with angles subtended by the intersection of mirror CA and circular contour with radius f_e . [ϕ] and the intersection between mirror CA and the diameter A [δ].

(c) Design space bordered by offset $f_e - A/2 = R_c$ and $f_e = 1.15 \cdot A$. Standard, commercially available mirrors indicated by \circ] 25.4 mm, \square] 50.8 mm, and Δ] 76.2 mm apertures.

Table 7 lists the azimuthal and elevation angles subtended by a 90° off-axis parabolic reflector parameterized with commercially available $f/\#$ s. Note that because the focusing geometry (Figure 4-5) is asymmetric the azimuthal coverage angle ($\theta_- + \theta_+$ (Figure 4-5(a)) is not bisected by the 90° ray; (i.e. $\theta_- > \theta_+$, $\forall f_e, A$). The 90° geometry results in the relation $\theta_+ < \delta < \phi < \theta_-$ therefore the angle θ_+ angle forms the lower bound on the OAP $f/\#$. The results in Table 7 indicate that the angles subtended by an $f/0.66$ are sufficient to cover the entire angular extent of the cornea.

Table 7.: Spherical coverage angle by imaging reflector f/#

f/# (f_e/A)	0.66	1	2	3
θ_-	62.8	36.9	16.3	10.4
θ_+	30.7	22.6	12.7	8.8
ϕ	44.5	29.0	14.4	9.6
δ	37.2	26.6	14.0	9.5

f/# is scale invariant and does not consider the size of the target relative to the size of the focusing objective. Practical considerations suggest that the combination of focal length and clear aperture should avoid positioning the apex of the cornea inside the mirror. In other words, the “flange distance” should be greater than the corneal radius of curvature: $f_e - A/2 > R_c$. The flange distance and f/# are displayed in Figure 4-5(c) where all combinations to the right of the $f_e - A/2 = R_c$ line yield sufficiently large flange offsets and all combinations to the left of the $f_e = 1.15A$ yield f/#s greater than 1.15. Markers representing standard, commercially available pairs of effective focal lengths and apertures are superimposed on this space with the 76.2 mm diameter mirrors denoted using a dotted contour. Parts A, B, and C utilized a 76.2 mm diameter f/0.66 OAP and an upcoming publication detailing *in vivo* human results utilized a 76.2 mm diameter f/1 OAP.

4.4. Quasioptical imaging system design

4.4.1. Single imaging mirror design

A straightforward method to implement the beam scanning described in Figure 3-1 utilizes a set of plane mirrors that scans the collimated input beam in two orthogonal directions parallel to the clear aperture plane of the OAP mirror. This concept is displayed in Figure 4-6 where the input and output beams are multiplexed/demultiplexed by a beam splitter that optically collocates the THz emitter and detector. The imaging system design was organized into three subsystems that are independent of each other, and can be separately optimized for desired imaging operation performance: (1) Transceiver subsystem, (2) scanning subsystem, and (3) imaging mirror.

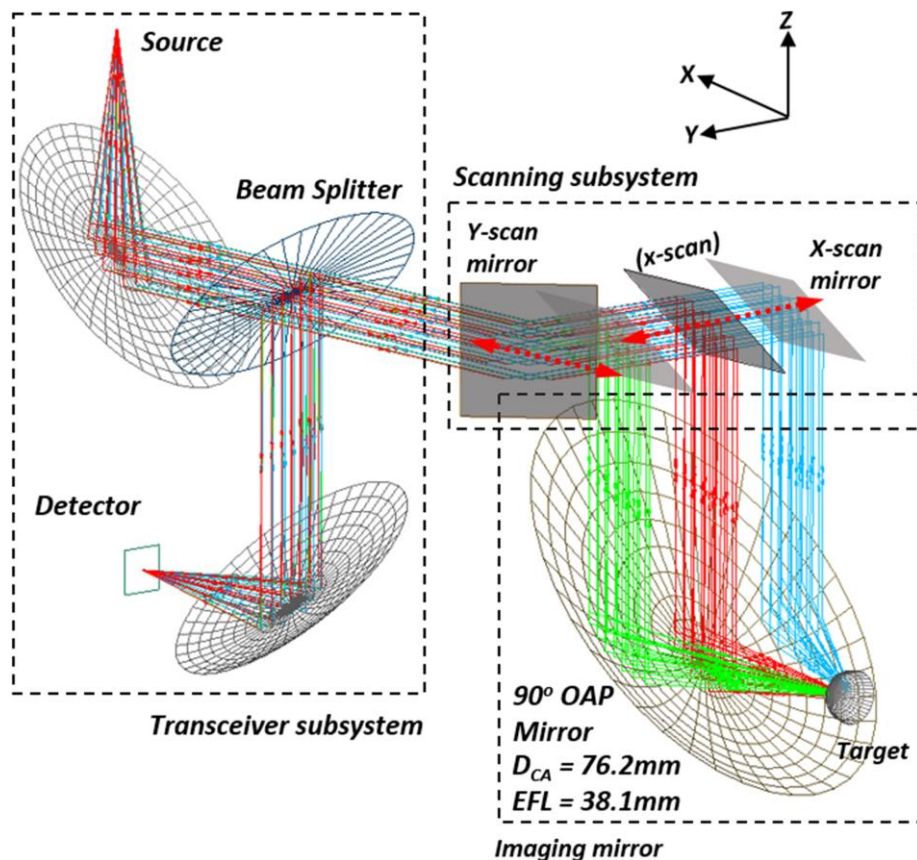


Figure 4-6: Single mirror, rectilinear scanning imaging system design comprised of three distinct subsystems; Three scan locations are plotted.

The plane mirrors labeled “x-scan” and “y-scan” are mutually orthogonal and linear translation of these optics enable transverse positioning of the collimated beam anywhere within the OAP CA. Since the OAP mirror is radially symmetric, the scanning methodology described in Figure 4-6 is valid for any plane orthogonal to the x-y- plane and coincident with the OAP focal point.

As discussed previously, the cornea CoC is coincident with the OCAP focal point and all rays of the focused beam are locally orthogonal to the spherical surface. Thus, in the limit of geometric optics, all reflected beams, independent of scan mirror position will arrive at the detector with identical beam convergence angle and beam transverse location and extent.

This concept is demonstrated with the three-superimposed beam paths in Figure 4-6. The y-scan mirror was held stationary and a parallel bundle of rays were traced (ASAP, Breault Inc.) for three separated x-scan mirror locations oriented symmetric about the OAP CA centroid. The results of this ray tracing demonstrate that three separate illuminated areas on the corneal target all result in identical, received beam properties/profiles at the detector.

4.4.1A Quasioptical Setup and modeling

A crucial observation in this beam scanning method is that the imaging mirror is over-dimensioned to the cross section of the beam. At any scan location, the beam effectively sees only the local surface of the imaging OAP mirror. Therefore, the transformation of the THz beam as a function of scan location can be approximated to be transformation by a local segment of the imaging mirror surface. Given a reasonable input collimated beam size, such segment spans moderate changes in curvature and focal distance. Above observations suggests that the mirror surface segment may be further approximated as a thin lens whose focal length is equal to the central beam path length from the mirror surface to the focus.

These approximations allow us to use the elegant technique of quasioptical analysis with Gaussian optics and ABCD matrices. The resulting beam transformation relation as a function of scan location characterizes the overall image transfer function by the imaging OAP mirror.

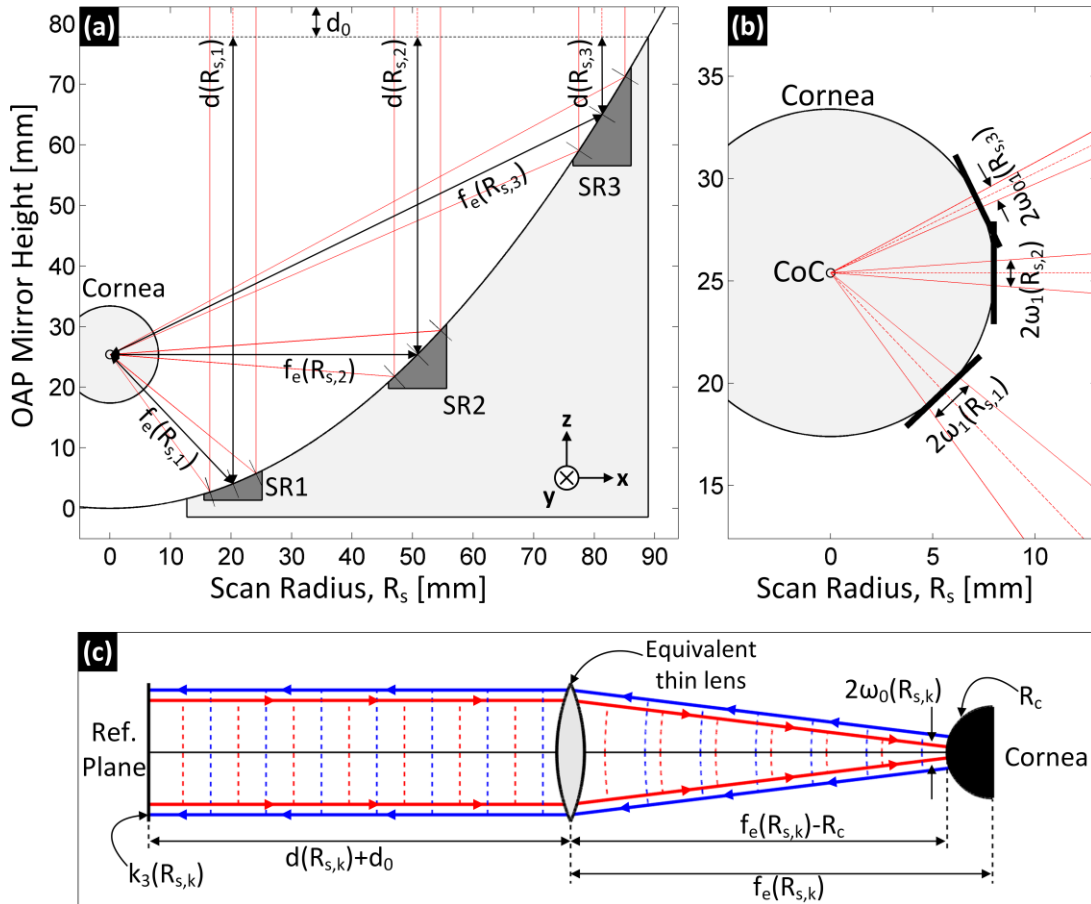


Figure 4-7. Raypath diagram of the beam scanning showing (a) respective parabolic mirror segmentation location, (b) definition of spot size on the surface of the cornea, and (c) thin lens equivalent of the overall beam path.

Three parallel ray bundles are parallel to the clear aperture and aligned with the center and 85% fill widths of the OAP. If the incident beam is much smaller in diameter than the CA the sub-reflector area defined by the beam diameter can be considered its own OAP mirror. A Gaussian beam can then be traced using the (1) Distance of free space travel between a reference plane and the mirror surface height defined by the intersection of the profile and collimated beam centroid

and (2) the effective focal length of the sub reflector defined by the line segment between the collimated beam centroid and parabolic intersection and the effective focal point of the entire OAP. In the limit of the paraxial approximation, this concept yields a collimated path length, focused path length, and effective focal length that are all dependent on distance between the mirror focal point and collimated beam centroid. The problem can be recast to that described by Figure 4-7(c). The collimated beam travels a distance $d(R_s)$, is focused by a thin lens of $f_e(R_s)$ and then travels $f_e(R_s) - R_c$ to a convex reflector of radius R_c (cornea). The mirror and cornea geometry ensures normal incidence for all R_s within the clear aperture of the mirror resulting in the beams retracing its path back through the mirror collinear with the incidence path.

$$f_e(R_s) = (4f_p)^{-1} R_s^2 + f_p = f_e \quad (46)$$

$$d(R_s) = (4f_p)^{-1} \left[\left(2f_p + \frac{A}{2} \right)^2 - R_s^2 \right] = d \quad (47)$$

Expressions for the radially dependent focal length and beam clear aperture path length are defined in equations (46) and (47). Note that these expressions are defined for the domain $R_m \in 2f_0 \pm A/2$ and are explicitly for a 90° OAP. R_s is the horizontal distance from the mirror focal point to the centroid of the collimated input beam and f_p is the parent focal length of the mirror.

$${}_{P \rightarrow C}(R_m) = \begin{bmatrix} 1 & f_e - R_C \\ 0 & 1 \end{bmatrix} \begin{bmatrix} 1 & 0 \\ f_e^{-1} & 1 \end{bmatrix} \begin{bmatrix} 1 & d + d_0 \\ 0 & 1 \end{bmatrix} \quad (48)$$

$$M_{C \rightarrow P}(R_m) = \begin{bmatrix} 1 & d + d_0 \\ 0 & 1 \end{bmatrix} \begin{bmatrix} 1 & 0 \\ f_e^{-1} & 1 \end{bmatrix} \begin{bmatrix} 1 & f_e - R_C \\ 0 & 1 \end{bmatrix} \quad (49)$$

$$M_C = \begin{bmatrix} 1 & 0 \\ 2/R_C & 1 \end{bmatrix} \quad (50)$$

$$\mathbf{M}_1 = M_{P \rightarrow C} \quad (51)$$

$$\mathbf{M}_2 = M_C M_{P \rightarrow C} = M_C \mathbf{M}_1 \quad (52)$$

$$\mathbf{M}_3 = M_{C \rightarrow P} M_C M_{P \rightarrow C} = M_{C \rightarrow P} \mathbf{M}_2 \quad (53)$$

To complete the problem description a reference plane is defined at a distance d_0 from the upper tip of the OAP. This reference plane is where the collimated beam (plane coincident with the beam waist) was launched and where the 2D coupling coefficient was computed. $\mathbf{M}_1 = M_{P \rightarrow C}$ (equations (48), (51)) is the transfer matrix describing the propagation of the beam from the reference plane (P) to the cornea (C). The beam traverses a path length $d + d_0$, is focused by a thin lens of the f_e , and propagates a distance $f_e - R_c$ to the surface of the spherical reflector (cornea). $\mathbf{M}_2 = M_C M_{P \rightarrow C}$ (Equations (50), (52)) describes the propagation of the beam through \mathbf{M}_1 and the subsequent reflection from the spherical reflector. The overall retrodirective transmission through the optical system is described by $\mathbf{M}_3 = M_{C \rightarrow P} M_C M_{P \rightarrow C}$ (equations (50), (53)) where the beam starts and stops at the reference plane.

$$\frac{1}{q_k} = \frac{1}{R_k} - j \frac{\lambda_0}{\pi n \omega_k} \rightarrow \frac{1}{q_0} = -j \frac{\lambda_0}{\pi n \omega_0} \quad (54)$$

$$\mathbf{M}_k = \begin{bmatrix} A_k & B_k \\ C_k & D_k \end{bmatrix} \quad (55)$$

$$q_k = \frac{A_k q_0 + B_k}{C_k q_0 + D_k} \quad (56)$$

The standard complex beam parameter relations listed in equations (54) – (14) were used to compute the spot size on target (\mathbf{M}_1), the beam radius of curvature immediately prior to (\mathbf{M}_1) and following (\mathbf{M}_2) reflection from the cornea, and the coupling coefficient between the input and output beams at the reference plane (\mathbf{M}_3). These factors were calculated for all relevant R_s with an input complex beam parameters q_0 parameterized by ω_0 and a constant $R_0 \rightarrow \infty$.

4.4.1B Analysis of spot size on cornea surface

The spot size on target was assessed as a function of input beam waist size at the reference plane and radial distance from the effective focal point of the OAP mirror using equations (51) and (54) – (14). ABCD matrix formulism and the complex beam parameter describes the properties of a beam at a defined distance along the optical axis, on a plane that is transverse to the optical axis at this defined distance. When applied to the analysis of the corneal imaging, we can compute the spot size on a plane tangent to the corneal surface and normal to the beam centroid as depicted in Figure 4-7(b). Due the relatively small extent of the focused beam with respect to the corneal RoC, the spot size computed on a plane was considered accurate estimate of the illumination spot size, computed by projecting the beam on to the corneal surface and assessing the extent of the intersection contour.

$$r_1 = \frac{\lambda}{\pi} \left[\Re \left\{ \frac{j}{q_1} \right\} \right]^{-1} \quad (57)$$

This analysis investigates the effect different input beam size, which is about the only parameter that can be varied by the system design other than the main imaging optic. In Figure 4-7(a), the resulting output spot radius as a function of input radius and mirror position (R_m) are plotted in solid lines over the shaded outline profile of a 76.2 mm CA, 25.4 mm PFL, 90° OAP mirror length for reference. The different color of the line represents the varying input Gaussian beam radius (w_0) at the reference plane from 4 mm to 12 mm. The pair of (o) markers and dotted line style at the extreme ends of each curve. These represent a practical CA limitation imposed by beam clipping. The extreme points on each size of the curve represent the edge of the mirror CA. The second set of points located closer to the mirror CA axis represent one input beam radius from the edge of the mirror. In practice, the focusing performance described by the solid curves bordered by the interior points is feasible and diffractive effects must be considered for beam centroid locations outside the solid line intervals.

The 4 mm input spot size demonstrates a decreasing focused spot size for decreasing $R_s \rightarrow f_e(R_s)$. In this case the effective $f/\#$, which is a combination of the focal length of the sub-reflector, the beam input diameter, and the center wavelength results in a beam waist that occurs “outside” of the cornea for large R_m and the beam is diverging prior to being incident on the corneal surface. As the effective $f/\#$ is decreased (decreasing R_s) and the focused path length decreases (decreasing R_s), the beam waist decreases and its location converges to the surface of the cornea. Further decreases in R_s result in the beam waist locating to “inside” the cornea paired with an increasing convergence angle. While the focused waist continues to decrease in size, the corneal surface intercepts the beam at a distance that is increasing from the location of the waist. This leads to an

increase in detected spot size. This interplay between spot size, waist location, and convergence angle produces a tradespace for a given spot size where the minimum beam diameter utilizes a beam centroid location that lies at $R_s \sim 37$ mm.

This behavior is somewhat reversed for the 12 mm input radius. The focused spot reaches its maximum at the shortest effective focal length and its minimum with an R_m that is nearly at the extreme edge of the OAP. Unlike the 4 mm radius beam, the 12 mm radius beam produces a waist that is “inside” the cornea for all R_s and the offset between the sub-reflector focal point and waist location is small with respect to R_c for nearly all R_s . Since the input beam is large, the effective beam $f/\#$ is small and leads to large convergence angles and thus large spot sizes on the corneal surface. The optimum tradeoff between competing factors occurs at $R_m \sim 82$ mm.

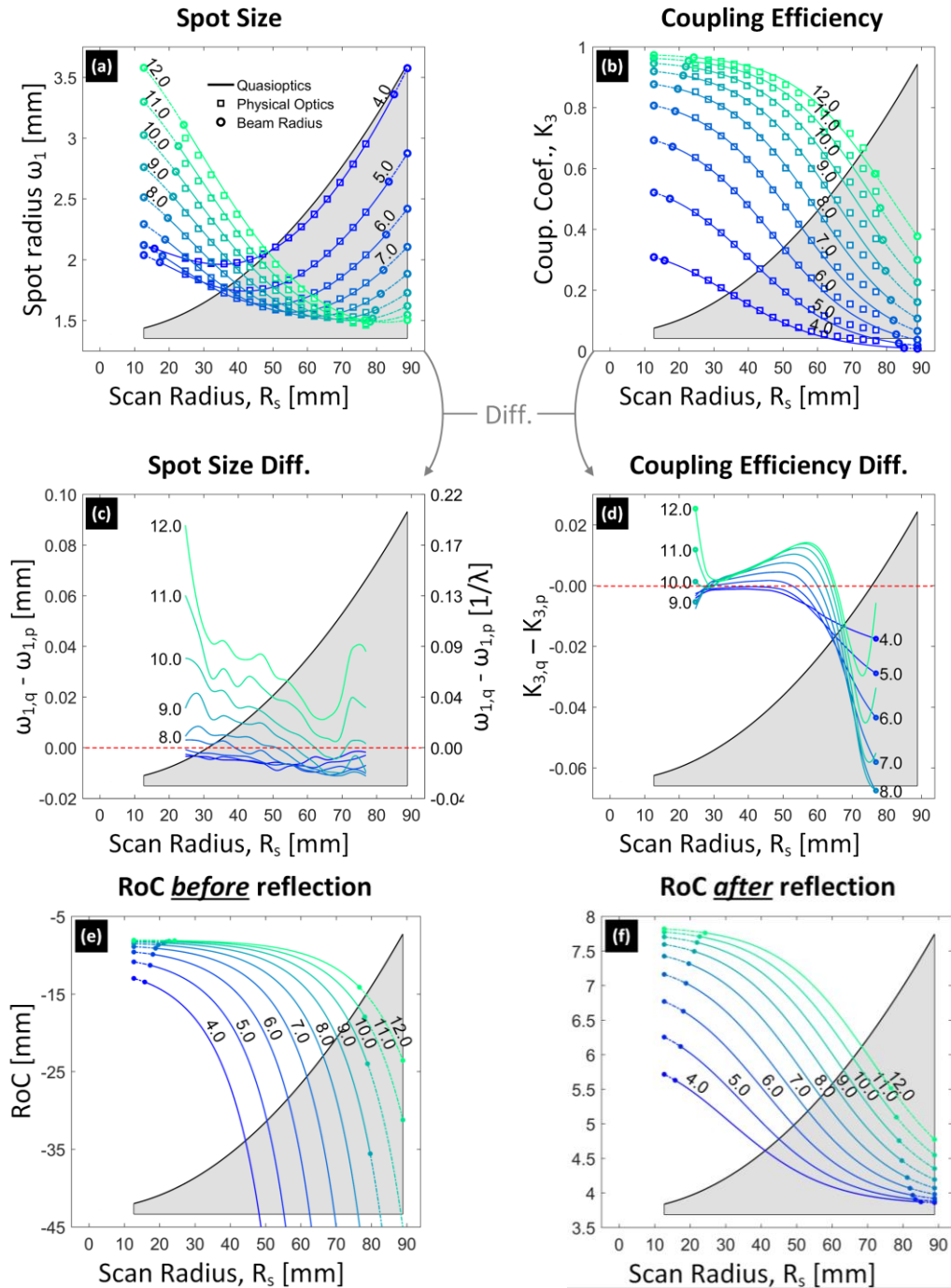


Figure 4-8. (a) Spot size and beam coupling efficiency of the imaging system

A scaled overlay of parabolic cross section is shown depicting the location of the collimated beam centroid.

- (a): Focused spot radius as a function of the input beam and radius (ω_0).
- (b) Coupling coefficient between the input and output beam
- (c), (d): Differentials between results computed by quasioptical analysis and physical optics simulation.
- (e) Radius of curvature of the focused beam immediately prior to the target surface
- (f) Radius of curvature immediately following reflection from the target surface.

The intermediate input spot sizes demonstrate varying dependencies on the above mentioned factors and it is clear by inspection that there is exist some intermediary that balances the following three competing factors:

1. Decreasing R_s decreases the effective focal length of the sub-reflector and thus decreases the size of the focused beam waist (geometric)
2. Decreasing R_s increases the convergence angle of the beam and can increase the beam spot size on the corneal surface depending on beam input parameters (geometric)
3. Decreasing the input beam waist decreases the convergence angle while increasing the offset between sub-reflector focal point (corneal center of curvature) and focused beam waist. This can result in an increase or decrease in the spot size on the corneal surface depending on the $f/\#$ of the OAP, the input diameter of the beam, and the wavelength (quasioptical).

The results in Figure 4-8 demonstrate an interesting tradeoff between input and output spot size and mirror clear aperture location (R_s) which arises from the fact that the focused beam parameters are characterized at a distance $R_c > 0$ from the geometric focal point of the considered sub-reflector.

4.4.1C Beam RoC and Coupling

In the original concept of this design is inherently based on geometric optic approximation. The quasioptical modeling effort in this section tries to account for the effect of diffraction and beam divergence in using THz wavelengths to see whether the THz beams in this system behave sufficiently similar as optical beam that imaging and sensing of the target surface can be realized.

In the geometric optics limit, the beam has the radius of curvature (RoC) that matches the curvature of the target when it is incident on the target surface, hence all of the beam front is

deflected back at the normal angle. As λ becomes larger, the actual location of the beam waist starts to be pulled from the geometric focus of the mirror. The RoC of the beam is found from the complex beam parameter q with equation (58).

$$R_{1,2} = \left[\Re \left\{ \frac{1}{q_{1,2}} \right\} \right]^{-1} \quad (58)$$

The RoC for the pre- and post- target reflection are displayed in Figure 4-8(a) and (b). The Rayleigh length of the radius of curvature also becomes larger for increasing λ because the beam waist is larger. As a result, it can be seen in Figure 4-8(e) that the illumination beam front is much flatter upon hitting the target surface. There are a couple immediate observations. The displacement of the beam waist location is a function of the focal distance and the beam size. Hence, beam radius of curvature at the target surface is also a function of scan location, as it is with spot size shown in Figure 4-8(a). It can be seen in Figure 4-8(e) that the beam actually moves very close to the surface as RoC rapidly approaches $-\infty$. Second, it is noticed that for smaller beams, faster beam divergence will make that displacement much faster. As the input spot size is increased the beam waist decreases and converges on the corneal CoC. This results in the effective phase center of the beam being located at the CoC and beam RoC converging towards the corneal RoC.

Upon reflection from the target, the beam is expected have dramatically different RoC. However, because the beam front before the reflection was already significantly flat compared to the transverse beam dimension, the range of RoC after the reflection is within 4mm– 8mm range. These observations helps explain the coupling efficiency of the input and the output beam, which can describe both the signal collection efficiency (how will this beam be coupled to the detector?) and comparison to the original beam shape (which was a collimated beam with beam radius ω_0).

4.4.1D Coupling efficiency

The source mirror and detector mirror, encircled with the dotted lines in the transceiver subsystem in Figure 4-6 were illustrated as identical in CA and PFL. They were oriented with respect to the beam splitter to maintain the “symmetric” configuration according to the design rule 1 (Chapter 2). However, it had become quickly apparent that it is beneficial to use different types of mirror for the source device and the detector device. According to the second design rule (Section 2.4.3), longer focal length mirrors should be used for the collimating the source because the larger f/D ratio creates more diffuse beam focus, and the alignment error is less impactful for the collimation. Conversely, a shorter focal length mirror should be used for the detector because we want to minimize the beam walk-off from the misalignment of the target.

There are many ways that the transceiver system can be designed. It may be the case that the source and the detector devices are combined to a single transceiver device and the collimating optic is shared for both devices. In order to compare and analyze the beam quality of the source beam and the measurement beam (returning after the reflection from the cornea), it is more applicable to consider the “ideal” case that is solely defined by the imaging optics. An ideal operation is defined by the beam maintaining a high level of collimation in all paths between the OAPS. Given the symmetry of the optical layout, the coupling efficiency between the source and detector can be accurately assessed as the similarity of the input and reflected output beams at the reference plane. To the coupling efficiency between input beam (q_0) and output beam (q_3) is given in equation (60):

$$q_3 = \frac{A_3 q_0 + B_3}{C_3 q_0 + D_3} \quad (59)$$

$$K_3(q_0, q_3) = \frac{4}{\left(\frac{\omega_0}{\omega_3} + \frac{\omega_3}{\omega_0}\right)^2 + \left(\frac{\pi\omega_0\omega_3}{\lambda}\right)^2 \left(\frac{1}{R_3} - \frac{1}{R_0}\right)^2} \quad (60)$$

The 2D beam coupling coefficient is defined in equation (60) with the relationship between the input and output complex beam parameters (q_{in} , q_{out}) defined in equation (59). The coupling coefficient is calculated at the reference plane and is written explicitly in terms of the input and output spot sizes and radii of curvature which together define their respective complex beam parameters. Note that equation (60) does not account for beam clipping due to finite aperture size and beam divergence.

The coupling coefficient as a function of mirror position and input beam diameter are displayed in Figure 4-8(b) and confirm the expected relation between input and output beam matching. As the beam input radius increases and the sub-reflector effective focal length decreases (decreasing R_m) the RoC matching between the focused beam and cornea improves resulting in a reduced perturbation of the illumination beam and increased matching at the reference plane. At 8 mm (nearest integer to the spot size optimized input beam of 7.6 mm) the coupling efficiency at the clipping threshold ranges from 0.17 to 0.87. The 12 mm beam ranges from 0.57 - 0.95 and the 4 mm beam ranges from 0.30 - 0.03. These results confirm a monotonically decreasing coupling efficiency for increasing input spot size independent of the input beam radius.

Visualization of the beam RoC prior to reflection yields further insight to this behavior. Inspection of the RoC following reflection gives an indication of overall beam coupling efficiency (Figure 4-8(b) and (d)). The reflected beam RoC demonstrates significantly less variation than the pre-reflection RoC as a function of mirror radius R_s and suggests that the post reflection RoC is the primary determinant of the coupling efficiency.

4.4.1E Observations

The quasioptical design and analysis space for corneal imaging is unique because (1) the target is spherical leading to increased divergence in reflection compared to the canonical flat target, (2) the target surface NOT located at the focal point defined by the optics or beam calculations leading to complex beam dynamics on target, (3) in the limit of ray tracing the beam is normally incident across the entire target surface suggesting a minimal dependence on beam polarization.

The results suggest that, in the limit of a fixed input beam, the signal from the lower region of the cornea will always be higher than the upper region of the cornea. These observations also suggest that the imaging field may be homogenized in terms beam radius and coupling efficiency if the input beam diameter can vary as a function of mirror position. These concepts motivated us to develop another optical design that will be discussed in Section 1.4.4.

4.4.2. Verifying quasioptical analysis: Physical Optics Analysis

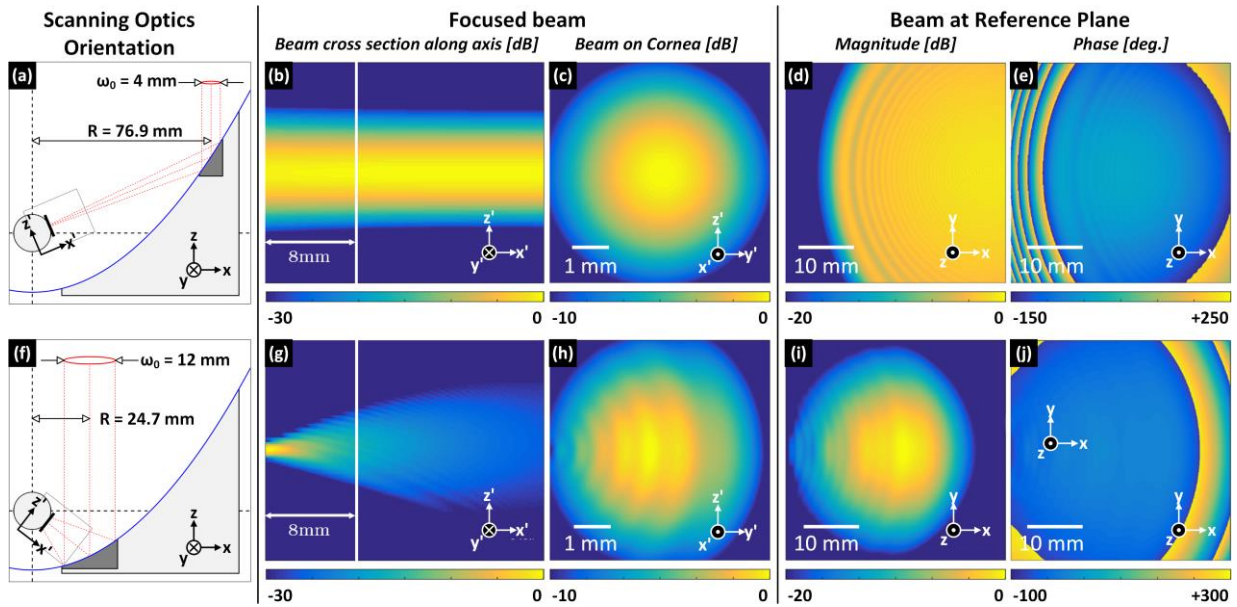


Figure 4-9: Physical optics analysis of the imaging system.

(a): Layout for $\omega_0 = 4$ mm at $R = 76.9$ mm.

(b): Cross section of beam in the x' - z' plane. The white vertical line denotes the location of the intercept plane tangential to the corneal surface

(c): Beam profile on the y' - z' plane tangent to the cornea and coincident with the intersection of the focused beam centroid and corneal surface.

(d), (e): Electric field magnitude and phase of the beam at the reference plane (x - y plane) following reflection from the cornea and re-collimation from the imaging mirror.

(f): Layout for $\omega_0 = 12$ mm at $R = 24.7$ mm.

(g)-(j) are same as (b)-(e).

4.4.2A Spot size

The propagation of THz beam in this imaging operation is rigorously computed with a reflector-antenna design tool (GRASP, Tica Inc., Denmark) that uses the physical optics (PO) method [107].

The input beam parameters presented in Figure 4-6 are used and the electric field distribution of the focused beam is calculated in the E-plane, H-plane, and transverse plane at the intersection of the beam centroid and at the corneal surface. These planes are defined by the x' , y' , and z' axes in the Figure 4-9(a) and (f).

An example of the focused beam for the input parameters $\omega_0 = 4$ mm, $R = 76.9$ mm is shown in Figure 4-9(a) – (c) in dB scale. The accompanying scale bars indicate FOV dimensions. The E-field distribution in the $x'-z'$ plane confirms that the fields are nearly Gaussian. A good agreement with simplified beam transformation model is also observed on the target ($y'-z'$) which demonstrates vanishingly small radial asymmetry (ellipticity ~ 1) and an apparent lack of cross polarization. The predicted short Rayleigh length at $\omega_0 = 4$ mm is also observed. The nearly Gaussian field distribution results from negligible effect of reflector geometry as the local curvature of the mirror surface is nearly symmetric about the beam centroid over the extent of the collimated beam.

A complementary example of a large input beam radius ($\omega_0 = 12$ mm) and short scan radius ($R = 24.7$ mm) is displayed in the Figure 4-9(f)-(h). The large collimated beam radius and increased mirror curvature result in the focused beam waist lying nearly coincident with the corneal CoC/OAP focal point which is visible in the $x'-z'$ cut in Figure 4-9 (g). Increased diffraction and the effects of increased mirror asymmetry about the beam centroid are also apparent and manifest as multiple local extremum in the field distributions of Figure 4-9 (g)-(h) and noticeable radial asymmetry in Figure 4-9 (h).

The average spot size on target ($x'-y'$ tangent plane) was computed numerically by obtaining the modulus of the E-field to suppress diffractive effects due to finite aperture size, finding the location of the peak amplitude, computing the $1/e$ closed contour of the modulus, and then computing the average radius of the $1/e$ contour. These results are superimposed with a square marker (\square) in Figure 4-8(a) and demonstrate good agreement between quasioptical analysis and physical optics. The level of fit is further explored in Figure 4-8(b) which reports the difference between quasioptical radius ($\omega_{1,q}$) and physical optics average radius ($\omega_{1,p}$): $\omega_{1,q} - \omega_{1,p}$. The spot

size differential further substantiates the general correlation between decreasing spot size radius and improved goodness of fit. Additionally, the graph elucidates the increased effects of diffraction and offset reflector configuration for larger input diameters and smaller scan radii.

4.4.2B Coupling

Similar to the spot size comparison analysis, the field distribution computed in GRASP platform was used to evaluate the coupling between the input beam and the reflected output beam at the reference plane. The magnitude of the reflected beam for the $\omega_0 = 4$ mm, $R = 76.9$ mm pair demonstrates a significant increase in main lobe extent compared to the initial 4 mm. This observation corroborates with the results obtained with quasioptical analysis that indicate substantial beam divergence upon reflection from the cornea surface.

On the other hand, the input beam with $\omega_0 = 12$ mm, $R = 24.7$ mm demonstrates a beam divergence at the reference plane only slight larger than the initial beam. The phase plot is also more uniform with extremum spaced farther apart. These plots indicate that the reference plane is likely well within the collimated beam's Rayleigh length and strongly corroborate with the quasioptical analysis.

$$\bar{K}_3 = \frac{|\iint (\vec{E}_0 \cdot \vec{E}_3) dA|^2}{\iint |\vec{E}_0|^2 dA \iint |\vec{E}_3|^2 dA} \quad (61)$$

The coupling coefficient was computed with equation (24) which references the square of the inner product of the vector fields with the product of the total energy in each field. The complex vector inner product accounts for mismatch between amplitude, phase, and polarization. The coupling coefficient computations were plotted as a square marker (\square) in Figure 4-9(c), and again demonstrate good agreement between quasioptical methods and physical optics. The differential between the quasioptical coupling coefficient ($K_{3,p}$) and the physical optics coupling coefficient

($K_{3,q}$): $K_{3,p} - K_{3,q}$ is plotted in Figure 4-9(f) and reveals a maximum deviation of $\sim 6.5\%$ at $\omega_0 \sim 8$ mm, $R \sim 76.9$ mm. The larger input spot radii are not monotonic across the scan range and this variation likely rise from edge diffraction.

4.4.3. Imaging system design analysis: Discussion

Quasioptic techniques were introduced that segment parabolic mirrors into an ensemble of thin lenses where the effective focal length and free space beam paths are proportional to the distance between the parent focal point and mirror clear aperture centroid. The Gaussian beam approximation and thin-lens approximation show very good agreement between the physical optics results. The mirror is over dimensioned ($A \gg \omega_0$) therefore diffractive effects were limited for the majority of the considered input parameter space. The concurrence of the results strongly supports the use of quasioptical techniques as a design and analysis tool.

The limited intra-patient geometric variation of the cornea is unique amongst all structures in the body and, when referenced to the typical center wavelength of a THz imaging system is unique amongst all applications where optical imaging is applied to diagnostic medicine. We believe that the presented systems and analysis techniques provide a good first step towards the *in vivo* translation of this technology to human subjects. The next section explores a more efficient, faster scanning method that augments the imaging method described in this section.

4.4.4. Angular scanning system design

One potential weakness of the system design outlined in the previous section (from here on, referred to as “rectilinear scan design” or “rectilinear system”) is the relatively large transverse displacement necessary to scan a comparatively small angular FOV on the cornea. This relationship creates a limitation on image acquisition rate that may. The eyes, exhibit rapid, random, and uncontrollable movement which necessitates corneal diagnostic imaging be performed in a short amount of time relative to the dynamics. Anesthetizing patients to reduce mobility are not feasible and such requirement reduces the utility of THz sensing. No contact mechanism shall be employed to combat positional disturbance. Therefore imaging must be rapidly performed.

Therefore, a scanning method is explored that performs the necessary transverse beam translation with comparatively small azimuthal and elevation perturbation of one plane mirror. Quasioptical design and analysis are paired with physical optics based verification to confirm working principles and identify design strengths and weaknesses.

4.4.4A Two-Imaging Mirror (angular) Scanning System

A more efficient scanning mechanism is displayed in Figure 4-10. This design was motivated by scanning microscopy (e.g. confocal microscopy, optical coherence tomography) which typically employ galvanometric or resonance mirrors to transform translation in the angular domain at some intermediary plane to transverse, planar translation at the imaging plane.

The optical system design presented in Section 4.4.3. scans azimuthal and elevation with separate planar mirrors whose axes are mutually orthogonal. Because of the comparatively short Rayleigh lengths at the design wavelength, the angular scanning design uses a single gimbal-mirror-like optical translation where rotational motion is about the center point of the mirror

surface. This design allows for an overall shorter optical path compared to the rectilinear scanning design.

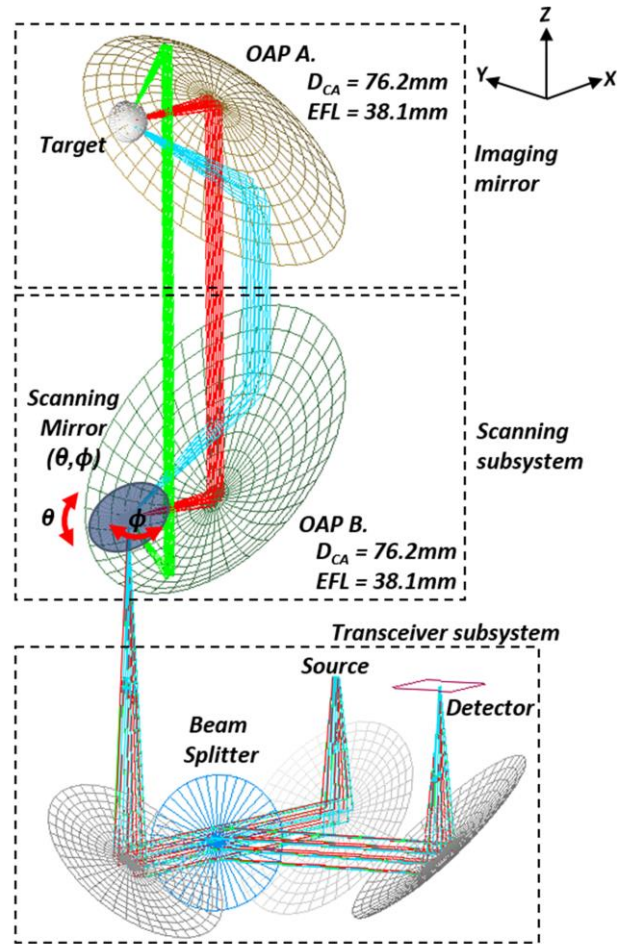


Figure 4-10. Double mirror, angular scanning imaging system design.

The transceiver subsystem utilizes one additional OAP mirror whose input is steered by the (θ, ϕ) scanning mirror. Three θ angle scan locations are plotted.

As illustrated in Figure 4-4, transverse translation of a collimated beam results in the angular scanning of a focused beam at the target plane. In this angular implementation a second parabolic mirror, identical to the focusing objective, is added to the beam path in the symmetric “tip-to-tip” orientation [108, 109]. The THz beam is focused onto the surface of the angular scanning mirror and then the diverging beam is directed to varying sub-segments of the added parabolic reflector.

This angular scan results in the transverse translation of a collimated beam in the clear aperture plane of the focusing OAP.

There are two key benefits to this design. First, angular scanning at moderate speeds can produce rapid transverse translation in the collimated beam path and the total image acquisition time can be greatly reduced. Second, the collimated beam diameter is a function of scanning angle resulting in a partial optimization of beam parameters with respect to the spot size on target. Recall that in the rectilinear scanning (constant collimated beam diameter) case, larger beam diameters at the far edge of the OAP minimized the spot size while smaller beam diameters at the near edge of the OAP minimized the spot size. This behavior is intrinsic to the angular scanning design as evidence by the ray paths in Figure 4-11(a).

4.4.4B Angular Scanning System Design: Quasioptical analysis

The quasioptical setup and problem definition are displayed in Figure 4-11(a) and (b). The mirror front surface centroid is coincident with the focal point of the OAP 1 and the cornea CoC is coincident with the focal point of OAP 2. The beam angle θ is designed with respect to the z-axis (standard spherical coordinates). In Figure 4-11(a), the beam is diverging from the scanning mirror at a divergence half angle of 5° . The beam centroids deflected towards sub-reflectors 1, 2 and 3 (SR1, SR2, and SR3) form angles of 125° , 90° , and 63° , respectively with the vertical axis. These beams result in collimated beam diameters (in the limit of geometric optics) of 5.54 mm, 8.89 mm, and 14.25 mm. The equivalent quasioptical thin lens problem is displayed in Figure 4-11(b) and the representative ABCD matrices are given in equations (62) - (63).

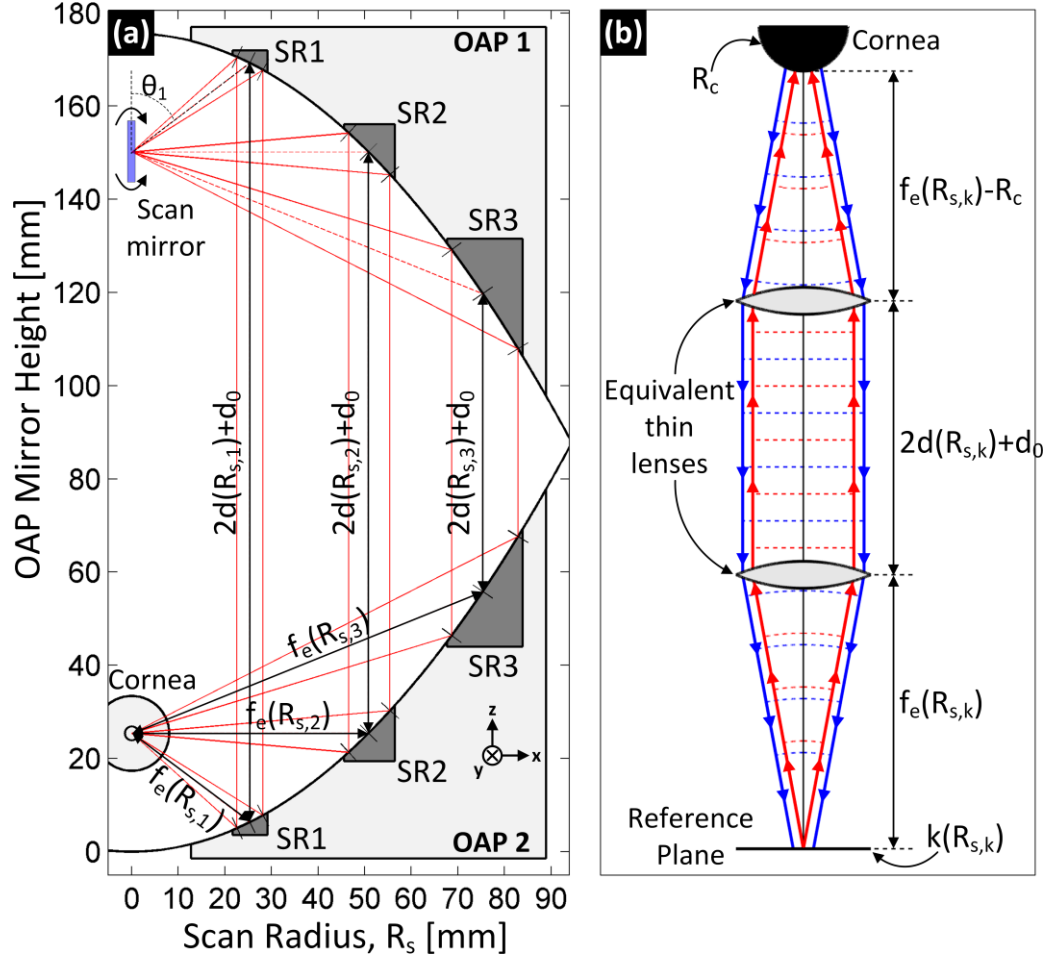


Figure 4-11. Raypath diagram of the double mirror, angular scanning system. (a) Parabolic mirror segmentation and (b) thin lens equivalent of the overall beam path.

$$R_s = 2f_p \left[\tan\left(\frac{\pi}{2} - \theta\right) + \sec\left(\frac{\pi}{2} - \theta\right) \right] \quad (62)$$

$$M_{P \rightarrow C}(R) = \begin{bmatrix} 2 - R_c f_e^{-1} & f_e - R_c \\ f_e^{-1} & 1 \end{bmatrix} \begin{bmatrix} 1 & 2d + d_0 \\ 0 & 1 \end{bmatrix} \begin{bmatrix} 1 & f_e \\ f_e^{-1} & 1 \end{bmatrix} \quad (63)$$

$$M_{C \rightarrow P}(R) = \begin{bmatrix} 2 & f_e \\ f_e^{-1} & 1 \end{bmatrix} \begin{bmatrix} 1 & 2d + d_0 \\ 0 & 1 \end{bmatrix} \begin{bmatrix} 1 & f_e - R_c \\ f_e^{-1} & 2 - R_c f_e^{-1} \end{bmatrix} \quad (64)$$

$$\mathbf{M}_1 = M_{P \rightarrow C} \quad (65)$$

$$\mathbf{M}_2 = M_C M_{P \rightarrow C} = M_C \mathbf{M}_1 \quad (66)$$

$$\mathbf{M}_3 = M_{C \rightarrow P} M_C M_{P \rightarrow C} = M_{C \rightarrow P} \mathbf{M}_2 \quad (67)$$

The notation and formulism in equations (62) - (67) is the same as used in Equations (4) – (9) with the exception that some matrix multiplication has been carried out in the interest of space. The reference, angularly scanned plane located at the focal point of OAP1. The beam travels a free space path length of $f_e(R_s)$, is collimated by a thin lens of $f_e(R_s)$, travels a free space path length of $2d(R_s)+d_0$ where d_0 is the tip-to-tip separation of the two OAPs, is focused by a thin lens of focal length $f_e(R_s)$, and then travels $f_e(R_s)-R_c$ to the corneal surface. This path is described in Equation (63) and the reverse is described in Equation (64). The complete path is $M_{C \rightarrow P} M_C M_{P \rightarrow C}$ where M_C is defined in equation (50). The scan radius dependent focal length was computed with , and the angularly dependent scan radius is given in equation (62).

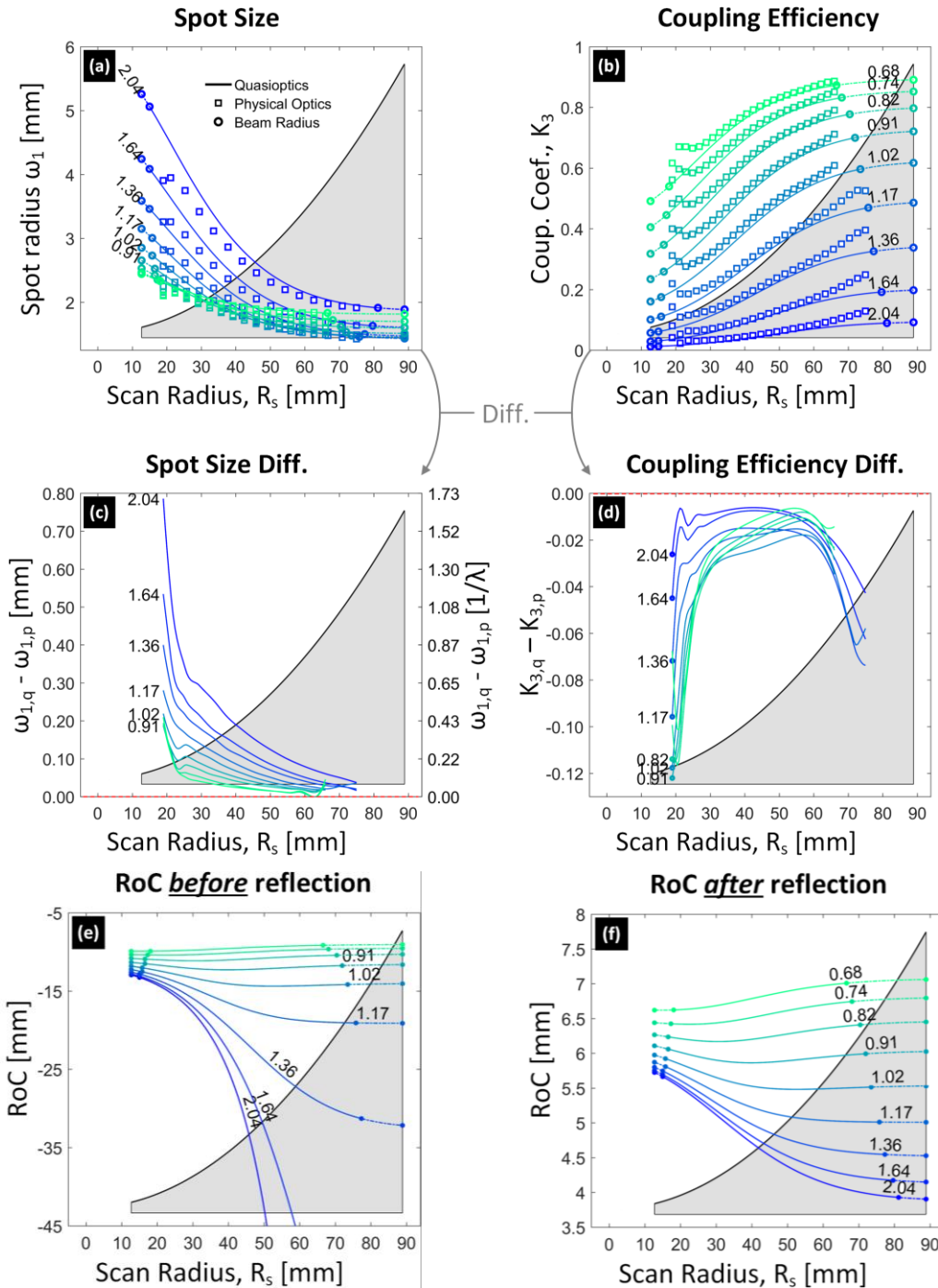


Figure 4-12. Spot size and beam coupling efficiency of the angular scanning system.

A scaled overlay of parabolic cross section is shown depicting the location of the collimated beam centroid.

- (a): Focused spot radius as a function of the input beam and radius (ω_0).
- (b) Coupling coefficient between the input and output beam
- (c), (d): Differentials between results computed by quasioptical analysis and physical optics simulation.
- (e) Radius of curvature of the focused beam immediately prior to the target surface
- (f) Radius of curvature immediately following reflection from the target surface.

4.4.4C Quasioptical computation: spot size

The spot size computations as a function of radially dependent scanning position and spot size at the scanning mirror plane are shown in Figure 4-12(a). To enable comparisons between these results and those in Figure 4-8 for the rectilinear scanning results, the computed parameters are displayed as a function of collimated beam centroid location following collimation by OAP1 (Equation (62)). Additionally, the considered focused beam radii (ω_{02}) were the collimated beam radii utilized in the rectilinear scanning simulations (ω_{01}) focused by a 76.2 mm CA, 38.1 mm parent focal length mirror (equation(68)).

$$\omega_{0,2} = \frac{2\lambda^2 \omega_{0,1} f_p (4f_p^2 + 1)^{1/2}}{4\lambda^2 f_p^2 + \omega_{0,1}^4 \pi^2} \quad \forall \omega_{0,1} = 4 \dots 12 \quad (68)$$

A key difference is the monotonic decreasing behavior the spot size as a function of mirror position of all considered scanned focused spot diameters. The interplay between Rayleigh length and beam effective f/# are apparent as evidenced by the varying crossover points between the larger and smaller spot size diameters however the effect is greatly reduced. Additionally, as the focused spot size become smaller, the overall slope of the spot size curve drops and the spot size on target becomes nearly uniform in its distribution.

4.4.4D Quasioptical computation: Coupling coefficient

The beam coupling coefficients for the two-mirror scanning system were computed with equation (10)-(14) and (64) where the reference plane was defined as the scanning mirror plane (Figure 4-11). The coupling efficiencies (Figure 4-12(b)) are all monotonically *increasing* as a function of mirror radius which contrasts with the previous design case where every curve is monotonically *decreasing*. This result stems from varying collimated beam parameters produced as a function of scan location.

Of note is the decrease in peak and mirror radius integrated average coupling coefficient in the angular scanning system as compared to the rectilinear scanning case. The angular scanning system produces a superior radii of curvature profile for nearly all the considered spot size diameters which suggests that it should achieve superior coupling. This is likely due to the apparent sensitivity of the coupling coefficient to beam Rayleigh length. However, the denominator of Equation (20) includes ratios of input and output spot sizes and input and output radii of curvature. These parameters did not change significantly in the collimated section of a beam path but can change rapidly over short distances in the converging/diverging parts of the beam path. These issues suggest that the angular scanning system may be more difficult to couple to a transceiver system and/or more sensitive to misalignment; an issue that was explored in section 4.4.6.

4.4.4E Quasioptical computation: Radius of curvature

The radii of curvature of the beam immediately prior and following reflection from the cornea are displayed in Figure 4-12(e) and (f) respectively. Two of the curves (2.04 mm and 1.64 mm) rapidly approach $-\infty$ for increase R and confirm that the beam waist goes from inside the cornea to outside the cornea. However, the remaining curves remain finite and negative for the entire mirror range indicating a beam waist inside the cornea. Additionally, as the beam gets smaller, the radius of curvature plot converges to a flat curve that is effectively invariant to mirror position. For example, 0.68 mm and 0.74 mm radius beams produce a radius of curvature, immediately prior to the cornea, of -10 ± 0.3 mm and -11 ± 0.3 mm respectively confirming that the variable beam diameter system produces geometric optics like performance at small input beam diameters that resembles a point source.

The output beam radius of curvature in Figure 4-12(e) is consistent with what is expected from the radius matching in Figure 7(e). The radii of curvature of the small input beam diameters are largely unperturbed. In contrast, the largest beam diameters with beam waists that traverse the corneal surface behave the same as those in the rectilinear scan system.

4.4.5. Double mirror (angular) scanning: Physical optics analysis

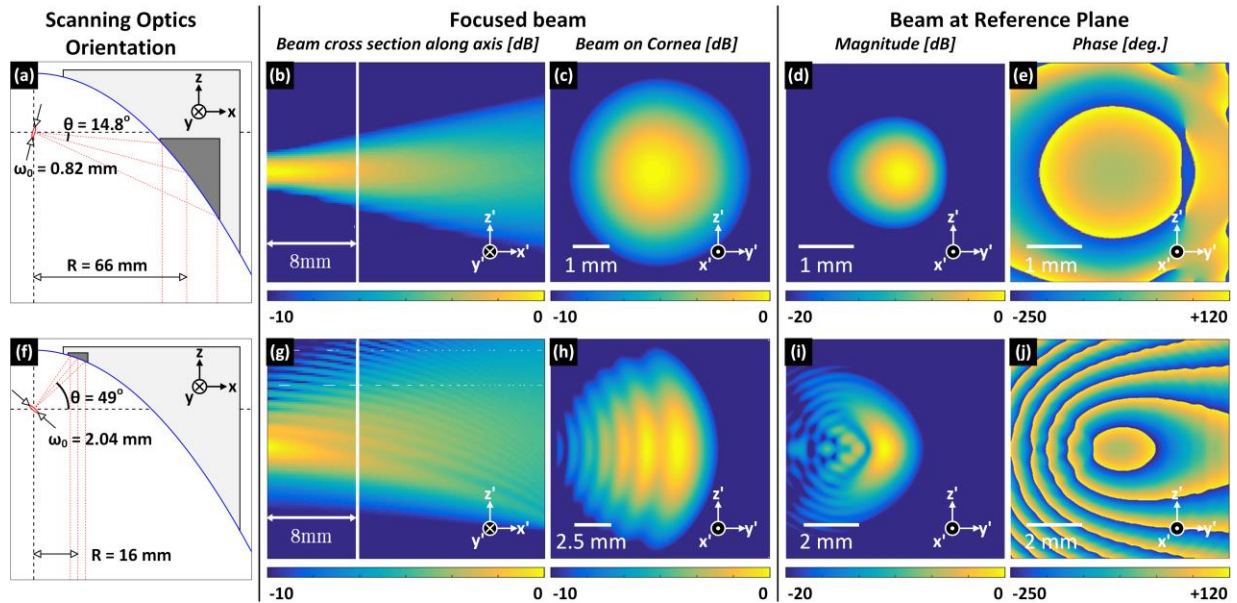


Figure 4-13. Field distribution computed with Physical Optics method for 2-mirror imaging system.

- (a): Layout for $\theta = -14.8^\circ$ ($R = 76.9$ mm) and $\omega_0 = 0.82$ mm.
 - (b): Cross section of beam in the $x'-z'$ plane. section
 - (c): Beam profile on the $y'-z'$ plane tangent to the cornea and coincident with the intersection of the focused beam centroid and corneal surface.
 - (d), (e): Electric field magnitude (d) and phase (e) of the beam at the reference plane ($x-y$ plane) following reflection from the cornea and re-collimation from the imaging mirror.
 - (f): Layout for $\theta = +49.0^\circ$ ($R = 76.9$ mm) and $\omega_0 = 2.04$ mm.
 - (g)-(j) are same as (b)-(e).
- Note that in configuration (a) the fields are nearly Gaussian while in configuration (f) they are not due to the offset reflector configuration and possible diffraction.

4.4.5A Spot size

Physical optics analysis is also applied to the 2-mirror imaging system. Analogous to Figure 4-9, the outcome of two specific configurations are shown in Figure 4-13 [107]: A small input beam waist paired with a large scan radius (Figure 4-13 (a)) and a large input beam waist paired with a small scan radius (Figure 4-13(f)). These configurations respectively resulted in a large scan radius paired with a larger scan diameter and a small scan radius paired with smaller beam diameter.

The larger beam diameter and reduced reflector asymmetry about the beam centroid represented by the configuration in Figure 4-13(a) results in a focused beam with limited Gaussian mode content both in the $x'-z'$ and $y'-z'$ plane. The configuration in Figure 4-13 (f) resulted in substantial beam diffraction and significant beam asymmetry as a result of the short Rayleigh length of the collimated beam following reflection from the initial OAP. However, the focused beam waist is still nearly coincident with the cornea CoC, thus supporting the partial optimization behavior predicted by ray tracing.

The physical optics results are superimposed with a square marker (\square) in Figure 4-12(a) and the differentials represented in Figure 4-12 (c). One immediate difference from the rectilinear scanning system is that the physical optics analysis predicts a spot size smaller than that predicted by physical optics for any input pair. The analysis also indicates that the two analysis methods converge as the input beam radius decreases.

4.4.5B Coupling efficiency

The reflected beam magnitude and phase at the reference plane is displayed in Figure 4-13(d)-(e) and Figure 4-13 (i)-(j). Quasioptical analysis predicts high coupling efficiency for the configuration in Figure 4-13(a) and this is confirmed with a high radial asymmetry in the magnitude and the relative uniformity of the phase across the majority of the beam. Similarly, the configuration in Figure 4-13 (f) to result in poor coupling between input and output beams and this prediction is supported by the beam asymmetry, multiple beam extrema, and substantial field curvature indicated by the phase plot. The physical optics results are superimposed with a square marker (\square) in Figure 4-12 (b) and the differentials represented in Figure 4-12(d). Similar to the

beam radius results, physical optics predicts a coupling efficiency that is higher than the quasioptical analysis for any input beam radius and angle.

4.4.6. Alignment sensitivity - Optical system POV analysis

Returning to the original concept of this spherical surface imaging method, this technique relies on accurate alignment of the target's center of curvature to the focus of the imaging optics. It is important to develop robust methods to align the target to the imaging system. Because the center of curvature of the cornea is inaccessible in the open space, target alignment may use known geometrical and visual features of the target for best alignment. Nevertheless, the imaging system must afford some level of tolerance to the misalignment of the target for a practical usage. Therefore, it is necessary to understand the sensitivity of the system to the alignment of the target, and how can the optical design of the system be optimized to improve misalignment tolerance. If we are to thoroughly consider signal acquisition characteristics for the entire imaging field, there are at least three degrees of freedom (x- y- z- misalignment of the cornea) for each pixels in the image and the analysis becomes quickly complicated. To begin, we performed an optical path analysis to provide a metric of alignment sensitivity.

4.4.6A Analysis set up

Signal sensitivity as a function of target misalignment was explored for the rectilinear and angular scanning systems with non-sequential ray tracing (ASAP, Breault Inc.). The systems were arranged as shown in Figure 4-6 (rectilinear scanning system) and Figure 4-10 (angular scanning system) with the optical elements placed at the minimum allowable separation thus reducing the free space path length for each optics train. A reference reflector with an 8 mm RoC was placed with its CoC coincident with the focal point of the focusing/scanning mirror in each system. The detector was modeled as a circular aperture measuring 2 mm on a side thus mimicking the zero bias Schottky diode package used in the actual implementation. The source was modeled as a

pencil beam with a 2° divergence angle corresponding to the 26 dB directivity output of a circular feedhorn. This produced a ~ 10 mm collimated beam radius.

In both systems, the scanning mirrors were positioned such that the centroid of the focused beam was collinear with the optical axis of the reference reflector. Then the rays from the source were traced to the corneal surface, reflected, and traced back towards the receiver. The total flux intercepted by the detector aperture in each system was quantified and defined as the reference level of each perfectly aligned system.

The reference detector position was then displaced transversely in two dimensions in a plane defined by the surface normal to the mirror and corneal optical axes and coincident with the reference reflector apex. The concept is demonstrated pictorially in Figure 4-14(a) where the transverse plane is denoted by the axes X' and Y' . The plane was 1.2 mm x 1.2 mm and discretized into a set of points with 0.2 mm center to center separation. At each transverse location, the source rays were retraced through the system and the total flux normalized by the reference flux to ascertain relative reductions in collected signal as a function of decentration.

The results of the simulation for the rectilinear scanning and double angular scanning systems are shown in Figure 4-14(b) and (c) respectively where the axes correspond to the deviation between the reference reflector optical axis and focused beam centroid and the colorbar corresponds to the relative collected flux. The angular scanning system demonstrated a substantial increase in sensitivity to non-optimal alignment as compared to the rectilinear system characterized by a full width half max (FWHM) of 0.4 mm x 0.25 mm and ~ 0.8 mm x 0.8 mm for the angular and rectilinear systems respectively. The apparent asymmetry in the beam collection efficiency of rectilinear system is due to the overall asymmetry of the system using only one OAP

mirror for the scanning function. This is in contrast to the mirror symmetry along both axis in the angular system as a result of the matched mirrored configuration of the OAP mirror pair.

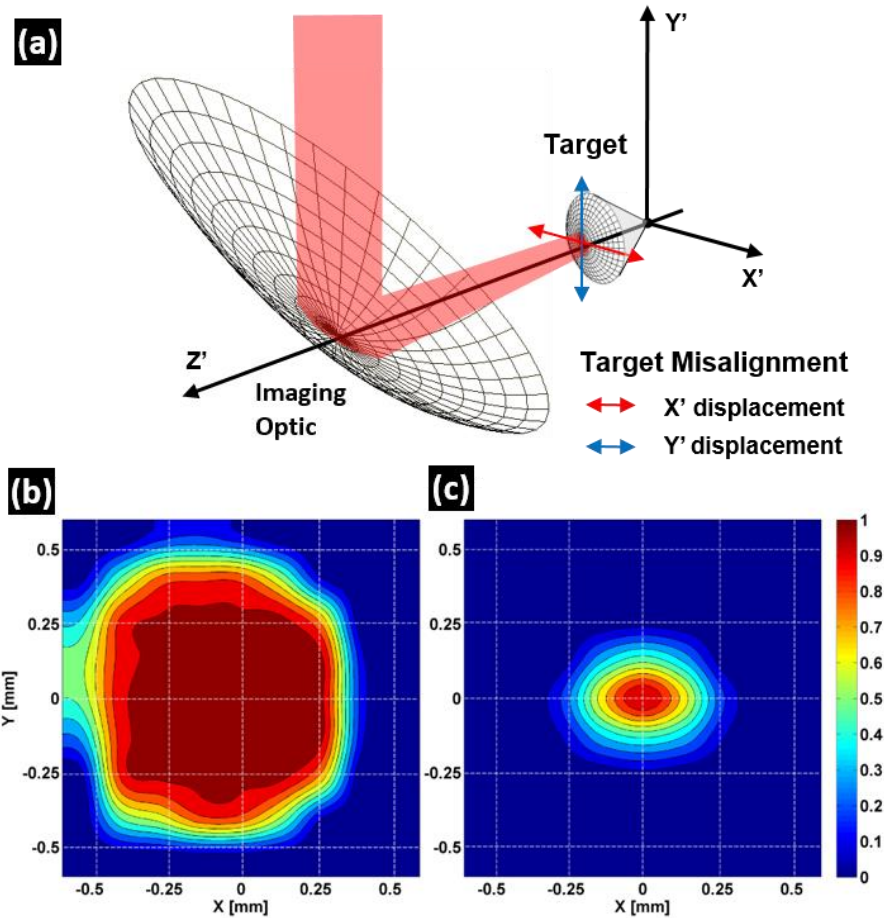


Figure 4-14. Target alignment tolerance gauged by observing signal distribution at the detector.

(a) The cornea is displaced from the ideal location in X' and Y' transverse plane, simulating decentration of the patient's cornea. An estimate of coupling efficiency was computed by tabulating the fraction of returning beam cross section collected by a circular detector aperture with 2 mm edges, placed at the "detector" location indicated in Figure 4-10 and Figure 4-11. Coupling efficiency is plotted by the location of the target for rectilinear scanning configuration. (b) Rectilinear scanning (c) angular scanning. The asymmetry apparent in rectilinear case is due to the overall asymmetry of the system using only one imaging mirror.

With consideration of the two-pass path, the rectilinear system beam path interfaces with four (x4) parabolic mirror surfaces while the angular scanning system interfaces with eight (x8). When an OAP mirror focal point is misaligned with the target surface the collected beam can be collimated on a path not parallel with the optical axis of the mirror and resulting in a transverse

walk-off of the beam after focusing from a subsequent OAP and/or complete beam walk-off in the collimated beam path.

It is important to note that the ray tracing simulation does not take into consideration field and beam pattern matching and therefore serves as both an upper bound on alignment sensitivity and, more importantly, a relative analysis between the systems that should give a good indication of trends computed with physical optics. Although the rectilinear system is inherently slower than the angular system and scanning speed is of critical importance, we believe that alignment issues justify the use of this design in our study.

4.4.7. Angular-Scanning System: Discussions

The preliminary alignment sensitivity suggests that having additional reflective aspheric elements in the beam path resulted in substantial increases in alignment sensitivity compared to the rectilinear design. This singular but critical challenge prompted us to implement the rectilinear scanning system first for proof-of-principle efforts. However, alignment problem can be addressed with the following. 1) Further reduction of the beam path and optimizing the choice of imaging OAP mirrors will help reduce beam-displacement behaviors that leads to narrow alignment tolerance. 2) The transceiver system can be designed to accept moderate displacement of the returning beam by optimized antenna design. For a wide scale clinical trial to evaluate the utility of THz based CTWC diagnostics will require high speed image acquisition made possible by, e.g., the angular scanning system. This effort to may be further assisted by incorporating THz imaging system technology with existing VIS/NIR based eye tracking technology; an engineering task the team is currently pursuing in earnest

4.5. THz Corneal Imaging System: System engineering, implementation, and image reconstruction

4.5.1. Coordinate transformations, Mapping, and Sampling Schemes

A set of simple geometric transformations defines the mapping from the scanning coordinate to the location on the target surface. The forward mapping from the transverse rectilinear coordinates of the parabolic mirror clear aperture (x, y) to the spherical coordinates of the cornea (θ, ϕ) are given in equations (69) and (70). The reverse mapping from the spherical coordinates of the cornea (θ, ϕ) the transverse rectilinear coordinates of the parabolic mirror clear aperture (x, y) are given in equations (71) and (72).

$$\theta = \frac{\pi}{2} - \tan^{-1} \left(\frac{\sqrt{x^2 + y^2}}{4f_p} - \frac{f_p}{\sqrt{x^2 + y^2}} \right) \quad (69)$$

$$\phi = \tan^{-1} \left(\frac{y}{x} \right) \quad (70)$$

$$x = 2f_p \cos(\phi) \left[\tan \left(\frac{\pi}{2} - \theta \right) + \sec \left(\frac{\pi}{2} - \theta \right) \right] \quad (71)$$

$$y = x \tan(\phi) \quad (72)$$

These relations perform both conformal and orthogonal mapping from the sampling coordinate to the target surface angular coordinate. f_p is the parent focal length of the parabolic mirror, whose focal point is at $(0, 0, f_p)$ and the parabolic vertex is coincident with the origin. The mapping assumes that the cornea is a spherical surface and that the input beam is perfectly collimated thus there is no dependence on the height, z , above the mirror and no dependence on the corneal radius of curvature R_c . All rays reaching the target surface are orthogonal to the local spherical surface. Therefore, each pixel position on the target can be fully described by the azimuthal (ϕ) and elevation (θ) angles corresponding to any pair of (x, y) coordinates.

Three different sampling grids were considered for the system and these are displayed in Figure 4-15(a)-(f) for a 76.2 mm CA, 25.4 mm PFL, 90° OAP imaging mirror. The placement of the

mirror in the coordinate follows the set up in Figure 3-1 and Figure 4-5: The vertical axis in the plots of the OAP mirror clear aperture corresponds to the x-axis and the horizontal axis corresponds to the y-axis. The mirror clear aperture axis is parallel to the z-axis and pierces the xy plane point $(x, y) = (2f_p, 0)$. The apex (center) of the cornea is pierced by the x-axis and the axis defined by its radial symmetry is collinear with the x axis. In spherical coordinates the apex of the cornea is located at $(R, \theta, \phi) = (8 \text{ mm}, +90^\circ, 0^\circ)$.

The sampling grid displayed in Figure 4-15(a) is termed “Equiangular scanning” and is the implementation of equal increments (10°) in both the θ and ϕ directions represented by the blue “vertical” traces and red “horizontal” respectively. The corresponding mapping back to the mirror clear aperture x-y plane is displayed in Figure 4-15(a). The black circular markers (\bullet) represent the intersections of the θ -scan ϕ -scan lines that intersect within the aperture of the OAP. The fixed- ϕ (isoazimuthal), varying- θ curves are mapped to straight lines, distributed radially, in the aperture space that intersect $(x, y) = (0, 0)$. The fixed- θ (isoelevation), varying- ϕ curves (latitude) are mapped to circles in the x-y plane where the radii were calculated with Equation (71) and $\phi = 0$.

The mapping of the equiangular scanning confirms that the beam scanning must be the densest towards the mechanical axis of the mirror CA and then progressively less dense as the beam is moved radially outward from the corneal center of curvature. This observation is consistent with the optical power of the OAP which is inversely proportional to the distance from the parent focal point (R_s). Figure 4-15(a), (b) also serve as a pictorial justification of orienting the mirror and the optic such that the mirror focal axis pierces the $(\theta, \phi) = (+90^\circ, 0^\circ)$ instead of the standard $(\theta, \phi) = (0^\circ, 0^\circ)$. Equiangular scanning about the $(0^\circ, 0^\circ)$ point results in a substantial decrease in sampling density as the beam is traversed from the corneal apex to the periphery. This sampling density

variation is significantly higher than that achieved with the $(90^\circ, 0^\circ)$ orientation and at this point in the development it is prudent to somewhat reduce the spatial bias.

The sampling grid in Figure 4-15(c) and (d) is termed “orthodromic” and is a modification of the equiangular scanning. In this sampling distribution the circular paths described by scanning ϕ at a given θ (red latitude lines in Figure 4-15(a),(b)) are replaced by orthodromes which are defined as a set of curves on the surface of a sphere that are formed by the intersection of the sphere and a plane that is coincident with the sphere center point. In spherical coordinates all longitudinal lines are orthodromes while only one of the latitude lines (equator) is an orthodrome. The orthodrome-scanning grid replaces the latitude scan paths with orthodromes that are defined by a sphere of radius 8 mm (cornea) and the intersection of a plane defined by the following three points, where point P3 defines the angle the plane makes with the z-axis. The spherical coordinates defining the orthodromic scanning path is described by equation (73).

- P1: $(R_C, \theta, \phi) = (8, 90^\circ, -90^\circ)$.
- P2: $(R_C, \theta, \phi) = (8, 90^\circ, +90^\circ)$.
- P3: $(R_C, \theta, \phi) = (8, \theta_0, 0^\circ)$.

$$\theta = \cot^{-1} \left(\tan \left(\frac{\pi}{2} - \theta_0 \right) \cos(\phi) \right), \forall \phi \in [-\pi, \pi] \quad (73)$$

The “latitude” orthodrome scan lines mapped to the OAP mirror CA plane are similar to the equiangular scan latitude lines with a comparative increased curvature closer to the mirror focal point decreased curvature at the extreme periphery of the mirror aperture.

The utility of the orthodromic-scanning is most readily apparent for spot size characterization of spherical “knife-edge” targets. Consider the intersection of every “latitude” with the longitude curve at $\phi=0^\circ$. At any given intersection point the tangent lines of both curves are perpendicular and coplanar. Now consider a spherical knife-edge target constructed of one dielectric hemisphere

and one metallic hemisphere. If the interface of the two hemispheres is coplanar with the $\phi=0^\circ$ longitude curve, then all orthodrome beam paths will be perpendicular to the metal-dielectric interface and the measured knife edge response will be the true knife edge response of the beam.

The final sampling grid considered is termed “Uniform-rectilinear” and is described in Figure 4-15(e),(f) with the uniform, rectilinear in Figure 4-15(e) mapped onto the corneal spherical surface in Figure 4-15(f). This sampling grid results in significant sparsity of sampling points towards the bottom section of the cornea. This sampling grid is the most straightforward to implement for linear translation stages and thus its sufficiency at resolving the equiangular and orthodromic scanning schemes was considered.

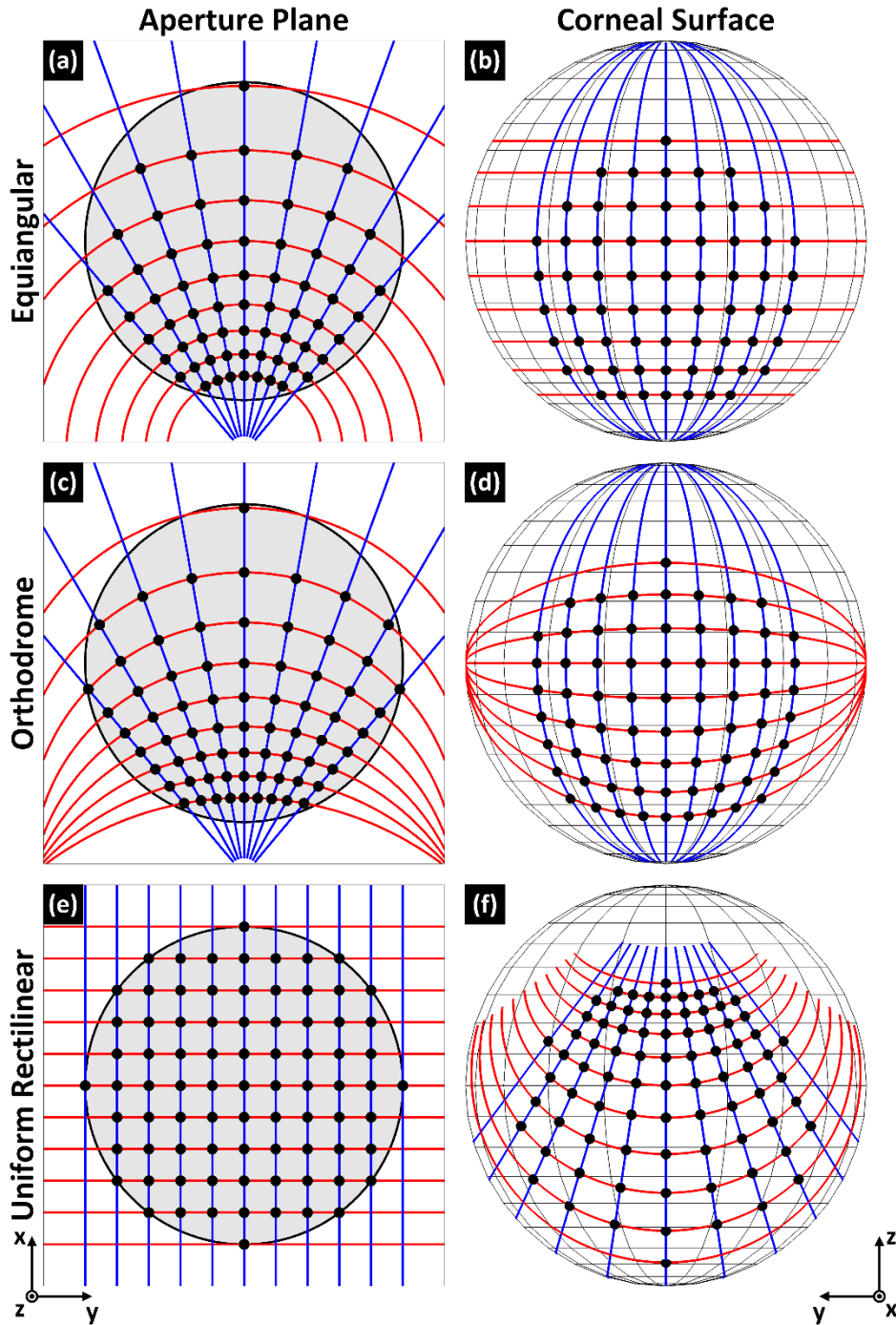


Figure 4-15. Sampling scheme mappings between a 90° , 76.2mm CA, 25.4 PFL OAP imaging mirror and an 8 mm RoC sphere (cornea).

Equiangular sampling in the (a) mirror clear aperture space and (b) corneal (spherical) space. Orthodromic sampling in the (c) mirror clear aperture space and (d) corneal (spherical) space. Uniform Rectilinear sampling scheme in the (e) mirror clear aperture space and (f) corneal (spherical) space. The black circle markers (\bullet) correspond to scan line intersections that fall within the mirror CA.

4.5.2. System implementation

A prototype system was constructed using a solid-state frequency-modulated continuous wave THz source (Amplifier-multiplier chain, Virginia Diodes, Virginia) with a frequency tuning range between 650 GHz-680 GHz. The detector was a WR1.5 waveguide mounted Schottky diode detector (ZBD) (Virginia Diodes, VA) with a 500GHz-700GHz detection bandwidth. Both the source and detector were coupled to diagonal feedhorn antennas with 26dB of gain and aperture dimensions of 2.4 mm x 2.4 mm. Because of the high coherence of the source and specularly of the cornea, a significant standing wave can be generated between source, target, and detector and observed as large variations in return signal as the scanning mirror position changes the total optical path length. To mitigate standing waves, the output was frequency modulated over ~2 GHz at a rate of 100 KHz, providing a frequency bandwidth that exceeds the expected full etalon period of the optical path. The source was also amplitude modulated at ~900 Hz and the rectified signal from the ZBD was detected with a Lock-in amplifier (Stanford Research Systems, CA) using an integration time of 3 milliseconds (ms). These parameters are summarized in the block diagram of Figure 4-16(a).

The optical layout of the system is similar to the original design shown in Figure 4-7. 25.4 mm PFL, 76.2 mm CA, 90° OAP mirrors were used to collimate radiation from the multiplier chain and focus reflected radiation into the detector aperture. The combination of feedhorn directivity and OAP PFL yielded a collimated spot 1/e field radius of ~ 10 mm as measured with a knife edge target. The focusing objective mirror was a 76.2 mm CA, 25.4 mm PFL OAP. Beam scanning was performed with two 50.8 mm diameter gold coated plane mirrors. A CAD design of the system and an image of the constructed system are shown in Figure 4-16(b) and (c) respectively.

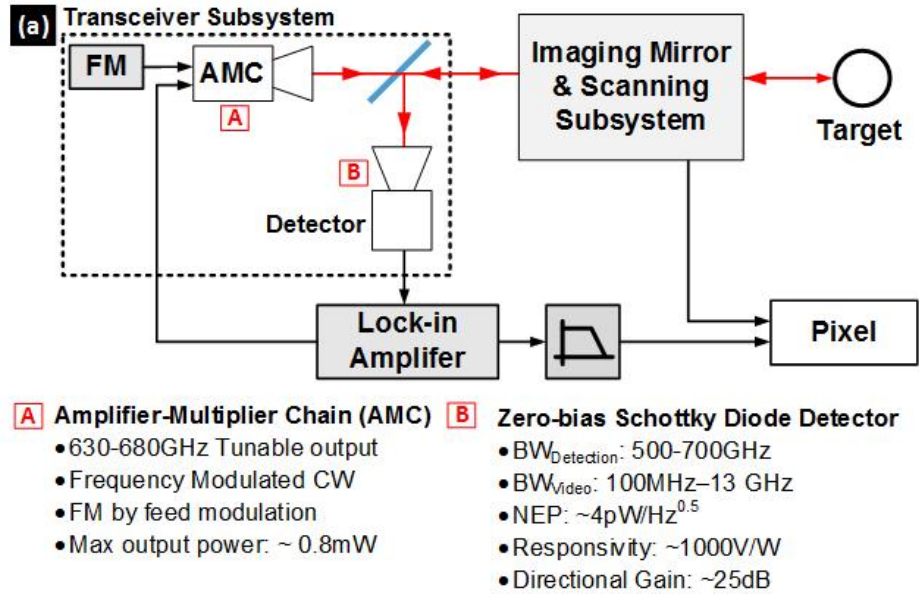


Figure 4-16. Non-contact THz imaging system implementation.

(a) Block diagram of the imaging system employing frequency-modulated CW THz source, zero-bias Schottky diode detector, and lock-in detection scheme. (b) CAD rendering (left) and (c) photograph (right) of the scanning imaging system. The imaging mirror is mounted on x-y microscope stage and can be positioned to the target location with full precision (indicated by red arrows).

The total coverage of a spherical surface obtained with the 25.4 mm PFL, 76.2 mm CA, 90° OAP is detailed in Figure 4-17 where the gray contour is the extent of the cornea and the black contour is the mapped CA of the scanning OAP and hence the coverage. These contour lines are superimposed on a set of mapped orthodrome scan lines that subtend the entire extent of the mirror.

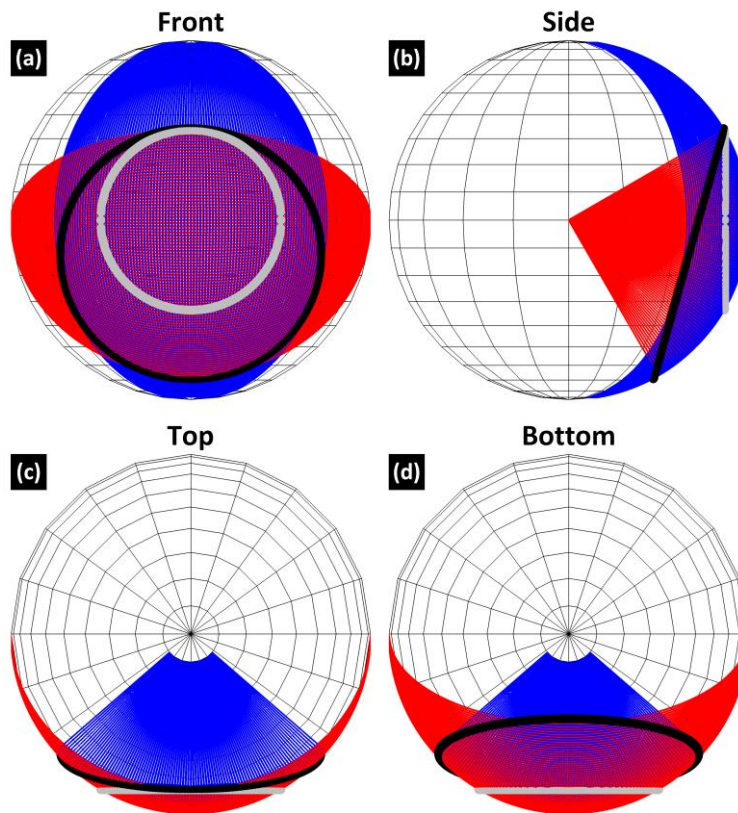


Figure 4-17. Corneal coverage by 76.2 mm CA, 25.4 PFL OAP.

The black circle on the surface denotes the mapped CA of the OAP. The gray circle denotes the extent of the cornea. Othodromic scan lines that span the extent of the mapped mirror aperture are shown in red and blue. (a) Front, (b) side, (c) top, and (d) bottom views.

4.6. Imaging Results

4.6.1. Imaging of characterization targets

The imaging operation is first demonstrated with three spherical targets with $5/16'' = 7.93$ mm radii of curvature, representing the geometry of an average human cornea: (1) A brass sphere to evaluate the uniformity of the FOV and its relation to the modeled coupling efficiency. (2) A polypropylene sphere with a 3 mm wide strip of Aluminum tape positioned such that the center of the strip was collinear with an orthodrome of the sphere. This target was rotated 90 degrees between image acquisitions to confirm that the mapping and sampling distributions behaved as expected. (3) A bespoke “checkerboard” target that consisted of quarter sphere sections of polypropylene and brass. This target was intended to provide knife edge measurements in two orthogonal dimensions on one surface thus removing the need to realign/reposition for characterization along different axes. Cad drawings of the strip and checkerboard target are shown in Figure 4-18(a). The images were sampled using the uniform rectilinear grid pattern (Figure 4-15(e),(f)) with a 5 mm step size. The mapping of pixel data from aperture plane to sphere was performed by first up sampling the aperture space image and then performing the mapping operation described by equations (69) – (72).

The characterization target imaging results are displayed in Figure 4-18(b) where the top row is the visible image of the target and its orientation in the system, the middle row is the 2D image of the aperture plane, and the bottom row is the data mapped to a 7.93 mm radius sphere using equations (71), (72).

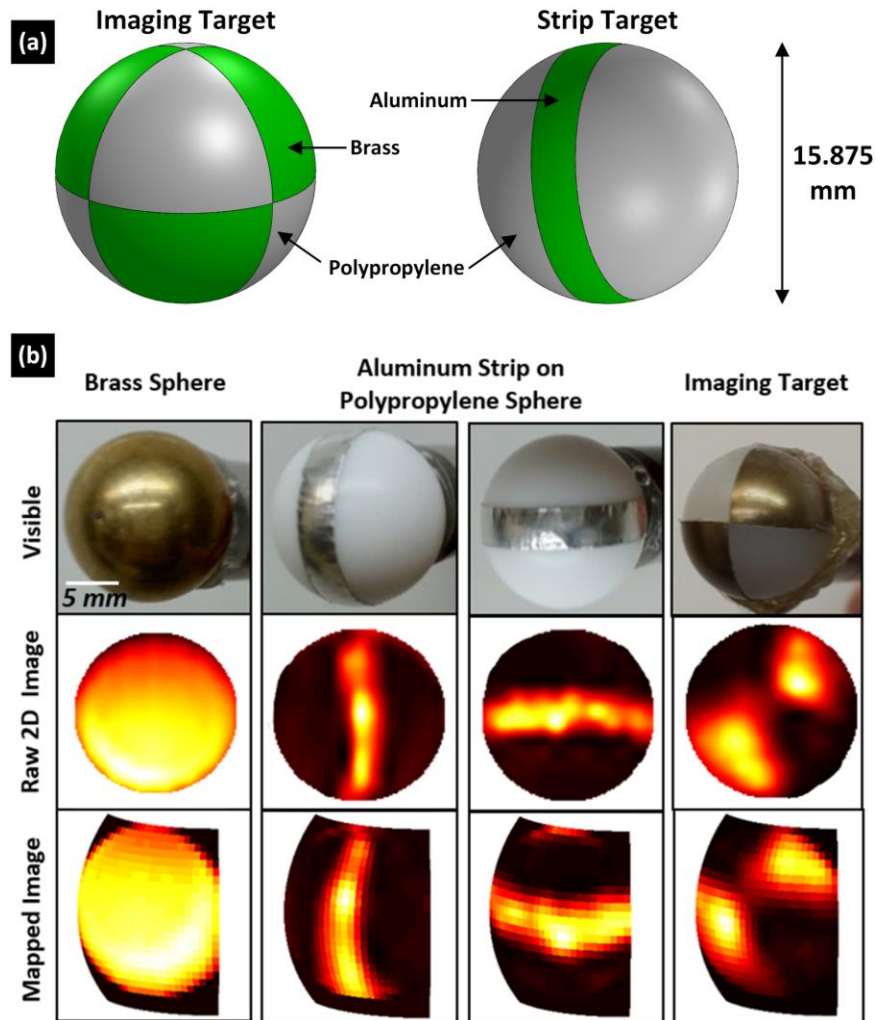


Figure 4-18. 650GHz of the characterization targets

(a) CAD drawings of characterization targets. (b) *top row*: visible images of characterization targets, *middle row*: aperture space image of characterization targets, *bottom row*: mapped images of characterization targets.

The image of the brass sphere displays an increase in signal from the top of the FOV to the bottom with a spatial gradient that is generally radially symmetric from target center of curvature. Assuming uniform reflectivity across the brass, this signal intensity is consistent with what was predicted by the coupling coefficient analysis in section 4.4. There are some breaks in the radial symmetry of the reflected signal on the outer periphery of the mirror which are likely due to diffraction arising from beam clipping and possible suboptimal alignment.

The vertically oriented aluminum strip displays similar behavior with the signal in the center of the strip generally increasing from the top of the FOV to the bottom with some local extrema in the signal. Additionally, the apparent strip width widens from top to bottom which is consistent with the expected increase in spot size (for a 10 mm input radius) as the radial distance from the target vertical axis and collimated beam centroid location is decreased (section VI of part A).

The mapped THz image of the horizontal strip maintains a fairly constant apparent thickness although there are also local extrema in the observed signal. Close inspection of the images reveals a slightly rough surface profile along both the center and the edges of the tape and we believe this is primarily responsible for the observed signal variation.

The checkerboard target serves as a clear demonstration of the asymmetry of the FOV about the OAP mirror optical axis. The intersection of the adjacent brass and polypropylene quarter spheres were aligned with the optical axis and this intersection is above the center of the FOV for the mapped image (bottom right of Figure 4-18). The edges also appear to be somewhat less sharp than that acquired with the Al tape strip target suggesting that the variation in edged height between dielectric and metallic regions strongly contribute to the overall contrast.

4.6.2. Imaging data fits to quasioptical and physical optics analysis

Model fits to data were applied to pixel values in the aperture plan space. The desired sampling locations on the sphere were defined and then mapped to scan trajectories on the aperture plane space. These scan trajectories were then superimposed on the aperture plan imaging data and image profiles along these trajectories were analyzed to determine coupling efficiency and resolution. All THz images in the mirror aperture plane space were masked to a circle with radius $A/2 - \omega_0$ to mitigate aberrations due to beam clipping.

4.6.2A Coupling Coefficient Fits

The brass sphere data was sampled with equiangular scan lines where the longitude and latitude was spaced at ~ 5 degrees and positions selected such that the majority of the ‘non-clipped’ clear aperture was visited. The brass sphere was assumed to have negligible variation in THz reflectivity across the imaged area and thus variation in measured reflectivity was attributed primarily to the expected variation in the quasioptical coupling coefficient derived with the quasioptical analysis in Part A. The coupling coefficient was expected to display radial symmetry thus equiangular scan lines were chosen for FOV sampling. The profiles extracted from the scan paths were then compared to Equation (75) for an input spot radius of 10 mm.

$$q_3 = \frac{A_3 q_0 + B_3}{C_3 q_0 + D_3} \quad (74)$$

$$K(q_0, q_3) = \frac{4}{\left(\frac{\omega_0}{\omega_3} + \frac{\omega_3}{\omega_0}\right)^2 + \left(\frac{\pi\omega_0\omega_3}{\lambda}\right)^2 \left(\frac{1}{R_3} - \frac{1}{R_0}\right)^2} \quad (75)$$

The latitude scan lines and their associated profiles are displayed in Figure 4-19(a) and (b) respectively where the coupling coefficient was assumed to be radially symmetric (independent of ϕ) and thus constant as a function of arc length. The scan paths in Figure 4-19(a),(b) corresponding

to the image profiles in Figure 4-19(c),(d) are color coded and the arrows in Figure 4-19(a),(b) denote the direction of increasing arc length which corresponds to the horizontal axis of Figure 4-19 (c),(d). Image profiles corresponding to the longitude scan lines in Figure 4-19 (a) are displayed in Figure 4-19 (c) and include a superimposed fit to equation (75). The image profiles were normalized to data obtained from a flat Al target placed such that the surface was coincident with the center of curvature of the brass sphere, and 0 reflection obtained by removing all targets from the imaging system.

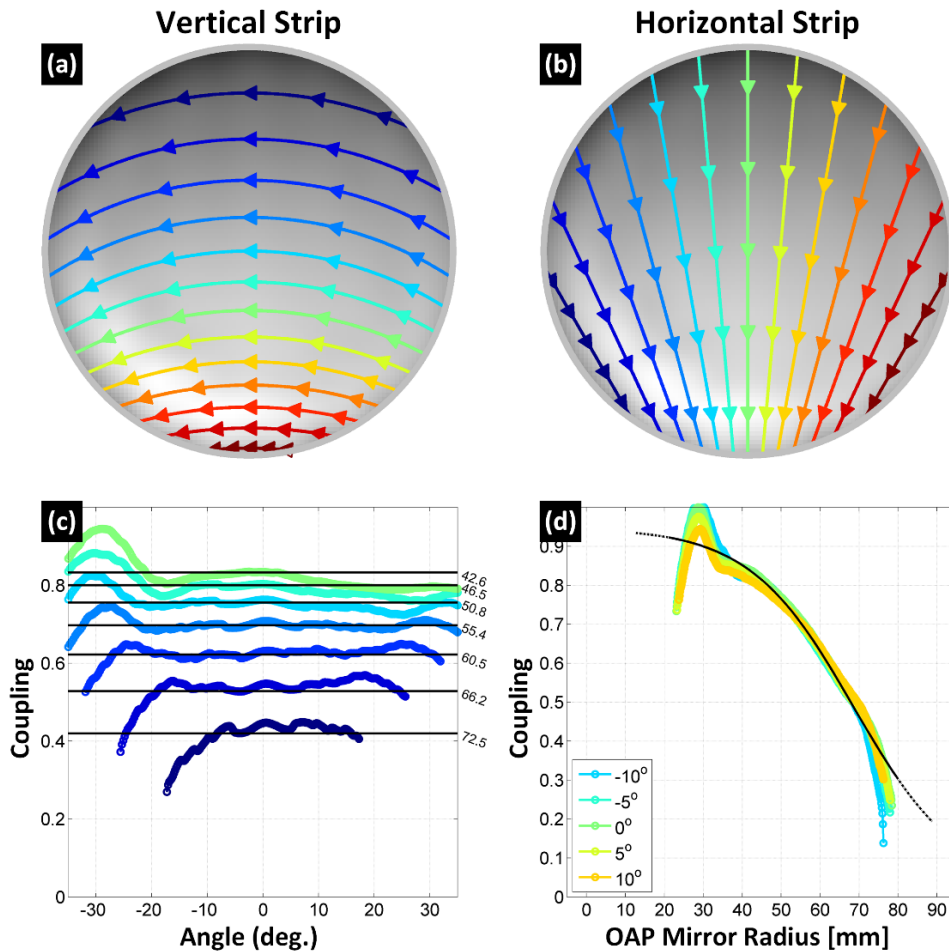


Figure 4-19. Imaging field analysis with uniform brass ball calibration target.

(a) Latitude (equiangular) scan lines superimposed on the imaging data, (b) Longitude (equiangular) scan lines on the imaging data, (c) latitude scan profiles, and (d) longitude scan profiles with fit to equation (75).

The coupling coefficient is dependent on four variable parameters: (1) input radius of curvature, (2) output radius of curvature, (3) input spot size, and (4) output spot size. The good agreement between theory and data between both the trends normalized return signal strongly support the utility of the quasioptical analysis. The deviation from theory at the extrema of each profile suggest that beam clipping may contribute significantly to the measured signal even at $1 \cdot \omega_0$ from the mirror aperture edge and these effects may be considered in future design iterations.

4.6.2B Aluminum strip target fits

The rotated Al strip images were analyzed with the orthodromic scan lines. These lines ensure that the scan path is always orthogonal to the reflectivity discontinuities (edges) of the target features.

$$\gamma(d) = 2(d_0 - d) \quad (76)$$

$$C_b(d) = A \left[1 - \Phi \left(\frac{\gamma(d) - D}{\omega_1} \right) + Q \left(\frac{\gamma(d) + D}{\omega_1} \right) \right] + B \quad (77)$$

Data from the Orthodromic profiles orthogonal to the center line of the bar in the vertical and horizontal positions (Figure 4-20(a) and Figure 4-20 (b) respectively) were fit to equation (77) which describes the convolution of a 1D Gaussian distribution of spot size ω_0 with a rect function of width D and center located at d_0 . The function $\Phi(\cdot)$ is the left sided integral of standard normal and the function $Q(\cdot)$ is the right sided integral of the standard normal. The variable d is the spatial arc length along the surface of the cornea. Offset parameters A and B were included to improve the fit. The “long” direction of the bar was much larger than the transverse extent of the focused beam so it was sufficient to model the data with an integral along one dimension.

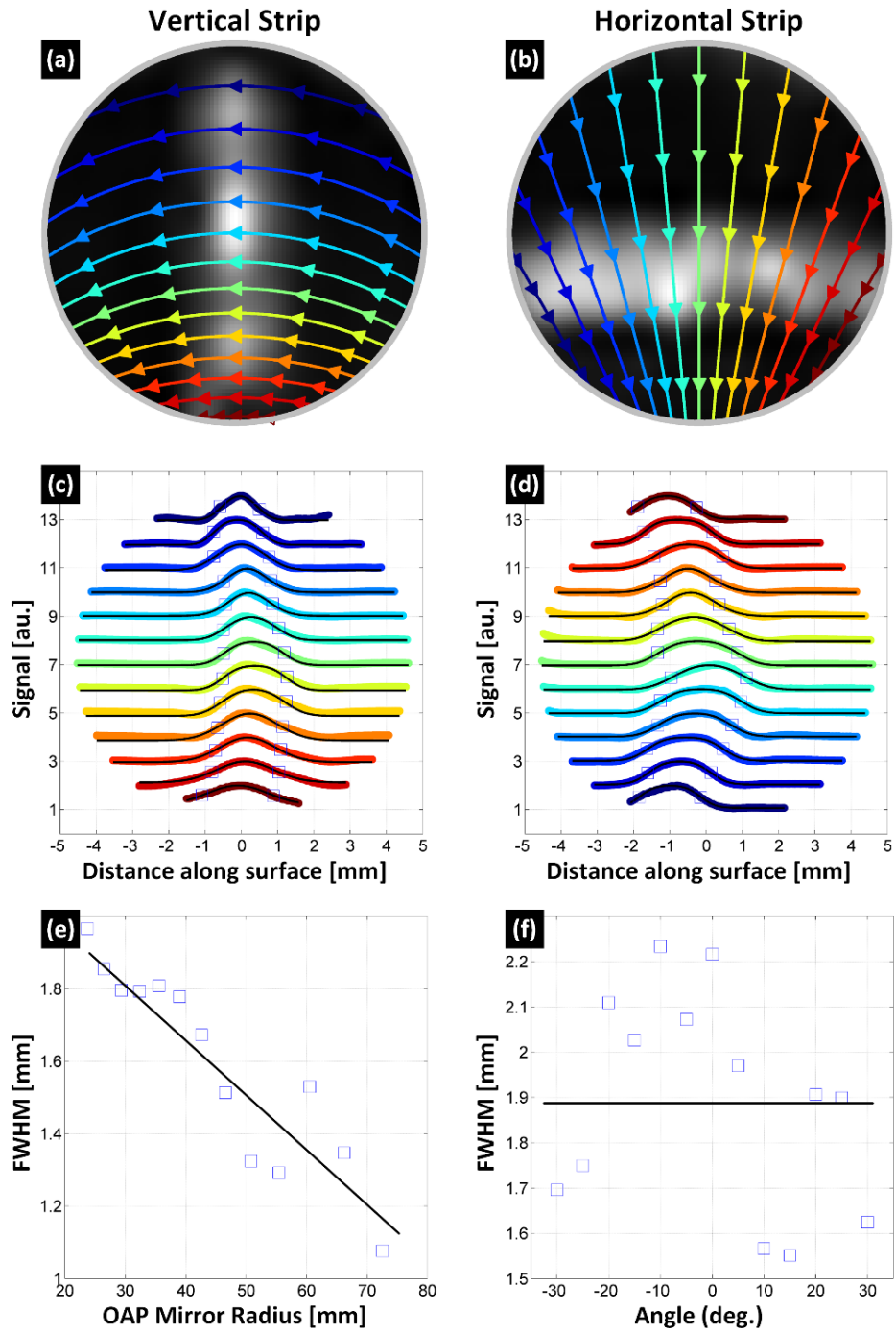


Figure 4-20. Imaging performance analysis with Al strip resolution target.

- (a): Orthdorme scan lines orthogonal to the vertical strip orientation,
- (b): Orthdorme scan lines orthogonal to the horizontal strip orientation,
- (c): Image profiles from the vertical strip orientation,
- (d): Image profiles from the horizontal strip orientation.
- (e): Extracted FWHM from the vertical strip orientation,
- (f): Extracted FWHM from the horizontal strip orientation

The profiles and superimposed fits are displayed in Figure 4-20(c) and Figure 4-20(d) for the vertical and horizontal orientations respectively. Additionally, the full width at half max (FWHM) as defined by the FWHM of equation (77) informed by the extracted fit parameters are demarcated (\square). As evidenced by Figure 4-20(e),(f) the extracted FWHM is substantially less than 3 mm (the width of the Al bar and thus lower limit of the convolved width) with the vertical bar FWHM ranging from 1.1 mm – 1.95 mm and the horizontal bar ranging from 1.55 mm – 2.25 mm. This is likely due to the geometric surface discontinuities between the Al tape and polypropylene ball. Wrinkles in both the tape surface and tape edges are visible in Figure 4-18(b) and we were unable to fabricate an optically smooth surface profile. As a result of large optical path lengths, we believe that when the tape surface normal is not parallel to the normal of the underlying spherical surface the beam walks away from the detector feedhorn. This behavior was also observed in the sensitivity analysis (Part A) and the end result was an effective tape thickness that is smaller than physical thickness.

The FWHM data from the fits to the vertical bar is plotted against mirror radius in Figure 4-20(e) with a least squares fit line superimposed on the data. While the FWHM are narrower than what was anticipated, the fits display a strong negative correlation between mirror radius (R_m) and measured apparent spot size; behavior consistent with that computed for in input field radius (ω_{in}) of ~ 10 mm. The extracted FWHM for the horizontal bar orientation are displayed in Figure 4-20(f) as a function of orthodrome angle with respect to the central orthodrome with the average of the data superimposed. The data demonstrates some variation but the correlation between spot size and angle is $\rho \sim 0.05$ supporting the expected independence of focused spot size over a large angle for a given scan radius.

Step response fits

The checker board images were also analyzed with orthodromic scan lines and the extracted image profiles were fit to equation (78) and (79) for rising edge and falling edge response respectively. Equation (78) and (79) describe the convolution of a Gaussian beam (field radius ω_0) with a unit step function centered at $d = d_0$. The amplitude factor A and offset B were included to maximize goodness of fit and Equations (78) and (79) are related by the equivalence in Equation (80).

$$C_{\Phi}(d) = A \cdot \Phi\left(\frac{2(d - d_0)}{\omega_1}\right) + B \quad (78)$$

$$C_Q(d) = A \cdot Q\left(\frac{2(d - d_0)}{\omega_1}\right) + B \quad (79)$$

$$C_{\Phi}(d) = -C_Q(d) + A + 2B \quad (80)$$

The horizontal orthodrome cuts and associated fits are displayed in Figure 4-21(a), (c), and (e). Eight cuts were analyzed comprising of the bottom and top regions of the FOV (labeled 1-8 in Figure 4-21(a)). The center ($\sim 2\omega_0$ width) area of the FOV was ignored to avoid artifacts due to the presence of the checker board corner.

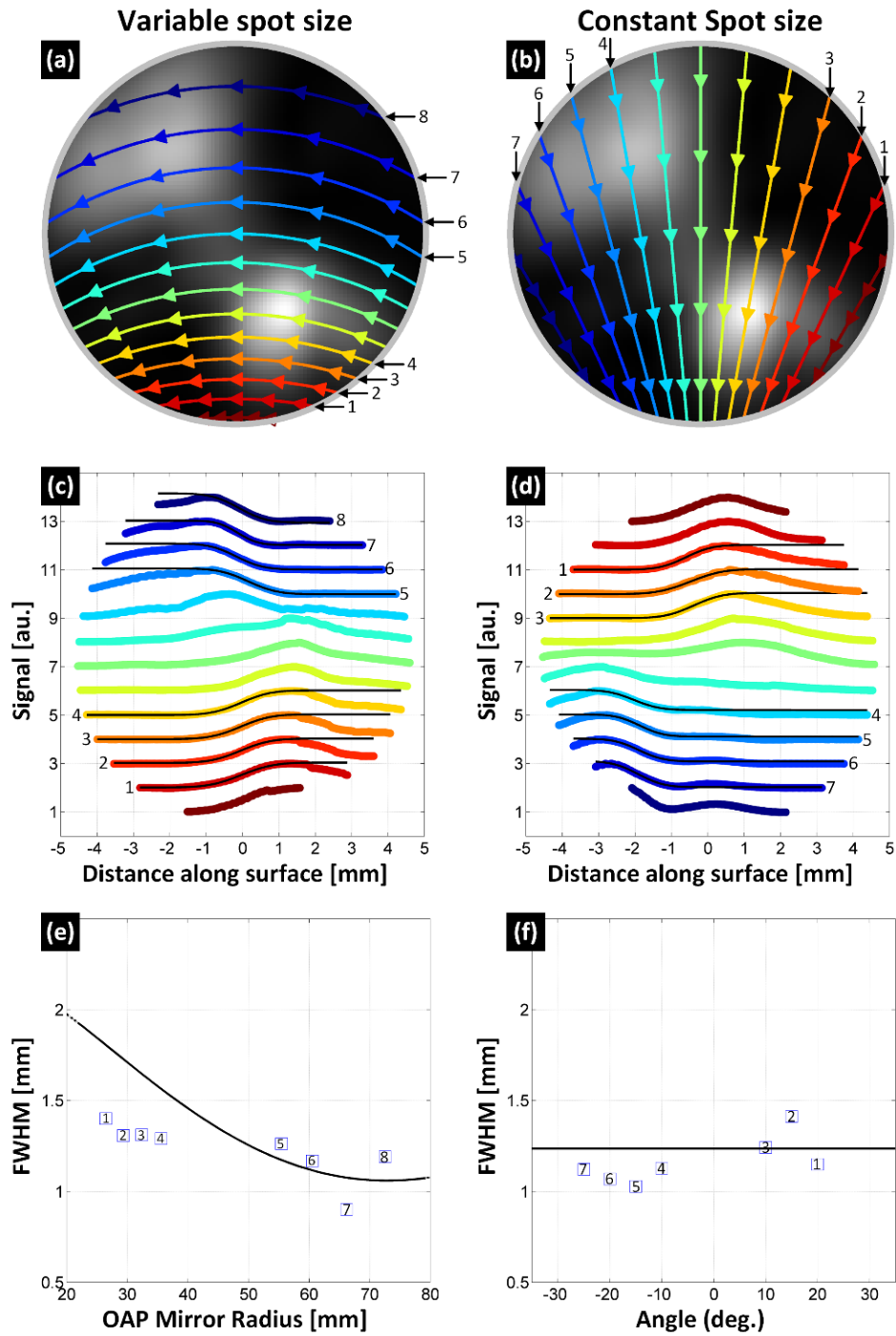


Figure 4-21. Imaging performance analysis with “checkerboard” target.

- (a): Orthodromic scan lines orthogonal to the vertical edges
- (b): Orthodromic scan lines orthogonal to the horizontal edges
- (c): Image profiles from the vertical edges
- (d): Image profiles from the horizontal edges
- (e): Extracted 1/e field radius from the vertical edges
- (f): extracted 1/e field radius from the horizontal edges.

The expected focused field radius for a collimated input beam of radius 10 mm (Figure 9, Part A) is superimposed on the extracted spot field radii (Figure 4-21(e)). The results are consistent with theory and demonstrate a maximum deviation from the focused spot radius curve of 0.473 mm and a standard deviation of 0.233 mm.

Closer inspection of Figure 4-21(c) reveal that for much of the image profiles the signal gradually falls off after the peak of the step response. The optical properties of the beam on target are radially symmetric and the circular lines of constant spot size and coupling efficiency are not co-linear with the orthodrome lines used to ascertain the spot size. A deconvolution of coupling efficiency will likely improve the fits.

Seven vertical orthodrome profiles and associated fits are displayed in Figure 4-21(b), (d), and (f) and, as in the previous analysis on the horizontal profiles, the center region was not analyzed. The extracted focused field radius is plotted vs orthodrome angle and the expected spot size at the mirror radius corresponding to the mapped target edge location is superimposed. There is a good agreement in fit between the measured data and the field radius computed with quasioptical analysis and the results support the relative invariance of the spot size to edges at the spherical target equator. The measured peak deviation was 0.175 mm and the standard deviation was 0.105 mm.

4.6.3. Characterization target limitations

The combination of path length of the optics train, low $f/\#$ of the OAPs, and high directivity of the source and detector resulted in a system that is sensitive to misalignment between the mirror focal point and corneal radius of curvature. This manifests as a sensitivity to surface discontinuities (geometric) which was observed in the characterization target data. The tape strip targets and, to a lesser extent, the checkerboard target both exhibited raised edges and uncontrollable surface roughness which confounded the acquisition of uncluttered resolution data. While these efforts reveal difficulties in characterizing the beam profile on target, there is little concern for these sources of performance degradation effecting *in vivo* corneal imaging as human cornea does not have sharp edges in the profile and the surface roughness ($\sim 15 \text{ um}$) [21] is minimal.

4.6.4. Corneal phantom

The hydration sensing capabilities of our system were demonstrated in time-lapse images of a cornea phantom (soft contact lens, chosen for their similar shape and hydration content as that of the cornea). A contact lens was immersed in water for 5 minutes prior to imaging and then gently placed on a polypropylene ball identical in size to the calibration brass ball target. Then it was left to dry while THz images were consecutively acquired over 30 minute period. THz images visualize the drying process of the contact lens from the thinner and exposed outer rim toward the center. This result is consistent with the predicted result by evaporation and diffusion, and it is similar to the process observed in drying of flattened ex-vivo cornea by [76].

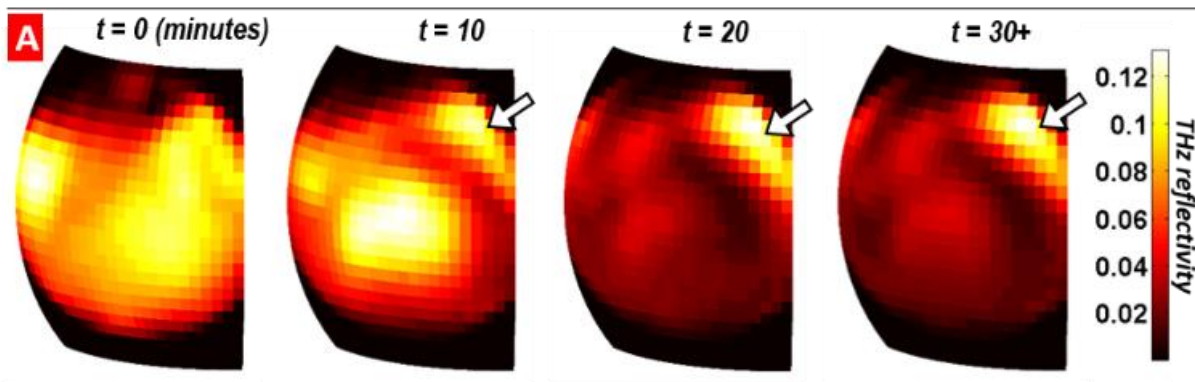


Figure 4-22. Time lapse Images of drying contact lens (Left to right).

A thin film etalon effect is observed due to the coherence of the source. A high reflectivity spot persists at the upper left corner as the contact lens is drying. We suspect that this is due to warping and rolling of the edges of lens as it dried, allowing a small airgap in between the contact lens layers and the polypropylene ball and producing larger effective impedance of the surface.

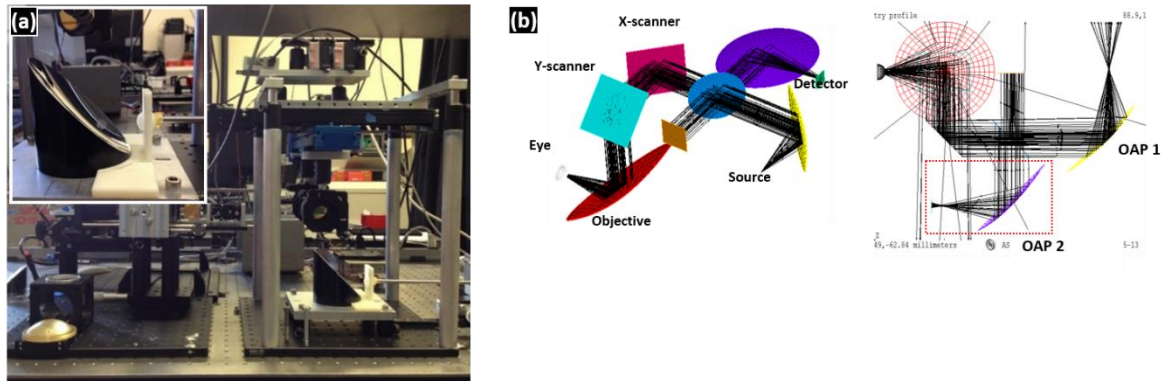
This experiment demonstrates THz reflectivity changes by hydration change are successfully captured by the imaging system. Overall good signal return from the entire extent of the contact lens surface suggests the imaging system can effectively perform imaging of the cornea target. In

this experiment, standing waves appear to be further suppressed due to the relatively low reflection coefficient of the target (~12%).

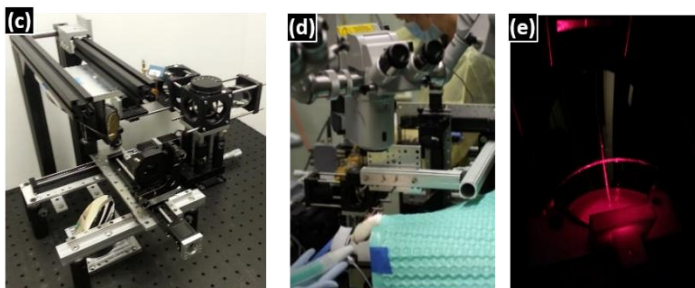
4.7. Conclusion: Non-contact THz Ophthalmic imaging system development

The challenges from our first *in vivo* imaging experiment and the shortfalls of existing THz imaging system designs motivated the development of the surface spherical imaging principle discussed in this section. The spherical shape of the target surface is projected onto the beam-scanning coordinate using an imaging mirror (off-axis parabolic mirror). A THz corneal imaging system employing this optical imaging concept is developed and tested. The unique imaging method also gave rise to a novel quasioptical analysis, which segments the imaging mirror according to the scanning beam location, and studies beam characteristic and receiver coupling performance. This analysis method is compared with full-wave simulations of the imaging system using the Physical Optics principle. With this approach, the full image transfer function of the system can be found with the quasioptical analysis method. For our first implementation of the system, an optimal input beam parameter is identified that minimizes the average focused spot radius on target.

2014 – First System Setup, Design Exploration



2015 - Refining system design & construction for animal studies



2016 – Readying the system for human imaging

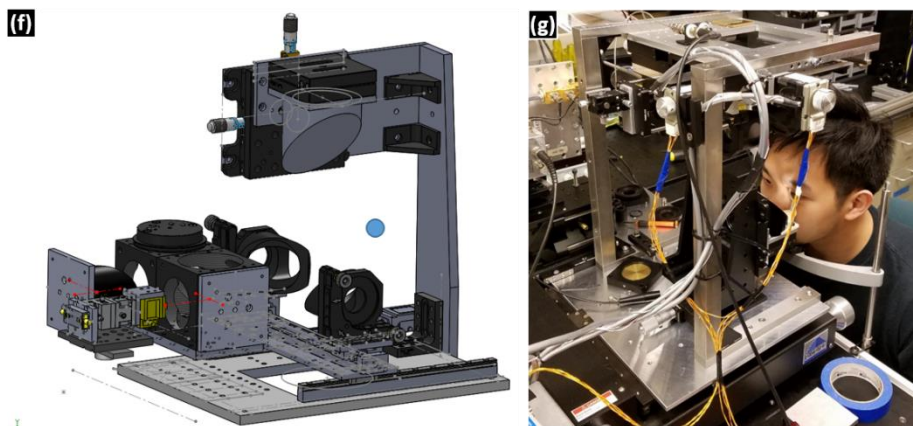


Figure 4-23. System Development timeline.

Our first implementation used a FMCW 650 GHz source and zero-bias Schottky diode detector. Image reconstruction is performed with three coordinate mappings and associated sampling schemes (Equiangular, Orthodromic, and Uniform Rectilinear). The imaging system hardware

design passed many iterations, improving in system robustness, imaging performance, reduced footprint, and many critical add-on devices that helped with alignment of the target. The system development timeline is shown in Figure 4-23. The first design focused on exploring the best component layout of the imaging optic and transceiver subsystem, helped by optical system modeling and analysis (Figure 4-23, (a,b)). In particular, beam distortion minimizing design rule outlined in Section 2.4.2 and source/receiver coupling design rule outlined in Section 2.4.3 were used. In the following year, the system design is further refined for the non-contact *in vivo* imaging study (Chapter 5). Most notably, this system iteration benefitted from using guiding lasers for optics and target alignment (Figure 4-23, (e)). For the feasibility of quick and efficient align-and-image procedure when working with living animals, we explored numerous design modifications and scanning system upgrade to achieve less than 1 minute acquisition time. The imaging system engineering further required optical design optimization and robust and practical human-machine interface. In addition, the human imaging system incorporated a second illumination wavelength at 100GHz. These efforts are outlined in the final chapter.

Chapter 5 : In vivo Imaging of Corneal Tissue in Human

The non-contact ophthalmic imaging system development lays the necessary groundwork for THz imaging in human. The last section of this work covers the following specific aims:

1) Hydration sensing capabilities of the THz imager must be tested in an *in vivo* model that incorporates a pathologically relevant disease model. Additionally, this second phase of the *in vivo* experiment investigates the effect of the tear film on the measurement.

2) The imaging system operation and study design must demonstrate sufficient experimental evidence for the safety of THz imaging. Data and conclusions from the most recent THz safety research consortium are taken into consideration when designing our own in-house THz eye safety experiment. This study is the first safety study done *in vivo* with a statistically significant number of subjects (N=10) and reflects the experimental conditions that will be used for our next phase of the study.

3) Additional imaging system engineering enables better interfacing of the imaging system with human subjects. Many improvements stem from the feedback from the previous animal imaging trials. Specifically, the first human imaging trial is made possible with a new imaging mirror parameter, a machine-vision assisted alignment camera, and a reduced image acquisition time (< 20 seconds).

5.1. Non-contact *in vivo* imaging study

An outstanding conclusion of the first *in vivo* experiment was that the non-surgical intervention method could not produce the intended CTWC changes. The procedure itself (application of dry heat and tear-producing eye drops) only induced the expected, rapid acute response in the animal, producing extra tears to maintain homeostasis that did not measurably alter the corneal thickness. Rather, it is suspected that corneal tissue gradually swelled because of the contact pressure on the tissue from the dielectric window. Therefore, a known mechanism of CTWC disturbance must be used to test the imaging system's ability to detect the CTWC change. Unfortunately, once again, there is no alternative to using *in vivo* models to observe relevant corneal hydration changes and tear film. An animal model that closely reflects the anatomy of the human cornea and human corneal disease pathology is necessary.

In this study design, CTWC perturbation is achieved by surgically damaging the Descemet's membrane, an endothelial layer immediately below the posterior stromal layer that plays a central role in CTWC equilibrium [110]. This procedure is commonly referred to as Descemet's membrane stripping, which is an intricate ophthalmic surgical procedure and a key step in cornea transplant surgeries. Damaging the Descemet's membrane emulates diseased/ malfunctioning of the endothelial layers and reflects the pathological basis of many corneal diseases. Descemet's membrane stripping results in inflammation and an influx of fluid into the stroma, resulting in a controlled increase in the water content of the eye without perturbing the cornea.

For THz illumination, a frequency-modulated continuous wave (FMCW) 650GHz source, used in the imaging characterization in section 4.6, was employed. Two key reasons motivated this frequency and device choice. First, the broadband output power of the PCS device (~50uW) was not expected to provide sufficient SNR in the non-contact system. The NE Δ WC of the system

discussed in section 3.4.1 was already more than 2%. Because of the non-contact system's coupling efficiency function (section 4.4.1), it is expected that the sensitivity of the system will further decrease from 2% if the same set of THz devices are used. In contrast, the FMCW device outputs nearly 1mW of average power. It is expected that improvements in the SNR of the system with a more powerful illumination source will better enable observations of hydration changes. Second, the 650GHz frequency choice provides sufficient imaging resolution to capture any local CTWC changes. Although a lower frequency band (100GHz – 300GHz band) offers more sensitivity and deeper penetration into the cornea, the imaging resolution with the non-contact system with the current optical design cannot provide imaging capabilities (< 3mm resolution) at frequencies below 400 GHz.

5.1.1. Descemet's Membrane Stripping (DMS) Experiment Protocol

The experimental protocol was developed under the review process by University of California's Institutional Animal Care and Use Committee (IACUC) (protocol #2013-087). Rabbits were handled under the care of a veterinarian staff throughout the experiment. The subject was placed under general anesthesia via an intramuscular injection of Pharmaceutical Ketamine (30 mg/kg) and Dexmedetomidine (.125 mg/kg). The animal was then intubated and the anesthesia was maintained with Isoflurane (1-5%). As needed, Pharmaceutical Grade pancuronium (0.1 mg/kg) was administered intravenously to prevent the cornea from descending during anesthesia. Administration of Pharmaceutical Grade Carprofen (4 mg/kg) prevented pain as a safety measure during the surgery. To provide bimodal anesthesia, a single dose of slow release (SR) buprenorphine (0.12 mg/kg) was administered intramuscularly prior to surgery.

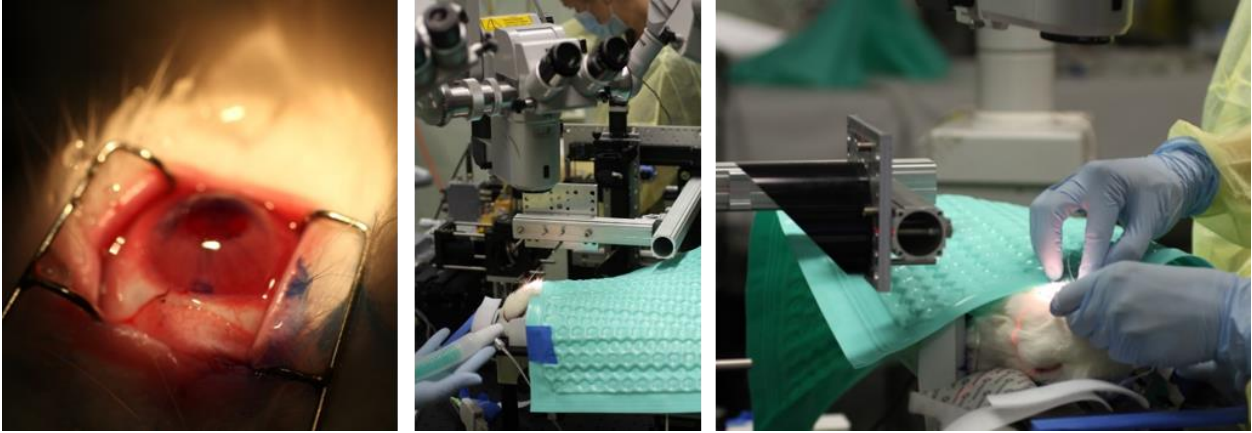


Figure 5-1. *In vivo* imaging study with non-contact THz imaging system.

Left: Speculum used to open the rabbit eye. Middle: THz imaging is performed under the surgical microscope for quick inspection. Right: Descemet's membrane stripping procedure.

Photographs of experiment progress is provided in Figure 5-1. At the beginning of the experiment, the subject was secured on an improved version of the custom mount used in the first *in vivo* study. In this version, the entire mount can be translated in x,y,z for the general positioning of the animal. The mount also provides five degrees of freedom for movement of the head (x,y,z translation, axial plane rotation, sagittal plane rotation centered on the rabbit's neck) as the rabbit rested in prone position for the duration of the imaging. The mount also incorporated a hinge frame that allows the animal to be repositioned to the lateral position for the DMS procedure, such that one of the eyes is facing up towards the surgical microscope.

The eye of interest was held open using an ophthalmological speculum, and an initial THz image was captured of the healthy eye. Next, the Descemet's membrane stripping was performed by an ophthalmic surgeon. The resulting corneal edema was allowed to progress up to 15 minutes, and the surgeon inspected the cornea for the onset of edema.

Confirming the onset of edema, the rabbit was moved back to the imaging position and THz images were acquired. Each imaging run required 90 seconds of acquisition time, and images were

taken every 3 minutes. Wetting drops (common eye-drops) were used as needed prior to imaging, but stopped once imaging began. Ultrasound Pachymetry measurements were taken at various time points. At the conclusion of the study, the subject was euthanized with an intravenous injection of pharmaceutical grade Pentobarbital (100 mg/kg).

5.1.2. Modifications to experiment protocol

In case that edema formed too rapidly before imaging can begin, the Descemet's membrane was only partially stripped (~1/4 of the area) and the eye was monitored for ~15 minutes. Following Descemet's membrane stripping, the edematous response was noticeable by the surgeon but its onset took more than 15 minutes. Thirty minutes after the partial stripping, the Descemet's membrane was fully removed, however the diffusion of the fluid into the stromal layer was slow. To avoid exposing the animal and the eye in the anesthetized and paralyzed state for a prolonged period of time, the surgeon opted to accelerate the edema formation by directly irrigating the posterior stromal layer with an irrigation aspiration cannula. Upon stromal irrigation, immediate swelling of cornea was apparent, confirmed by a slit lamp and surgical microscope inspection. Immediately following this procedure, THz images were taken every 3 minutes as long as we could observe changes in reflectivity (~30 minutes). Over the course of image acquisition, the subject was undisturbed and the muscular movements of the eyes were stabilized with medication.

5.1.3. Imaging results and discussion of the experimental outcome

Figure 5-2 shows the consecutive images of *in vivo* cornea plotted with a shared color map acquired over a 30 minute period. The first image was taken immediately after the stromal irrigation, and each image was acquired over 90 seconds. The subject was undisturbed throughout the 30 minute period and eye movements were prevented with medication (eye drops) prior to imaging, ensuring that each image shares the same field of view.

Overall reflectivity of the surface peaked around ~6 minutes post-procedure, then gradually dropped until after 24 minutes post-procedure. We noticed that the reflectivity profile change was much more noticeable than the result shown in Figure 3-17, although the higher-frequency choice (650GHz instead of ~525GHz) was expected to return a lesser contrast. It was also clear that the 650GHz measurement was not sensitive to the corneal thickness change, therefore the image contrast is attributed to variation in CTWC. These observations confirm that the DMS procedure induced a significant CTWC change by emulating the known disease model.

It is hypothesized that the onset of the corneal edema is directly responsible for increases in reflectivity for the first 6 minutes. Over the duration of the experiment, the surgeon noticed that the edema continued to progress. However, the cornea remained transparent throughout the experiment. The drop in reflectivity after 6 minutes, on the other hand, resulted from drying of the anterior layers. Because the eye was kept open and undisturbed for the entire duration of the experiment, the tear film was not replenished since the beginning of the imaging. As a result, evaporation from the anterior surface quickly depleted the tear film and the anterior layer of the cornea started to dry. The dried state of the eye could be directly confirmed by touching and gently stretching the cornea after the experiment. This observation explains the superior reflectivity contrast in this image set. This scenario resembles the “pinned back” case discussed in Figure 3-4.

Reflectivity changes as a result of CTWC change are expected to be largest in the pinned back case out of the three different CTWC change profiles.

The rise and fall of the 650GHz reflectivity is thought to be the result of competing processes: CTWC elevation from corneal edema formation acted against unrestricted loss of water from evaporation in the anterior surface. The drying of the anterior surface demonstrated the CTWC dependent signal contrast of the imaging system, however, this process prevented the observation of further changes in CTWC from the edema development. In addition, the dramatic drying process in this experiment is not expected to be significantly relevant to most clinical cases. Ideally, the animal should be allowed to blink in between each image to re-create the normal environment for the cornea. However, allowing natural blinking is not possible with standard protocols for the animal, which must remain paralyzed and anesthetized for the duration of the experiment. There is no humane way to prevent the conscious/unconscious eye movement of the animal while it is awake.

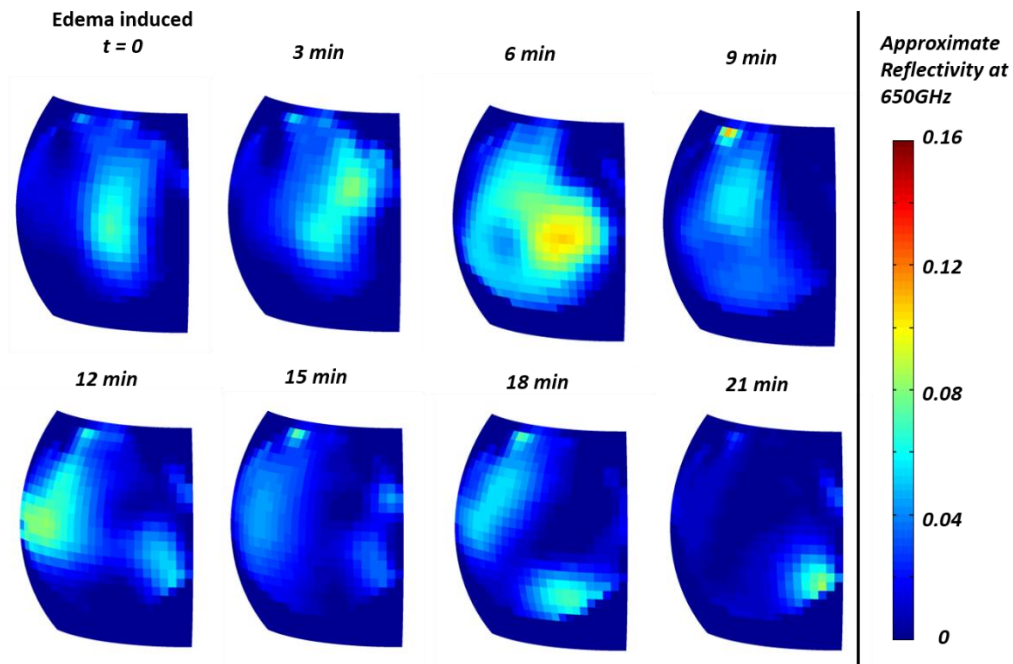


Figure 5-2. Time series 650GHz image of the left eye immediately after the Descemet's membrane stripping.

5.1.4. Discussion: Experimental Challenges and Pitfalls

Although the animal experiment was carefully prepared with mock-imaging trials with *ex vivo* porcine eyes and calibration targets, this experiment proved to be particularly challenging. First, the target alignment process with living animals required minutes of careful adjustments.

To prevent excessive drying of cornea before the imaging sequence begins, wetting eye drops were used after each unsuccessful alignment attempt. The assisting guide laser device facilitated this process, however the alignment process was not efficient enough to be performed repeatedly and reproducibly. In addition, the anesthetized animal needed to be frequently disturbed with periodic biometric measurements over the duration of the experiment, and the alignment was often lost. Although human subjects can cooperate with the measurement process, these challenges are considered realistic representations of the imaging system operation in the clinic. For practical usage in the clinic, the imaging routine must be able to perform reproducible eye alignment and imaging operation within ~20 seconds.

Alignment reproducibility also complicated data analysis. At this stage of the imager instrumentation, minor alignment differences produced a large signal variation in the captured image. Reflectivity measurements were not comparable between the baseline (pre-DMS) and the CTWC perturbed eye. Meaningful comparison of reflectivity differences was possible only for the set of images taken in a sequence. These unexpected difficulties prevented the complete collection of the corneal thickness data for comparison as in the first *in vivo* experiment.

The thickness data set obtained for the same eye (Figure 5-2) is shown in Table 8. Partial CCT data. The time label is assigned relative to the same reference (0 minute at the beginning of the experiment) used in Figure 5-2 for clarity. In contrast to the first experiment, in which the CCT increased monotonically over time when the cornea was distressed, the CCT was thinner in the

fully edematous cornea. It is an unexpected result and we could not provide an explanation. While it is possible that this result was from a pachymeter user error, the surgical procedure disturbed the cornea - aqueous humor interface may have affected the CCT measurement.

Table 8. Partial CCT data

Time	Baseline s -65 minutes	Partial DM stripped (no induced edema) -35 minutes	Full DM strip + induced edema 0 minutes
CCT (μm)	380 \pm 12	378.2 \pm 9	358.6 \pm 14

5.2. Safety of THz imaging

The American National Standards Institute (ANSI) provides safety guidelines on radiation exposure, especially to the eye, in workspace and healthcare environments. According to the study results compiled in the American National Standard for Safe Use of Lasers, OSHA Technical Manual (OSHA Instruction TED 01-00-015 [TED 1-0.15A], Section III, Chapter 6) provides Maximum Permissible Exposure (MPE) level limits for direct ocular exposures for electromagnetic radiation at various frequency bands. In order to establish minimal risk/no risk justification of this study, this section discusses the radiation safety consideration at our frequency band of interest (THz band - 0.1 THz – 10 THz) and the safety of the proposed exposure level of maximum 2.9 mW/cm².

5.2.1. Mechanisms of Possible Tissue Damage

The photon energy of radiation at our frequency of interest (4.1meV at 1 THz) is far below the ionization level of any known biological molecules. Looking at the photon energy only, molecular level damage is considered not possible, which is one of the key advantages of using THz waves for medical imaging. However, the THz frequency band has not been studied in depth and there is no specific ANSI or OSHA guideline for THz frequency waves. However, it is clear that the electromagnetic wave at THz band is sharply absorbed by the water and almost no power can penetrate below more than 3 mm of body mass (Absorption coefficient is $> 150 \text{ cm}^{-1}$ for typical tissue at 1THz). For the frequency band of interest, most of the THz wave will be absorbed by the cornea (by its water content), and the fluids in the anterior chamber, the lens, and the posterior chamber. Hence, practically no radiation power can ever reach the retina no matter how powerful the THz frequency irradiation. Therefore, any possibility of damage is restricted to the corneal tissue.

Recent studies into the safety of THz irradiation on biological tissues have yielded contradictory results that appear to vary depending on the thermal controls, specific frequency bands, power densities, and durations of exposure investigated in each experiment. Nevertheless, the THz BRIDGE project – a collaboration between 25 research groups investigating the biological effects of THz radiation – reported that across the 25 studies, no biological effects were detected except under very specific exposure conditions in which an increase in lysosome permeability [111, 112] and some induction of genotoxicity in lymphocytes occurred.

Many of the studies performed by collaborators in the THz BRIDGE project concluded that thermal effects were the dominant cause of harmful results suggesting that the potential damage mechanisms mirror those in the shorter wavelength regimes of the IR band [113]. On the other hand, the *IEEE Standard for Safety Levels with Respect to Human Exposure to Radio Frequency Electromagnetic Fields, 3 kHz to 300 GHz*, (IEEE Std C95.1TM - 2005) [114] offers a similar view on the damage mechanism for the direct ocular exposure to the RF and microwave region below the THz band:

“Adverse effects of RF exposure of the eye (e.g., cataracts) are associated only with significant temperature increases due to the absorption of RF energy. There is no evidence of other significant ocular effects (including cancer) that would support a change in the adverse effect level of 4 W/kg. [114]”

To the entire body, it cites MPE of $10\text{mW}/\text{cm}^2$ in the frequency band of 30GHz -300GHz (0.03-0.3THz) of radiation in a controlled environment. Such a measure considers the prolonged heating effect due to the specific absorption rate, and there is no specific consideration to an eye with short-term exposure.

5.2.2. Animal radiation safety study

Under the UCLA Animal Research Committee approved protocol (#2013-087), we performed our own THz radiation safety study with an *in vivo* rabbit model with pulsed, broadband THz illumination with an average power density exceeding $2.9\text{mW}/\text{cm}^2$ over the frequency band spanning from $\sim 100\text{GHz}$ to $> 1.5\text{THz}$. The current debate regarding THz safety discussed above indicates the potential for biological tissue damage depending on the THz frequency, power density, time of exposure, and tissue being investigated, and therefore, safety studies customized for specific applications are required. The study was conducted using 0.439ps pulsed THz irradiation at an average power density of at least $2.9\text{mW}/\text{cm}^2$ with exposure times of 2 minutes. These parameters were chosen to specifically assess the corneal imaging application, as similar THz parameters would be used, and exposure times are expected to be on the order of seconds rather than minutes.

Experiments were performed on 10 New Zealand white rabbits (*Oryctolagus cuniculus*). All subjects were placed under general anesthesia with an intramuscular injection of Ketamine (30 mg/kg) and Xylazine (5 mg/kg), and intubated and maintained under anesthesia with Isoflurane (1-5%). In addition, pharmaceutical grade Pancuronium (0.1 mg/kg) was administered to prevent corneal descent during anesthesia. THz irradiation was applied to *in vivo* rabbit cornea at a peak power density of at least $\sim 17.68\text{mW}/\text{cm}^2$ for two minutes. Irradiation was isolated to one eye per subject, while the unexposed eye was used as a control. Upon completion of the irradiation, animals were euthanized according to IACUC protocols. Experiments were performed in compliance with IACUC guidelines. Corneal tissue was harvested immediately post-treatment, and prepared for histological and proteomics analysis. Corneal specimens were sectioned sagittally and stained using Hematoxylin and Eosin staining. A Difference Gel Electrophoresis (DIGE) assay

was used for proteomics specimens to determine changes in protein expression between irradiated and control tissues. DIGE results were evaluated using student's t-tests and mass spectrometry was used to identify proteins that were expressed differently in treated eyes.

We investigated both microanatomical and proteomic discrepancies between irradiated and control samples using paraffin histological and Difference Gel Electrophoresis (DIGE) analyses, respectively. Our histological evaluation did not reveal observable differences between the control and irradiated corneal specimens. In both control and irradiated specimens, the superficial epithelium, the Bowman's membrane, the substantia propria, and the endothelial cells and Descemet's membrane appeared to remain intact, and little damage was observed (Figure 5-3 A, B). In addition, a clear distinction was observed between layers. There was no indication of congealed collagen or mechanical damage in the stroma, suggesting that thermal damage did not occur. There was no indication of any mechanical damage to the squamous epithelium due to laser impingement (Figure 5-3B). Finally, the nuclei of epithelial cells, as well as keratocytes within the stroma, appeared healthy and indistinguishable from those of the control specimens (Figure 5-3 A, B).

The DIGE results suggest that no changes in protein expression occur between treated and control samples. Across the 1,144 protein spots evaluated, only 9 resulted in significantly different protein expression when compared to the control spots. Given the small number of gels that result in significantly different spots, and the identities of these samples, our results suggest that negligible changes in protein expression occur under the method of THz irradiation of the cornea in this experiment.

Our histological and proteomics analyses reveal no significant biological changes. These results, taken with previous research, lend support to the hypothesis that a combination of high power

density and exposure time might lead to deleterious biological effects, however, when minimized, these variables seem to be benign. To this research team's knowledge, this is the first *in vivo* safety study of THz irradiation to ocular tissue to date.

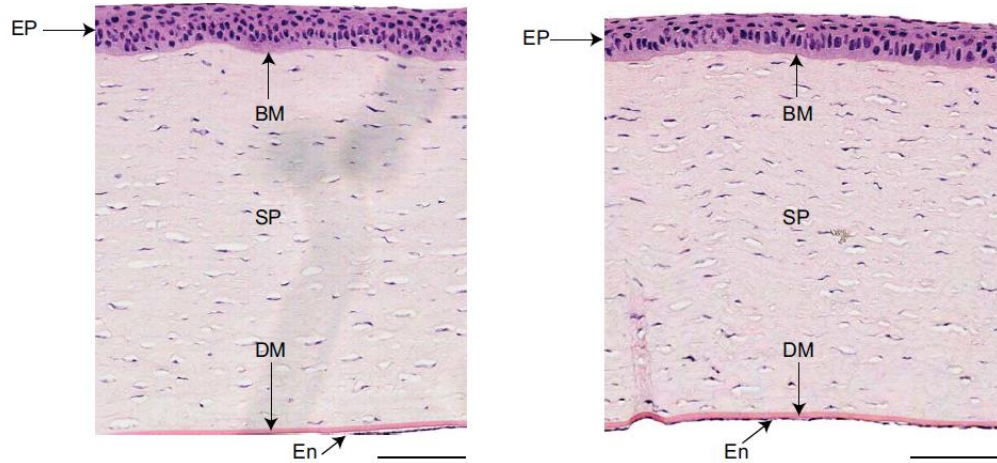


Figure 5-3. Histological analysis of corneas from control and experimental group.

Left: Histology of an undamaged control group cornea. Right: Histology of the an experimental group cornea irradiated with THz radiation.

EP: Epithelium; BM: Bowman's membrane; SP: Stroma; DM: Descemet's membrane; En: Endocelium

Additional comment

Notwithstanding this conclusion, several recent studies have demonstrated some changes in *in vitro* cell permeability, cell growth, and genotoxicity as a result of THz irradiation at a much higher fluence level. Often times the effect is associated with an increase in temperature. For example, in an investigation of human Jurkat and fibroblast cells irradiated with a 2.52 THz using a Continuous Wave (CW) at 227 mW/cm² power density for up to 40 minutes, heat shock proteins and other thermal effects including apoptosis and necrotic cell death were revealed for all samples irradiated for more than 20 minutes [115]. Further studies performed on human fibroblasts resulted in an

increase in temperature of more than 3°C and an increase in expression of heat shock proteins as well, this time operating at a lower power density of 84.8 mW/cm² for 80 minutes [116]. Based on these studies, and the few previous studies in the THz Bridge project, it appears that high magnitude power densities coupled with long exposure duration leads to thermal changes that induce heat shock protein expression. Several other studies reveal that both CW and pulsed THz irradiation also result in biological effects including increased cell growth and permeability of membranes from wide ranges of experimental conditions: Over the ranges of 0.1-2.5 THz, irradiation time between 1 minute up to 24 hours, and at power densities ranging between 0.031-30 mW/cm² [115-117]. While the exposure parameters vary greatly from the earlier studies, these lower power investigations also report a thermal change ranging between 0.03-0.3°C. Thus, it seems that even at low power densities and low duration exposure, some thermal change can occur and might lead to biological effects. Whether or not a change in temperature of 0.03°C is clinically relevant is up for debate. However, these are not the only conditions under which a biological effect has been shown from THz irradiation [118-120].

5.2.3. Safety of the Exposure Level

The MPE guidelines for the infrared (IR) band are studied and compiled by the OSHA. Figure 3 plots the MPE listed in the TABLE III:6-6, for 10 second exposure duration – similar to our study design. Two extrapolation possibilities are considered: 1. The general trend of MPE value is extended into the THz region, and 2. The same MPE level is extended throughout the lower frequency region. The blue arrow bar indicates ranges of illumination power proposed in this study. In the former case, the trend (red dotted line) suggests the MPE level exceeds $1\text{W}/\text{cm}^2$ in the illumination frequency band of our interest (shaded red). The second possibility is a conservative case in which the same MPE level of $100\text{mW}/\text{cm}^2$ at $10.6\mu\text{m}$ extends into the THz region. In both cases, our proposed illumination power ($2.9\text{ mW}/\text{cm}^2$ or below) is at most 3% of the most conservative estimate of the MPE level.

MPE limit data in the lower frequency region close to the THz band is scarce. Notably, however, a study by Kues et al. [121] concluded that there was no observed corneal damage, changes in vascular permeability of the iris, or lens opacities in the rabbit or monkey eye exposed to 60 GHz fields $10\text{mW}/\text{cm}^2$ for 8 hours. With these considerations, we believe the proposed exposure level of $2.9\text{ mW}/\text{cm}^2$ or below for ~10 seconds exposure are far below the MPE limit in the THz band, interpolated from the adjacent IR and microwave band. This exposure level have an extra margin of safety from the limited duration of exposure. These values were deemed acceptable to begin clinical trial studies by the IRB review (#16-001818).

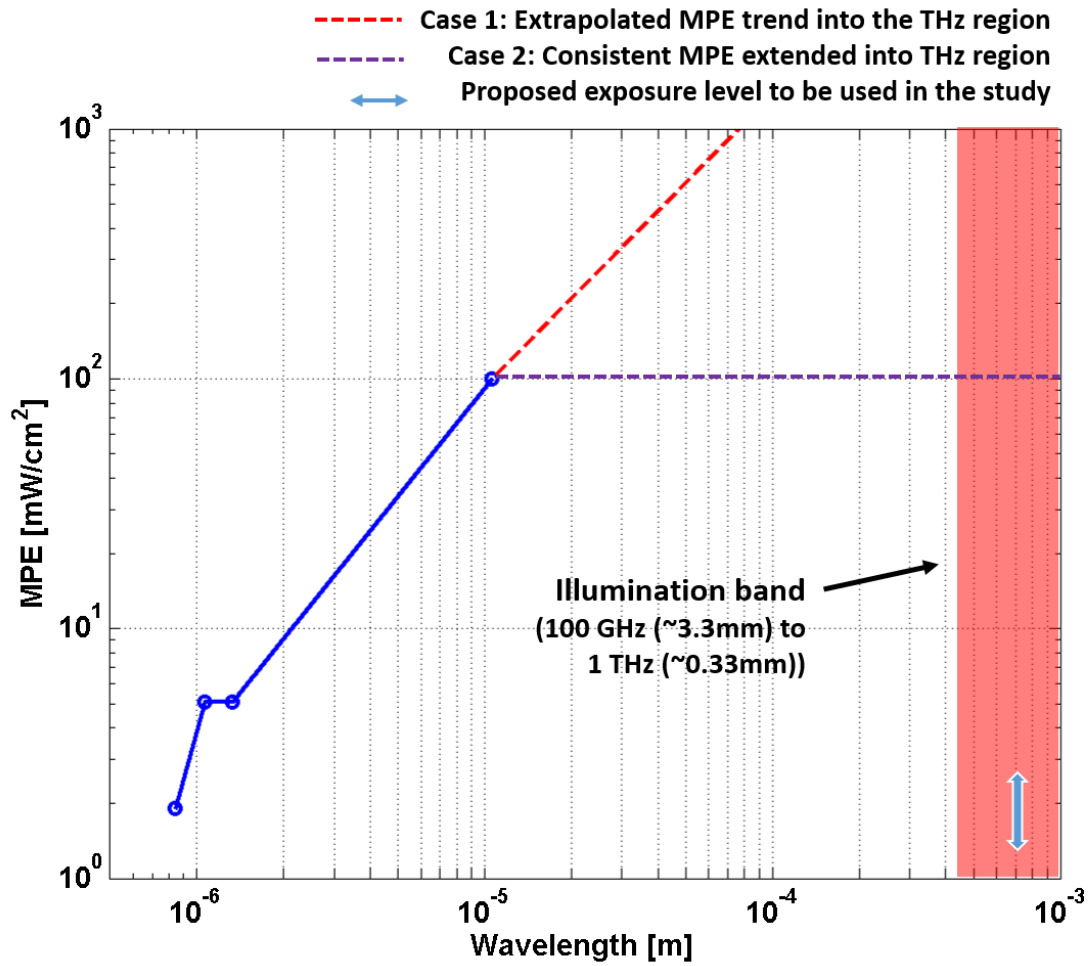


Figure 5-4. Maximum Exposure Level limit listed by ANSI standard (Blue) for 10 seconds CW exposure, and extrapolated MPE level into the lower THz region (Shaded red).

Two extrapolation possibilities are considered: 1. MPE increase trend is extended into the THz region, and 2. The same MPE level is extended throughout the lower frequency region. Blue arrow bar indicates ranges of illumination power proposed in this study

5.3. Human imaging system engineering

The challenges discussed in section 5.1.4. provided key feedbacks to improve the non-contact imaging system. The system layout was re-designed to accommodate human facial structure and more secure placement of the THz devices in a reduced footprint.

Many of the ideas came from observing and studying actual ophthalmology instruments used by physicians. First, a standard clinic-ready chin rest was installed and the imaging system was mounted on a heavy duty, precision manual X-Y translation stage used in examination microscopes. The stage provided X-Y- free positioning of the imaging system to the target. The Z- positioning could not easily be implemented with a manual lab-jack, as an additional heavy duty Z-stage would add substantial footprint and weight to the instrument. Instead, the imaging mirror assembly was mounted on a compact Z-stage. Because the input beam is collimated and incident parallel to the optical axis of the imaging mirror, the imaging mirror could be moved in $\pm z$ freely. This approach was highly efficient because the precise final positioning only required a maximum of $\pm 3\text{mm}$ of translation range. The rough positioning of the target is assisted by the chin rest. The resulting system set-up is shown in Figure 5-5.

The previous iteration of the imaging system used for the animal study simply acquired an image with a step-and-shoot algorithm, in which the scan mirrors are brought to each position in a step-wise manner. The scanning subsystem hardware is upgraded with encoder-enabled motor controllers that can send out X- and Y- positions of each scanning mirror at nearly KHz bandwidth. The scanning can be performed much faster and more flexibly because the image can be reconstructed from the encoder position signals. Considering the collimated beam sizes ($w_0 = \sim 9\text{mm}$) that scan over the imaging mirror clear aperture ($D = 76.2\text{mm}$) (Section 4.3), the raw image only needs to have $\sim 13 \times 13$ pixels. Therefore, the entire imaging routine can be performed under

10 seconds. The scanning subsystem is programmed to acquire the image row-by-row using the “uniform rectilinear” path, and the resulting image is reconstructed using the mapping relation discussed in Chapter 4.

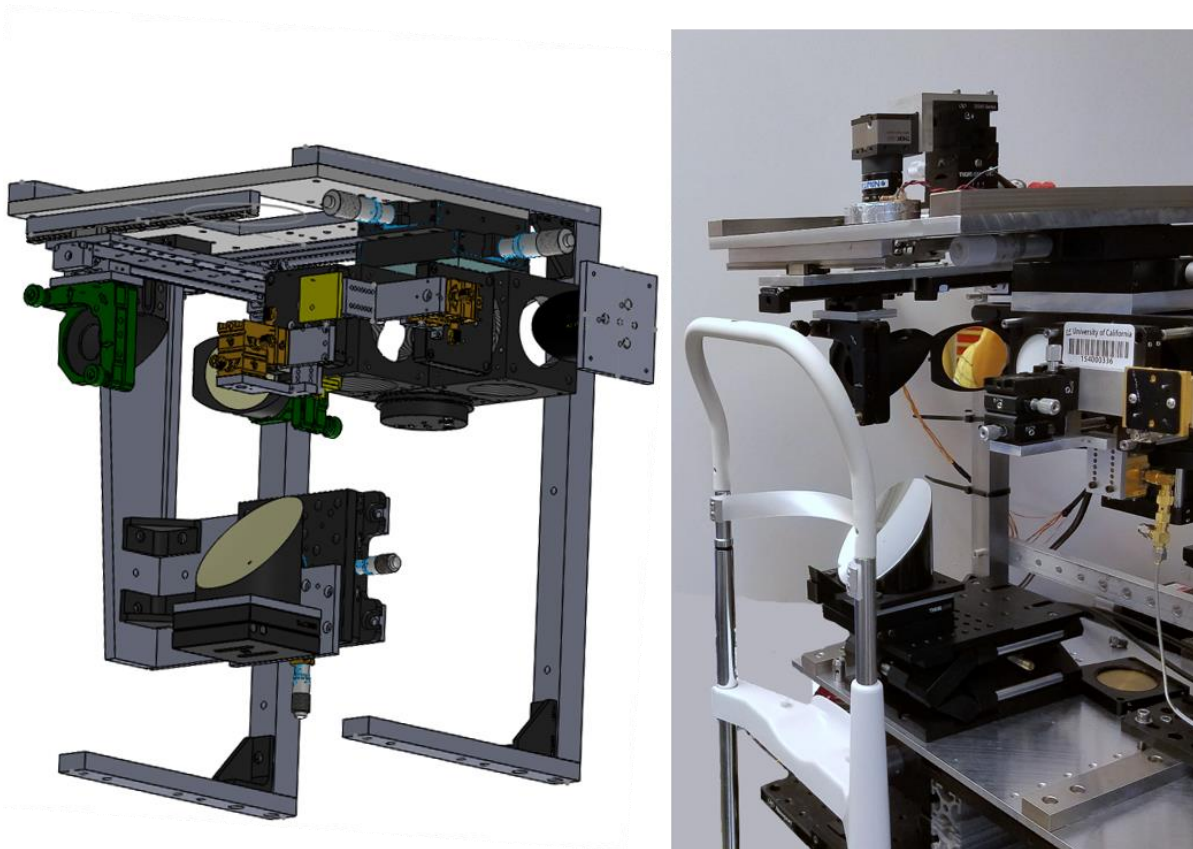


Figure 5-5. Non-contact THz imaging system equipped with human subject interfaces

The most pressing requirement was reproducible, precise target positioning. Although laser-guided positioning of the eye was partially successful, the imaging mirror heavily obstructed the eye and it was difficult to see the laser lines en-face. Moreover, the width of the laser grid line produced by laser diodes were rather wide (~1mm), cluttering the visual field. There were additional difficulties in finding the appropriate brightness of the laser beam. An overly bright

beam scattered in the cornea and cluttered the visual field. Darker beams were not easily recognizable, and we were not able to find an appropriate compromise. Lastly, this method is not desired to be used in humans. No matter how attenuated the laser beam power is, patients and clinicians would resent the idea of shining visible laser irradiation directly onto the eye. Many alternatives to using the laser beam were explored. We eventually narrowed down our approach to two innovative solutions.

5.3.1. Human interfacing

5.3.1A Eye positioner

A guide structure is attached to the imaging mirror assembly to indicate the position of the mirror's focus. Figure 5-6 shows a version of the positioner used in the first human imaging trial. The ring structure is positioned concentric to the mirror's focus and the ray path through the optical axis of the mirror. The position of the ring is recessed 8mm away from the focus so that it can be pressed gently on the lower eye lid. This structure greatly facilitates the positioning process and also provides a resting point for the patient to prevent tilting of the head. These structures are conveniently fabricated with 3D printers using soft plastic materials. The structure design can be easily revised to conform to specific facial features, and several different versions of the positioners were fabricated. These positioners can be easily removed from the imaging mirror assembly, and the subjects can choose the positioner that is most comfortable. Ideally, these items will be made in disposable soft foam materials to eliminate any potential for injuries.

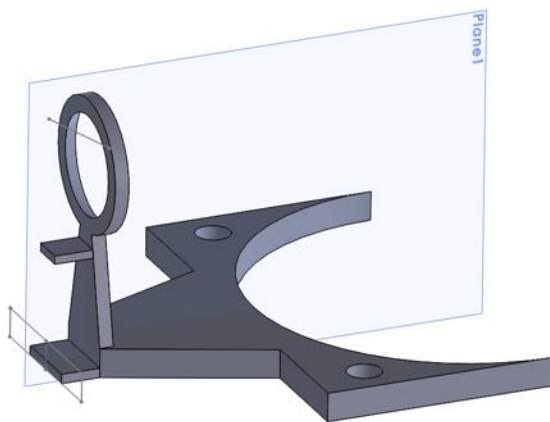


Figure 5-6. Eye positioner apparatus.

5.3.1B Eye camera

Although the eye positioner structure makes initial positioning much easier, the imaging mirror still blocked the visual field of the eye. The system operator only could look at the alignment at an angle, and accurate alignment was difficult to be confirmed. On the other hand, manual positioning of the target was also somewhat imprecise without any real-time visual feedback.

The imaging system's mechanical frame was revised such that the aperture of the imaging mirror can be accessed with a compact digital camera. The camera is mounted on an X-Y- stage and a tilt goniometer, and precisely aligned to the optical axis of the imaging mirror. The camera looks directly into the target and provides the operator with real time visual feedback during the alignment. The anatomical feature of the eye helps with this process. The operator can align the circular aperture, the iris, and pupil of the eye to be concentric. Additional machine-vision features were added to the monitor to aid the positioning process, as shown in Figure 5-7. The OAP imaging mirror is expected to distort the image of the target seen by the camera. However, such distortion is minimal at the center of the mirror and the alignment operation above can be still performed. All of the optics geometry is fixed, therefore it is also feasible to undistort the image real-time using a re-mapping algorithm.

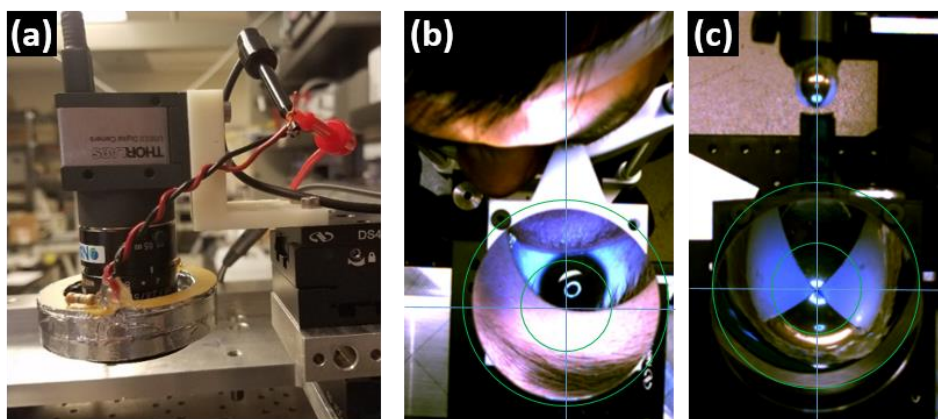


Figure 5-7. Eye camera and machine-vision assisted alignment process.

Additionally, the camera is equipped with an LED illuminated ring similar to a ring-light flash used in digital cameras. This feature projects a ring contour to the eye, as shown in Figure 5-7(b) and (c), and helps with the alignment process. It also provides flood illumination to the target, helping to illuminate the iris and pupil structures.

Lastly, a dot marker is placed on the center of the imaging mirror as a staring target for the subject. The subject is asked to comfortably focus on the dot during the image acquisition process. This simple implantation dramatically reduces random eye movements and distractions and keeps the eye in a fixed direction. The alignment of the eye was stable enough that the subject could comfortably blink as needed. As the imaging system advances each “row”, a 0.5 second pause is added in between the row scan to give time for the subject to blink. After several iterations of improvement, the combined eye positioner and the camera approach finally produced a reproducible alignment procedure that took less than 10 seconds.

5.3.2. Multiple frequency (spectrally resolved) measurements

Another key conclusion of the *in vivo* studies was that the spectrally resolved measurement is highly useful in calibrating the reflectivity scale and distinguishing confounders specific to an individual frequency. In both experiments, it was difficult to directly translate the measured THz reflectivity to CTWC because there is no exact calibration standard for *in vivo* corneas. For these experiments, it was difficult to assign an absolute reflectivity scale because of the target alignment reproducibility. It is possible to eliminate measurement offset with a careful alignment process, however target misalignment is always a possibility. Nevertheless, in the first study, measurements with two different sensing system were used together to validate the key hypothesis of the EM model.

Therefore, it is imperative to start acquiring spectrally resolved measurement for the non-contact THz imaging system. The current system can easily incorporate this change thanks to the system architecture that divides the imaging system into three distinct subsystems; only the transceiver system needs to be modified. There are several options to implement a spectral measurement. The source and the detector can be directly replaced with photoconductive switch (PCS) based devices for THz time-domain spectroscopy. This method is especially attractive for two reasons: 1) THz TDS is a powerful technique that can produce the THz spectrum over a wide band (100GHz – 5 THz) using ultrafast broadband THz pulse. THz TDS technique and devices have substantially improved in compactness and stability [122]. A single spectrum can be now acquired much faster thanks to continuously improving PCS emitter power and the electronic delay line sweeping technique. 2) Because the THz spectrum of water-containing tissue is mostly monotonic, the measurement does not need high spectral resolution, which is one of the weaknesses of the THz TDS technique.

However, THz TDS spectral data have dramatically compromised SNR compared to the direct measurement technique used throughout this study. Moreover, the maximum output power of the typically available photoconductive switch emitters is below $100\mu\text{W}$, compared to $> 1\text{mW}$ provided by narrowband solid state sources. Considering that the THz corneal hydration sensing environment is already heavily SNR limited, THz TDS is not currently a viable choice.

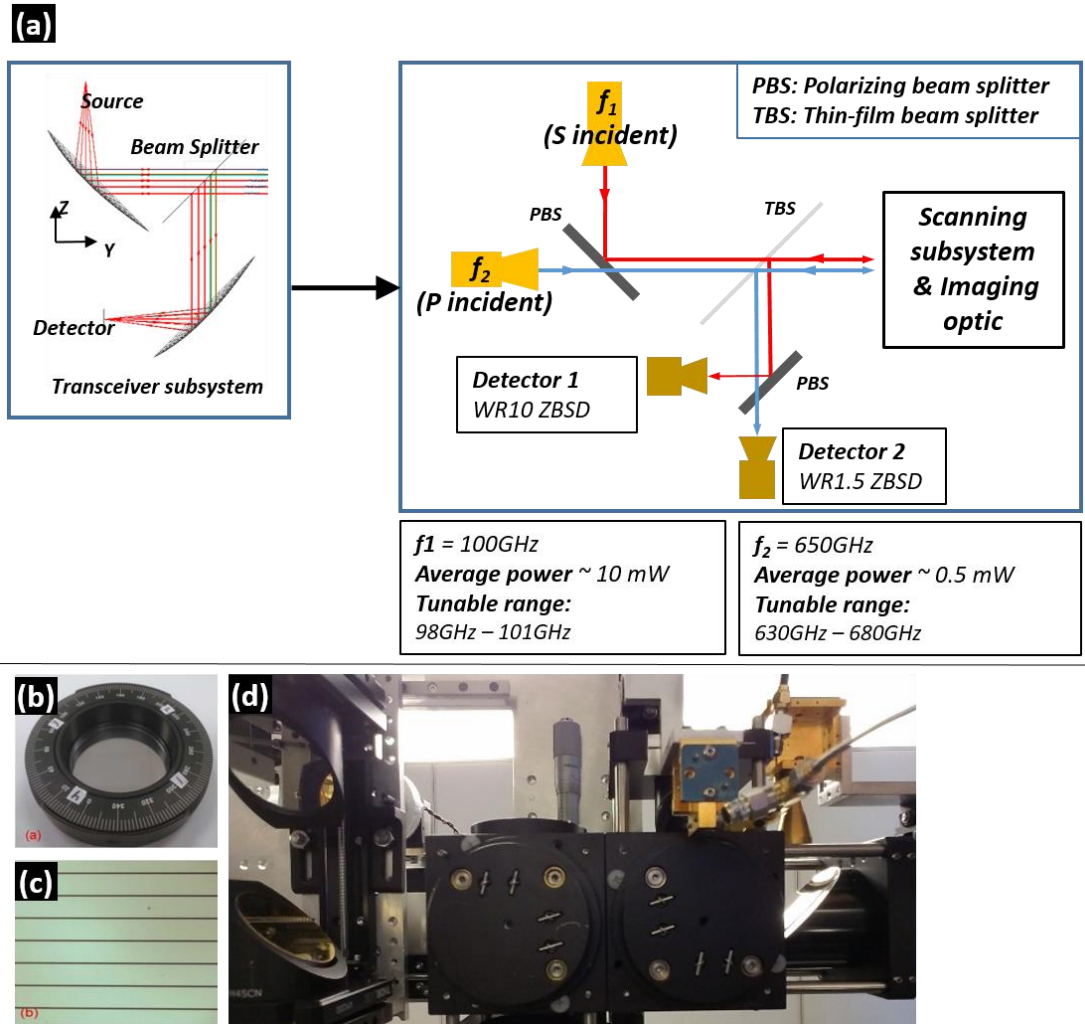


Figure 5-8. Two-frequency transceiver subsystem.

(a): Block diagram showing the modifications made to the original transceiver subsystem design. f_1 (100GHz) and f_2 (650GHz) beams are multiplexed in orthogonal polarization. A polarizing beam splitter (PBS).

(b), (c) Photograph of the polarizing beam splitter used in this system and the microscope image of the polarizer surface. Image adapted from [123].

(d) Photograph of the assembled transceiver subsystem.

Instead, the transceiver subsystem is augmented to multiplex a second measurement frequency at 100GHz in addition to the existing 650GHz set up. Recapitulating the findings of the Cornea EM model, the lower frequency (100GHz) is expected to perform more sensitive measurements of the CTWC while being sensitive to the corneal thickness change as well. The high frequency (650GHz) measurements target changes in anterior CTWC. The modified transceiver subsystem design is shown in Figure 5-8. A Gunn diode emitter described in Section 3.4.1 is used as the f_1 emitter. A second zero-bias Schottky diode detector is used for the *Detector 1* which incorporates WR10 waveguide (70-110GHz band) and conical horn antenna [63]. Since this switch to a solid state detector (from the pyroelectric detector in Figure 3-11), the AM modulation frequency can be dramatically increased to improve SNR and enable faster image acquisition. Therefore the modulator circuit that performed AM and FM sweep of the Gunn Diode in Figure 3-11 was redesigned to operate at FM sweeping at ~20KHz and AM modulation by the lock-in amplifier at 1KHz. Both the source and detector devices are linearly polarized. The f_2 emitter and detectors are the same devices as described in Figure 4-16, which are also linearly polarized devices.

f_1 and f_2 beams are multiplexed and de-multiplexed using polarizing beam splitters fabricated on quartz substrate [123]. f_1 and f_2 beams are incident on the first PBS in orthogonal polarization states. The PBS is rotated such that the f_1 beam passes through with maximum transmission while f_2 is reflected at maximum rejection. The resulting multiplexed beam follows the same scanning path to the cornea and back to the thin-film beam splitter, while maintaining orthogonal polarization states between the two frequency components. The return beam is de-multiplexed by the second PBS. The receivers are oriented to the respective polarization of each de-multiplexed beam.

There are several comments on this system implementation. First, because the incidence angle

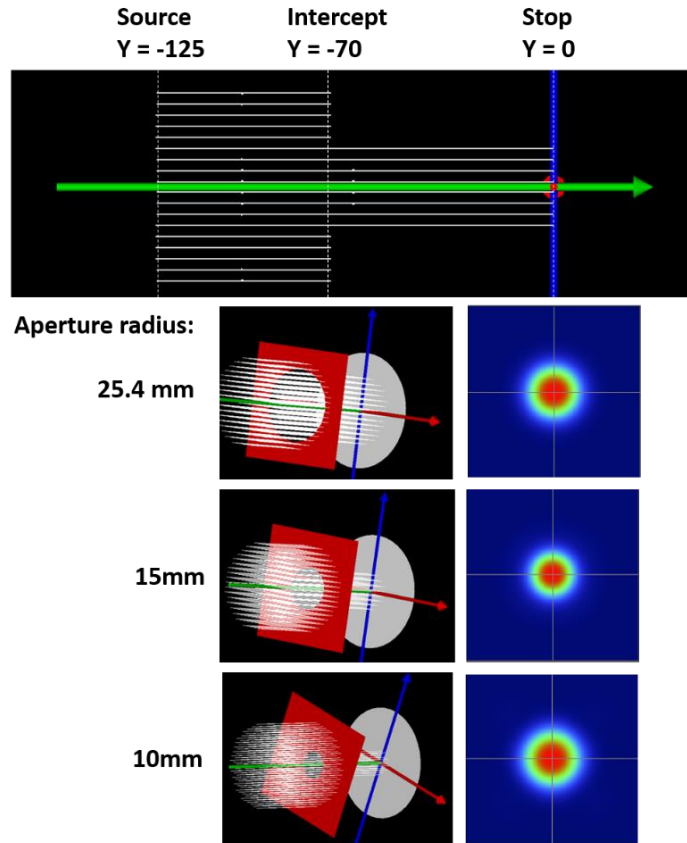


Figure 5-9. Preliminary analysis of field distribution of truncated collimated 100GHz beam

on the cornea is uniformly 90° , there is no modification to the reflection coefficient from the polarization difference. Furthermore, because the path of both f_1 and f_2 beams are coincident, the orthogonality of their initial polarization states is expected to be maintained. Second, it is noted that the 100GHz beam is significantly larger than the 650GHz beam. The longer wavelength of the f_1 beam almost completely fills the $\sim 50.8\text{mm}$ diameter optics in the transceiver subsystem. Therefore, appreciable clipping of the beam is expected, which will increase its divergence angle. However, a preliminary analysis shows that the modified beam shape still remains mostly Gaussian for the range of pass diameter (Figure 5-9). Third, a quasi-optical analysis similar to that presented in Chapter 4 is performed for the 100GHz beam. However, given the dimension of the current imaging OAP mirror ($D = 76.4\text{mm}$) and the diameter of the input beam at $\sim 40\text{mm}$, the

100GHz input beam can only be scanned over a small area centered at the axis of the mirror. f_1 and f_2 images are acquired simultaneously in a single scan over the same FOV, however the 100GHz raw image only contains a few usable pixels near the center of the cornea. This problem can be solved by extending the imaging OAP mirror cut and increasing the available clear aperture area.

The first ever captured THz images of human cornea is shown in Figure 5-10. Mapping algorithms described in Chapter 4 are used to produce the *en face* reflectivity map of both eyes. The 650GHz image of the left eye shows fairly uniform distribution of the THz reflectivity, while the image of right eye is less so. The shadow of from eyelashes result in consistently lower reflectivity near the top edge (the effect of varying signal coupling coefficients over the imaging field has been corrected). The mean reflectivity within the region of interest (dotted circle) are reproducible within 1% for both 650GHz and 100GHz measurement, acquired simultaneously. Calibrated to the reflectivity of a spherical brass target, the mean reflectivities (11% at 650GHz, 37% at 100GHz) are within the expected range of a healthy cornea with tear film thickness of at least 10 μ m.

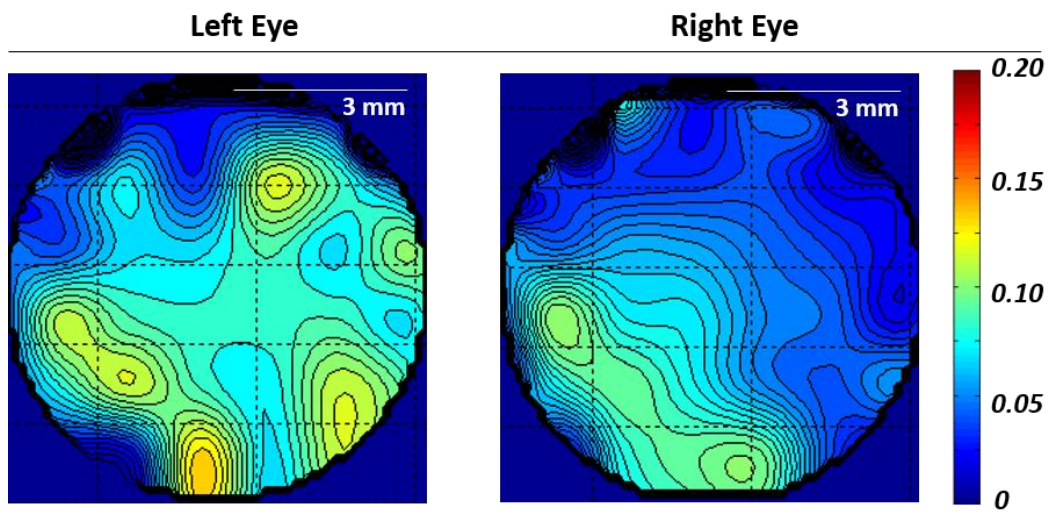


Figure 5-10. 650GHz images of healthy human cornea

Chapter 6 Conclusion

This work describes our team's effort to leverage unique advantages of the THz band to develop a new ophthalmological imaging technology. We developed novel THz sensing and imaging techniques to measure corneal hydration, which is a critical and delicate homeostatic parameter for visual clarity. Current conventional methods that indirectly infer corneal tissue water content (CTWC) are shown to be inaccurate, while other powerful imaging methods in ophthalmology, such as Optical Coherence Tomography (OCT), cannot effectively measure tissue hydration properties. This technology is applied to study and screen for corneal diseases and dystrophies, which affect more than 250,000 people in U.S., especially of the aging population.

The THz band offers unique advantages for tissue hydration sensing. Due to its long wavelength, a THz wave is less affected by scattering in tissue, thus it can be used to efficiently probe the bulk-dielectric properties of tissue. Hydration-dependent tissue properties at the THz band are modeled with dielectric media theory (Debye relaxation model) and effective medium theory (Bruggeman model). These fundamental relations are combined to develop a rigorous electromagnetic model of THz-corneal tissue interaction. Recognizing that the cornea has a ordered, layered structure, this study used stratified media formulation to model axially varying CTWC and compute the THz reflectivity as a function of CTWC and corneal geometry change.

As a function of the frequency choice, CTWC perturbation mechanics, and possible concurrent changes in corneal thickness, corneal THz reflectivity provides various information about the CTWC changes. At lower frequencies (300GHz and below), THz waves have larger sensitivity to

hydration and deeper penetration into the cornea. As a result, THz reflectivity is also sensitive to the corneal thickness change that can accompany the CTWC change. At the higher frequency band, THz waves sense CTWC of the anterior layers and do not reach the aqueous humor back-short.

Our first *in vivo* animal study (N=5) confirmed expected outcomes of the cornea electromagnetic model with measurements at two frequencies (100GHz and 525GHz). With concurrent measurement of the THz reflectivity and corneal thickness, this experiment provided contrary evidence to the thickness-CTWC relationship used in clinical practice.. We also empirically demonstrated the sensitivities of the 100GHz and 525GHz sensing systems to physiologic changes in live rabbit corneas. However, pitfalls of the ‘conventional’ imaging approach (i.e. requirement of using rigid flattening window; Chapter 2) results in critical limitations on the experimental method. To achieve practical application of THz sensing techniques, other imaging approaches must be pursued.

Insights from previous THz imaging studies led to the development of a novel spherical surface imaging methodology by creatively using the Fourier transform properties of an over-dimensioned focusing geometry (Chapter 4). Using this technique, a non-contact THz imager was developed with a uniform normal incidence imaging field. The imaging system is composed of three distinct subsystems that can be optimized separately for the desired imaging performance. The imaging target (cornea), illumination source, and detector are all kept stationary in this system.

The imaging system design process was greatly facilitated from application of the quasioptical theory. Compared to more rigorous computational analysis methods, quasioptical approximation provided highly accurate modeling of THz beam propagation in the imaging system. Using quasioptical modeling, the image transfer function of the system was analyzed. The imaging performance was optimized for corneal application by tuning the parameters of the imaging optic

(90° off-axis parabolic mirror) and the input THz beam. The optical system design was further optimized by using two design rules developed for off-axis optics.

The first implementation of the system used a frequency-modulated CW emitter at 650GHz with ~0.5mW average power and a zero-bias Schottky diode detector. The combination of these devices is chosen for maximum allocation of the active THz energy for SNR and for the large post-detection bandwidth (~10GHz) of the solid state detector. This system is tested in the second *in vivo* imaging study, in which a corneal disease model is emulated with Descemet's membrane stripping. A series of THz images acquired in this experiment captures dramatic 650 GHz reflectivity changes resulting from the onset of corneal edema, and subsequently from CTWC loss from evaporation in the anterior layers of the cornea. This experiment was the first successful attempt in capturing CTWC images of *in vivo* cornea without making contact to the eye.

In preparation for the human imaging trial, a safety framework for THz eye imaging was developed with a thorough survey of THz safety researches and established radiation safety standards. The in-house animal study (N=10) rigorously investigated any possible morphological or cellular function alteration from exposure to THz radiation. These investigations concluded that while THz radiation does not pose hazards at the molecular level, tissue heating from energy deposits may possibly alter tissue equilibrium. Our communication with the institutional Internal Review Board (IRB) that overlooks safety of clinical studies helped to develop additional measures for safety in the imaging system engineering.

The non-contact imaging system incorporated a number of auxiliary devices for practical and reliable operation with human subjects. The current version of the imaging system can acquire the CTWC map of entire cornea under 10 seconds. This design still has ample signal bandwidth. Thus, more efficient beam scanning methods can further reduce the acquisition time to less than 1

seconds. Assembly of the second generation of this system is currently underway with the 2-mirror, angular scanning design presented in section 4.4.5, which will allow near real-time capture of the CTWC map.

The next phase of this work consists of three major goals. First, Multiple-frequency sensing and imaging methodologies will be further developed with a more sophisticated calibration algorithm. It is possible to obtain more accurate CTWC value with an ensemble of measured reflectivities at different frequencies. Rather than directly calibrating the reflectivity measurements to CTWC value, spectrally resolved data is used to find the “best match” that is computed with the cornea-THz interaction model discussed in chapter 3. This approach leverages statistical signal processing technique to improve the confidence in our interpretation.

The non-contact imaging system will be used in the first clinical study to study the range of CTWC measured by THz imaging in normal healthy eyes. 120 eyes of 60 patients with no ocular disease or history of ocular surgery will be recruited for this baseline pilot study. The inclusion criteria covers all groups of population with no history of major corneal damage. Participants will be recruited to include 30 individuals < 40 years old (15 male and 15 female), and 30 individuals > 50 years old (15 male and 15 female). The initial study will also include routine clinical evaluation of cornea health: visual acuity using the ETDRS chart; intraocular pressure using the Goldman tonometer; corneal morphology data with anterior segment OCT, and 2D corneal topography measured with videokeratography. Using this data, the range of corneal hydration in the normal population can be established and correlations between the standard measurements and THz data will be calculated. This initial study and the non-contact imaging system has been reviewed and approved by University of California’s Internal Review Board. (#16-001818)

The next clinical study will investigate THz imaging of corneal edema at various stages of disease/ conditions. CTWC will be evaluated *in vivo* in patients undergoing Descemet's stripping endothelial keratoplasty (DSEK) to treat corneal dystrophy. The goal of this study is to test the ability of the THz imaging system to evaluate pathological edema and detect a change in CTWC over time. 20 patients will be enrolled and tested at multiple time points, including preoperatively, 1 day post-op, 1 week post-op, 1 month post-op and 3 months post-op. Similar to the healthy cornea imaging study, the corneal health parameters will be acquired for each eye and we will investigate any strong correlations among these parameters. In addition, critical clinical observations of the graft healing process will be weighed against CTWC information.

6.1. Final Words








THz technologies are becoming more scaleable. This study benefitted from the recent (~10 years) growth in availability of THz devices that are more compact, better-calibrated, and robust. This trend was mostly a result of better device packaging/ design effort fueled by commercial interests in communication and security imaging applications. THz devices can be integrated with existing Silicon/semiconductor technologies. Hence, THz technologies have a good potential to produce a cheap and readily available imaging technology for medical imaging applications.

Our system engineering endeavors are inspired by many great examples of medical device technology development originating from mainly scientific/research fields. Technologies that has become indispensable in many clinics, such as Magnetic Resonance Imaging, pulse oximetry, Optical Coherence Tomography, and ultrasound imaging, owe to the engineering innovations and methodologies that put them in practice, unlocking their remarkable utilities to the practice of medicine.

Innovative engineering efforts will help to fully harness the potential of the THz band and its unique set of properties. THz wave responds to macroscopic and microscopic environment of the water; there is so much to explore on the rich interactions of THz wave with tissue hydration and how such interactions can be developed into a useful medical diagnostic technology. In ophthalmology, if our measurement method can additionally resolve axially varying tissue properties of thin structures such as cornea, THz imaging can address several clinical needs for critical corneal evaluations in fundamental ways.

 Sensing  Imaging  Axial Resolution

Clinical interest

1. Screening for endothelial layer malfunction   
2. Direct indicator for: Fuchs Dystrophy & pseudophakic bullous keratopathy  
3. Assessing healthiness of corneal graft  

References

1. Gullstrand, A., *Appendix*, in *Handbuch der physiologischen Optik*, H.v. Helmholtz, Editor. 351-352: New York, Dover. p. 351-352.
2. Doughty, M.J. and M.L. Zaman, *Human Corneal Thickness and Its Impact on Intraocular Pressure Measures: A Review and Meta-analysis Approach*. Survey of Ophthalmology, 2000. **44**(5): p. 367-408.
3. AAO Cornea/External Disease PPP Panel, H.C.f.Q.E.C., *Corneal Edema and Opacification PPP - 2013*. 2013.
4. Musch, D.C., et al., *Prevalence of Corneal Dystrophies in the United States: Estimates from Claims Data*. Investigative Ophthalmology & Visual Science, 2011. **52**(9): p. 6959-6963.
5. Communications, L.H.N.C.f.B., *Fuchs endothelial dystrophy*. U.S. National Library of Medicine, 2017.
6. Eghrari, A.O. and J.D. Gottsch, *Fuchs' corneal dystrophy*. Expert review of ophthalmology, 2010. **5**(2): p. 147-159.
7. Aiken-O'Neill, P. and M.J. Mannis, *Summary of Corneal Transplant Activity: Eye Bank Association of America*. Cornea, 2002. **21**(1): p. 1-3.
8. Gokhale, N.S., *Epidemiology of keratoconus*. Indian Journal of Ophthalmology, 2013. **61**(8): p. 382-383.
9. Riazuddin, S.A., et al., *Missense Mutations in TCF8 Cause Late-Onset Fuchs Corneal Dystrophy and Interact with FCD4 on Chromosome 9p*. The American Journal of Human Genetics. **86**(1): p. 45-53.

10. Adamis, A.P., et al., *Fuchs' endothelial dystrophy of the cornea*. Survey of Ophthalmology, 1993. **38**(2): p. 149-168.
11. Klintworth, G., *Corneal dystrophies*. Orphanet Journal of Rare Diseases, 2009. **4**(1): p. 7.
12. Yue, B.Y., J. Sugar, and K. Schrode, *Histochemical studies of keratoconus*. Curr Eye Res, 1988. **7**(1): p. 81-6.
13. Borderie, V.M., et al., *Outcome of Graft Central Thickness After Penetrating Keratoplasty*. Ophthalmology, 2005. **112**(4): p. 626-633.
14. Ytteborg, J. and C.H. Dohlman, *Corneal edema and intraocular pressure: Ii. clinical results*. Archives of Ophthalmology, 1965. **74**(4): p. 477-484.
15. *Corneal transplants*. Ophthalmic Consultants of Rockland.
<http://www.ocreyemd.com/site/services/corneal-transplant/>.
16. Sobol, A., *Stem cell transplant*. <http://drsobol.com/Default.aspx?blogentryid=23>.
17. *Fuchs' Endothelial Dystrophy*. WillsEye Hospital. <https://www.willseye.org/health-library/fuchs%E2%80%99-endothelial-dystrophy>. .
18. *Keratoconus*. Virginia Eye Consultants.
<https://www.virginiaeyeconsultants.com/procedures/eye-conditions/cornea/keratoconus/>.
19. Brugin, E., et al., *Central Corneal Thickness: Z-Ring Corneal Confocal Microscopy Versus Ultrasound Pachymetry*. Cornea, 2007. **26**(3): p. 303-307
10.1097/ICO.0b013e31802e1dea.
20. Ytteborg, J. and C.H. Dohlman, *Corneal Edema and Intraocular Pressure: II. Clinical Results*. Arch Ophthalmol, 1965. **74**(4): p. 477-484.

21. Taylor, Z.D., et al., *THz and mm-Wave Sensing of Corneal Tissue Water Content: Electromagnetic Modeling and Analysis*. IEEE Transactions on Terahertz Science and Technology, 2015. **5**(2): p. 170-183.
22. Bechmann, M., et al., *Central Corneal Thickness Measurement with a Retinal Optical Coherence Tomography Device Versus Standard Ultrasonic Pachymetry*. Cornea, 2001. **20**(1): p. 50-54.
23. Hitzenberger, C.K., W. Drexler, and A.F. Fercher, *Measurement of corneal thickness by laser Doppler interferometry*. Investigative Ophthalmology & Visual Science, 1992. **33**(1): p. 98-103.
24. ANSI, *Z136.1 - Safe Use of Lasers*. 2007.
25. Bauer, N.J., et al., *Noninvasive assessment of the hydration gradient across the cornea using confocal Raman spectroscopy*. Invest Ophthalmol Vis Sci, 1998. **39**(5): p. 831-5.
26. Bauer, N.J., F. Hendrikse, and W.F. March, *In vivo confocal Raman spectroscopy of the human cornea*. Cornea, 1999. **18**(4): p. 483-8.
27. Fisher, B.T., et al., *Assessment of transient changes in corneal hydration using confocal Raman spectroscopy*. Cornea, 2003. **22**(4): p. 363-70.
28. Tonouchi, M., *Cutting-edge terahertz technology*. Nat Photon, 2007. **1**(2): p. 97-105.
29. Brown, E.R., *Fundamentals of Terrestrial Millimeter-Wave and THz Remote Sensing*. International Journal of High Speed Electronics and Systems, 2003. **13**(04): p. 995-1097.
30. Neil W. Ashcroft, N.D.M., *Solid State Physics*. 1976: Holt, Rinehart and Winston.
31. Yeh, C., F. Shimabukuro, and P.H. Siegel, *Low-loss terahertz ribbon waveguides*. Applied Optics, 2005. **44**(28): p. 5937-5946.

32. Berry, C.W., et al., *Significant performance enhancement in photoconductive terahertz optoelectronics by incorporating plasmonic contact electrodes*. Nature Communications, 2013. **4**: p. 1622.
33. Williams, B.S., et al., *Operation of terahertz quantum-cascade lasers at 164 K in pulsed mode and at 117 K in continuous-wave mode*. Optics Express, 2005. **13**(9): p. 3331-3339.
34. Xu, L., et al. *Metasurface quantum-cascade VECSELs from 2.5 to 3.5 THz*. in *2016 41st International Conference on Infrared, Millimeter, and Terahertz waves (IRMMW-THz)*. 2016.
35. Semenov, A., et al., *Application of Zero-Bias Quasi-Optical Schottky-Diode Detectors for Monitoring Short-Pulse and Weak Terahertz Radiation*. Electron Device Letters, IEEE, 2010. **31**(7): p. 674-676.
36. Kliebisch, O., D.C. Heinecke, and T. Dekorsy, *Ultrafast time-domain spectroscopy system using 10 GHz asynchronous optical sampling with 100 kHz scan rate*. Optics Express, 2016. **24**(26): p. 29930-29940.
37. *Hand-Held THz imaging*; https://www.nasa.gov/pdf/626494main_3-3-A_Zimdars.pdf.
38. Advantest, <https://www.advantest.com/products/terahertz-spectroscopic-imaging-systems/terahertz-wave-spectroscopy-and-imaging-analysis-platform>.
39. Kindt, J.T. and C.A. Schmuttenmaer, *Far-Infrared Dielectric Properties of Polar Liquids Probed by Femtosecond Terahertz Pulse Spectroscopy*. The Journal of Physical Chemistry, 1996. **100**(24): p. 10373-10379.
40. Smye, S.W., et al., *The interaction between Terahertz radiation and biological tissue*. Physics in Medicine and Biology, 2001. **46**(9): p. R101.

41. van Exter, M., C. Fattinger, and D. Grischkowsky, *Terahertz time-domain spectroscopy of water vapor*. Optics Letters, 1989. **14**(20): p. 1128-1130.
42. Taylor, Z.D., et al., *THz Medical Imaging: in vivo Hydration Sensing*. Terahertz Science and Technology, IEEE Transactions on, 2011. **1**(1): p. 201-219.
43. Liebe, H., G. Hufford, and T. Manabe, *A model for the complex permittivity of water at frequencies below 1 THz*. International Journal of Infrared and Millimeter Waves, 1991. **12**(7): p. 659-675.
44. Ronne, C., et al., *Investigation of the temperature dependence of dielectric relaxation in liquid water by THz reflection spectroscopy and molecular dynamics simulation*. The Journal of Chemical Physics, 1997. **107**(14): p. 5319-5331.
45. Echchgadda, I., et al., *Using a portable terahertz spectrometer to measure the optical properties of in vivo human skin*. Journal of Biomedical Optics, 2013. **18**(12): p. 120503-120503.
46. Pickwell, E., et al., *In vivo study of human skin using pulsed terahertz radiation*. Phys Med Biol, 2004. **49**(9): p. 1595.
47. Pickwell, E. and V.P. Wallace, *Biomedical applications of terahertz technology*. Journal of Physics D: Applied Physics, 2006. **39**(17): p. R301.
48. Ashworth, P.C., et al., *Terahertz pulsed spectroscopy of freshly excised human breast cancer*. Optics Express, 2009. **17**(15): p. 12444-12454.
49. Landauer, R., *Electrical conductivity in inhomogeneous media*. AIP Conference Proceedings, 1978. **40**(1): p. 2-45.

50. Karkkainen, K.K., A.H. Sihvola, and K.I. Nikoskinen, *Effective permittivity of mixtures: numerical validation by the FDTD method*. Geoscience and Remote Sensing, IEEE Transactions on, 2000. **38**(3): p. 1303-1308.
51. Niklasson, G.A., C.G. Granqvist, and O. Hunderi, *Effective medium models for the optical properties of inhomogeneous materials*. Appl. Opt., 1981. **20**(1): p. 26-30.
52. Devaty, R.P. and A.J. Sievers, *Far-Infrared Absorption by Small Metal Particles*. Physical Review Letters, 1984. **52**(15): p. 1344-1347.
53. Puranik, S.M., A.C. Kumbharkhane, and S.C. Mehrotra, *The static permittivity of binary mixtures using an improved bruggeman model*. Journal of Molecular Liquids, 1994. **59**(2): p. 173-177.
54. Maccabi, A., et al. *Reflectivity measurements of water and dioxane mixtures using a 100 GHz Gunn diode source*. 2013.
55. Salhi, M.A., I. Pupeza, and M. Koch, *Confocal THz Laser Microscope*. Journal of Infrared, Millimeter, and Terahertz Waves, 2010. **31**(3): p. 358-366.
56. Ruth, M.W., et al., *Terahertz pulse imaging in reflection geometry of human skin cancer and skin tissue*. Physics in Medicine and Biology, 2002. **47**(21): p. 3853.
57. Grossman, E., et al., *Passive terahertz camera for standoff security screening*. Applied Optics, 2010. **49**(19): p. E106-E120.
58. Bowman, T., M. El-Shenawee, and L.K. Campbell, *Terahertz transmission vs reflection imaging and model-based characterization for excised breast carcinomas*. Biomedical Optics Express, 2016. **7**(9): p. 3756-3783.
59. Goldsmith, P.F., *Quasi-optical techniques*. Proceedings of the IEEE, 1992. **80**(11): p. 1729-1747.

60. Siegman, A.E., *Lasers*. 1986.
61. Goldsmith, P.F., *Quasioptical Systems*. 1998: Wiley.
62. Murphy, J.A., *Distortion of a simple Gaussian beam on reflection from off-axis ellipsoidal mirrors*. International Journal of Infrared and Millimeter Waves, 1987. **8**(9): p. 1165-1187.
63. Diodes, V., *Nominal Horn Specifications*.
http://vadiodes.com/images/AppNotes/VDI_Feedhorn_Summary_2016.02.pdf.
64. Sung, S., *Terahertz Imaging and Remote Sensing Design for Applications in Medical Imaging*. 2013.
65. Azartash, K., et al., *Pre-corneal tear film thickness in humans measured with a novel technique*. Mol Vis, 2011. **17**: p. 756-67.
66. King-Smith, P.E., et al., *The thickness of the human precorneal tear film: evidence from reflection spectra*. Invest Ophthalmol Vis Sci, 2000. **41**(11): p. 3348-59.
67. Dong, J., Q. Wu, and X.G. Wang, *Measurement of central corneal thickness and pre-corneal tear film thickness of rabbits using the Scheimpflug system*. Int J Ophthalmol, 2013. **6**(5): p. 584-7.
68. King-Smith, P.E., S.H. Kimball, and J.J. Nichols, *Tear film interferometry and corneal surface roughness*. Invest Ophthalmol Vis Sci, 2014. **55**(4): p. 2614-8.
69. Xu, J., et al., *0.15-3.72 THz absorption of aqueous salts and saline solutions*. Applied Physics Letters, 2007. **90**(3): p. 031908-031908-3.
70. Born, M. and E. Wolf, *Principles of optics: electromagnetic theory of propagation, interference and diffraction of light*. 1980: Cambridge University Press.

71. Fatt, I. and T.K. Goldstick, *Dynamics of water transport in swelling membranes*. Journal of Colloid Science, 1965. **20**(9): p. 962-989.
72. Spoler, F., M. Frentz, and N.F. Schrage, *Towards a new in vitro model of dry eye: the Ex Vivo Eye Irritation Test*. Dev Ophthalmol, 2010. **45**: p. 93-107.
73. Glass, D.H., et al., *A Viscoelastic Biomechanical Model of the Cornea Describing the Effect of Viscosity and Elasticity on Hysteresis*. Investigative Ophthalmology & Visual Science, 2008. **49**(9): p. 3919-3926.
74. Bennett, D., et al., *Assessment of corneal hydration sensing in the terahertz band: in vivo results at 100 GHz*. Journal of Biomedical Optics, 2012. **17**(9): p. 097008-1.
75. Taylor, Z.D., et al., *Analysis of Pulsed THz Imaging Using Optical Character Recognition*. Sensors Journal, IEEE, 2009. **9**(1): p. 3-8.
76. Bennett, D.B., et al., *Terahertz sensing in corneal tissues*. Journal of Biomedical Optics, 2011. **16**(5): p. 057003-057003.
77. Tewari, P., et al., *In vivo terahertz imaging of rat skin burns*. Journal of Biomedical Optics, 2012. **17**(4): p. 040503-3.
78. Bennett, D.B., et al., *Stratified Media Model for Terahertz Reflectometry of the Skin*. IEEE Sensors Journal, 2010. **11**(5): p. 1530-437X.
79. Taylor, Z.D., et al., *Reflective terahertz imaging of porcine skin burns*. Opt. Lett., 2008. **33**(11): p. 1258-1260.
80. Taylor, Z.D., et al., *THz and mm-Wave Sensing of Corneal Tissue Water Content: Electromagnetic Modeling and Analysis*. Terahertz Science and Technology, IEEE Transactions on, 2015. **5**(2): p. 170-183.

81. Taylor, Z.D., et al., *THz and mm-Wave Sensing of Corneal Tissue Water Content: In Vivo Sensing and Imaging Results*. Terahertz Science and Technology, IEEE Transactions on, 2015. 5(2): p. 184-196.
82. Maccabi, A., et al. *Reflectivity Measurements of Water and Dioxane Mixtures using a 100 GHz Gunn Diode Source*. in *SPIE Terahertz and Ultrashort Electromagnetic Pulses for Biomedical Applications I*. 2013. San Francisco: SPIE.
83. Bajwa, N., et al. *Reflective THz and MR imaging of burn wounds: a potential clinical validation of THz contrast mechanisms*. in *SPIE Terahertz Emitters, Receivers, and Applications III*. 2012. San Diego, CA.
84. Taylor, Z.D., et al. *THz imaging using broadband direct detection*. in *SPIE Terahertz, RF, Millimeter, and Submillimeter-Wave Technology and Applications VI*. 2013. San Francisco: SPIE.
85. Tewari, P., et al. *Terahertz imaging of biologic tissues*. in *Medicine Meets Virtual Reality*. 2011. Long Beach.
86. Taylor, Z.D., et al. *THz Medical Imaging*. in *6th ESA Workshop on millimetre Wave technology and applications and 4th Global symposium on millimeter Waves*. 2011. Helsinki, Finland.
87. Tewari, P., et al. *Advances in biomedical imaging using THz technology with applications to burn-wound assessment*. in *SPIE Terahertz Technology and Applications V*. 2012. San Francisco, CA.
88. http://spaceklabs.com/cm/Products/Frequency_Sources/Gunn%20Oscillators.html.
89. <https://www.gentec-eo.com/products/thz-detectors>.

90. Lamb, J.W., *Miscellaneous data on materials for millimetre and submillimetre optics*. International Journal of Infrared and Millimeter Waves, 1996. **17**(12): p. 1997-2034.
91. Sung, S., et al. *Reflective measurement of water concentration using millimeter wave illumination*. in *SPIE Health Monitoring of Structural and Biological Systems 2011*. 2011. San Diego, CA.
92. Taylor, Z.D., et al. *THz imaging based on water-concentration contrast*. in *SPIE Terahertz for Military and Security Applications VI*. 2008. Orlando, FL, USA: SPIE.
93. Xiong, C., et al., *A Rabbit Dry Eye Model Induced by Topical Medication of a Preservative Benzalkonium Chloride*. Investigative Ophthalmology & Visual Science, 2008. **49**(5): p. 1850-1856.
94. Hunter, P.A., et al., *Corneal graft rejection: a new rabbit model and cyclosporin-A*. British Journal of Ophthalmology, 1982. **66**(5): p. 292-302.
95. Gimbrone, M.A., et al., *Tumor Growth and Neovascularization: An Experimental Model Using the Rabbit Cornea*. Journal of the National Cancer Institute, 1974. **52**(2): p. 413-427.
96. Taylor, Z.D., et al., *THz and mm-Wave Sensing of Corneal Tissue Water Content: In Vivo Sensing and Imaging Results*. IEEE Transactions on Terahertz Science and Technology, 2015. **5**(2): p. 184-196.
97. Hesler, J.L. and T.W. Crowe. *NEP and responsivity of THz zero-bias Schottky diode detectors*. in *Infrared and Millimeter Waves, 2007 and the 2007 15th International Conference on Terahertz Electronics. IRMMW-THz. Joint 32nd International Conference on*. 2007.

98. Ehlers, N. and J. Hjortdal, *Corneal thickness: measurement and implications*. Experimental Eye Research, 2004. **78**(3): p. 543-548.
99. Ruberti, J.W. and S.D. Klyce, *NaCl osmotic perturbation can modulate hydration control in rabbit cornea*. Exp Eye Res, 2003. **76**(3): p. 349-59.
100. Bogan, S.J., et al., *Classification of normal corneal topography based on computer-assisted videokeratography*. Archives of Ophthalmology, 1990. **108**(7): p. 945-949.
101. Hockwin, O., et al., *Biometry of the Anterior Eye Segment by Scheimpflug Photography*. Ophthalmic Research, 1983. **15**(2): p. 102-108.
102. Applegate, R.A. and H.C. Howland, *Noninvasive measurement of corneal topography*. IEEE Engineering in Medicine and Biology Magazine, 1995. **14**(1): p. 30-42.
103. SCHWIEGERLING, J. and J.E. GREIVENKAMP, *Using Corneal Height Maps and Polynomial Decomposition to Determine Corneal Aberrations*. Optometry & Vision Science, 1997. **74**(11): p. 906-916.
104. Hjortdal, J.Ø., L. Erdmann, and T. Bek, *Fourier analysis of video-keratographic data. A tool for separation of spherical, regular astigmatic and irregular astigmatic corneal power components*. Ophthalmic and Physiological Optics, 1995. **15**(3): p. 171-185.
105. RAASCH, T.W., *Corneal Topography and Irregular Astigmatism*. Optometry & Vision Science, 1995. **72**(11): p. 809-815.
106. Snyder, J.P., *Map projections used by the U.S. Geological Survey*. USGS Numbered Series, 1982. **1532**: p. 101.
107. Nuria Llombart Juan, S.D. TU Delft.
108. Taylor, Z.D., et al. *Optical design for translation of THz medical imaging technology*. 2014.

109. Murphy, J.A., *Distortion of a simple Gaussian beam on reflection from off-axis ellipsoidal mirrors*. International Journal of Infrared and Millimeter Waves. **8**(9): p. 1165-1187.
110. Jakus, M.A., *STUDIES ON THE CORNEA. II. THE FINE STRUCTURE OF DESCHEMET'S MEMBRANE*. The Journal of Biophysical and Biochemical Cytology, 1956. **2**(4): p. 243-252.
111. Ramundo-Orlando, A., et al., *Permeability changes induced by 130 GHz pulsed radiation on cationic liposomes loaded with carbonic anhydrase*. Bioelectromagnetics, 2007. **28**(8): p. 587-598.
112. Olshevskaya, J.S., et al. *Effect of terahertz electromagnetic waves on neurons systems*. in *Computational Technologies in Electrical and Electronics Engineering, 2008. SIBIRCON 2008. IEEE Region 8 International Conference on*. 2008.
113. GP, G., *THz-BRIDGE Final Report: Tera-Hertz radiation in Biological Research, Investigations on Diagnostics and study on potential Genotoxic Effects*. 2004. **THz BRIDGE Project**: p. 1-72.
114. *IEEE Standard for Safety Levels with Respect to Human Exposure to Radio Frequency Electromagnetic Fields, 3 kHz to 300 GHz*. IEEE Std C95.1-2005 (Revision of IEEE Std C95.1-1991), 2006: p. 1-238.
115. Wilmink, G.J., et al., *In vitro investigation of the biological effects associated with human dermal fibroblasts exposed to 2.52 THz radiation*. Lasers in Surgery and Medicine, 2011. **43**(2): p. 152-163.
116. Wilmink, G.J., et al. *Determination of death thresholds and identification of terahertz (THz)-specific gene expression signatures*. 2010. San Francisco, California, USA: SPIE.

117. Korenstein-Ilan, A., et al., *Terahertz Radiation Increases Genomic Instability in Human Lymphocytes*. Radiation Research, 2008. **170**(2): p. 224-234.
118. Bock, J., et al., *Mammalian Stem Cells Reprogramming in Response to Terahertz Radiation*. PLOS ONE, 2011. **5**(12): p. e15806.
119. Alexandrov, B.S., et al., *Non-thermal effects of terahertz radiation on gene expression in mouse stem cells*. Biomedical Optics Express, 2011. **2**(9): p. 2679-2689.
120. Alexandrov, B.S., et al., *Specificity and Heterogeneity of Terahertz Radiation Effect on Gene Expression in Mouse Mesenchymal Stem Cells*. Scientific Reports, 2013. **3**: p. 1184.
121. Kues, H.A., et al., *Absence of ocular effects after either single or repeated exposure to 10 mW/cm² from a 60 GHz CW source*. Bioelectromagnetics, 1999. **20**(8): p. 463-473.
122. Withayachumnankul, W. and M. Naftaly, *Fundamentals of Measurement in Terahertz Time-Domain Spectroscopy*. Journal of Infrared, Millimeter, and Terahertz Waves, 2014. **35**(8): p. 610-637.
123. Middendorf, J.R., et al., *High Fill-Factor Substrate-Based Wire-Grid Polarizers With High Extinction Ratios*. IEEE Transactions on Terahertz Science and Technology, 2014. **4**(3): p. 376-382.